HARVARD
Kenneth C. Griffin

GRADUATE SCHOOL
OF ARTS AND SCIENCES

DISSERTATION ACCEPTANCE CERTIFICATE

The undersigned, appointed by the

Harvard John A. Paulson School of Engineering and Applied Sciences
have examined a dissertation entitled:

"Interferometry of Integer and Fractional Quantum Hall Edge States in Graphene"

presented by: Thomas Werkmeister

Signature _____
Typed name: Professor Philip Kim

Signature _____
Typed name: Professor Donhee Ham

Signature _____
Typed name: Professor Bertrand Halperin

Date: April 29, 2025

Interferometry of Integer and Fractional Quantum Hall Edge States in Graphene

A dissertation presented
by
Thomas Werkmeister
to
The School of Engineering and Applied Sciences

in partial fulfillment of the requirements
for the degree of
Doctor of Philosophy
in the subject of
Applied Physics

Harvard University
Cambridge, Massachusetts
April 29, 2025

©2025 – Thomas Werkmeister
all rights reserved.

Thesis advisor: Professor Philip Kim Thomas Werkmeister

Interferometry of Integer and Fractional Quantum Hall Edge States in Graphene

Abstract

In this thesis, we develop Fabry-Pérot quantum Hall interferometers in graphene and measure anyon braiding in the fractional quantum Hall effect. Our results demonstrate the potential of van der Waals materials for constructing quantum coherent electronic devices with advanced functionalities in order to unveil a wealth of physics that is otherwise inaccessible via transport measurements. We begin by first demonstrating clear Aharonov-Bohm resistance oscillations in integer quantum Hall states, overcoming a major technical challenge of "Coulomb dominated" oscillations, which plagued decades of experiments in traditional semiconductor-based platforms. Next, we develop an improved, density-tunable interferometer and measure tunable Coulomb coupling between copropagating integer edge states, revealing the physics behind anomalous interference phase jumps and Aharonov-Bohm oscillation frequency doubling in the integer quantum Hall effect. Similar observations in other semiconductor platforms had been unexplained for a decade. The combined theoretical developments and precise tuning knobs added by our work enable further experiments probing correlations in strongly coupled one-dimensional chiral edge channels. Finally, we observe robust Aharonov-Bohm oscillations in two distinct fractional quantum Hall states, filling fractions $\nu = 1/3$ and $\nu = 4/3$, and discover 3-state telegraph noise consistent with localized anyon number fluctuations, which we put to use to directly measure the $\frac{2\pi}{3}$ abelian anyon braiding phase in both states. This final work enables further experiments to demonstrate control of the localized anyon number and eventually measure the braiding properties of non-abelian anyons in even-denominator fractional quantum Hall states. Many open questions, such as whether non-abelian order describes these states, how robust topological order really is, which excitations belong to which fractional states in real devices, and whether we can build a technology leveraging the exotic physics of the fractional quantum Hall effect will soon be directly addressable.

Contents

Title Page **i**

Copyright Page **ii**

Abstract **iii**

Table of Contents **iv**

List of figures **vii**

Dedication **ix**

Acknowledgments **x**

1 Introduction **1**
- 1.1 Organization of this thesis 5
- 1.2 Citations to previously published works 6

2 Quantum Hall Anyons in Graphene **7**
- 2.1 Identical particles in two dimensions: emergent anyons 8
- 2.2 Graphene: atomically thin electrons 15
- 2.3 Landau levels and quantum Hall ferromagnetism 23
- 2.4 Edge states and ballistic current 32
- 2.5 Fractional quantum Hall anyons and topological quantum bits 37
- 2.6 Edge state interferometers 44
- 2.7 Summary 48

3 Experimental Methods **49**
- 3.1 Assembling van der Waals heterostructures 49
- 3.2 Constructing gate-defined interferometers 55
- 3.3 Performing low electron temperature transport measurements 57

3.4 Summary 60

4 Integer Aharonov-Bohm Interference **61**
4.1 Design of the graphene-based interferometer 64
4.2 Tunable quantum point contact architecture 66
4.3 Fabry-Pérot interferometer 68
4.4 Aharonov-Bohm vs. Coulomb dominated oscillations 69
4.5 Coherence lengths and edge mode velocities 71
4.6 Conclusion 76

5 Strongly Coupled Integer Edge States **77**
5.1 Improved interferometer design and tuning 80
5.2 Phase jumps and AB oscillation frequency transition 82
5.3 AB frequency doubling from strongly coupled QHE edge states 87
5.4 Conclusion 91

6 Fractional Interference: Anyon Braiding and Fluctuations **92**
6.1 Tuning for fractional quantum Hall interference 94
6.2 Three-state anyon telegraph noise 96
6.3 Aharonov-Bohm magnetic field dependence 98
6.4 Telegraph noise across the quantum Hall plateau 101
6.5 Temperature scaling of telegraph noise 104
6.6 Conclusion 107

7 Discussion and Outlook **108**

Appendix A Additional information for chapter 4 **111**
A.1 QPC operation 111
A.2 Phase coherence length analysis 113
A.3 Interference in various bulk integer fillings and plunger gate capacitance 119
A.4 Visibility decay with temperature 122
A.5 Interference of additional integer edge in fractional bulk filling 123

Appendix B Additional information for chapter 5 **124**
B.1 Device characterization and QPC operation 124
B.2 Weak and strong backscattering limits 128
B.3 Temperature and finite source-drain bias dependence 130
B.4 Additional interference data across coupling transition 131
B.5 Estimation of the coupling strength 136
B.6 Physics of AB frequency doubling at strong coupling 138
B.7 Influence of bulk-edge coupling and screening by nearby gates 139

B.8 Robustness of the theoretical predictions 141

Appendix C Additional information for chapter 6 **143**
C.1 Device tuning details 143
C.2 Algorithm used for determining RTN switching events 149
C.3 Phase fitting and uncertainty 150

References **175**

List of Figures

2.1 Configuration space of indistinguishable particles in 2D . . . 12
2.2 Configuration space of indistinguishable particles in 3D . . . 15
2.3 Graphene lattice and low-energy band structure . . . 19
2.4 Graphene single-particle Landau levels . . . 28
2.5 Symmetry broken Landau levels . . . 31
2.6 Edge states and Hall transport measurement . . . 34
2.7 Edge state interferometers in GaAs . . . 45
2.8 Fabry–Pérot quantum Hall interferometer . . . 46

3.1 Stacking procedure . . . 52
3.2 Cleaning van der Waals interface . . . 54
3.3 Nanofabrication process schematic. . . . 56
3.4 Interferometer fabrication. . . . 58

4.1 Gate-defined Fabry-Pérot interferometer in graphene . . . 64
4.2 Fabry-Pérot device and measurement schematic . . . 65
4.3 Tunable QPCs and oscillations controlled by plunger gate . . . 67
4.4 Aharonov-Bohm (AB) dominated Fabry-Pérot interference . . . 70
4.5 Gate vs. etch defined interferometer . . . 72
4.6 Edge mode velocity and comparison of oscillations in different filling factors . . . 74
4.7 Aharonov-Bohm interference of an integer edge with a fractional bulk filling . . . 75

5.1 Highly tunable Fabry-Pérot interferometer in graphene . . . 81
5.2 Density-tuned Aharonov-Bohm frequency doubling transition . . . 84
5.3 Phase jump extraction in the transition regime . . . 86
5.4 Inner and outer EC interference and couplings across transition . . . 89

6.1 Graphene FQH interferometer telegraph noise . . . 95
6.2 Aharonov-Bohm magnetic field trend of $\nu = \frac{1}{3}$ branches . . . 99
6.3 Phase fitting and uncertainty. . . . 101
6.4 Telegraph noise dependence on filling in $\nu = \frac{1}{3}$ . . . 102

6.5 Temperature dependent telegraph noise and visibility in $\nu = \frac{1}{3}$ 104
6.6 Wiring schematic and effect of shielding on telegraph noise 106

A.1 QPC operating at various bulk fillings. 112
A.2 Gate voltages used to set QPC operating points for interferometer 113
A.3 Theoretical plots of oscillation amplitude and shape with finite phase coherence. . 114
A.4 Extracting phase coherence length from oscillation amplitude. 115
A.5 Example fitting to a particular sampling of visibility over QPC transmissions. . . . 116
A.6 $R_{\mathrm{T}}(B)$ and its FFT taken at $\nu_{\mathrm{PG}} = 1.67$, corresponding to region III. 118
A.7 $R_{\mathrm{T}}(V_{\mathrm{PG}}, B)$ and its 2D-FFT near $\nu_{\mathrm{PG}} = 1.67$, corresponding to region III. . . . 118
A.8 AB interference in the (B, V_{PG}) plane for various integer edges. 119
A.9 Plunger gate periodicity for various edge configurations. 120
A.10 Plunger gate to edge channel capacitance C_{EG} as a function of V_{PG}. 121
A.11 Fitting the decay of visibility with temperature for the inner edge for $\nu_{\mathrm{B}} = 2$. . . . 122
A.12 Integer interference with fractional bulk filling. 123

B.1 Device image and gating structure. 126
B.2 Device quantum Hall characterization. 127
B.3 QPC tuning via back and split gates. 129
B.4 Weak and strong backscattering limits of intermediate-coupling regime. 130
B.5 Temperature dependence of intermediate-coupling regime. 131
B.6 Finite-bias dependence of outer EC interference. 132
B.7 Comparison of the outer and inner EC interference for different parameters. . . . 133
B.8 Magnetic field dependence of outer EC interference through the transition. 134
B.9 Magnetic field dependence of inner EC interference through the transition. 135
B.10 Interference of a single edge into a dual-edge cavity. 136
B.11 Extracted radii and EC separation through the periodicity transition. 140

C.1 Device contacts, gates, and measurement schemes. 145
C.2 QPC tuning details in $\nu = \frac{4}{3}$ and $\nu = \frac{1}{3}$. 146
C.3 Interwoven conductance branches extracted from static measurements in $\nu = \frac{1}{3}$. . 147
C.4 Magnetic field dependence in $\nu = \frac{4}{3}$. 148
C.5 Branch switching detection algorithm. 150
C.6 Plateau analysis of RTN for $\nu = \frac{4}{3}$. 152
C.7 $\nu = \frac{4}{3}$ RTN temperature scaling. 153

To my family, and to all future scholars.

Acknowledgments

The PhD is a long and life-changing journey, which I feel that I could never have finished without the support of many people. I will acknowledge a few of these people here, but I want to thank every person over the years who made the journey possible and enjoyable.

First and foremost, I thank my advisor, Philip Kim, for guiding me through this voyage over the past seven and a half years. I feel exceptionally lucky to have been able to work with and learn from Philip over the years, and I am grateful to have had an advisor who always encouraged and supported me, both scientifically and personally. Philip is an extremely creative and passionate scientist, and equally important, he is a wise and kindhearted person. I always left meetings with Philip feeling excited about my research and inspired to continue exploring. Though he is an extremely busy professor, I always felt that Philip was available and eager to discuss with me; he always makes time for his students, always responding to emails and setting up meetings promptly, even when there seems to be an insurmountable time zone difference. I learned much more than would be possible to write down from Philip, both as a scientist and as a person, and I aspire to be a great mentor like him one day.

I thank my committee members over the years, Bert Halperin, Amir Yacoby, and Donhee Ham. It has been a great privilege to have lively discussions about both experimental data and theory with Bert and Amir, and I am very grateful to have benefited from their extremely deep insights and crucial guidance at various stages of my PhD. This thesis certainly could not have been completed without their support, and my thanks extends to their collaborators and students who they brought into the efforts. In particular, I thank Marie Wesson and Andrew Pierce, who each were a joy to work with and who ensured that two of Amir's bespoke dilution fridges, codenamed MX400 and Frossati, worked for all of the experiments in this thesis. I also thank Dima Feldman and Zezhu Wei, who worked with Bert and us on explaining our coupled integer edge state data and took many train trips from Providence for our discussions. Lastly, a special thanks goes to Donhee Ham for being an extremely effective lecturer (I strive to become so good one day!), teaching me much about quantum Hall physics in my first year of graduate school, and for ensuring that the final few weeks of my time at Harvard went smoothly by serving on my thesis committee at the last minute. Bert, Amir, and Donhee have been deeply inspirational for me over the years, and I cannot thank them enough.

Next, I thank the many wonderful people who I had the opportunity to work with in Philip's lab. I am extremely grateful to have had Yuval Ronen as a postdoc mentor and collaborator over the first four and a half years or so of my PhD. Yuval started around the same time as I did in Philip's lab with

coincidentally very similar research interests, and he was extremely generous in teaching me nearly everything to do with experimental physics from scratch. We share too many happy and interesting memories working in the cleanroom, at Maglab, and at the Frossati fridge together to write here. I again consider myself lucky beyond measure to have had his great mentorship and guidance through my PhD, both scientifically and personally. At critical moments when I need a push, I still hear "Yalla!" in my head, while at equally crucial moments when it is better to stop and think, I hear "Slowly..." among many other characteristic slogans in various languages that Yuval created.

The interferometry subgroup that started out as me and Yuval has grown and evolved over the years. For the first half of my PhD, I enjoyed working with Danial Haei Najafabadi, who put in enormous efforts to perfect the van der Waals transfer techniques necessary for creating large-area bubble-free stacks at the time, and I enjoyed mentoring a hard-working undergrad student Bobae Johnson and stacking under the extremely patient guidance of Si Young Lee. I again feel incredibly lucky to have been able to work with James Ehrets, who brought some much-needed electronics design expertise as well as many physics insights to the subgroup. We had the interesting experience of beginning to work together over zoom during the COVID-19 lockdown, and from then (which feels like a lifetime ago!) until now it has always been fruitful and fun to work with James. Lastly, I thank Christina Henzinger, who I have had the pleasure of mentoring even before she joined the interferometry subgroup in the last year. I am confident that James and Christina can take interferometry to the next level and succeed in any experiments that they pursue, and I thank them for being excellent collaborators.

In addition to quantum Hall interferometry, it was great to collaborate with and learn from Joon Young Park on topological insulators and superconductors in the second half of my PhD. Though these experiments are a bit too different to write about in this thesis, they were equally interesting and challenging, and I always enjoyed discussing the deep physics of the Josephson effects and our often unexpected data with Joon Young. Like the quantum Hall experiments, this research benefited from several generations of collaborators, from Yuval in the early stages to Laurel Anderson (who I also enjoyed collaborating with on graphene quantum dot physics and having many fab discussions!), theory collaborators Omri Lesser and Yuval Oreg, and finally Jonathan Zauberman for the final round of devices and control devices. It has been a pleasure to work with each of you!

Outside of the Kim lab, I also enjoyed collaborating with folks down the street at MIT and in other labs at Harvard. In particular, I thank Sameia Zaman, Liqiao Xia, Sergio de la Barrera, and Aviram Uri from MIT for collaborations and very interesting discussions. I also thank Christina Spägele for sharing some of her optics expertise with me and collaborating on her experiments.

Besides the people who I collaborated with, I am thankful for the many fun and pleasant people who made spending time in lab enjoyable over the years. In the Kim lab, I enjoyed working alongside everyone including Xiaomeng Liu, Austin Cheng, Nicola Poccia, Jonah Waissman, Ke Wang, Young Jae Shin, Hyobin Yoo, Hiroshi Idzuchi, Luis Jauregui, Jing Shi, Katie Huang, Andy Joe, Frank Zhao, Rebecca Engelke, Mehdi Rezaee, Artem Talanov, Onder Gul, Zeyu Hao, Zhongying Yan, Alex Cui, Andrés Valdivia, Isabelle Phinney, Tamar Mentzel, Andrew Zimmerman, Antti Laitinen, Dapeng Ding, Qi Yang, Thao Dinh, Abhishek Banerjee, Terry Phang, Grace Chen, Kierstin Torres, Nadine Leisgang, Jue Wang, Sejoon Lim, Talieh Ghiasi, Gabriele Pasquale, Jun Wei Lam, Sangmin Lee, and Hong Kuan Ng. I particularly thank my office-mates Zhongying, Jonathan, Laurel, and Andrés dur-

ing the majority of the PhD for making LISE 404 a pleasant office, and I thank Isabelle and James for their friendship and the many interesting conversations and happy memories we shared over the years. I am also deeply thankful for everyone in the Yacoby lab who has made it a very stimulating workplace and a fun place to hang out when not doing work. These many friends include Zihan Yan, Nick Poniatowski, Elizabeth Park, Ruolan Xue, Nikola Maksimovic, Zhuozhen Cai, Shantam Ravan, Johannes Cremer, Dan Fernandez, Guo Yu, Yiran Zhang, Anuva Aishwarya, Marie Wesson, Jann Ungerer, Zui Tao, Yuan Cao, Patrick Forrester, Taeho Kim, Shaowen Chen, Ziwei Qiu, Andrew Pierce, Seung Hwan Lee, Charlotte Bøettcher, and DiDi Wei. I particularly thank Marie for being a kind friend and for heroically rescuing me when an over-pressurized oil pump exploded, and I thank Seung Hwan, Andrew, Patrick, Zihan, and Nick for their friendship and for sharing lunch over the years. Thank you all for our many humorous and often philosophical conversations!

Graduate school can be very difficult at times, requiring great mental strength to keep going. I thank my family for their love and support over the years that kept my spirits up. Nothing in my life would be possible without the courage to pursue challenges and persevere through hardships that they instilled in me as a child, and I thank them for always nurturing my dreams and sending me warmth from far away. I thank my parents and my late grandparents for teaching me to read and to explore many creative pursuits at a young age, sparking my interests both in figuring out how things work and imagining how things may work better in the future. I am especially grateful to my late grandfather for sharing his passion for repairing electronics and old gadgets with me, which turns out to be a vital skill for experimental physics. I am also grateful for the many evening phone calls with my parents and late grandmother over the years, which often gave me the calm strength to keep going. Thank you for all of your wisdom and care!

Last but certainly not least, I thank my partner Yujie for our many adventures as we journeyed through graduate school together. My luckiest break was meeting her during our first year at Harvard, both of us living in a GSAS residence hall, and I feel fortunate that we continue to support each other over the many ups and downs of life. Through our many late nights studying together, brainstorming our research directions, and debating our thoughts, she has given me extremely insightful support and advice, allowing me to see further and think deeper at each step. I thank her for her indomitable spirit and her contagious enthusiasm, both for our careers and lives. She inspires me daily to strive for excellence and to explore the frontiers of knowledge; I owe my successes to her!

This thesis is dedicated to all of you and to the next generations of scholars. Thank you all!

To see a world in a grain of sand
And a heaven in a wild flower,
Hold infinity in the palm of your hand
And eternity in an hour.

William Blake

1

Introduction

One is drawn to studying physics by the desire to explain and predict phenomena. There has been great success in finding elementary principles regarding fundamental particles, such as quarks, electrons, and photons, and describing higher-level phenomena such as protons, neutrons, atoms, and their interactions in terms of the fundamental particles. Moving to higher levels, the utility of the original objects often wanes; for example, we find little use of quarks, electrons, or even atoms in

explaining the boiling of water. Rather, we must consider the intermolecular forces between H_2O molecules, which emerge as new objects, each composed of two hydrogen atoms bonded by shared electrons to oxygen. Nevertheless, in many cases, the properties of the emergent objects can be derived directly from their constituents. The charge of a proton is the sum of the charges of the quarks it contains, while the charge of a nucleus is the sum of the charges of the protons it consists of. Such hierarchical patterns of emergent objects composed of different, more fundamental objects repeat across physics and the sciences in general. One often begins the study of physics with a strong belief in the principle of *reductionism*, that properties of complex systems can always be constructed from simpler, fundamental objects and laws.

However, one is eventually faced with exceptions which prove more interesting than the rule. In the condensed matter systems of concern in this thesis, which are composed of periodically arranged atoms bonded together to form crystals with enormous numbers of itinerant electrons, reductionism must be abandoned in favor of a new principle called *emergence*. Even though we can write down microscopically correct Hamiltonians and imagine solving for equations of motion for the electrons in the crystal, we would not know what information to glean from the vast number of equations that would come out, let alone how to solve for such equations including interactions. In other words, the *scale* and *complexity* of the problem precludes efforts to construct phenomena from microscopic fundamentals. Instead, to make progress, we cut off the hierarchy and search for new organizational principles and objects within (and emerging from) the more complex level, often without reference to any fundamental constituents. The phrase "more is different" summarizes this sentiment [1,2].

While hints of this idea existed in previous physical theories including the statistical mechanics of the 19th century, it has grown to increasing prominence in condensed matter physics since the experimental discovery of the quantum Hall effect in 1980 by von Klitzing, Dorda, and Pepper [3,4]. In this pioneering experiment, it was found that the Hall conductivity σ_{xy} of electrons confined to a two-dimensional (2D) plane and exposed to a strong out-of-plane magnetic field becomes exactly

quantized in integer multiples of $\frac{e^2}{h}$ while the longitudinal conductivity σ_{xx} vanishes, where e is the electron and h is Planck's constant. The observation that a large-scale chunk of material, including countless numbers of electrons, defects, and impurities, could exhibit electrical conductivity that is precisely quantized in units of fundamental constants caused a paradigm shift in condensed matter physics.

Theory rapidly developed and explained the exact quantization using certain global properties that are insensitive to microscopic details and thus apply equally well to any two-dimensional electron system in a large enough magnetic field [5,6,7,8,9]. Surprisingly, this emergent phenomena called the *integer quantum Hall effect* can be explained using single-particle quantum mechanics (neglecting electron-electron interactions) and the concepts of *localized* and *extended* states. Moreover, the exact integer quantization can be understood to be of an essentially *topological* origin. The set of electron wavefunctions describing quantum Hall states fall into distinct classes defined by a topological invariant i.e. Chern number, also called TKNN invariant in this specific case, which exactly corresponds to the integer Hall conductivity [9]. Changing the integer Chern number requires a global change of the set of occupied states, hence the quantization is robust against local perturbations. In more practical terms for an experimentalist, the integer Chern number and quantized Hall conductivity are directly related to the presence of extended states, called *edge states*, that necessarily exist at the boundaries of a finite two-dimensional sample with populated Landau levels [7]. The edge states closest to the Fermi level (also called *edge channels*) carry the current at low energies in the system while all bulk states are localized, and the quantization arises from the fact that the current propagates ballistically in each Landau level's edge states [10,11,12,13]. For the experimental discovery of the integer quantum Hall effect, von Klitzing was awarded the 1985 Nobel prize in Physics, while the 2016 Nobel laureates were awarded for theoretical developments in topological phases of matter including the TKNN invariant.

In the midst of the developing theoretical understanding of the integer quantum Hall effect, an experimental surprise came in 1982 when Tsui, Störmer, and Gossard discovered that the Hall conduc-

tivity could also be quantized in fractional multiples of $\frac{e^2}{h}$. In particular, they observed a σ_{xy} plateau at precisely $\frac{1}{3}\frac{e^2}{h}$ with an associated σ_{xx} minimum [14]. In a groundbreaking insight, Laughlin showed that this *fractional quantum Hall effect* arises from a novel many-body quantum ground state that admits *fractionally charged* particles as excitations [15]. The proposed ground state, now called the Laughlin state, naturally minimizes the residual electron-electron Coulomb interactions present in the system, which are thus essential to stabilizing the fractional quantum Hall effect, and opens an energy gap within the fractionally-filled Landau level [16]. The fact that a system composed of many interacting electrons, each with charge e, could spontaneously reorganize itself and host charge $\frac{e}{3}$ quasiparticles is a somewhat mind-boggling example of emergence, with many open questions [17], but the existence of fractionally charged quasiparticles is intimately tied to the robustness of the measured fractional quantum Hall plateaus. Additionally, the charge has been directly measured by resonant tunneling [18], quantum shot noise [19,20,21,22], and several other techniques [23,24,25], so the existence of such fractionally charged quasiparticles is well-verified. Tsui, Störmer, and Laughlin were awarded the 1998 Nobel Prize in Physics for discovering "a new quantum fluid with fractionally charged excitations".

Related to yet even more surprising than fractional charge (after all, quarks also have charge $\frac{e}{3}$), these fractional quantum Hall quasiparticles were then shown to have a property unlike any other known particles; they obey neither fermionic nor bosonic *exchange statistics* [26,27]. Therefore, fractional quantum Hall quasiparticles are the first examples of *anyons*, particles postulated to exist in 2D systems that can aquire "any" phase upon identical particle exchange, unlike fermions or bosons [28,29]. Exchange statistics has a profound impact on the behavior of indistinguishable particles in quantum mechanics. For example, the Pauli exclusion principle of electrons and consequently the major structure of the periodic table of elements follows from the fact that electrons are fermions, while many optical phenomena follow directly from the fact that photons are bosons. As an exception to the fermion-boson dichotomy, anyons exhibit fundamentally unique emergent properties, and certain anyons are expected to enable fault-tolerant topological quantum computation [30,31,32,33,34].

1.1 Organization of this thesis

This thesis aims to experimentally measure the exchange statistics of anyons in the fractional quantum Hall effect realized within a single-atom thick crystal of carbon atoms called *graphene*. In particular, we construct edge state interferometers in graphene, where the conductance of the interferometer depends on the self-interference condition of the injected current carried around a confined cavity. We first demonstrate the self-interference condition by measuring Aharonov-Bohm interference of electrons in the integer quantum Hall effect in Chapter 4. We then probe the tunable coupling between co-propagating integer edge channels and the unexpected consequences of this coupling in an improved interferometer design in Chapter 5. Finally, we measure interference in the fractional edge states of $\nu = 1/3$ and $\nu = 4/3$, from which we can extract the anyon's fractional charge as well as the braiding phase shift when the localized quasiparticle number changes in Chapter 6. These form the core results of this thesis, culminating with direct measurements of the abelian anyon exchange statistics through their braiding phase. Before presenting the results, we begin by reviewing the essential theoretical background in Chapter 2 and the experimental methods in Chapter 3.

1.2 Citations to previously published works

The contents of Chapter 4 were previously published in:

Y. Ronen*, **T. Werkmeister***, D. Najafabadi, A. T. Pierce, L. E. Anderson, Y. J. Shin, S. Y. Lee, Y. H. Lee, B. Johnson, K. Watanabe, T. Taniguchi, A. Yacoby, P. Kim.

Aharonov–Bohm effect in graphene-based Fabry–Pérot quantum Hall interferometers.

Nature Nanotechnology 16, 563–569 (2021). Link

The contents of Chapter 5 were previously published in:

T. Werkmeister, J.R. Ehrets, Y. Ronen, M.E. Wesson, D.H. Najafabadi, Z. Wei, K. Watanabe, T. Taniguchi, D.E. Feldman, B.I. Halperin, A. Yacoby, P. Kim.

Strongly coupled edge states in a graphene quantum Hall interferometer.

Nature Communications 15, 6533 (2024). Link

The contents of Chapter 6 were previously published in:

T. Werkmeister*, J.R. Ehrets*, M.E. Wesson, D.H. Najafabadi,, K. Watanabe, T. Taniguchi, B.I. Halperin, A. Yacoby, P. Kim.

Anyon braiding and telegraph noise in a graphene interferometer.

Science 388, 730–735 (2025). Link

* denotes equal contributions.

Nothing in life is to be feared, it is only to be understood.
Now is the time to understand more,
so that we may fear less.

Marie Curie

2

Quantum Hall Anyons in Graphene

An introductory physics student may be surprised to learn that the three-body problem is not analytically solvable. In this thesis, we study condensed matter physics, which concerns the 10^{23}-body problem. Actually, the two-dimensional (2D) materials we use with areas $\sim 1\ \mu\text{m}^2$ have only about 1000 mobile electrons to consider in the states we study. Nevertheless, in these kinds of systems, closed-form solutions are certainly hopeless. One may be further surprised that even brute-force classical

computations are hopeless. Simply recording the quantum state of 1000 interacting electron spins alone requires 2^{1000} coefficients. Current estimates are that all of the known matter in the visible universe amounts to about $\sim 10^{80}$ bits of information [35], which is unfortunately hundreds of orders of magnitude short of even being able to record the complete state, let alone simulate any dynamics. With every bit in use, the most we could record would be a state of about 265 interacting electrons.

All is not lost. Out of the complexity of the dancing electrons, patterns emerge that almost miraculously we can begin to understand. In this chapter, we shall outline the basic phenomenology and robust patterns that emerge when electrons are confined to 2D and placed in large magnetic fields. It turns out that electrons in such a system can and do break the rules that we are familiar with in our ordinary three-dimensional (3D) universe; that is to say, they can behave as emergent particles called anyons, which are unlike all other particles known to exist. Here, we begin by outlining the theoretical foundation of anyons. Then, we proceed with describing the important aspects of the 2D electron system we use, graphene, and the theoretical understanding of the integer and fractional quantum Hall effects in this material. Finally, we explain the tool of electronic interferometry, which we employ in the rest of this thesis to experimentally probe quantum Hall electrons and the emergent anyons in graphene.

2.1 Identical particles in two dimensions: emergent anyons

In introductory quantum mechanics we are taught that there are two fundamental types of indistinguishable (identical) particles that can exist, fermions and bosons (see e.g. refs. [36,37]). The standard justification for this claim is that the physical situation must be unchanged if we make any permutation P of the N indistinguishable particle's coordinates so that we have the constraint

$$|\Psi(P\{x_1, x_2, ..., x_N\})|^2 \equiv |\Psi(x_1, x_2, ..., x_N)|^2$$

where Ψ is the complex-valued many-body wavefunction and $x_i \in \mathbb{R}^d$ stands for the spatial coordinate (for simplicity) of particle i existing in ordinary d-dimensional space $\mathbb{R}^d$. If we now consider the simplest possible permutation P_{ij}, which is simply the exchange $x_i \leftrightarrow x_j$ from which all more complex permutations can be constructed, then we are told that the constraint implies that the eigenvalues of P_{ij} must be ± 1, because repeated action is the identity, $P_{ij}^2 \Psi = \mathbb{I}\Psi$. Explicitly, for the case of two indistinguishable particles we have the exchange statistics

$$\Psi(x_2, x_1) = P_{12}\Psi(x_1, x_2) = \pm\Psi(x_1, x_2)$$

where the option $+1$ defines the particles as bosons and -1 defines fermions. This trivially extends to N indistinguishable particles. Though at first glance the argument appears reasonable, we find that it is unsatisfactory upon close inspection, as it seems to simply reflect a redundancy in our labeling. The particles are meant to be physically indistinguishable, yet we subtly distinguished them in specifying an ordering of x_i in the wavefunction, which we attempt to correct after the fact using the constraint. It is unclear why physical consequences should emerge from our notational inadequacy. It is also unclear to what extent the constraint should practically hold, without considering the physical process that corresponds to permuting the indices. Most importantly, why are ± 1 the only solutions when any phase factor would satisfy the original constrain? It turns out that this argument only happens to give the right exchange statistics for particles living in three or more spatial dimensions ($d \geq 3$) and indeed is incorrect for lower dimensions. The reason for this becomes clear when we construct a more rigorous argument that properly accounts for the *curvature* and *topology* of the indistinguishable particles' configuration space from the beginning, before constructing wavefunctions.

We now briefly sketch why anyons, particles with anyonic exchange statistics (i.e. not ± 1), are mathematically possible in two spatial dimensions, $d = 2$, and why indeed only bosons and fermions are allowed in $d = 3$. Our discussion follows the original paper[28] and Wen[2]. See the chapter by

Myrheim in ref.[38] for more details. A particular configuration of N indistinguishable particles existing in ordinary d-dimensional space $\mathbb{R}^d$ is simply the set of points

$$x = \{x_1, x_2, ..., x_N\} \subset \mathbb{R}^d$$

where, in order to make the particles indistinguishable, we need to enforce that the order in which we list the particle positions is arbitrary, so that the two sets x and Px which differ by a permutation P represent the same configuration of the N-particle system. The set of all possible permutations P of N objects is called the symmetric group S_N, which acts as a group of transformations on $\mathbb{R}^{d \cdot N}$ in our case. The proper configuration space for a system of N indistinguishable particles is thus restricted to the set $\mathbb{R}^{d \cdot N}$ with the identification that $Px = x$ for any $x \in \mathbb{R}^{d \cdot N}$ and any $P \in S_N$. We label this restricted set $\mathbb{R}^{d \cdot N}/S_N$. We can now simplify to center-of-mass and relative coordinates so that

$$\mathbb{R}^{d \cdot N}/S_N = \mathbb{R}^d \times \left(\mathbb{R}^{d \cdot (N-1)}/S_N\right)$$

where $\mathbb{R}^d$ is the center-of-mass configuration space and $\mathbb{R}^{d \cdot (N-1)}/S_N$ is the relative configuration space. To enable visualization, we now specialize to the case of two indistinguishable particles ($N = 2$), though the results generalize to $N > 2$ particles[38], and we focus on the relative configuration space, which contains the curvature and nontrivial topology that affect exchange statistics.

Two indistinguishable particles existing in a two-dimensional plane ($d = 2$) have a relative configuration space given by

$$\mathbb{R}^2/S_2 = \{r \mid_{r \sim -r, r \neq 0}\}$$

where $r = r_1 - r_2$ is the relative coordinate of the two particles, which from now on is simply a point in the relative coordinate space. The identification $r \sim -r$ encodes the fact that the particles are identical, and we have removed the point $r = 0$ because the identification $r \sim -r$ is singular at this

point. Removing $r = 0$ physically corresponds to enforcing a hard-core repulsion between particles, which, though not strictly necessary, prevents some inessential subtleties in defining the topology.

The space $\mathbb{R}^2/S_2$ locally looks similar to $\mathbb{R}^2$. In fact, in any small neighborhood of points that excludes the origin, the two spaces are isometric ($\mathbb{R}^2/S_2$ is locally flat). Globally, however, $\mathbb{R}^2/S_2$ differs drastically in the sense that it is a *curved* space, where the global curvature arises from the singular point at the origin, $r = 0$. The global curvature can be visualized from our vantage point of $\mathbb{R}^3$ by observing that the space $\mathbb{R}^2/S_2$ is actually a circular cone of half-angle $30°$. This construction is shown in Fig. 2.1a. Since the space is locally flat, identical particles should indeed behave as distinguishable particles as long as they are forbidden from exchanging coordinates i.e. as long as they are only allowed to take "trivial" paths through coordinate space, which correspond to r staying within some local neighborhood and not winding around the origin (hence, never physically exchanging coordinates).

Now, in order to define exchange statistics, we need to define what happens to wavefunctions living in such configuration spaces upon the action of particle exchange. We will not go into the details required to do this rigorously, which involves defining the quantum state as an object called a fiber bundle and ensuring that it satisfies certain gauge invariance conditions (see ref. [38]). In the end, defining the state in globally curved space puts a constraint on the wavefunction and whether the space's curvature induces a force. Namely, we have either (I) a possibly multi-valued wavefunction with no force (maintaining free particles) or (II) a single-valued wavefunction with a possible force induced by the curvature. We choose option (I) to see the exchange statistics more directly.

The action of particle exchange is the process of moving along a closed path in the space $\mathbb{R}^2/S_2$ from r to $-r$, which due to the identification are the same point somewhere on the conical surface. We see that any exchange loop necessarily requires winding around the singularity at the origin and that there are distinct classes of particle exchange loops given by different integer windings around the singularity. These exchange paths cannot be deformed into one another and, crucially, cannot be

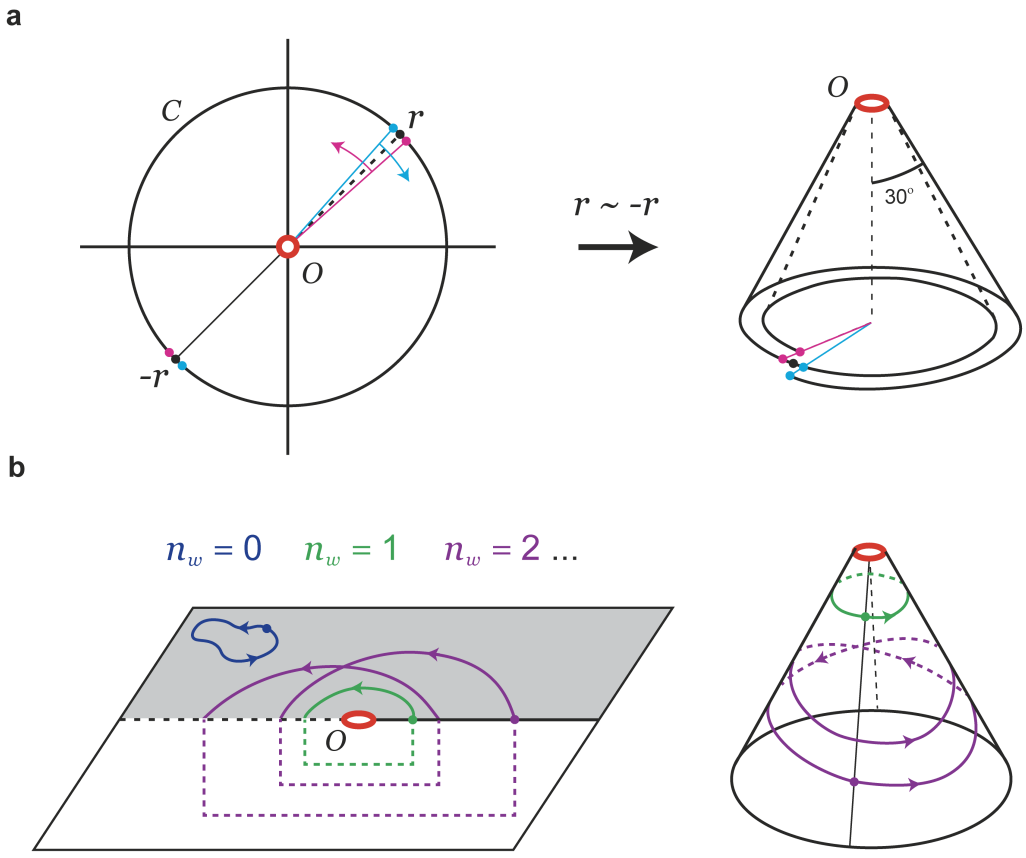


Figure 2.1: Configuration space of indistinguishable particles in 2D. (a) The space $\mathbb{R}^2/S_2$ can be visualized by considering a circle C in the 2D plane, viewed from the top. In order to identify $r \sim -r$ i.e. make every point coincide with its reflection across the origin O, we take a slice along the dashed line. Then, rotate the two parts (blue and pink edges) in opposite directions until they line up with the corresponding blue/pink dots. This transformation ensures that every point will exactly overlap with its reflection, and the circle C now wraps twice around the origin. The achieve this, the space becomes curved, forming a cone tipped at the origin. The reader is encouraged to perform this exercise with a roughly circular piece of paper! **(b)** Classes of closed loops in the space with winding numbers n_w, where $n_w = 0$ corresponds to a trivial loop (no exchanges), $n_w = 1$ corresponds to a single exchange, etc. The cone can equivalently be flattened and represented as the upper half-plane with the positive and negative real line identified. In any case, the origin is singular.

deformed back into a trivial loop which does not wind i.e. there exist non-contractible loops in configuration space. Hence, there are distinct exchanges distinguished by their *winding number* around the singularity $n_w \in \mathbb{Z}$, as shown in Fig. 2.1b. Closed loops with $n_w \neq 0$ are allowed to physically differ from the identity operation, so the simplest case is to allow one-dimensional, unitary operations on the wavefunction Ψ, which is now multi-valued. In particular, we are now allowed to have $\Psi \to e^{in_w\theta}\Psi$ under the action of a winding given by n_w, where we arbitrarily choose that positive windings are counterclockwise. The free parameter θ thus categorizes the type of indistinguishable particles that we have. It describes the global phase that the many-particle wavefunction acquires upon particle exchange. In summary, we have the allowed exchange statistics in 2D

$$\Psi(x_2, x_1) = e^{\pm i\theta}\Psi(x_1, x_2)$$

where the ± 1 defines counterclockwise/ clockwise exchange. We name these types of particles anyons.

It turns out that the existence of non-contractible loops, paths that cannot be smoothly deformed back to the trivial loop or a single point, defines the space as topologically non-trivial i.e. not *simply connected*. A simply connected space can be defined as one in which all loops are deformable into each other so all loops are contractible. Anyons are allowed to exist in 2D because the identical particle configuration space is globally curved and topologically non-trivial. The integer numbers $n_w \in \mathbb{Z}$ that exist and get assigned to the distinct loops in the space characterize the space's topology. In particular, we say that $\mathbb{Z}$ is the *fundamental group* of $\mathbb{R}^2/S_2$. In the N particle case in $d = 2$, the fundamental group becomes B_N which is called the braid group ($B_2 = \mathbb{Z}$). Since particle exchange operations in 2D correspond to a representation of the braid group operating on the wavefunction, exchanges of various winding numbers are commonly called *braids*. In contrast, the configuration space's fundamental group for the N particle case in $d \geq 3$ is actually the permutation group S_N, and this is why the allowed exchange statistics are ± 1, which we will now derive.

For the case of two indistinguishable particles in three dimensions ($d = 3$), the relative configuration space $\mathbb{R}^3/S_2$ is also globally curved, while it is locally flat and isometric to $\mathbb{R}^3$ for any neighborhood excluding the origin. The space is the set of all $r \in \mathbb{R}^3$ with the condition $r \sim -r$, and a singularity at the origin $r = 0$ that again we can exclude. We can break up the space by realizing that $\mathbb{R}^3/S_2$ is the Cartesian product of the line $(0, \infty)$ with the surface of a 3D sphere centered at the origin with all antipodal points identified. Unfortunately, we cannot visualize the whole space, but it suffices to consider the spherical surface, which is physically equivalent to considering a fixed separation $|r|$ between the particles. Exchange paths correspond to loops which connect the identified antipodal points on the sphere. By examining the possible closed loops in this space, we observe that the single exchange loop (Fig. 2.2b) necessarily wraps halfway around the sphere (thus halfway winding around the singularity that still exists in the center of the sphere) and cannot be deformed back into a trivial loop (Fig. 2.2a) while holding the endpoints fixed. Hence, all single exchange paths are non-contractible. However, the double-exchange loop (Fig. 2.2c) that winds fully around the surface and returns to its starting point can be smoothly deformed back to a trivial loop or a point, so physically we have that two exchanges must be equivalent to the identity operation. Deforming the double-exchange path along the spherical surface completely avoids the singularity at the origin, and this is the benefit of 3D space. The technical name for this fact is that the configuration space is *doubly connected*, because there are two classes of closed loops passing through any point. The fundamental group of the configuration space is simply $S_2 = \mathbb{Z}_2$ which can at most be represented by the phases ± 1 upon particle exchange. We say then that only fermions and bosons exist in 3D because the identical particle configuration space is doubly connected.

In this section, we have seen that mathematically consistent quantum theories exist in 2D with indistinguishable particles called anyons, which have non-trivial exchange statistics. The fact that we only have fermions and bosons in 3D was shown to be a consequence of the simpler topology of the configuration space of identical particles in 3D compared to 2D. Though these concepts are mathe-

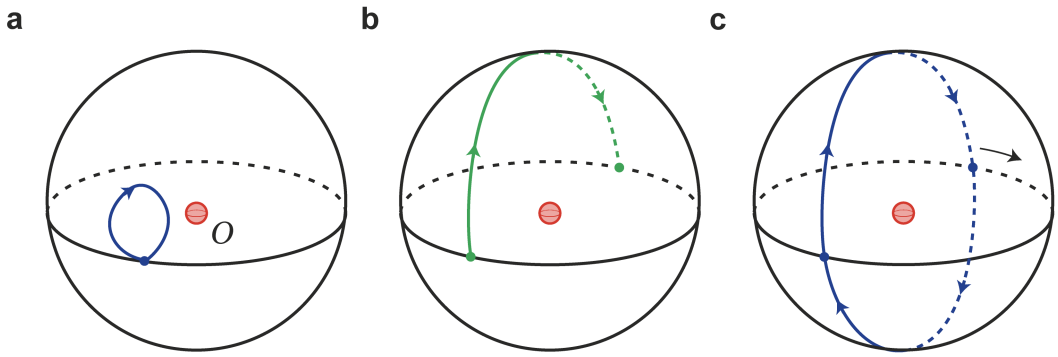


Figure 2.2: Configuration space of indistinguishable particles in 3D. (a) Considering a fixed separation between the particles, the relevant part of the space $\mathbb{R}^3/S_2$ is a spherical surface with a singularity at the origin and every antipodal point identified. A trivial closed loop identical to the identity operation is shown. **(b)** A closed loop corresponding to a single exchange of the particles. This loop effectively winds the singularity once. **(c)** A closed loop corresponding to a double-exchange of the particles. This loop can be smoothly wound around the sphere and deformed into a trivial loop.

matically correct and beautiful, we now may wonder whether they are realized in physical reality; to what extent mathematical truths correspond to physical reality in general is a deep question, which I for one do not know the answer. The surprising answer in the case of anyons is that they are indeed realized when we confine electrons to move in 2D and allow sufficiently strong electron-electron interactions in a large magnetic field, as we shall soon see.

2.2 Graphene: atomically thin electrons

Through the rapid technological progress following the invention of the solid-state transistor, numerous platforms emerged in which electrons could be confined to effectively 2D surfaces[39]. Most notably, the silicon metal-oxide-semiconductor field-effect transistor allowed realization of the 2D electron system in which the integer quantum Hall effect was discovered[3], and higher electron mobility 2D electrons realized in GaAs-AlGaAs heterojunctions enabled the discovery of the fractional quantum Hall effect[14]. In the many years since the initial discovery, the GaAs quantum well platform has made many orders of magnitude improvement in mobility by reducing disorder from the

molecular beam epitaxy growth of the materials, enabling the observation of a plethora of emergent correlated states like Wigner crystals and new fractional quantum Hall states[40]. The ultimate spatial confinement (quantum well width) realizable in the ultra-high mobility GaAs platform is still of order $\sim$ 10 nm, however, which is the width at which surface and interface roughness induced scattering begins to degrade performance[41]. The finite thickness of the electron layer limits the energy gaps attainable for fractional quantum Hall states, such that the largest energy gaps measured via transport so far are roughly $\Delta_{1/3} \approx 7$ K and $\Delta_{5/2} \approx 820$ mK for the states at $\nu = 1/3$ and $\nu = 5/2$, respectively[42,40]. This limitation can be overcome by stabilizing fractional quantum Hall states in intrinsically two-dimensional materials, as we will see.

Graphene is perhaps the ultimate 2D material, consisting of a single layer of carbon atoms in a hexagonal lattice. The effective "electronic thickness" has been measured to be about 0.26 nm (ref.[43]), which likely arises from the finite extent of the conducting electrons' wavefunctions that occupy the π bands normal to the layer. Nevertheless, electrons in graphene are confined 10 to 100 times more strongly than in GaAs. It has been somewhat a mystery why graphene can exist in the first place. Indeed, the so-called Hohenberg-Mermin-Wagner theorem states that true long range order is not possible for many purely 2D systems[44,45,46], even crystalline order[47], yet it need not apply for finite samples. Nevertheless, it was surprising when the single-atom thick crystal of carbon atoms was experimentally isolated from bulk graphite crystals using the simple "scotch-tape" method in 2004 (ref.[48]), and shortly after its unique electronic properties were discovered by measuring the quantum Hall effect in the 2D crystal[49,50]. The 2010 Nobel prize in physics was awarded for the isolation and control of graphene and its unique electronic properties, which are the starting point of this thesis. Interestingly, the tight-binding model of graphene was discussed and solved already in 1947, long before its eventual experimental isolation[51]. Here, we review graphene's electronic structure, focusing on the important symmetries and degeneracies that arise and become important later in understanding the quantum Hall effects in graphene. See the standard literature for more details[52,53,54].

Graphene consists of a single layer of carbon atoms covalently bonded together into a hexagonal lattice. An isolated Carbon atom has filled electron orbitals given by $(1s)^2(2s)^2(2p)^4$. To form bonds in a solid-state crystal, the $(2s)$ and $(2p)$ electrons usually hybridize, for example in the best known solid form of carbon, diamond, they hybridize to four sp^3 orbitals, which naturally tend to establish a tetrahedral bonding pattern in 3D. These bonds essentially localize all of the available electrons, making diamond an exceptional electrical insulator with a ~ 5 eV bandgap. On the contrary in graphene, the $(2s)$ and $(2p)$ electrons hybridize instead to three sp^2 orbitals, which naturally arrange themselves at 120° angles in the plane to form a honeycomb (hexagonal) lattice tiling 2D space. This bonding leaves behind essentially p_z orbitals, oriented normal to the plane, which have vanishing overlap with the other orbitals and collectively form π bonds throughout the plane, allowing for electronic conduction that we can treat in the tight-binding approximation (see refs. [55,56] about tight-binding models). The low-energy electronic properties of graphene that are important for this thesis are well-described by a tight-binding model that includes only nearest-neighbor hopping, but we will comment on higher order corrections to the band structure in the following.

To proceed with the tight-binding calculation, we notice that the honeycomb lattice can be described by a hexagonal Bravais lattice with a two-atom basis, with the two carbon atoms in the basis labeled A and B, as shown in Fig. 2.3a. The lattice vectors are given by

$$\mathbf{a_1} = \frac{a}{2}\left(3,\ \sqrt{3}\right), \quad \mathbf{a_2} = \frac{a}{2}\left(3,\ -\sqrt{3}\right),$$

where $a \approx 0.246$ nm. The carbon-carbon bond length is about 0.142 nm. It helpful to view this arrangement as two separate groups of A and B atoms, which each form triangular lattices themselves that we call the A and B *sublattices*. The reciprocal lattice (Fig. 2.3b) is simply given by another

hexagonal lattice rotated 90° from the original lattice, with reciprocal lattice vectors given by

$$\mathbf{b_1} = \frac{2\pi}{3a}\left(1,\ \sqrt{3}\right), \quad \mathbf{b_2} = \frac{2\pi}{3a}\left(1,\ -\sqrt{3}\right)$$

that can be verified to satisfy $\mathbf{a_i} \cdot \mathbf{b_j} = 2\pi\delta_{ij}$. The most important points in the first Brillouin zone (B.Z.), the so-called Dirac points where the low-energy physics occurs, as we will see, are located at the particular crystal momenta defined as the valleys $\mathbf{K}$ and $\mathbf{K}'$ given by

$$\mathbf{K} = \frac{2\pi}{3a}\left(1,\ \frac{1}{\sqrt{3}}\right), \quad \mathbf{K}' = \frac{2\pi}{3a}\left(1,\ -\frac{1}{\sqrt{3}}\right).$$

Now, to carry out the tight binding calculation, we note that the nearest neighbors in real space to any A atom are the three atoms on B sites given by the relative displacements

$$\delta_1 = \frac{a}{2}\left(1,\ \sqrt{3}\right), \quad \delta_2 = \frac{a}{2}\left(1,\ -\sqrt{3}\right), \quad \delta_3 = a\left(-1,\ 0\right)$$

while the nearest neighbors to every B atom are the surrounding A atoms at $-\delta_j$. Denoting the creation operator for an electron occupying a conduction orbital centered on atom 'i' in the A sublattice with spin σ by $a^\dagger_{i,\sigma}$ and the creation operator for an electron on atom 'j' in the B sublattice with spin σ by $b^\dagger_{j,\sigma}$, then the nearest-neighbor tight-binding Hamiltonian has the simple form

$$\mathcal{H} = -t \sum_{\langle i,j\rangle,\sigma} a^\dagger_{i,\sigma} b_{j,\sigma} \ + \text{H.c.}$$

where H.c. is the Hermitian conjugate of the explicit terms (i.e. $b^\dagger_{j,\sigma} a_{i,\sigma}$) and $t \approx 3$ eV to fit to experiments, though the value does not affect our conclusions. In the following we will drop the spin index, which does not contribute to lowest order due to extremely weak intrinsic spin-orbit coupling at the $\mathbf{K}/\mathbf{K}'$ points[57], and remember that the solutions will be spin-degenerate to a good approximation.

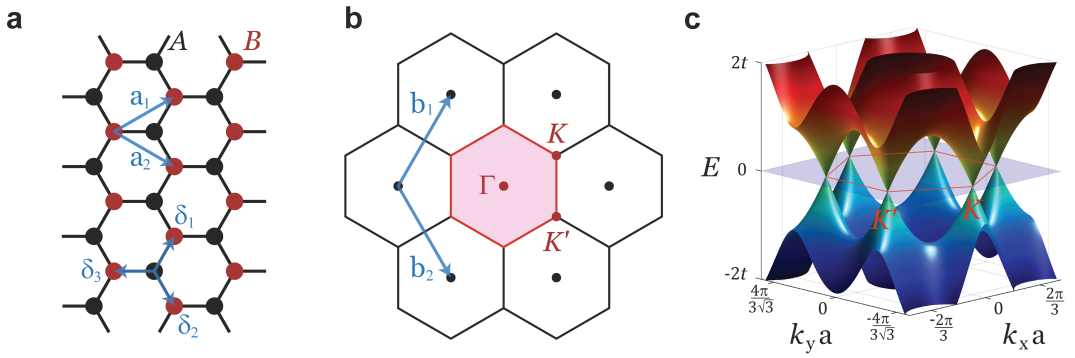


Figure 2.3: Graphene lattice and low-energy band structure. **(a)** Hexagonal lattice of graphene with A (black) and B (red) sublattices labeled. **(b)** Reciprocal lattice of graphene with the first Brillouin zone (B.Z.) shaded in pink and high symmetry Γ and $\mathbf{K}/\mathbf{K}'$ points indicated. **(c)** Energy bands $E_{\pm}(\mathbf{k})$ from the nearest-neighbor tight-binding model, with Dirac cones at the inequivalent $\mathbf{K}$ and $\mathbf{K}'$ valleys. We see the emergence of cones from a 2D system again!

We can simplify the Hamiltonian then diagonalize it directly by enforcing the translational invariance of the lattice and going to Fourier (reciprocal) space. We use the (conventional) transforms

$$a^{\dagger}(\mathbf{R}_{\mathrm{i}}) = a_{\mathrm{i}}^{\dagger} = \frac{1}{\sqrt{N}} \sum_{\mathbf{k}\in \mathrm{B.Z.}} a_{\mathbf{k}}^{\dagger} e^{i\mathbf{k}\cdot\mathbf{R}_{\mathrm{i}}} \quad , \quad b(\mathbf{R}_{\mathrm{j}}) = b_{\mathrm{j}} = \frac{1}{\sqrt{N}} \sum_{\mathbf{q}\in \mathrm{B.Z.}} b_{\mathbf{q}} e^{-i\mathbf{q}\cdot\mathbf{R}_{\mathrm{j}}},$$

where $\mathbf{R}_{\mathrm{i}}$ is the vector giving the location of the lattice site 'i' and N is the total number of sites. Rewriting the nearest-neighbor condition using the relative displacements vectors $\boldsymbol{\delta}_{\mathrm{j}}$ and introducing the Fourier transforms to the Hamiltonian, we find

$$\begin{aligned}
\mathcal{H} = -t \sum_{\mathrm{i,j}} a^{\dagger}(\mathbf{R}_{\mathrm{i}}) b(\mathbf{R}_{\mathrm{i}} + \boldsymbol{\delta}_{\mathrm{j}}) \; + \mathrm{H.c.} &= -\frac{t}{N} \sum_{\mathrm{i,j}} \sum_{\mathbf{k},\mathbf{q}\in \mathrm{B.Z.}} e^{-i\mathbf{q}\cdot\boldsymbol{\delta}_{\mathrm{j}}} e^{i\mathbf{R}_{\mathrm{i}}\cdot(\mathbf{k}-\mathbf{q})} a_{\mathbf{k}}^{\dagger} b_{\mathbf{q}} \; + \mathrm{H.c.} \\
&= -t \sum_{\mathrm{j}} \sum_{\mathbf{k},\mathbf{q}\in \mathrm{B.Z.}} e^{-i\mathbf{q}\cdot\boldsymbol{\delta}_{\mathrm{j}}} a_{\mathbf{k}}^{\dagger} b_{\mathbf{q}} \left(\frac{1}{N} \sum_{\mathrm{i}} e^{i\mathbf{R}_{\mathrm{i}}\cdot(\mathbf{k}-\mathbf{q})} \right) \; + \mathrm{H.c.} \\
&= -t \sum_{\mathrm{j}} \sum_{\mathbf{k}\in \mathrm{B.Z.}} e^{-i\mathbf{k}\cdot\boldsymbol{\delta}_{\mathrm{j}}} a_{\mathbf{k}}^{\dagger} b_{\mathbf{k}} \; + \mathrm{H.c.}
\end{aligned}$$

so that we can naturally represent the wavefunctions in the form of spinors $\psi_{\mathbf{k}} \equiv (a_{\mathbf{k}},\, b_{\mathbf{k}})^{T}$, whose

components correspond to the amplitudes of the state with momentum $\mathbf{k}$ on the A and B sublattices, and we thus arrive at the purely off-diagonal Hamiltonian in this basis

$$\mathcal{H} = -t \sum_{\mathbf{k}} \psi_{\mathbf{k}}^{\dagger} \begin{pmatrix} 0 & e^{-i\mathbf{k}\cdot\boldsymbol{\delta}_1} + e^{-i\mathbf{k}\cdot\boldsymbol{\delta}_2} + e^{-i\mathbf{k}\cdot\boldsymbol{\delta}_3} \\ e^{i\mathbf{k}\cdot\boldsymbol{\delta}_1} + e^{i\mathbf{k}\cdot\boldsymbol{\delta}_2} + e^{i\mathbf{k}\cdot\boldsymbol{\delta}_3} & 0 \end{pmatrix} \psi_{\mathbf{k}}$$

which we can rewrite as

$$H = \sum_{\mathbf{k}} \psi_{\mathbf{k}}^{\dagger} h(\mathbf{k}) \psi_{\mathbf{k}}$$

where

$$h(\mathbf{k}) \equiv \begin{pmatrix} 0 & \Delta(\mathbf{k}) \\ \Delta^*(\mathbf{k}) & 0 \end{pmatrix}.$$

For a given $\mathbf{k}$, we can diagonalize this matrix to find the energy bands

$$\begin{aligned} E_{\pm}(\mathbf{k}) &= \pm\, |\Delta(\mathbf{k})| \\ &= \pm\, t\sqrt{3 + 2\cos\left[\mathbf{k}\cdot(\boldsymbol{\delta}_1 - \boldsymbol{\delta}_2)\right] + 2\cos\left[\mathbf{k}\cdot(\boldsymbol{\delta}_2 - \boldsymbol{\delta}_3)\right] + 2\cos\left[\mathbf{k}\cdot(\boldsymbol{\delta}_3 - \boldsymbol{\delta}_1)\right]} \\ &= \pm \sqrt{3 + 2\cos\left(\sqrt{3}k_{\mathrm{y}}a\right) + 4\cos\left(\frac{\sqrt{3}}{2}k_{\mathrm{y}}a\right)\,\cos\left(\frac{3}{2}k_{\mathrm{x}}a\right)} \end{aligned}$$

that we plot in Fig. 2.3c. We get two bands since there are two atoms in the basis, and recall that each band is spin-degenerate. Since each carbon contributes one free electron to the π bands, we get by taking spin into account that the band $E_{-}(\mathbf{k})$ is exactly filled while the band $E_{+}(\mathbf{k})$ is empty in undoped graphene. Therefore, the Fermi surface is unusual: it consists of two 'Fermi points', one at $\mathbf{K}$ and the other at $\mathbf{K}'$ where the bands touch with $E_{\pm}(\mathbf{K}) = E_{\pm}(\mathbf{K}') = 0$. This means that graphene is a zero-gap semiconductor with a vanishing density of states at the Fermi. More importantly for this thesis, it means that the low-energy (low-doping) electronic properties are determined by the details of the band structure near the valleys $\mathbf{K}$ and $\mathbf{K}'$, which we now derive.

The band structure at small momentum $\mathbf{q}$ around the $\mathbf{K}$ valley, defined as $\mathbf{q} \equiv \mathbf{k} - \mathbf{K}$ can be derived by expanding $\Delta(\mathbf{k})$ to linear order in $\mathbf{q}$ around $\mathbf{q} = 0$. From the explicit expression

$$\Delta(\mathbf{k}) = -t \sum_{j=1}^{3} e^{-i\mathbf{k}\cdot\boldsymbol{\delta}_j} = -t \left(e^{ik_{\mathrm{x}}a} + 2e^{-i\frac{1}{2}k_{\mathrm{x}}a} \cos\left(\frac{\sqrt{3}}{2} k_{\mathrm{y}} a \right) \right)$$

we find that the expansion around $\mathbf{K}$ is given by

$$\Delta_{\mathbf{K}}(\mathbf{q}) \approx -2te^{iK_{\mathrm{x}}a} \mathbf{q} \cdot \nabla_{\mathbf{k}} \left(e^{-i\frac{3}{2}k_{\mathrm{x}}a} \cos\frac{\sqrt{3}}{2} k_{\mathrm{y}} a \right) \Big|_{\mathbf{k}=\mathbf{K}} = -\frac{3ta}{2} e^{iK_{\mathrm{x}}a} \left(iq_{\mathrm{x}} + q_{\mathrm{y}} \right).$$

Plugging in the known constants, we have that the Fermi velocity $v_F \equiv \frac{3ta}{2\hbar} \approx 10^6$ m/s, and we note that the expansion for small $\mathbf{q}$ around $\mathbf{K}'$ gives the complex conjugate of the same expression. It is conventional to factor out an overall phase $-ie^{iK_{\mathrm{x}}a}$, which can be removed by choosing a gauge, so that we may write

$$\Delta_{\mathbf{K}}(\mathbf{q}) = \hbar v_F \left(q_{\mathrm{x}} - iq_{\mathrm{y}} \right) = \Delta^*_{\mathbf{K}'}(\mathbf{q}).$$

Since we need to expand the Hamiltonian around both valleys to describe the full low energy theory, we can add the valley index $\xi = \pm 1$ where $+1$ (-1) is for $\mathbf{q}$ around the $\mathbf{K}$ $(\mathbf{K}')$ valley, respectively. Then for both valleys the Hamiltonian at low energies (small $\mathbf{q}$) can be written in the form

$$h_\xi(\mathbf{q}) = \hbar v_F \begin{pmatrix} 0 & q_{\mathrm{x}} - i\xi q_{\mathrm{y}} \\ q_{\mathrm{x}} + i\xi q_{\mathrm{y}} & 0 \end{pmatrix} = \hbar v_F \boldsymbol{\sigma}_\xi \cdot \mathbf{q}$$

where $\boldsymbol{\sigma}_\xi = (\sigma_x, \xi\sigma_y)$ and σ_j are the standard Pauli matrices, here in the pseudospin basis of the weight on the A and B sublattices. At either valley, diagonalizing the Hamiltonian gives the linearly dispersing cones (Dirac cones) that can be seen emanating from the $\mathbf{K}$ and $\mathbf{K}'$ points in Fig 2.3c:

$$\epsilon(\mathbf{q}) = \pm\hbar v_F |\mathbf{q}|.$$

Thus we have an effective low energy model which is mathematically the same in its spinor structure and linear dispersion as that of massless (i.e. ultra-relativistic) fermions proposed by Dirac [58], with the speed of light c replaced by the Fermi velocity v_F and the real spin replaced by a pseudospin related to the graphene sublattices, so we may call it a Dirac theory with Dirac quasiparticle excitations. We note that the Dirac excitations near $\mathbf{K}$ are not the antiparticles of those near $\mathbf{K}'$. The particles/antiparticles are the two possible combinations of A and B sublattice polarizations within a single valley i.e. the eigenstates of $h_\xi(\mathbf{q})$ given by

$$\psi_\xi^\pm(\mathbf{q}) = \frac{1}{\sqrt{2}} \begin{pmatrix} e^{i\xi\theta_\mathbf{q}/2} \\ \pm e^{-i\xi\theta_\mathbf{q}/2} \end{pmatrix}, \qquad \theta_\mathbf{q} = \arctan\left(\frac{q_y}{q_x}\right)$$

with energies $\epsilon(\mathbf{q}) = \pm\hbar v_F|\mathbf{q}|$. Also recall that the real spin has remained a degeneracy as have the two inequivalent valleys. Real spin and valley each separately provide $\mathrm{SU}(2)$ symmetries, which combine to give an overall $\mathrm{SU}(4)$ symmetry. Therefore, there are 4 species of Dirac quasiparticles/antiparticles i.e. 4-fold degenerate Dirac cones contributing to the low energy transport, one for each combination of valley index and real spin projection. Nevertheless, the similarity has led to several analogues of relativistic effects that were able to be measured in graphene, such as Klein tunneling and the Klein-Schwinger effect [59,60]. We will see how the Dirac cones lead to the formation of a unique series of "relativistic" Landau levels under a perpendicular magnetic field in the next section.

In completing this discussion, it is important to note the robustness of the Dirac cones; in fact they are protected by $\mathcal{C}_2\mathcal{T}$ symmetry, the combination of spatial inversion symmetry $\mathcal{C}_2$ and time-reversal symmetry $\mathcal{T}$. If neither symmetry is broken, the approximate Dirac cones at low energy survive, though possibly displaced in momentum [61]. Next-nearest neighbor and higher terms in the tight-binding Hamiltonian do not break $\mathcal{C}_2$, so they preserve the Dirac cones, though they produce distortions at higher energies (e.g trigonal warping) and particle-hole asymmetry away from the valleys.

2.3 Landau levels and quantum Hall ferromagnetism

In this section, we begin reviewing aspects of the quantum Hall effects needed to understand the experiments presented in this thesis, most notably regular and "relativistic" Landau levels, localized states, and symmetry breaking in graphene. Good introductions can be found in the notes by Tong[62], book by Jain[63], and review articles in ref.[64].

The plethora of quantum Hall effects emerge from a deceptively simple looking microscopic Hamiltonian, that of electrons in a perpendicular magnetic field with Coulomb interactions. We begin by turning off Coulomb repulsion so that we can derive the relevant single-particle states. The Hamiltonian for a non-relativistic electron occupying free 2D space with a constant magnetic field $\nabla \times \mathbf{A} = B\hat{z}$ is given by

$$\mathcal{H} = \frac{1}{2m}\left(\mathbf{p} - e\mathbf{A}\right)^2$$

where e is the electron charge (assumed positive: $1.602... \times 10^{-19}$C), and m is the free electron mass. We can solve for the spectrum directly in a gauge-independent manner by using the gauge-invariant mechanical momentum $\mathbf{\Pi} = \mathbf{p} - e\mathbf{A}$, so that the Hamiltonian becomes

$$\mathcal{H} = \frac{1}{2m}\left(\Pi_x^2 + \Pi_y^2\right).$$

By definition, Π_x and Π_y are canonically conjugate variables, satisfying the commutator

$$\left[\Pi_x, \Pi_y\right] = i\hbar eB = i\left(\frac{\hbar}{\ell_B}\right)^2, \qquad \ell_B \equiv \sqrt{\frac{\hbar}{eB}} \approx \frac{26\,\text{nm}}{\sqrt{B[\text{T}]}},$$

where we have found the only length scale of the problem, called the *magnetic length* ℓ_B. We see that the Hamiltonian is mathematically equivalent to that of a harmonic oscillator. Therefore, to solve for its spectrum by analogy to the harmonic oscillator, we can define the canonical raising/lowering

(ladder) operators to satisfy the commutator $\left[a, a^\dagger\right] = 1$ as

$$a^\dagger \equiv \frac{\ell_B}{\sqrt{2}\hbar}\left(\Pi_x + i\Pi_y\right), \qquad a \equiv \frac{\ell_B}{\sqrt{2}\hbar}\left(\Pi_x - i\Pi_y\right),$$

so that the Hamiltonian becomes

$$\mathcal{H} = \frac{\hbar\omega_c}{2}\left(aa^\dagger + a^\dagger a\right) = \hbar\omega_c\left(a^\dagger a + \frac{1}{2}\right), \qquad \omega_c = \frac{eB}{m}.$$

This form directly gives us the spectrum of an electron in a magnetic field i.e. *Landau levels*

$$E_N = \hbar\omega_c\left(N + \frac{1}{2}\right), \qquad N = 0, 1, 2, ...$$

We call N the orbital index, and the eigenstate $|N\rangle$ the Nth Landau level. It is important to recall the physical picture at this point. Classically, we expect an electron in a magnetic field to follow uniform circular motion i.e. cyclotron orbits at the *cyclotron frequency* ω_c defined above. The Landau levels arise from quantization of the circular motion, but the center of the orbit, the so-called *guiding center*, has not entered the problem yet. This is because there is no spatial dependence in the Hamiltonian, so that formally each eigenvalue N is infinitely degenerate due to the infinite possibilities of placing the guiding center throughout the 2D plane. This fact can be restated by defining the canonically conjugate operators for the spatial coordinate of the guiding center, which then themselves produce an infinite ladder of states for a given N i.e. infinite degenerate states within each Landau level (see refs. [63,65]). Similarly, there is an extensive degeneracy of each Landau level for finite systems. The number of degenerate states in a finite system can be counted by fixing a gauge (canonically either the Landau or symmetric gauge), and one finds that each Landau level has exactly one state per magnetic flux quantum $\phi_0 \equiv \frac{h}{e}$ piercing the sample. Thus, the degeneracy is $\frac{AB}{\phi_0}$ where A is the area of the finite 2D region exposed the the uniform magnetic field B, in this case. We can also say that there are

$\frac{B}{\phi_0} = \frac{1}{2\pi\ell_B^2}$ states per unit area. Then we can define the important quantity called the *filling factor* ν, which is simply the ratio of the number of electrons to the number of flux quanta piercing the sample:

$$\nu \equiv 2\pi\ell_B n = \frac{n\phi_0}{B},$$

where n is the 2D density of electrons. In the absence of interactions and at temperature $T = 0$, the filling factor (also simply called filling) ν then gives the number of occupied single-particle Landau levels in the system, where non-integer values correspond to filling a portion of a level's degenerate states. We continue to use ν to name states even when there are strong interactions in the system and the single-particle picture breaks, such as for quantum Hall ferromagnets and fractional quantum Hall effects, because these states emerge from the non-interacting Landau levels and have similar basic phenomenology, albeit different internal structures and excitations.

So far we have discussed Landau levels that form for an electron in free 2D space. It turns out that a very similar spectrum forms in GaAs quantum wells, with the simple replacement of the free electron mass m by an effective mass $m^* \approx 0.067\, m$ due to the parabolic band structure. In graphene, however, this is not the case, and we must consider the effect of the graphene band structure on the single-particle Landau levels that form in a finite out-of-plane magnetic field. We now have two valleys ξ so keeping the same convention as in the free space case, we can define ladder operators

$$a_\xi^\dagger \equiv \frac{\ell_B}{\sqrt{2}\hbar}\left(\Pi_x + i\xi\Pi_y\right), \qquad a_\xi \equiv \frac{\ell_B}{\sqrt{2}\hbar}\left(\Pi_x - i\xi\Pi_y\right), \qquad a_{-1} = a_{+1}^\dagger.$$

It suffices to consider the effective low energy Hamiltonian $h_\xi(\mathbf{q})$ and similarly assume the minimal coupling[66] $\mathbf{q} \to \mathbf{\Pi} = \mathbf{q} - e\mathbf{A}$ so then

$$h_\xi(\mathbf{q}) \to \hbar v_F \begin{pmatrix} 0 & \Pi_x - i\xi\Pi_y \\ \Pi_x + i\xi\Pi_y & 0 \end{pmatrix} = \frac{\sqrt{2}\hbar v_F}{\ell_B} \begin{pmatrix} 0 & a_\xi \\ a_\xi^\dagger & 0 \end{pmatrix},$$

We see that the square of the Hamiltonian is a diagonal matrix given by

$$h_\xi^2 = 2\left(\frac{\hbar v_F}{\ell_B}\right)^2 \begin{pmatrix} a_\xi a_\xi^\dagger & 0 \\ 0 & a_\xi^\dagger a_\xi \end{pmatrix} = 2\left(\frac{\hbar v_F}{\ell_B}\right)^2 \begin{pmatrix} a_\xi^\dagger a_\xi + 1 & 0 \\ 0 & a_\xi^\dagger a_\xi \end{pmatrix},$$

so that the Landau levels for graphene are given by

$$E_N = \pm\frac{\sqrt{2}\hbar v_F}{\ell_\mathrm{B}}\sqrt{|N|} = \mathrm{sgn}(N)\frac{\sqrt{2}\hbar v_F}{\ell_\mathrm{B}}\sqrt{|N|}, \qquad N = 0, \pm1, \pm2, ...$$

which is the same spectrum for each valley and spin. However, the eigenstates in each valley are given by different combinations of the free-space orbital Landau level wavefunctions $|N\rangle$ defined previously. For example, the eigenstates of h_{+1} i.e. at the $\mathbf{K}$ valley, in our convention, are given by

$$|\Psi_{N=0}\rangle = \begin{pmatrix} 0 \\ |0\rangle \end{pmatrix}, \qquad |\Psi_N\rangle = \begin{pmatrix} \mathrm{sgn}(N)||N|-1\rangle \\ ||N|\rangle \end{pmatrix}, \quad N = \pm1, \pm2, ...$$

The fact that graphene's single-particle Landau levels are in general mixtures of orbital Landau level wavefunctions with different components on the A and B sublattices leads to some interesting differences between the states that can form through interactions and symmetry breaking in graphene. Most notably, this difference could account for the absence of even-denominator fractional states observed in the $N = 1$ Landau level as well as the existence of novel even-denominator states in the $N = 3$ level for graphene[67]. There have also been differences in the odd-denominator fractional sequences observed with different index N in graphene[68,69,70,71]. However, the $N = 0$ Landau level in graphene is unique since the full weight is on a single sublattice. Effectively this locks the valley index and sublattice polarization, removing a degree of freedom and making the $N = 0$ Landau level of graphene equivalent to that of GaAs, leading to similar states[72], though the observed sequence and excitations can differ between $|\nu| < 1$ and $|\nu| > 1$ when valley-anisotropic interactions are present[73].

Observing how graphene's Landau levels evolve with magnetic field and comparing to those of GaAs in the same range in Fig. 2.4a shows that, at the single-particle level, graphene has unprecedentedly large energy gaps, especially at relatively low magnetic fields. Graphene's Landau level spectra measurements using scanning tunneling microscopy agree to within a factor of two in energy with this single-particle theory[74,75], and the large energy gap between E_1 and E_0 has allowed the $\nu = 2$ quantum Hall effect to even be observed at room temperature[76]. If we visualize the density of states as a function of energy, the single particle picture gives us a series of delta functions at each E_N, each of height $4\frac{B}{\phi_0}$ due to the SU(4) symmetry (Fig. 2.4b), but in realistic scenarios a finite amount of external disorder causes a broadening of each energy level shown in Fig. 2.4c. This is because a disorder potential breaks translational invariance: there are now some potential "valleys" where electrons would prefer to localize, corresponding to states at lower energy and "hills" where electrons would require higher energy to occupy randomly dispersed throughout the 2D system, which we could draw as some roughness or blurring of the originally flat Landau levels. Semi-classically, the guiding centers of electrons in cyclotron orbits will drift along equipotential curves of V_{disorder}, the disorder potential landscape (i.e. they drift perpendicular to the gradient, $\nabla V_{\text{disorder}}$) and so can get trapped locally even in the presence of an applied external electric field. Localized states are those which are sufficiently strongly perturbed by the disorder so that they become trapped, cover a finite spatial extent, and do not contribute to the zero-frequency conduction in the $T = 0$ limit. In contrast, extended states (delocalized states) are those which are not sufficiently perturbed by the disorder to get trapped, so that they still contribute to the zero-frequency conduction at $T = 0$. We picture these states as percolating paths through the disorder potential landscape[77].

The presence of disorder to break translational invariance and create localized states in the Landau level tails turns out to be crucial to the quantum Hall effects. In fact, one can show that a system which has translational invariance must always have a Hall conductance given by the classical formula (see Girvin's chapter in Ref.[38] in particular). Therefore, some mechanism of breaking translational

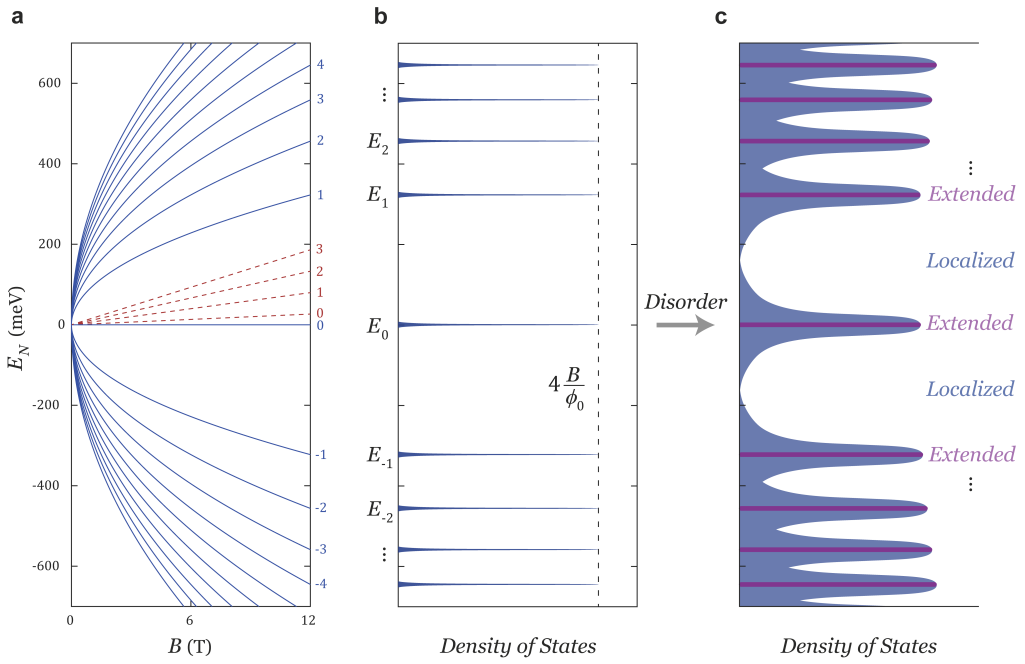


Figure 2.4: Graphene single-particle Landau levels. (a) Plot of graphene Landau levels' (blue) evolution with magnetic field B for $-10 \leq N \leq 10$, where $E_N \sim \frac{1}{\ell_B} \sim \sqrt{B}$. Extremely large energy gaps form, especially between the $N = 0$ and $N = 1$ Landau levels. Some Landau levels expected for GaAs are shown (red dashes) for comparison, which are linear in B and have nearly an order of magnitude smaller gap $E_1 - E_0$ at the largest field shown. At low fields the difference is even more dramatic. **(b)** Density of single-particle states for graphene at a large magnetic field B. Each single-particle Landau level is perfectly flat in energy and has $4\frac{B}{\phi_0}$ states per unit area, where the 4 comes from the combined spin and valley degeneracy, so the density of states are represented by delta functions. **(c)** Density of single-particle states in the same condition at (b) but now including the effect of a small disorder potential. Disorder breaks translational invariance and gives each Landau level a finite width, requiring the classification of states as either localized or extended.

invariance is required to observe anything else, like the rich physics of the quantum Hall effects. Actually, breaking this symmetry does not need to be done by disorder; it has been proposed to also spontaneously break in the absence of disorder due to quasiparticle Wigner crystal formation in fractional quantum Hall states[78]. Even in integer quantum Hall states, there is experimental evidence from single-electron transistor probes of the localized states that the single-particle picture of disorder-induced localization breaks down at moderate B fields and is replaced by more subtle Coulomb driven screening effects that promote localization[79]. Nevertheless, it suffices to think of the translational symmetry breaking and the resulting localized states as arising from small residual disorder for understanding the basic picture, and we can adopt the nomenclature that disorder means any translational symmetry breaking terms. The existence of extended states (percolating paths) near the center of the Landau levels are also essential to explain the quantum Hall effect. In particular, the extended states that necessarily exist near the boundary of finite samples, called *edge states* are essential to explaining what is measured in low-frequency transport experiments[7]. These edge states carry the low energy non-equilibrium currents that we inject and measure in the sample. We discuss edge states and the way that we measure Hall conductance in detail in the next section.

Before ending this section, we must point out the consequences of the single-particle Landau levels on the expected quantization of σ_{xy} in the quantum Hall regime and why more than the single-particle Landau levels are seen in high-quality samples. In the classical theory, we know that the Hall conductivity, which is commonly used to measure charge carrier density n, is given by $\sigma_{xy} = \frac{ne}{B}$ where we are using the convention that electrons give positive conductivity. In the presence of both localized and extended states, however, we need to be careful since localized states cannot contribute to the conductivity. We want to understand what happens to σ_{xy} when we change the filling factor ν of graphene's Landau levels shown in Fig. 2.4c. Changing ν is most simply accomplished by tuning the overall density of electrons directly using an electrostatic gate voltage V_g which serves as a capacitor plate coupled to the graphene, so that $n = CV_g$ where C is the capacitance per unit area. Alternatively, we could

change magnetic field. Note that increasing magnetic field will increase the number of states in each Landau level, reducing ν (schematically moving the Fermi level downwards in Fig. 2.4c). Each disorder broadened Landau level has an overall density of states, $4\frac{B}{\phi_0}$, so that filling all the states of a single level requires a density $n = 4\frac{B}{\phi_0}$. If there are no localized states, the classical equation for σ_{xy} holds so that we would expect a fully filled level to contribute a conductivity $\sigma_{xy} = 4\frac{B}{\phi_0}\frac{e}{B} = 4\frac{e^2}{h}$. Though the classical equation no longer needs to hold with disorder, it turns out that it still gives the correct result for filled Landau levels. First, the same result can be properly calculated from the single-particle quantum states of a (disorder-free) finite sample in an external electric field by summing over the currents of each state. Second and more importantly, the existence of localized states does not alter the total current, as first showed by Prange for a delta-function impurity model[80]. This is because, quite surprisingly, the remaining extended (delocalized) states carry additional current to exactly compensate for the current lost by the localized states. The argument is closely related to Laughlin's famous charge-pump argument, which proves that any system (including disorder) that can be adiabatically evolved into ideal Landau levels without having states cross the Fermi level has an exactly quantized Hall conductance[5,16].

In summary, populating the total band of extended states within a Landau level contributes the full conductivity $\sigma_{xy} = 4\frac{e^2}{h}$. Once the extended states are filled, further increasing ν through localized states contributes nothing to σ_{xy}, so we theoretically have a constant plateau until the next band of extended states are filled. Simultaneously, $\lim_{T\to 0}\sigma_{xx} = 0$ while the Fermi level is at the localized states, since they cannot carry current, while σ_{xx} is a finite nonuniversal value when the Fermi level is within the extended states. The fact that σ_{xy} is a finite *measurable* plateau while σ_{xx} and R_{xx} vanish when the Fermi level is in the localized states is a bit subtle, but the picture will be made clear when we consider the edge states that are carrying the current in finite samples. Nevertheless, the single-particle theory gives a series of plateaus occurring at $\sigma_{xy} = \pm 2\frac{e^2}{h}, \pm 6\frac{e^2}{h}, \pm 10\frac{e^2}{h}, \ldots$ corresponding to $\nu = \pm 2, \pm 6, \pm 10, \ldots$, which were exactly seen in the first quantum Hall transport experiments[49,50].

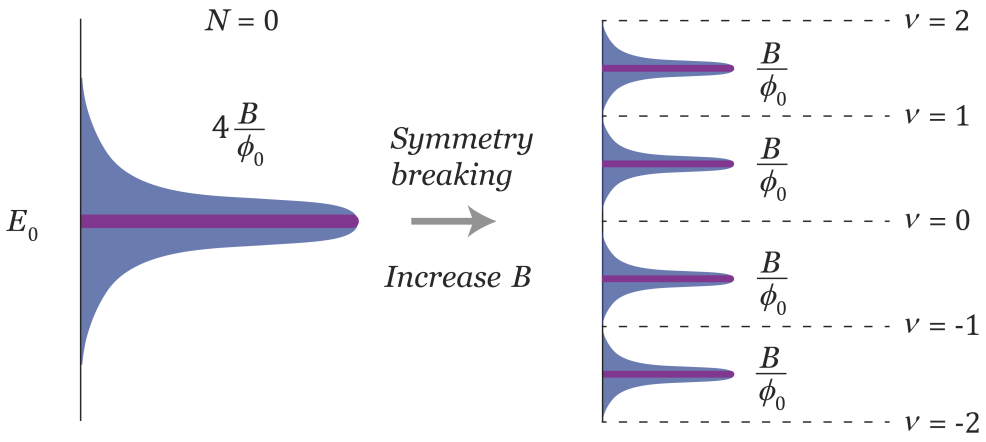


Figure 2.5: Symmetry broken Landau levels. The degenerate single-particle Landau levels spontaneously break spin and valley symmetry due to the combination of Coulomb repulsion and exchange interaction, forming fully polarized Landau levels, each acquiring a quarter of the original states. The symmetry broken states of $N = 0$ level are shown.

For non-integer ν (partial filling) of a Landau level, a large number of degenerate states need to be filled across space while ensuring that Pauli exclusion is obeyed, since we are dealing with indistinguishable electrons (aside: what if we instead enforced 2D statistics?). Including Coulomb interactions then naturally leads to symmetry breaking, because in a fully polarized spin/valley state, the spatial wavefunction needs to be antisymmetric, causing exchange interaction. Each electron is surrounded by an "exchange hole", effectively increasing the separation of particles and reducing the Coulomb energy[38]. Thus, the fully polarized states are the most energetically favorable, and spontaneous symmetry breaking occurs due to the electron-electron interactions: the phenomenon called *quantum Hall ferromagnetism*. In graphene, quantum Hall ferromagnetism manifests as a breaking of the spin and valley degeneracies of each single-particle Landau level into 4 fully polarized levels[81,82], shown schematically in Fig. 2.5. Breaking both symmetries is favored in clean samples and moderate magnetic fields, so that the full sequence of integer quantum Hall plateaus are now generally observed: $\nu = \pm 1, \pm 2, \pm 3, \ldots$ where generally every state alternates in real-spin polarization though they can also have combined spin-valley polarizations outside of $N = 0$. Spin degeneracy also breaks in GaAs.

A unique point about graphene is the state that forms at half-filling of the $N = 0$ Landau level, $\nu = 0$ i.e. doped near zero carrier density or "charge neutrality". At zero magnetic field, this point shows insulating behavior due to the vanishing density of states, and in early samples its resistance grew dramatically in magnetic field[83]. In higher-quality samples, it became clear that the $\nu = 0$ state is generally consistent with a canted anti-ferromagnet phase that is spin-unpolarized[82]. This is because the state is prevented from fully polarizing in both spin and valley simultaneously, so the competition determines the state. Applying an in-plane magnetic field to boost the Zeeman energy drove a transition to a fully ferromagnetic phase[84] which was theoretically predicted to be an analog of the quantum spin Hall state with a pair of helical, counter-propagating edge modes[85,86,87]. A similar regime was also reached by strongly screening the Coulomb energy to be smaller than Zeeman using proximity effect to $SrTiO_3$, a material with an extremely large dielectric constant[88]. The nature of the states that can be realized under different experimental conditions remains an open research question[89,90,91], but in the samples studied in this thesis, we only observe signatures of a large bulk gap and the absence of edge states near $\nu = 0$. Therefore, we can view graphene as a "trivial" charge insulator at neutrality.

2.4 Edge states and ballistic current

Recall that Landau levels in the presence of disorder have both localized and extended states. The localized states are sufficiently strongly perturbed by the disorder potential variations that they do not contribute to conductivity, while extended states can connect the source and drain and contribute to conductivity in the $T = 0$ limit. As first shown by Halperin, extended states *must exist* at the boundaries (edges) of any finite sample, and these so-called edge states are essential to explaining the transport properties of quantum Hall states[7,92,10]. In particular, they help us to understand why real measurements of σ_{xy} are possible and still show the proper value when all of the states in the bulk are localized near integer ν, and edge states carry the low energy currents required for our experiments.

To consider what happens for a finite sample, we need to incorporate a confining potential into the Hamiltonian, so that states must have vanishing occupancy at the boundaries. For demonstration purposes, we work with the single-particle Hamiltonian of the free electron case (the results are expected to be the same for graphene when all symmetries are broken). We begin by considering an infinite or periodic sample along both x and y and fixing a useful gauge $\mathbf{A} = (0, Bx, 0)$ for the symmetry of the confining potential we will consider later. The original Hamiltonian in this gauge becomes

$$\mathcal{H} = \frac{1}{2m}\left(\mathbf{p} - e\mathbf{A}\right)^2 = \frac{\hat{p}_{\mathrm{x}}^2}{2m} + \frac{1}{2m}\left(\hat{p}_{\mathrm{y}} - eB\hat{x}\right)^2 = \frac{\hat{p}_{\mathrm{x}}^2}{2m} + \frac{1}{2}m\omega_{\mathrm{c}}^2\left(\hat{x} - \frac{\hbar k}{m\omega_{\mathrm{c}}}\right)^2$$

where we have replaced $\hat{p}_{\mathrm{y}}$ with its eigenvalue $\hbar k$ in the last step, since $\hat{p}_{\mathrm{y}}$ commutes with the Hamiltonian. This is identical to the Hamiltonian of a quantum harmonic oscillator with a minimum of potential centered at $x_0 = \frac{\hbar k}{m\omega_{\mathrm{c}}} = \frac{\hbar k}{eB} = k\ell_{\mathrm{B}}^2$, so that the momentum in y is tied to the spatial position x_0. The eigenstates take the form of plane waves along y and harmonic oscillator wavefunctions in x with various centers: $\psi(x, y) = \frac{1}{\sqrt{L_{\mathrm{y}}}} e^{iky} f_k(x)$, where L_{y} is the length along y. The eigenstates are infinitely degenerate due to the arbitrary parameter k, with energies given by $E_N = \hbar\omega_{\mathrm{c}}\left(N + \frac{1}{2}\right)$ as found before without fixing a gauge.

We now consider what happens when we constrain the x coordinates to a finite extent. This is achieved by adding in a confinement potential $V_{\text{conf.}}(x)$ which is flat for some region but ascends to infinity outside, so that states will be forbidden by an increasing energy cost towards the boundary of the sample. If we assume that $V_{\text{conf.}}(x)$ changes smoothly on the scale of the magnetic length ℓ_{B}, so that it can be treated as a constant over each of the eigenstates already derived, then the potential can be added in perturbatively as a continuous shift to each state's energy:

$$E = \hbar\omega_{\mathrm{c}}\left(N + \frac{1}{2}\right) + V_{\text{conf.}}\left(\frac{\hbar k}{eB}\right)$$

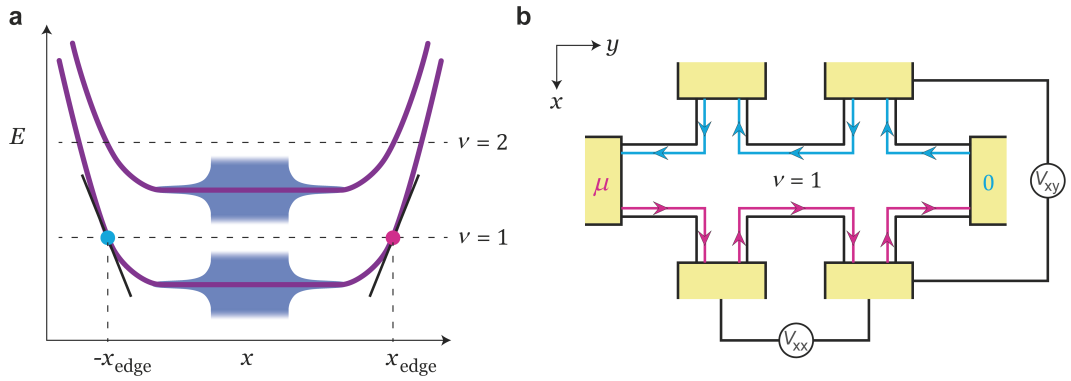


Figure 2.6: Edge states and Hall transport measurement. (a) The lowest two electron-like symmetry broken Landau levels of graphene with disorder and a confining potential along x. The Fermi levels (dashed lines) corresponding to the center of the $\nu = 1$ and $\nu = 2$ plateaus are marked. **(b)** Top-down schematic of a Hall transport measurement in $\nu = 1$ where there is a single chiral edge channel.

Two of these energy levels across x, including the effect of disorder, are shown schematically in Fig. 2.6a. The effect of disorder is to localize states towards the center of the sample, far from the edges, while states that disperse at the sample edges must eventually necessarily become extended states, as the confining potential diverges while V_{disorder} remains bounded. We call these extended states at the edge the *edge states*. Semi-classically, the edge states are cyclotron orbits that experience $E \times B$ drift perpendicular to the electric field E, which is determined by the gradient of the confining potential. From the quantum solution, we get the same result since we have that the wave packet group velocity is given by

$$v_{\text{y}} = \frac{1}{\hbar}\frac{\partial E}{\partial k}\hat{y} = \frac{1}{eB}\frac{\partial V_{\text{conf.}}}{\partial x}\bigg|_{x=x_0}$$

Since this is of opposite signs at $x = x_{\text{edge}}$ and $x = -x_{\text{edge}}$, the edge state currents are *chiral*, flowing around the boundary of the sample in a fixed direction perpendicular to the boundary (Fig. 2.6b). These edge states are effectively states of 1D wires that are forced to conduct in one direction. When the system is near integer ν, all low energy non-equilibrium current injected in must flow through the edge states near the Fermi level. At $\nu = 1$, we say that 1 chiral *edge channel* contributes.

To calculate the conductance at $\nu = 1$, we enforce a fixed voltage bias and calculate the current generated by it, exactly as we may perform the measurement. Using the Landauer-Büttiker formalism [13,63,56] to analyze the transport problem, we assume that the DC voltage applied, V, leads to a chemical potential difference $\Delta\mu = eV$ between the opposite right and left moving edge states (we assume V is too small to generate significant electrostatic potential gradients and continue the convention of positive electron charge). We can view the effect of V as raising the Fermi level of the right-moving edge up to $\mu = eV$ and leaving the left-moving edge unchanged, defined as 0. Therefore, we simply need to add up the currents carried by the right-moving edge states between 0 and μ to get the current along $\hat{y}$:

$$I = e\int_{\frac{x_{\text{edge}}}{\ell_B^2}}^{\infty} \frac{dk}{2\pi}\frac{1}{\hbar}\frac{\partial E}{\partial k}n_k = \frac{e}{h}\int_0^{\mu} dE = \frac{e}{h}\mu = \frac{e^2}{h}V$$

where we have assumed that the occupancy of states n_k is a step function. Since we measure the Hall voltage V_{xy} as the difference between the bottom edge and top edge (Fig. 2.6b), we see that V_{xy} is exactly V that we have applied. Therefore, extending to the case of ν edge channels, we have that the Hall conductivity $\sigma_{xy} = \nu\frac{e^2}{h}$. It is now easy to see why the quantized plateaus are robust and why $\sigma_{xx} \to 0$. The reason for both is the fact that the current is *ballistic*, or in other words dissipationless, *unless* extended states percolate through the bulk (e.g. near $\nu \approx \frac{1}{2}$). Ballistic means that there is vanishing probability for the injected current to backscatter. Backscattering would require a wavepacket on the right-moving edge to tunnel through all of the localized states in the bulk to reach the left-moving edge and return to the source contact, which is exceedingly unlikely for any Hall bar that is wide compared to the magnetic length (more precisely the localization length). Since there is no such backscattering, the entire right-moving edge channel is fixed at the chemical potential of the source, μ, while the upper edge channel is fixed at 0. Therefore, the measured V_{xx} will be simply $(\mu - \mu)/e = 0$ so that $R_{xx} \equiv \frac{V_{xx}}{I} = 0$. Similarly, σ_{xx} is zero since the current is flowing entirely perpendicularly to V.

In the Landauer-Büttiker language, a single-channel, one-dimensional wire with a disordered region in its center has a conductance given by $G = \frac{e^2}{h}t$ where t is the probability for an electron to be transmitted through the disordered region. We say that we have conductance from transmission, and the transmission probability t can be calculated via scattering matrices or non-equilibirum Green's functions methods for many models[13]. We see that in our case, we have *perfect transmission* i.e. $t = 1$ for each edge channel around integer ν. For this reason, we can consider the edge channels as perfect 1D wires. However, we note that this only holds within the edge channels themselves and not where they meet the source/drain. There is inevitable dissipation when the "hot" edge at chemical potential μ must enter the drain contact at 0, as well as when the "cold" edge at 0 must suddenly equilibrate up to μ entering the source. These sudden jumps in the chemical potential lead to so-called "hot spots" at these two points in the quantum Hall sample. Applying a large enough voltage bias can even cause magnons (i.e. spin waves) to be launched into the quantum Hall bulk from from the hot spots, which opens the door for spin transport and novel probes of the bulk states[93,94,95,96].

In closing this section, we note that the edge channels themselves acquire a width in the presence of Coulomb interactions and disorder. Accounting for these effects leads to the famous self-consistent screening model of the edge channels, where it is found that near the edge of the sample, the quantum Hall state spontaneously forms a series of alternating compressible and incompressible stripes[11,97,56]. The extended states which cross the Fermi level now become compressible stripes pinned to the Fermi level, and the nonequilibrium current continues to flow in these regions while equilibrium currents flow in the incompressible regions. We discuss this model more to understand our data in chapter 5.

Lastly, since graphene is a 2D electron system with an exposed surface, unlike GaAs, a variety of probes have been able to directly image the edge channels, such as Kelvin probe microscopy[98], scanning SQUID microscopy[99,100], and scanning tunneling microscopy[101]. There are also interesting older experiments in GaAs that imaged signatures of the "hot spots" generated by the equilibration of chemical potential at the corners of the contacts[102].

2.5 Fractional quantum Hall anyons and topological quantum bits

Up until now, we have mostly neglected the effect of electron-electron interactions, except in discussing quantum Hall ferromagnetism. It turns out that, even after all degeneracies are broken and we have the fully polarized Landau levels from Fig. 2.5, if we have clean enough samples with a large enough inter-electron Coulomb interaction energy $E_c \sim \frac{e^2}{\epsilon \ell_B}$ (i.e. requiring larger B in general), then the electrons can spontaneously reorganize to new ground states with their own bulk gaps and edge states at particular fractional values of ν. These rich phenomena are called the *fractional quantum Hall effects*, and here we will primarily consider the state at $\nu = \frac{1}{3}$ as the simplest and most relevant state for this thesis. We actually investigate both the $\nu = \frac{1}{3}$ and $\nu = \frac{4}{3}$ fractional quantum Hall states in graphene, which are formally equivalent to the state in GaAs due to the lack of sublattice structure within the $N = 0$ Landau level of graphene, so we can restrict ourselves to discussing the state at $\nu = \frac{1}{3}$ in GaAs and seeing how anyon quasiparticles with fractional charge and statistics emerge from the so-called Laughlin state [15,16,63]. Good modern overviews can be found in refs. [62,103,104,105].

To gain insight into the many-body quantum state that can describe $\nu = \frac{1}{3}$, we need to begin by understanding the wavefunctions for many electrons filling degenerate states in the lowest Landau level, which we have yet to write down. It is most convenient in this discussion and our positive electron charge convention to use the symmetric gauge $\mathbf{A} = -\frac{1}{2}\mathbf{r} \times \mathbf{B} = -\frac{1}{2} y B \hat{x} + \frac{1}{2} x B \hat{y}$ corresponding to a magnetic field $\mathbf{B} = B\hat{z}$, so the annihilation operator for the free 2D electron Hamiltonian becomes

$$a = \frac{\ell_B}{\sqrt{2}\hbar}\left(\Pi_x - i\Pi_y\right) = \frac{\ell_B}{\sqrt{2}\hbar}\left(-i\hbar\left(\frac{\partial}{\partial x} - i\frac{\partial}{\partial y}\right) - \frac{ieB}{2}\left(x + iy\right)\right) = -i\sqrt{2}\left(\frac{z}{4\ell_B} + \ell_B\bar{\partial}\right)$$

where we have used $p_x = -i\hbar\frac{\partial}{\partial x}$ etc. and defined $z \equiv x + iy$ and $\bar{\partial} \equiv \frac{1}{2}\left(\frac{\partial}{\partial x} - i\frac{\partial}{\partial y}\right)$. It is then readily seen that any single particle wavefunction in the lowest Landau level (i.e. $N = 0$), defined by

$a\psi = 0$, must be given by

$$\psi(z, \bar{z}) = f(z) e^{-\frac{1}{4\ell_{\mathrm{B}}^2}|z|^2}$$

where $f(z)$ is any holomorphic function and $|z|^2 = z\bar{z}$. This is the one-body state. The simplest possible form of $f(z)$ is a polynomial, and since angular momentum is a good quantum number for this radially symmetric gauge, the $N = 0$ Landau level is actually macroscopically degenerate (like in all gauges) with states that can be enumerated by the angular momentum quantum number l:

$$\psi_l(z) \sim z^l e^{-\frac{1}{4\ell_{\mathrm{B}}^2}|z|^2}, \qquad l = 0, 1, 2...$$

The state with quantum number l is localized on a ring of radius $r = \sqrt{2l}\ell_{\mathrm{B}}$.

A general many-body state for N particles must be of the form

$$\Psi(z_1, ..., z_{\mathrm{N}}) = f(z_1, ..., z_{\mathrm{N}}) e^{-\frac{1}{4\ell_{\mathrm{B}}^2}\sum_{\mathrm{j}=1}^{\mathrm{N}}|z_{\mathrm{j}}|^2}$$

where $f(z_1, ..., z_{\mathrm{N}})$ is analytic in all variables and must obey anti-symmetry under exchange of any two particles $z_{\mathrm{i}} \leftrightarrow z_{\mathrm{j}}$, since the underlying electrons are fermions. In order to write the state of N indistinguishable electrons filling the explicit orbitals ψ_l above, we need to take a Slater determinant of the orbital momentum polynomials to get the form of $f(z_1, ..., z_{\mathrm{N}})$. This particular Slater determinant is called the Vandermonde determinant and has a convenient form:

$$f(z_1, ..., z_{\mathrm{N}}) = \begin{vmatrix} z_1^0 & z_2^0 & \cdots & z_{\mathrm{N}}^0 \\ z_1^1 & z_2^1 & \cdots & z_{\mathrm{N}}^1 \\ \vdots & & & \vdots \\ z_1^{\mathrm{N}-1} & z_2^{\mathrm{N}-1} & \cdots & z_{\mathrm{N}}^{\mathrm{N}-1} \end{vmatrix} = \prod_{\mathrm{j}<\mathrm{k}} (z_{\mathrm{j}} - z_{\mathrm{k}})$$

so that the full many-body state at $\nu = 1$, up to the normalization constant, can be expressed as

$$\Psi_1(z_1, ..., z_N) = \prod_{j<k}(z_j - z_k)e^{-\frac{1}{4\ell_B^2}\sum_{j=1}^{N}|z_j|^2}$$

Laughlin's wavefunction [15,16] for the $\nu = \frac{1}{m}$ state, where m is an odd integer is of a similar form. It was discovered to be

$$\Psi_{1/m}(z_1, ..., z_N) = \prod_{j<k}\left(z_j - z_k\right)^m e^{-\frac{1}{4\ell_B^2}\sum_{j=1}^{N}|z_j|^2}$$

which satisfies the antisymmetric condition since m is odd. Laughlin postulated this form as a variational wavefunction for a model Hamiltonian [16], and it was shown both to be the exact solution for a variety of model Hamiltonians [106] and to have $> 99\%$ numerical overlap to exact states that can be computed [63]. We can see that the state $\Psi_{1/3}$ (i.e. $m = 3$) indeed corresponds to filling factor $\nu = \frac{1}{3}$ in the thermodynamic (large N) limit because if we single out a particular coordinate, say z_1, and count the maximum power that it will be raised to in the prefactor, we find a maximum term $\sim z_1^{m(N-1)}$. Therefore, the maximum angular momentum is $m(N-1) \approx mN$ which corresponds to a state that is localized at a radius of $\sqrt{2mN}\ell_B$. The total area of the states is simply then $A = 2\pi mN\ell_B^2$ so that the number of states is $\frac{A}{2\pi\ell_B^2} = mN$. Therefore, since we have N electrons filling mN states, $\nu = \frac{N}{mN} = \frac{1}{m} = \frac{1}{3}$ as required. See the original papers (particularly the charge-pump/flux threading thought experiment, which is clearest in the Corbino geometry [7]) for the proof that the state is indeed incompressible and has the observed Hall conductivity $\sigma_{xy} = \frac{1}{3}\frac{e^2}{h}$. The existence of the bulk energy gap at this filling essentially implies the fractional charge which is pumped per each flux quantum, which implies the fractionally quantized σ_{xy}. Moreover, from the explicit wavefunction we can see that the state very efficiently minimizes Coulomb interactions by maintaining space between electrons, since Ψ vanishes very quickly with an m-th order zero if any particles coincide. In a real system,

Coulomb interactions will be slightly screened so that the state should not vanish as quickly, and the zeros do not exactly coincide with the electron coordinates[105]. Nevertheless, the state gets the basic properties correct, accurately yielding the experimental results, and it is believed to be in the same "universality class" as any realistic state[62].

We now discuss how we can see the two most important properties of the quasihole and quasiparticle excitations above this ground state, their *fractional charge* and *fractional statistics*, from the form of the wavefunction itself. The wavefunction for a state with a quasi-hole at coordinate η in the 2D (complex) plane can be reasonably approximated as

$$\Psi_{1/3,\eta}(z_1, ..., z_N) = \prod_{i=1}^{N}(z_i - \eta)\prod_{j<k}(z_j - z_k)^3 e^{-\frac{1}{4\ell_B^2}\sum_{j=1}^{N}|z_j|^2}$$

so that Ψ and the corresponding electron density completely vanish at the point η, which can physically represent a sharp defect site which pokes a hole in the fluid. Perhaps more accurately, it's an anti-vortex of the fluid. Interestingly, we can see that if we have 3 such holes in the same location, the wavefunction is similar to that which we would get if we had added an electron by hand at a fixed coordinate of η. However, since the coordinate is a fixed parameter and not a dynamical variable (in particular it is absent from the exponential), from the perspective of the other electrons it behaves like an absence of an electron i.e. a hole. If the electron is charge $-e$ then the combination of 3 quasiholes is charge $+e$ and hence a single quasihole has charge $+\frac{e}{3}$. Quasiparticles would have charge $-\frac{e}{3}$.

To see the fractional statistics, we need to compute what happens when we take a state with two quasiholes and adiabatically exchange their coordinates. As first calculated by Arovas[27], we can consider a state of two quasiholes

$$\Psi_{1/3,\eta_1,\eta_2}(z_1, ..., z_N) = \mathcal{N}(\eta_1, \eta_2)\prod_{i=1}^{N}(z_i - \eta_1)(z_i - \eta_2)\prod_{j<k}(z_j - z_k)^3 e^{-\frac{1}{4\ell_B^2}\sum_{j=1}^{N}|z_j|^2}$$

where $\mathcal{N}(\eta_1, \eta_2)$ is a normalization constant. Arovas then computed the adiabatic phase acquired when winding one quasihole around the other, which is the Berry phase [107,108] γ, formally given by

$$i\gamma = \oint d\tau \left\langle \Psi(\eta_1(\tau), \eta_2) \left| \frac{d}{d\tau} \right| \Psi(\eta_1(\tau), \eta_2) \right\rangle$$

where τ parametrizes the path that takes the quasihole coordinate $\eta_1(\tau)$ on a loop once counterclockwise back to its starting point, winding once around the coordinate η_2. It was found that the Berry phase in the case of the general $\Psi_{1/m}$ Laughlin state with two quasiholes is exactly

$$\gamma = \frac{2\pi}{m}\frac{\Phi}{\phi_0} + 2\frac{\pi}{m} = \frac{2\pi}{m}\frac{\Phi}{\phi_0} + 2\theta_{\text{exchange}}$$

where the parameter $\theta_{\text{exchange}} = \frac{\pi}{m}$ is the phase that would be acquired for a single exchange [103] that characterizes the anyon statistics. The factor of 2 in front of θ_{exchange} is simply because the full winding back to the original coordinate is equivalent to two exchanges [109]. The first term in γ is the Aharonov-Bohm phase [110,111] acquired by winding the charge $\frac{e}{m}$ quasihole around a loop enclosing a total magnetic flux $\Phi = AB$. We will see that the phase that we can extract from our interferometer measurements is to lowest order given by exactly the same equation.

Beyond the Laughlin state which describes the fractions at $\nu = \frac{1}{m}$ and their hole-conjugate states $\nu = 1 - \frac{1}{m}$ (e.g. $\frac{1}{3}$ and $\frac{2}{3}$ for $m = 3$) there exists a whole sequence of states at other odd-denominator fractions evident in experiments [40] (see also our data in chapter 6). It is possible to understand many of these states, for example the states at $\nu = \frac{2}{5}$ and $\nu = \frac{2}{7}$ as emerging from the Laughlin state via successive condensation of residual quasiparticle excitations [106,26], so we may call them "hierarchy states". The composite fermion approach pioneered by Jain also gives an explanation for the so-called "Jain series" of states at $\nu = \frac{2}{5}, \frac{3}{7}, \frac{4}{9}, \ldots$ extending from $\nu = \frac{1}{3}$ (as the first in the sequence) and many other deep insights into the fractional states [112,63]. These sequences of states have also been observed in

graphene, where the transport gap of for example $\nu = \frac{1}{3}$ has already been observed to be $\Delta_{1/3} > 20\,\mathrm{K}$ (refs. [113,114]), larger than the state-of-the-art in GaAs[40].

Beyond the hierarchy and Jain states, there are also even-denominator fractional quantum Hall states, for example $\nu = \frac{5}{2}$ first observed in GaAs by Willet et al.[115] and more recently many states observed in bilayer graphene, including at $\nu = \pm\frac{1}{2}, \pm\frac{3}{2}, \pm\frac{5}{2}, \frac{7}{2}$ in several experiments[116,117,118,119] as well as quarter-filling states[119]. These bilayer graphene states are particularly exciting because the energy gaps appear to be nearly an order-of-magnitude larger than their GaAs counterparts, for example $\Delta_{7/2} \approx 5 - 10\,\mathrm{K}$ in bilayer graphene[120] compared to $\Delta_{5/2} \approx 0.81\,\mathrm{K}$ in GaAs[40]. Several candidate states were proposed to explain the fractional quantum Hall effect at filling factor $\nu = \frac{5}{2}$ in GaAs that are expected to extend to any even-denominator state that may be stabilized. These are various types of paired states[121,122,123,124,125], most notably the Moore-Read Pfaffian, anti-Pfaffian, and PH-Pfaffian states that host *non-abelian* anyon quasiparticles[126]. These can be viewed as paired states of composite fermions with various pairing symmetries[127]. Non-abelian anyons obey non-abelian exchange statistics, so that the space of states for a collection of indistinguishable non-abelian quasiparticles at fixed positions is necessarily degenerate. When non-abelian quasiparticles are exchanged adiabatically, the effect is a matrix operation on the space of degenerate states i.e. a change of the many-body wavefunction within the degenerate subspace. In contrast, *abelian* anyons would only acquire a phase, such as $\theta_{\text{exchange}} = \frac{\pi}{m}$ that we saw before.

Anyons with non-abelian exchange statistics are expected to enable the field known as topological quantum computation[30,31], where states encoded within the degenerate subspace could store information in a way that is "topologically protected" i.e. if we imagine preparing a state through quasiparticle exchange operations, undoing or destroying such information would require uncontrolled noise to precisely undo each exchange operation, in the right order. Since the exchanges are physically equivalent to braids of particle trajectories in spacetime, such a loss of information would be akin to a physical knot spontaneously undoing itself. We know from experience, however, that knots, like

an aggressively tied shoelace, can be very challenging to undo. In fact, there are sophisticated knots called quipus that the Incan civilization famously used to record information, and the oldest known quipus from the ancient Andean civilizations are still knotted together after enduring over 5000 years of environmental noise [128,129]. Storing and processing information with anyons promises to be the electronic equivalent of the quipu. Moreover, the stability of operations would be exponentially enforced by the separation between the quasiparticles in configuration space, say spatially for simplicity, so exchanges or braids themselves could be performed in a fault-tolerant way.

The fractional quantum Hall effect at even-denominators remains the most convincing and well-established platform expected to host non-abelian anyons, though the direct evidence for their exotic exchange properties remains elusive. We note that there have been great (and often controversial) efforts to stabilize states that may host such quasiparticles using other materials such as superconductor-semiconductor hybrids [130,131], and there has also been progress in directly preparing such states and demonstrating braiding using existing superconducting quantum processors [132,133].

More generally, fractional quantum Hall states represent a new class of physical systems that obey an emergent principle called topological order. Phases of matter with topological order, called topological states or topological phases, have long-range entanglement within their many-body wave functions [134]. Other states with topological order include proposed spin liquids [135,136,137] and chiral superconductors [138]. However, despite the name, topological insulators and superconductors [139,140] should not have long-range entanglement and topological order in the same sense, making the zoo of quantum-topological phases of matter rather subtle and complicated [134]. There is much work left to do in classifying and understanding the possible topological orders and their physical realizations.

In the fractional quantum Hall states in particular, the topological order leads to a deep connection between the edge states, which we can probe through transport measurements, and the bulk states and excitations, akin to a bulk-boundary correspondence [141,103]. We naively expect there to be excitations on the edge which have the same charge and exchange statistics as those localized in the bulk at $\nu = \frac{1}{3}$.

2.6 Edge state interferometers

Since we saw that the chiral, 1D edge states carry the low-energy current through the device without backscattering or dissipation and furthermore the typical drift velocity at the edge is quite fast ($\sim 10^5$ m/s as we measure in chapter 4), it follows that the phase coherence of current carried through the edge channels can practically be maintained over long distances, hundreds of microns in some cases. This long phase coherence length has allowed the exploration of a variety of electronic analogues of experiments typically performed in the field of quantum optics such as single and double-slit interference phenomena. See refs. [142,143] for good reviews. The essential element of many of these experiments is the use of electrostatic gates to guide the paths that the edge channels take through the device and force the edge channels of opposite chirality to selectively tunnel at particular points. These tunneling points are then tunable backscattering sites, analogous to partially silvered mirrors or beamsplitters in quantum optics. We call the split-gate structures required to create these electron beamsplitters "quantum point contacts" (QPCs), since the structure is physically identical to the canonical point contact structures used to discover conductance quantization at zero magnetic field [144,13].

Although the first experiment to observe signatures of phase coherence and interference in integer quantum Hall edge channels was already done in 1989 (ref. [167]), the theoretical proposal to use such structures to measure signatures of anyons in the fractional quantum Hall regime arrived in 1996 with the proposal of the two point-contact interferometer for quantum Hall systems [168]. The general idea is that the edge currents can be thought of as adiabatic transport of quasiparticles winding around localized quasiparticles that naturally exist, assumed pinned to defects or otherwise static spatially but varying in overall number. Measuring conductance oscillations then enables direct observation of the fractional charge and statistics of the quasiparticles, as well as probing the Luttinger liquid nature of the 1D edge channels [168]. There have been immense efforts to realize the proposal in the GaAs quantum well platform, as highlighted in Fig. 2.7. These efforts were pioneered by the Heiblum group with

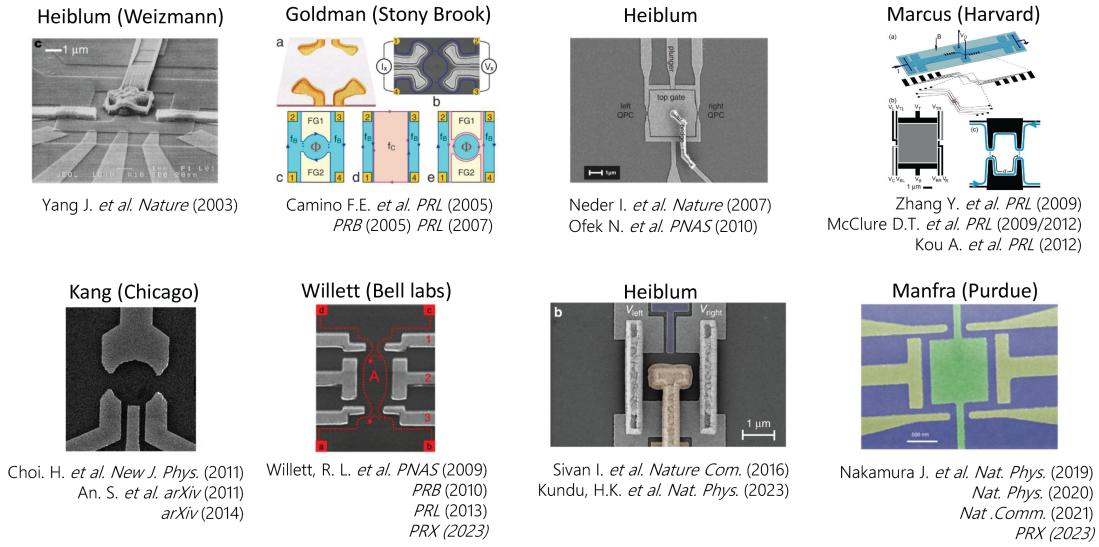


Figure 2.7: Edge state interferometers in GaAs. Images of the various quantum Hall edge state interferometers studied in GaAs quantum wells over the last two decades, in roughly chronological order: Heilblum[145], Goldman[146,147,148], Heiblum[149,150], Marcus[151,152,153,154], Kang[155,156], Willett[157,158,159,160], Heiblum[161,162], Manfra[163,164,165,166].

the first Mach-Zehnder style edge state interferometer in 2003, which showed robust Aharonov-Bohm oscillations in integer edge channels[145]. There were then a series of experiments by the Goldman, Heiblum, Marcus, Kang, and Willett groups changing to the Fabry–Pérot geometry and discovering strong signatures of fractional charge in the devices, though clear signatures of the anyon statistics remained elusive. Finally, clear signatures of the statistics in $\nu = \frac{1}{3}$ came around 2020 from the Manfra group, enabled by specialized quantum well heterostructures that incorporated screening well layers. In the following chapters, we will comment on the relevant results in GaAs in more detail, especially the discoveries by the Manfra group that were made while this thesis work was in progress.

In this thesis, we will continue to focus on the Fabry–Pérot geometry, which is analogous to the the ubiquitous optical interferometer and identical to the original proposal[168]. We show a schematic of the Fabry–Pérot interferometer measurement in Fig. 2.8. Here, the coherent beam of photons in an optical interferometer is replaced by a coherent current, which we can model as a stream of

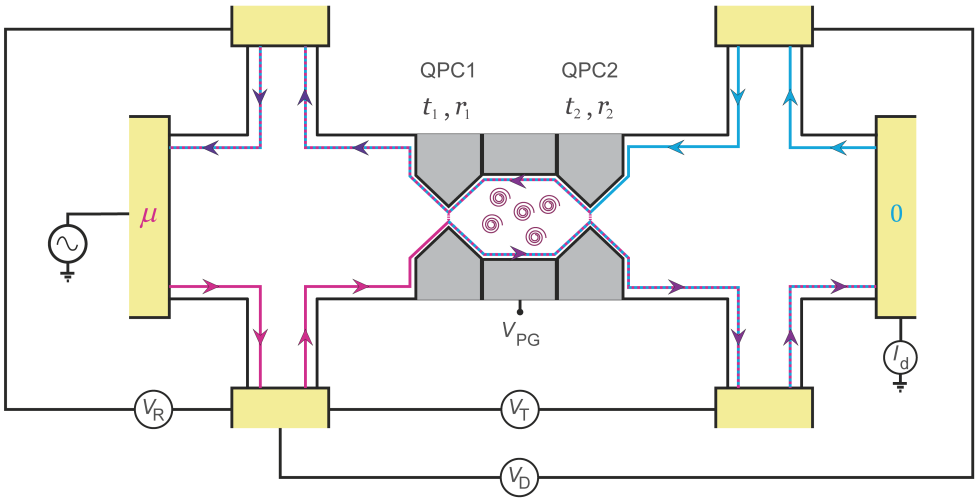


Figure 2.8: Fabry–Pérot quantum Hall interferometer. Schematic of the interferometer geometry used in this thesis, the electronic analogue of the Fabry–Pérot cavity common in optics. The ballistic edge states carry the low energy current, which has a probability to backscatter at the two quantum point contact gate structures (marked QPC1 and QPC2) where the opposite chirality edge states are pushed close enough together to tunnel. The conductance across the cavity, extracted most accurately from the ratio $\frac{I_d}{V_D}$ but also related to "transmission" and "reflected" resistances ($\frac{V_T}{I_d}$, and $\frac{V_R}{I_d}$, respectively), where I_d is the measured drain current, will oscillate according to the phase θ acquired by winding counterclockwise around the cavity, which includes contributions from braiding around localized quasiparticles in the bulk. The localized quasiparticles ($n = 5$) are shown schematically in the cavity. Gray regions are gates.

electron wavepackets that overlap and are much larger than the cavity perimeter in the DC transport limit. The wavepackets propagate ballistically along the chiral edge channels as previously seen. To construct a Fabry–Pérot interferometer, we introduce two QPCs in series to allow two points where backscattering can now occur. The conductance across the cavity (i.e. from the source on the left side to the drain on the right) can be modeled in the Landauer-Büttiker formalism by obtaining the single-particle transmission amplitude at the Fermi energy. If we model each QPC as a structureless tunneling point, where QPC 'i' has an amplitude of transmitting the wavepacket through τ_i (from left to right) and an amplitude of reflecting to the opposite chiral edge ρ_i, where $|\rho_i|^2 = 1 - |\tau_i|^2$ neglecting inelastic processes, then we can find the total transmission amplitude by summing over the amplitudes for all current paths, assuming an infinite phase coherence length:

$$\begin{aligned}\tau &= \tau_1 e^{i\frac{\theta}{2}}\tau_2 + \tau_1 e^{i\frac{\theta}{2}}\left(\rho_2 e^{i\frac{\theta}{2}}\rho_1 e^{i\frac{\theta}{2}}\right)\tau_2 + \tau_1 e^{i\frac{\theta}{2}}\left(\rho_2 e^{i\frac{\theta}{2}}\rho_1 e^{i\frac{\theta}{2}}\right)^2\tau_2 + \dots \\ &= \tau_1 e^{i\frac{\theta}{2}}\sum_{n=0}^{\infty}\left(\rho_2 e^{i\frac{\theta}{2}}\rho_1 e^{i\frac{\theta}{2}}\right)^n\tau_2 \\ &= \frac{e^{i\frac{\theta}{2}}\tau_1\tau_2}{1 - e^{i\theta}\rho_1\rho_2}\end{aligned}$$

where θ is the winding phase of a particle counterclockwise around the central cavity and we have used the fact that $|\rho_i| < 1$. The conductance $G \equiv \frac{I_d}{V_D}$ is then proportional to the transmission probability given by

$$t = |\tau|^2 = \frac{|\tau_1|^2|\tau_2|^2}{1 + |\rho_1|^2|\rho_2|^2 - 2|\rho_1\rho_2|\cos(\theta)}.$$

If the adiabatic theorem holds and the quasiparticles carrying the current on the edge have the same charge e^* and statistical phase θ_{exchange} as those in the bulk, we expect that the winding phase θ is equivalent to the Berry phase γ derived previously. In experimental terms we should have

$$\theta = 2\pi\frac{e^*}{e}\frac{A(V_{PG})B}{\phi_0} + n\theta_a$$

where $A(V_{PG})$ is the total area of the cavity, tunable by the "plunger gate" voltage V_{PG} and $\theta_a \equiv 2\theta_{\text{exchange}}$ is the winding phase of an edge quasiparticle around an individual quasiparticle in the bulk. We assume a net number n of localized quasiparticles (formally the number of quasiparticles - number of holes) static in the bulk over the duration of the measurement. In the decades since this proposal, the theory has developed to account for important corrections to the predictions for realistic devices, most importantly the residual Coulomb coupling between the localized charges and the edge charges [169,170,104,171]. We will see that in our devices, this capacitive coupling is effectively negligible due to efficient screening in the van der Waals platform with nearby atomically-flat graphite gates.

2.7 Summary

In this chapter, we have seen how 2D systems can have emergent particles called anyons, and that these exotic particles with fractional charge and statistics (and perhaps more exotic non-abelian statistics) are expected to exist in certain fractional quantum Hall states. We introduced how graphene is in some sense an ideal, clean 2D platform which hosts robust fractional quantum Hall states. Lastly, we have described the history and promise of quantum Hall interferometers to probe anyon exchange statistics. We now move on to construct and measure such interferometers in graphene.

I fear not the man who has practiced 10,000 kicks once...

I fear the man who has practiced one kick 10,000 times.

Bruce Lee

3

Experimental Methods

3.1 Assembling van der Waals heterostructures

We need to take special care in how we fabricate our devices to ensure that after lengthy fabrication procedures we are left with graphene with low enough disorder that we can observe strong symmetry broken and fractional quantum Hall states at reasonable magnetic fields. This is quite an art, since we need to handle and control atomically-thin materials. The current state-of-the-art involves encapsulat-

ing graphene between insulating hexagonal boron nitride (hBN) layers [172], usually of order $10-50$ nm thick, as well as conducting graphite gates [173,174], which are simply $\sim$ 5 nm thick crystals containing enough layers of graphene to behave as effectively metallic graphite. Encapsulating graphene in these other 2D van der Waals materials serves several purposes. First of all, graphene is mechanically unstable on its own; it would tend to spontaneously crumple up if it were free standing at room temperature [175,176,177]. Therefore, the earliest graphene devices were made by depositing the graphene onto SiO_2 substrates, which is an exposed, chemically polished surface of oxide that graphene tends to stick well to. However, perhaps for the same reasons that it sticks well to the relatively rough and disordered oxide, graphene tends to be doped and have relatively poor electronic mobility on such surfaces. Instead of sticking it to an oxide, encapsulating graphene between atomically-flat hBN flakes pins the graphene between the van der Waals layers while squeezing out residual disorder such as bubbles at the interface [178], as we will see. The result is a graphene layer with a much larger electron mobility. Furthermore, encapsulating the hBN layers with top and bottom graphite layers serves to further enhance the quality of transport in the graphene, since the metallic layers will screen out external charge disorder that would have been able to leak through the dielectric hBN on its own.

To create the van der Waals flakes of graphene and hBN that we work with, we follow the surprisingly simple "scotch tape" method originally pioneered to create graphene flakes [48,179] with a few modifications and improvements. First, we mechanically cleave graphene and hBN from bulk crystal using thermal release tape (enter part number), which leaves less residue than scotch tape. The tape containing exfoliated flakes is then brought into contact with SiO_2 at 100 °C and baked for 1 minute. The tape is then allowed to naturally cool to room temperature over 10 minutes, then it is slowly removed (by mechanically pulling with tweezers) from SiO_2. The result is that a random distribution of thin van der Waals flakes will be left stuck to the SiO_2. We then search through the flakes and identify good candidates for creating a vertical heterostructure (akin to a sandwich of flakes, one on top of the other). Creating this heterostructure follows a procedure called "stacking" that we now describe.

To proceed with stacking, we use a polycarbonate (PC) polymer-based dry transfer method. PC films are made using 8 wt% solution; droplets of solution are squeezed between two glass slides and left to cure at room temperature. The transfer stamp is made by placing a small block of polydimethylsiloxane (PDMS) (Gel-pak) cut into a diamond shape (8×5 mm) on the glass slide and transferring the PC film on top of it (PC film extends laterally beyond the PDMS block, adhering to the glass slide). Therefore, the stamp consists of a glass slide, PDMS block, and PC film as shown in Fig. 3.1a. The stamp is baked at 180 °C for $20 - 30$ minutes to ensure the film is pinned to the glass slide. After baking, the adhesion between PC-Glass slide is higher than adhesion between PC-PDMS, therefore selecting a larger PC film than PDMS will ensure the film remains fully attached during transfer. The main advantage of a diamond shaped stamp compared to a standard square stamp is that the diamond stamp has 50% less contact area compared square stamp. This reduced contact area decreases the probability of the PC film getting stuck on the substrate and failure of the transfer.

Stacking starts by placing the glass slide with the stamp in a micro-manipulator under a microscope and picking up a large flake of graphite ($\sim 80 \times 80$ μm). The transfer stage is heated to 50 °C and a graphite flake ($\sim 4 - 6$ nm thick) is pressed into contact with PC while lowering the stamp at a 1° tilt angle to the plane. The stage is then heated to 110 °C and cooled down to 80 °C with natural convection. During cool down the stamp is lifted mechanically to pick up the graphite flake. Subsequent layers are picked up by replicating the same procedure. It is crucial that subsequent layers are fully covered by previous layers to utilize the van der Waals force to assist in picking them up. After all flakes (graphite-hBN-graphene-hBN-graphite) are picked up on the stamp with desired orientations, a clean substrate is heated to $160 - 180$ °C and the stack is pressed on SiO_2 to remove bubbles and hydrocarbons trapped in between the layers[178]. The stacking phase finishes by placing the substrate containing the stack in Chloroform for a minimum of 3 hours, followed by annealing in vacuum at 300 °C to partially remove the polymer residue and enhance the adhesion to the substrate.

More details on the transfer method for each layer are shown in Fig. 3.1b. For each pick up the

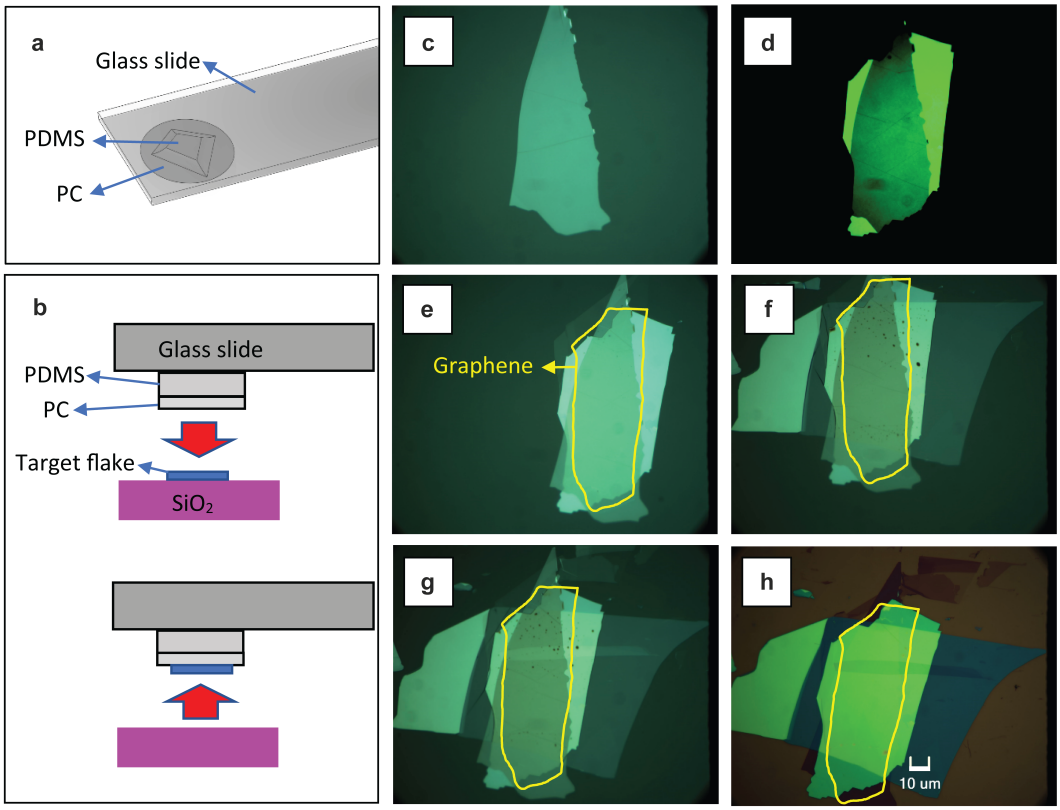


Figure 3.1: Stacking procedure. **(a)** Components of the PC stamp. **(b)** Pick up process. The stamp is tilted 1° alongside longitudinal axis of diamond shape contact area (not shown in figure). **(c)** Optical image of graphite on the stamp after picking it up. It is common to see folds or cracks on graphite due to the large lateral area of the flake and thermal expansion, but they are not fixed until the last step. **(d)** Optical image of graphite-hBN on stamp. **(e)** Graphite-hBN-graphene on stamp. **(f)** Graphite-hBN-graphene-hBN on stamp. Most bubbles are formed during this step at the interface of graphene. **(g)** Optical image of stack graphite-hBN-graphene-hBN-graphite on stamp. **(h)** Stack on SiO_2 after laminating at 160 °C to 180 °C. During this step bubbles are pushed to the edges of the flakes or accumulate at defects and folds.

contact is initiated at 50 °C and a 1° tilt angle. The flake is brought into contact with the stamp while the temperature is raised to $\sim 100 - 110$ °C, and the flake is picked up during natural convection cool down at a temperature range below 90 °C. In our transfer method, graphite is used for the top layer. Compared to the more common hBN assisted pick up method (i.e. using hBN as the top layer), this simplifies the etching process when fabricating our devices. Optical images of the stack assembly progress are shown in Fig. 3.1c-h. Selecting a large flake of graphite as the top layer provides an assistive van der Waal force for picking up subsequent layers.

One of the most critical steps in this method is the drop sequence shown in Fig. 3.2. After all the layers are picked up on the stamp, the stage is heated to $\sim 160 - 180$ °C and the stack is pressed to the substrate. This method has proven to remove the bubbles with an approximately 70% success rate. However, it requires precise control of wave front to achieve a sufficiently slow and steady rate of expansion, which remains challenging. Now that the stack is stuck to the substrate, along with melted and rehardened PC, we remove the PC residue by immersing in Chloroform and annealing the stack at 300 °C for 3 hours (as previously mentioned) to ensure that it adheres to the substrate and will remain mechanically and chemically stable through subsequent processing, which are the nanolithography processes outlined in the next section.

We note in closing the discussion on stacking that a variety of improvements to the technique have been made since the fabrication of the samples used in this thesis. It is a quickly changing art. Most importantly, it has been found that using dome-shaped PC stamps has generally been able to reduce overall bubble formation in stacks by allowing the stamp contact area to generally move more smoothly than in the flat stamps described above. To create a dome, we can mix our own PDMS in two separately cured parts. The first forms a solid stamp that can be placed on the glass slide using a hole puncher, and the second less cured half is then dropped onto the bottom half using a pipette and allowed to cure on a flat surface, which naturally creates a dome. Second, the quality and thickness of PC film can be controlled precisely by dropping the PC droplets dissolved in Chloroform directly onto SiO_2

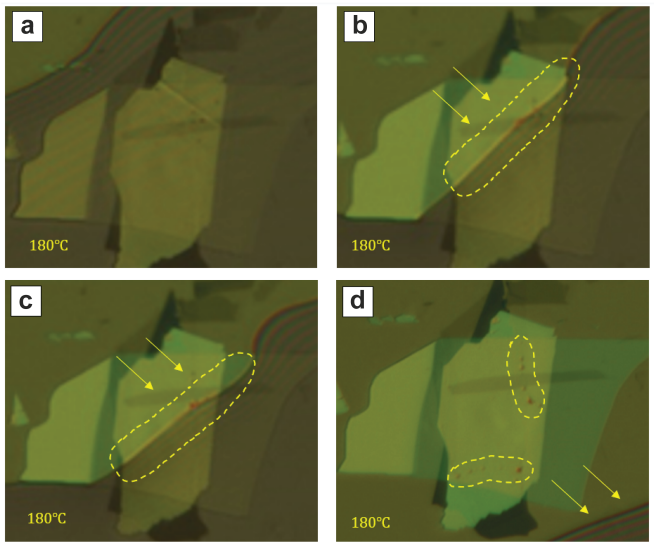


Figure 3.2: Cleaning van der Waals interface. Here we show snapshots of the stack during the lamination on SiO_2 and "bubble pushing" process. The stamp is tilted $\sim 1^{\circ}$ and mechanically pressed onto a SiO_2 surface at a fixed temperature of $180\ ^{\circ}$C. Arrows indicate the direction of wave front movement. **(a)** The wave front of the PC in contact with the SiO_2 approaches the stack. **(b-c)** As the wave front smooths out at temperatures above the glass transition temperature of PC, the visible bubbles and fold defects are pushed along the contact front. **(d)** When the stack has been fully pressed onto the substrate, bubbles have been moved and pinned to the outer edge of graphene flake. A second line of bubbles are visible at the bottom of the stack where the graphene was cracked.

substrates while spinning at 6000 rpm. The film then naturally reaches a desirable thickness and uniformity. The PC film can then be peeled off from the SiO_2 using scotch tape and redeposited onto the dome of PDMS or other type of stamp.

Throughout this thesis, we primarily report data taken from 3 characteristic devices made from 3 different stacks. Chapter 4 reports on an interferometer device with a top (bottom) hBN thickness of 50 (17) nm, as well as a single QPC device with a top (bottom) hBN thickness of 31 (74) nm. Throughout both chapters 5 and 6, we report data taken from the same device, which consists of a top (bottom) hBN thickness of 49 (27) nm.

These relatively thin hBN dielectric layers serve a dual purpose of bringing the conducting graphite layers close to the graphene, which tends to screen interactions within the graphene channel. We believe that this is crucial for observing Aharonov-Bohm oscillations in the device, as similar graphene-based devices without close screening layers displayed Coulomb-dominated oscillations [180]. Likewise, GaAs devices approaching the small areas of our device displayed Coulomb-dominated oscillations [151,181]. It required special sample growth utilizing screening wells to reduce the interactions sufficiently strongly (but not enough to ruin fractional states) to drive the device into the Aharonov-Bohm regime and observe fractional interference, which was only achieved in the most recent devices [163,164,165].

3.2 Constructing gate-defined interferometers

Now that we have large-area stacks without too many visible surface residues or bubbles (checked with atomic force microscopy), we can begin constructing interferometer devices. The general fabrication order is shown in Fig. 3.3, which we now describe.

We fabricate devices from the stacks using standard nanolithography processes involving electron-beam lithography, reactive ion etching, and thermal evaporation of metals. Throughout the process the stacks are kept adhered to doped Si substrates with a 285 nm thick layer of SiO_2. All electron-beam

lithography steps are performed using a Rath 150 series 30 keV beam and polymethyl methacrylate (PMMA) type resists. We cure all resists by baking at 180 °C for at least 5 minutes on a hotplate before exposure. Typical exposure doses range from $450 - 500\ \mu C \cdot \mathrm{cm}^{-2}$, except for 100 nm or narrower lines used in the top graphite trench etches, which requires $1000\ \mu C \cdot \mathrm{cm}^{-2}$ due to the reduced proximity exposure. After exposure, we develop all PMMA masks by letting the sample sit for 2 minutes in a solution consisting of 3 parts isopropanol to 1 part deionized water, by volume, which is chilled at 5 °C, followed by rinsing in pure isopropanol and blow drying in nitrogen.

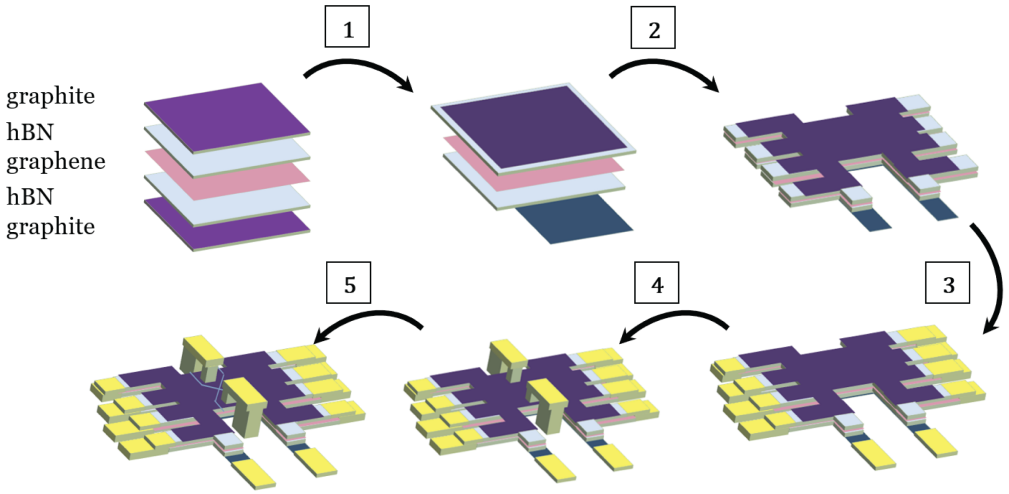


Figure 3.3: Nanofabrication process schematic. **(1)** Etch the top graphite into the desired shape; it must extend from the bottom graphite (recolored blue) to avoid drastic filling factor changes or PN junctions from forming at the contacts, since we use the Si back gate to dope electrons and the Cr/Pd/Au edge contacts naturally dope electrons. **(2)** Etch through the entire stack to define desired geometry and distinct regions for contacts. **(3)** Deposit edge contacts to the exposed graphene and bottom graphite regions, as well as leads to the bridge locations. **(4)** Deposit gold air bridge contacts to top graphite. Note: this device would also have 2 additional bridges to contact the other regions that are separated after the next step. **(5)** Etch $70 - 100$ nm width lines into the top graphite to define the split-gates.

The device geometry is first defined by reactive ion etching in O_2/CHF_3 plasmas using a PMMA resist (950A6, spun 3000 rpm) patterned by electron-beam lithography as the etch mask. This etching is accomplished in two steps: first a pure O_2 plasma (30 W) etch of the top graphite, then a process with $O_2 + CHF_3$ to etch through the entire stack where needed. Edge contacts to the exposed graphene

are then made by using a double-layer PMMA mask (MMA EL6 bottom layer, spun 3000 rpm, and 495A4 top layer, spun 3000 rpm) for a stronger undercut and CHF_3 etching through the top and into the bottom hBN, followed by thermal evaporation of 2/7/150 nm of Cr/Pd/Au at an angle with rotation according the standard edge contact recipe in ref. [182]. Then, air bridges are patterned using a bilayer PMMA process (495A4 bottom layer, spun 2000 rpm, and MMA EL9 top layer, spun 2500 rpm) followed by a short 20 s O_2 plasma PMMA residue clean and thermal evaporation of 2/7/350 nm Cr/Pd/Au. The suspended regions receive 40% of the full dose, leaving the bottom PMMA layer intact to later be dissolved in acetone. For the full interferometer devices, the air bridge to contact the middle graphite gate region is not deposited at this step; it is instead deposited after the lines in the top graphite are etched. To etch the $\sim 70 - 100$ nm width trenches into the top graphite, a thinner PMMA resist (495A4 spun at 1000 rpm) is used and again a reactive ion etch with weak O_2 plasma alone is performed in short ~ 30 s steps. In between etching steps, the two-probe resistances between each bridge-contacted gate are checked until they are all separated ($> G\Omega$ resistance), such that the hBN is minimally etched and line width is minimized. Fig. 3.3 shows the fabrication process of a single QPC device in flowchart form. The fabrication process for interferometer devices follows the same sequence of steps, except that additional bridges are added to contact various regions (Fig. 3.4).

3.3 Performing low electron temperature transport measurements

In addition to the need for a low-disorder device, an interference experiment in the fractional quantum Hall regime requires extremely low electron temperatures for large enough phase coherence of the interfering quasiparticle wavefunction, which necessitates measurements in a well-tuned $He^3 - He^4$ dilution fridge and, crucially, carefully designed electronic filtering.

Therefore, we perform the experiments in chapters 5 and 6 in an Oxford MX400 dilution fridge with base temperature of 20 mK. All DC transport lines are thermalized through Thermocoax cables

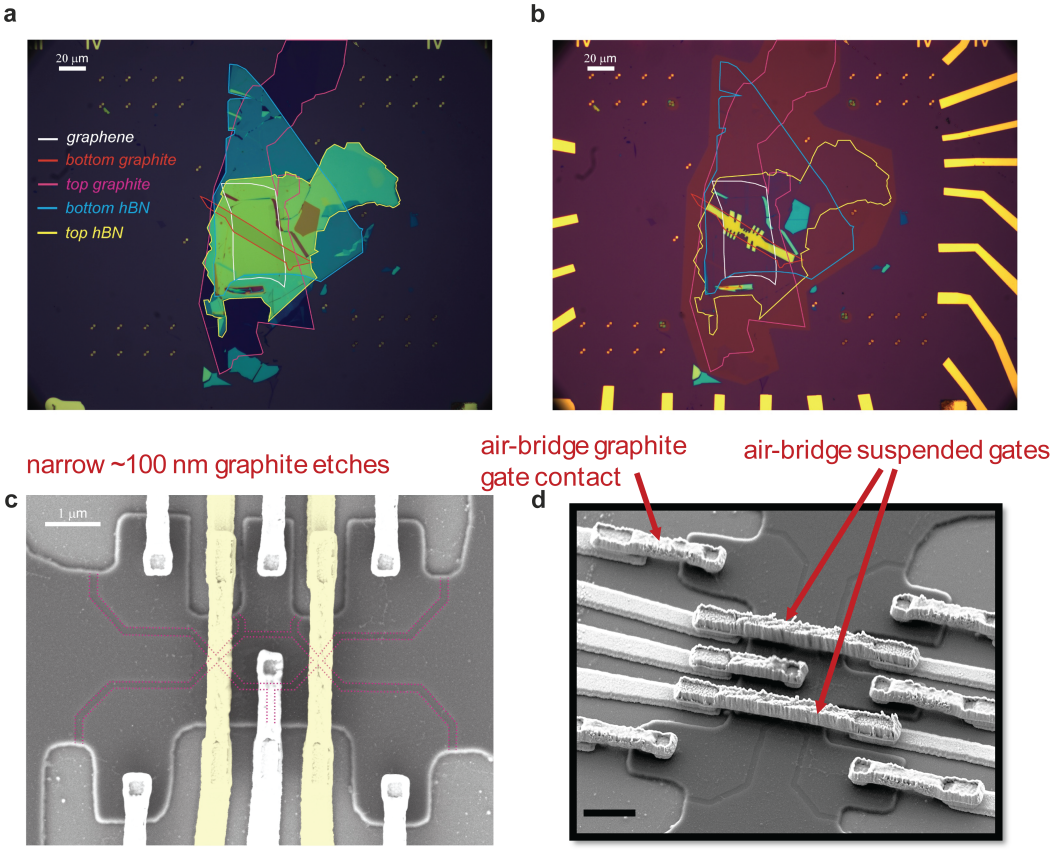


Figure 3.4: Interferometer fabrication. **(a)** Finished stack adhered to substrate with each flake highlighted. This is the stack used for the experiments in chapters 5 and 6. **(b)** Stack after etching processes were completed, before edge contacts are made to the graphene layer and before any trenches or bridges are made. **(c)** Top-down scanning electron microscopy (SEM) image highlighting the narrow width lines etched out of the top graphite layer to create 8 separate top graphite gates. **(d)** Tilted view SEM image highlighting the suspended bridge gates over the two QPCs as well as the bridge contacts to the various separate top graphite gate regions.

and 3 Sapphire plates between room temperature and the mixing chamber before breaking out into copper wire to feed into a custom passive component filter PCB assembly. This circuit consists of three Mini-Circuits LFCN-xxxx+ low pass filters (stepped down in frequency cutoff from 5000 MHz-1800 MHz-80 MHz) followed by a single-pole RC filter (R = 10 kΩ, C = 3.3 nF). While the engineered RC cutoff is 4.8 kHz, the practical cutoff is significantly lower (we estimate a cut-off as low as 50 Hz when the sample resistance is high) due to the device's many contacts to the same 2DEG, allowing the capacitor of the measurement lines to be weighted by the others seen through the device's resistance. The PCB uses 370HR as the dielectric base material and the trace finish coating uses an immersion silver process with no strike layer. An exposed ring of the ground plane is clamped to a soft gold-coated copper enclosure that is directly connected to the mixing chamber copper chassis. The enclosure also acts as a Faraday cage around the PCB components. This thermalizing and filtering scheme (shown in Fig. 6.6) ensures low electron temperature likely within a few mK of the fridge base temperature.

Most top graphite gate regions and the bridge gates are controlled with a home-made 16-bit digital-to-analog converters (DACs), while the silicon backgate is supplied a constant voltage, usually ~ 40 V using a Keithley 2400. Special care is taken to ensure that the middle gate (V_{MG}), which sits above the interferometer cavity and sets its density, and the plunger gate (V_{PG}), are as electrostatically stable as possible to ensure high interferometer visibility and minimal dynamical effects. To this end, these two gates are controlled with additional custom built 20-bit DACs based around the AD5791 integrated circuit. Each channel uses its own ovenized Zener diode voltage reference circuit that has been run continuously for over 3 months with efforts made to thermally insulate it from the rest of the circuitry and environment. This results in an overall DAC output drift of < 11 μV/day. The output noise floor of the DAC is < 25 nV/$\sqrt{\mathrm{Hz}}$ within a 100 kHz measurement bandwidth.

We perform the measurements using low-frequency lock-in amplifier techniques with SR830 lock-in amplifiers, SR560 voltage preamps, and Ithaco 1211 current preamps. For interferometer and QPC measurements, we typically voltage bias using the SR830 connected to a voltage-divider to apply 15 μV

to the sample, resulting in current of order 100 pA to minimize reduction of the oscillation visibility due to finite-bias effect. We measure Hall data using 1 mV bias at 1.0777 Hz to minimize capacitive contribution and increase the resulting measurement accuracy of V_{xx} and V_{xy}. In contrast, the majority of the interference data was measured at 73.77 Hz, allowing fast enough sampling ($\sim$20 samples/s) to resolve the telegraph noise events. However, due to filter attenuation, the amplitude of the signal was partially attenuated at this frequency. As we only consider conductance oscillations due to the interference, i.e. δG on top of the mean conductance, this attenuation does not affect our results and conclusions. Lastly, to achieve accurate QPC calibrations, where we need accurate values of conductance G, as well as when we measure oscillation visibilities, we instead use an intermediate frequency of 11.117 Hz that reduces measurement time while getting accurate enough values.

An exception to the above apparatus and measurement modalities is in chapter 4, where we measure in a Leiden wet dilution system with base temperature 32 mK and without aggressive filtering. Therefore, in this chapter the electron temperature is likely significantly higher, around 100 mK or more offset from the mixing chamber temperature. In addition in chapter 4, we measure using less optimized lock-in amplifier techniques with an ac excitation current of 1 nA at 17.77 Hz applied to the sample. Graphite gates are all controlled with the 16-bit DACs through only room temperature RC filters, and bias dependence is taken by adding a DC current in series and afterwards integrating to give voltage. The relatively high electron temperature likely led to the absence of oscillation signatures in fractional edge states at the time of those measurements.

3.4 Summary

In this chapter, we described the construction of van der Waals heterostructures and fabrication of interferometer devices, as well as the low-frequency lock-in measurement modalities we employ. The remainder of this thesis focuses on the physics that we discover using graphene interferometers.

All that is gold does not glitter,

Not all those who wander are lost;

The old that is strong does not wither,

Deep roots are not reached by the frost.

J.R.R. Tolkien

4

Integer Aharonov-Bohm Interference

Interferometers probe the wave-nature and exchange statistics of indistinguishable particles, for example electrons in the chiral one-dimensional edge channels of the quantum Hall effect (QHE). Quantum point contacts can split and recombine these channels, enabling interference of charged particles. Such quantum Hall interferometers (QHIs) can unveil the exchange statistics of anyonic quasiparticles in the fractional quantum Hall effect (FQHE). Here, we present a fabrication technique for QHIs in van der Waals (vdW) materials and realize a tunable, graphene-based Fabry-Pérot (FP) QHI.

The graphite encapsulated architecture allows observation of FQHE at $B = 3$ T magnetic field and precise partitioning of integer and fractional edge modes. We measure pure Aharonov-Bohm interference in the integer QHE, a major technical challenge in small FP interferometers, and find that edge modes exhibit high visibility interference due to large velocities. Our results establish vdW heterostructures as a versatile alternative to GaAs-based interferometers for future experiments targeting anyonic quasiparticles.

While interferometry techniques originated in the domain of optics, electron-based interferometry has become a powerful probe of coherent quantum phenomena. The optical FP interferometer measures self-interference in a cavity formed between two reflectors [183]. In a two-dimensional electronic system (2DES) in the QHE regime, quantum point contacts (QPCs) that control the number of transmitting one-dimensional (1D) electronic channels serve as tunable reflectors (i.e., beamsplitters) [142]. Combining two QPCs in the 2DES, FP interferometers [167,157,153,159,150] and related QHIs [145,146] were realized in semiconductor heterojunctions. In the FP QHI [168], the magnetic flux contained in the area between the QPCs induces single-particle interference via the Aharonov-Bohm (AB) effect. It has been heavily investigated as a platform for topological quantum computation using the FQHE [31]. However, as both experimental and theoretical studies showed [150,151,169,161,181], Coulomb charging effects can obscure the AB interference signal, which has prevented realizations of the platform. While the charging effect is more significant in small area FP interferometers, small interferometers are preferable for resilience against decoherence. This longstanding hurdle was addressed only recently, where Coulomb interactions were suppressed by incorporating screening layers in proximity to the 2DES [163]. While this approach enabled observation of AB interference in the FQHE regime, the presence of global screening layers limits the versatility and tunability. Encouragingly, strong signatures of abelian anyon braiding were recently seen in such GaAs heterojunctions [164], and signatures of their exchange statistics were seen in collision experiments [184].

Graphene provides an alternative platform. Recent studies on ultraclean hBN/graphite encapsu-

lated graphene vdW heterostructures report FQHE states at moderate magnetic fields, as well as even-denominator FQHE states which may host non-Abelian anyons[185,67]. The large energy gaps of these states, ease of tuning the density, and, crucially, the ability to engineer the paths of the edge modes with local gates[186] make graphene vdW heterostructures a promising platform to realize versatile interferometers. Importantly, the graphite gate and thin hBN dielectric layers should serve to suppress charging effects without additional screening layers.

A few quantum-coherent devices have previously been fabricated in graphene-based vdW heterostructures[59,187,188,189,190]. While QHE interference was observed in Mach-Zehnder interferometers built across a graphene pn junction[191,192], scattering at the physical edge served as uncontrolled beam splitters in these devices, limiting tunability and coherence. Furthermore, recent local probe measurements have shown that edge modes near etched graphene edges suffer from dissipation due to counterflowing edge modes[99]. Therefore, to increase the edge mode coherence length, which is essential for high visibility interference, we electrostatically defined QHIs to enforce bulk separation from the etched edges of graphene. Additionally, this design allows an electrostatically defined, sharp confining potential, which should prevent edge state reconstruction and maintain large edge mode velocities[11]. Aiming at the goal of implementing a QHI in the FQHE, we developed vdW stacking and fabrication techniques (outlined in Chapter 3) to realize a FP QHI in a high mobility graphene heterostructure. In this chapter, we observe widely tunable AB interference with no charging effects, allowing us to extract edge mode phase coherence lengths and velocities to support the claims made above. We demonstrate the versatility of our QPC design with operation in the FQHE, enabling further experiments probing anyons in graphene, such as the experiment discussed in Chapter 6.

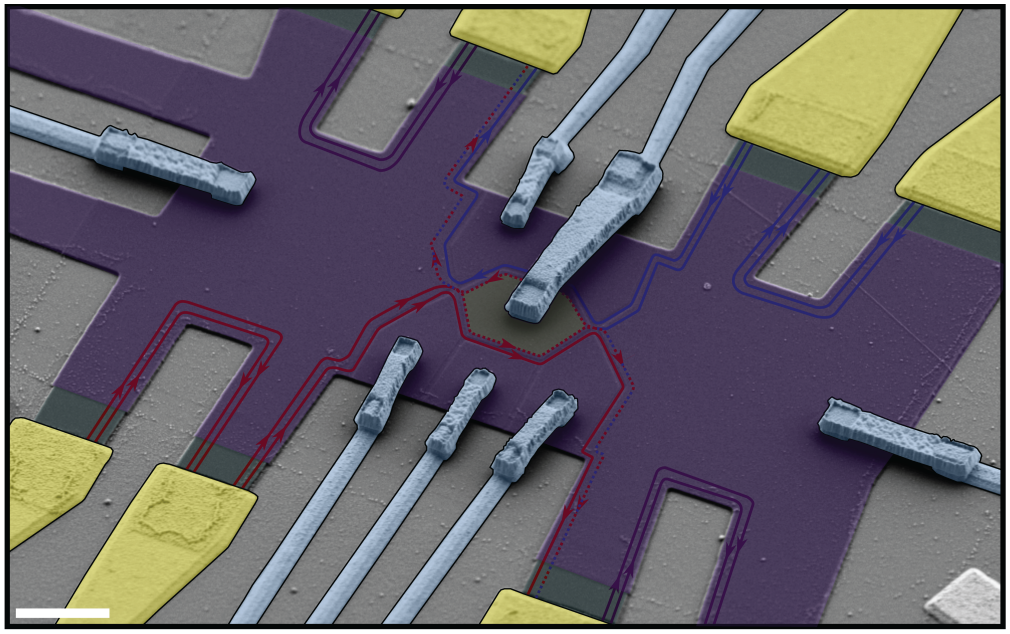


Figure 4.1: Gate-defined Fabry-Pérot interferometer in graphene. False color Scanning Electron Microscopy image of a FP device. Contacts are yellow and bridges connecting to each region of the top graphite layer are blue. Scale bar: 2 μm. The paths of the chiral edge states are shown for interference of the inner edge in $\nu = 2$

4.1 Design of the graphene-based interferometer

Figure 4.1 shows an electron microscope image of a representative device out of 4 devices we studied, consisting of a graphene active layer encapsulated in hBN insulating layers and top/bottom graphite gates. An image of the device that we actually measured is shown in Fig. 4.2a (since scanning electon microscopy tends to degrade devices). A FP QHI requires two QPCs where edge channels are brought sufficiently close to induce backscattering, shown schematically in Fig. 4.2b. There are 8 Ohmic contacts C_{n}, where $\mathrm{n} = 1 : 8$, four on each side of the interferometer, to source current and detect transmission and reflection by measuring the chemical potential of the QHE edges. We employ a double-ground scheme, which enables us to confirm that no bulk conductance is present[150]. Each

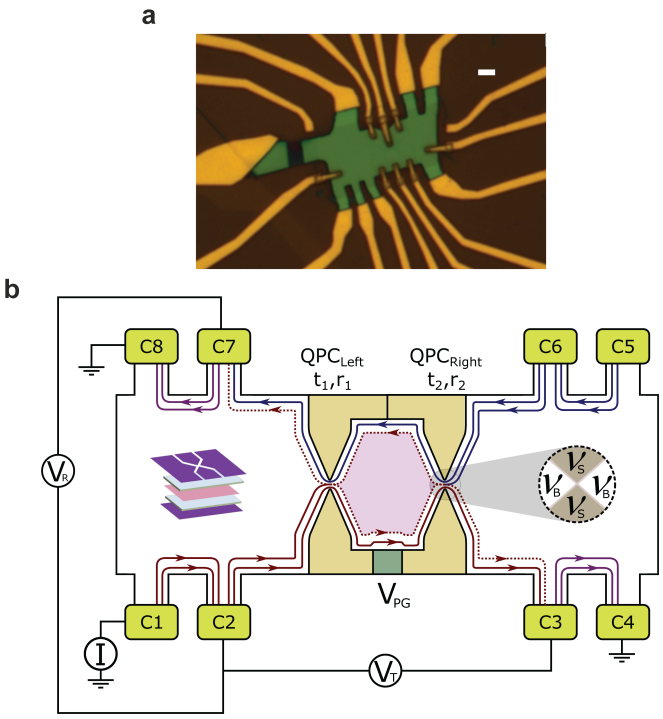


Figure 4.2: Fabry-Pérot device and measurement schematic.(a) Optical image of the FP device measured in this chapter. Note that unlike in the electron microscope image in Fig. 4.1, the actual device measured has an additional bridge and separated gate such that there are 4 top gates to control the QPCs: 2 gates each. Scale bar: 2 m. **(b)** Schematic of a FP QHI at filling factor 2 illustrating interference of the second Landau level edge (inner edge). Each QPC is realized by a pair of split gates, and a plunger gate (PG) tunes the area enclosed by the interfering edge (shaded red). For each QPC, the top graphite gates (inset illustrations) enable control of filling factors in the bulk ν_{B}, split gates ν_{S}, and QPC saddle point ν_{QPC}. Current (1 nA) is injected into C_1 while C_4 and C_8 are grounded. We measure $V_{\mathrm{T}} = V_{2-3}$ and $V_{\mathrm{R}} = V_{2-7}$.

ith QPC ($i = 1, 2$) may be described by two parameters: the probability of transmitting (t_i) and reflecting ($r_i = 1 - t_i$) a quasiparticle on the edge, where reflecting means backscattering to the opposite chiral edge. Note that we have now defined $t_i = |\tau_i|^2$ and $r_i = |\rho_i|^2$. Note also that reflection and transmission coefficients refer only to current which is carried by the portioned edge. Neglecting dephasing, the probability for a quasiparticle emitted in the edge channel from C_1 to transmit through both QPCs and reach the ground contact C_4 is given by $t_{\mathrm{FP}} = \frac{(1-r_1)(1-r_2)}{1+r_1r_2-2\sqrt{r_1r_2}\cos(\theta)}$, where θ is the phase acquired by a propagating particle in one revolution around the perimeter of the FP cavity.

4.2 Tunable quantum point contact architecture

Since graphene has no intrinsic bandgap, creating a QPC for edge states requires different implementation than in gapped semiconductors. For the ubiquitous QPC in a semiconductor, the Fermi level under the split gates needs to be set in the intrinsic band gap, depleting electronic states from the region. In graphene, we use the Landau level gaps that form in the QHE regime in an analogous way[193,194]. Figure 4.3a shows transmission and reflection measurements for a QPC, demonstrating the operation of a single QPC device for bulk filling $\nu_{\mathrm{B}} = 2$. We measure the voltage difference V_{T} (V_{R}) between the transmitted (reflected) edge states and the incoming edge states as defined in Fig. 4.2. The transmission and reflection coefficients are related to the transmission resistance $R_{\mathrm{T}} \equiv \frac{V_{\mathrm{T}}}{I}$ and reflection resistance $R_{\mathrm{R}} \equiv \frac{V_{\mathrm{R}}}{I}$, where I is the total injected current. The reflection probability (per partitioned edge) is obtained for non-integer QPC filling ν_{QPC} from $r = \lceil \nu_{\mathrm{QPC}} \rceil - \frac{R_{\mathrm{R}}}{R_{\mathrm{Q}}}\nu_{\mathrm{B}}^2$, where $R_{\mathrm{Q}} \equiv \frac{h}{e^2}$ is the quantum resistance of a single channel and $\lceil \nu_{\mathrm{QPC}} \rceil$ is the smallest integer greater than or equal to ν_{QPC}. Experimentally, we find a $\sim 10\%$ reduction in measuring R_{R} when the QPC is open (fully transmitting) due to the two-ground scheme used for our measurement and an imperfect edge state equilibration in one of the grounds.

Each edge mode can be tunably transmitted separately by tuning the gates in the device simultane-

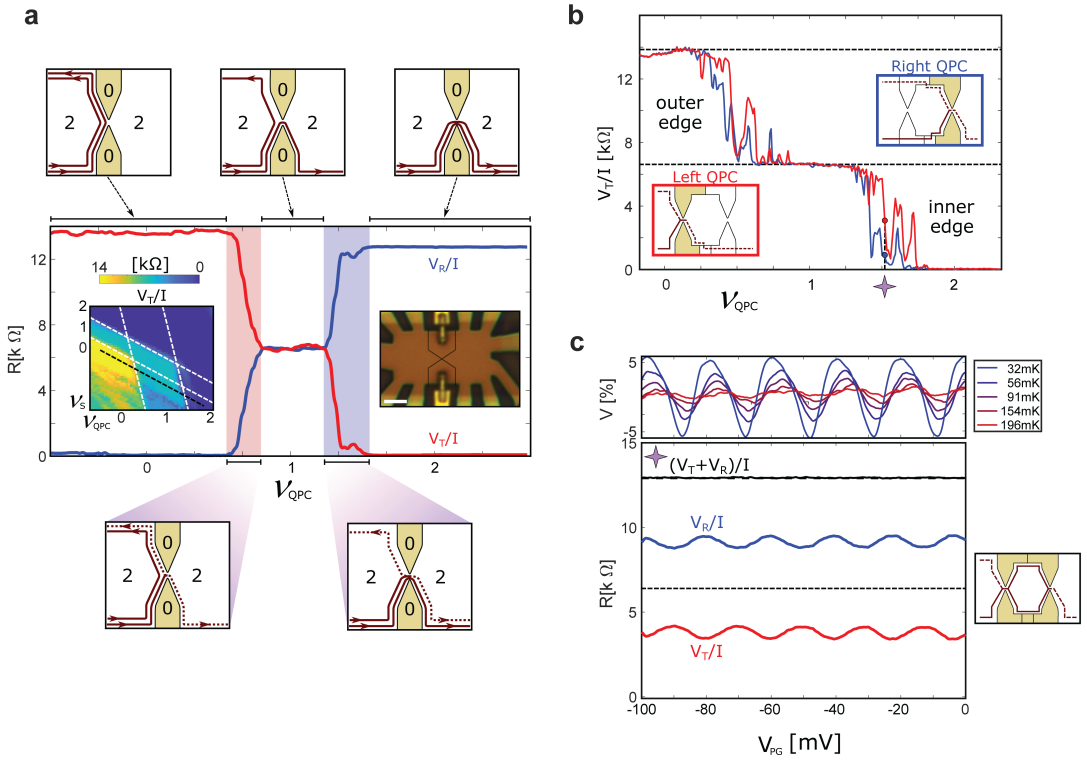


Figure 4.3: Tunable QPCs and oscillations controlled by plunger gate. (a) Tunable single QPC device (inset: optical image). Scale bar: 2 µm. A 2D map of QPC operating points for $\nu_B = 2$ is shown; $\frac{V_T}{I}$ as a function of ν_S and ν_{QPC} (see Fig. A.1 for gate voltages on each). The outer two top gates compensate to keep $\nu_B = 2$ as the bottom gate sweeps along the horizontal axis. Top split gates scan the vertical axis. White dashed lines show transitions between regions of quantum Hall states ν_S or ν_{QPC}. The black dashed line marks constant filling under the split gates, $\nu_S = 0$, and changing ν_{QPC}. Line-cuts along the black dashed line measuring $\frac{V_T}{I}$ (red) and $\frac{V_R}{I}$ (blue) demonstrate QPC operation for $\nu_B = 2$. **(b)** Transmission $\frac{V_T}{I}$, across each QPC measured separately (as shown in the inset figures) as a function of ν_{QPC}. The star symbol indicates ν_{QPC} corresponding to an operating point with reflection 0.14 and 0.51 of the inner edge for QPC1 and QPC2, respectively. **(c)** FP interference at the inner edge of $\nu_B = 2$ as a function of plunger gate voltage for QPC operating points shown in Fig. 4.1d. $V_{PG} = 0$ corresponds to the filling under the plunger gate $\nu_{PG} = 0$. Top inset: temperature dependence of the oscillation visibility.

ously at a fixed magnetic field, since all regions are separately gated by the etched top graphite layer. This enables us to keep ν_B and split-gate filling ν_S constant while different edge channels are partitioned by tuning ν_{QPC} using the bottom graphite and split gates. The 2D plot (inset of Fig. 4.3a) demonstrates the full range of tunability for $\nu_B = 2$, while line-cuts are taken for $\nu_S = 0$. Even in $\nu_B = 6$ at a QPC width of 150 nm, we can measure full transmission of all 6 edge modes (see Fig. A.1), which means the average edge mode width is less than 12 nm. This mode width is comparable to the magnetic length, $l_B \equiv \sqrt{\frac{\hbar}{eB}} = 9$ nm for $B = 8$ T, in agreement with the single-particle picture. The capability to independently tune ν_B, ν_S, and ν_{QPC} for a given magnetic field while preserving high-mobility samples presents an advantage of our platform.

4.3 Fabry-Pérot interferometer

By cascading two QPCs in series, we construct a FP interferometer device (illustrated in Fig. 4.2). In this FP device, each QPC is tuned using their respective split-gates and a common graphite bottom gate. In Fig. 4.3b, we display line-cuts of R_T for independently measured QPCs in the range of $0 < \nu_{QPC} < 2$ while the split gate voltages are set to $\nu_S = 0$. We can either partition the inner edge mode by adjusting gates in the range $1 < \nu_{QPC} < 2$ or the outer edge mode using $0 < \nu_{QPC} < 1$. We observe the transmissions through the two QPCs are nearly identical in the plateau region but differ along the plateau transitions, where they show fluctuations. These fluctuations differ between thermal cycles, indicating that the residual disorder configuration near the QPCs determines them. We observe fewer fluctuations in the single QPC device (Fig. 4.3a), which has a thicker bottom hBN (74 nm) compared to the FP device (17 nm). We expect that increased distance from the screening bottom gate reduces compressible state formation near the saddle point of the QPC potential, which is consistent with the proposed mechanism for transmission fluctuations being resonant charging of compressible, localized states in the QPC region [195].

Tuning to partial transmission through both QPCs allows interference. Our FP device uses a side plunger gate (with voltage V_{PG}) between the two QPCs to modify the QHE edge mode trajectory within the FP cavity. Figure 4.3c shows the simultaneously measured reflection and transmission across the FP as a function of V_{PG}. We set the bulk (including the FP cavity region) to $\nu_{\mathrm{B}} = 2$ while $\nu_{\mathrm{S}} = 0$ and partition the inner edge channel with QPC reflection probabilities $r_1 = 0.51$ and $r_2 = 0.14$, left and right respectively. The outer edge channel passes fully through both QPCs. Oscillatory R_{T} and R_{R} are observed as a function of V_{PG}. They sum to a constant $\frac{R_{\mathrm{Q}}}{\nu_{\mathrm{B}}}$, demonstrating that transport is governed solely by edge states. The oscillation visibility, calculated from $V \equiv (R_{\mathrm{T/R,max}} - R_{\mathrm{T/R,min}})\frac{\nu_{\mathrm{B}}^2}{R_{\mathrm{Q}}}$, is $\sim 11\%$ at $T = 30$ mK and persists through $T = 200$ mK (top inset of Fig. 4.3c). Recall that we expect the electron temperature to be significantly higher than this mixing chamber temperature.

4.4 Aharonov-Bohm vs. Coulomb dominated oscillations

The observed oscillatory behavior of $R_{\mathrm{T}}(V_{\mathrm{PG}})$ in the FP QHI can be attributed to the AB effect that modulates the interference phase θ. As we scan V_{PG}, the enclosed effective area A occupied by the interfering edge mode changes. At a fixed B, this area change δA is related to the added (subtracted) charge $\delta Q = \frac{eB\delta A}{\phi_0}$ in δA, where $\phi_0 = \frac{h}{e}$. Since $\delta Q \approx C_{\mathrm{EG}}\delta V_{\mathrm{PG}}$, where C_{EG} is the capacitance between the edge channel and plunger gate, the plunger gate modulates the total interference phase $\theta = 2\pi\frac{BA}{\phi_0}$ by $\delta\theta = 2\pi\frac{B\delta A}{\phi_0}$, leading to $\delta\theta \approx 2\pi\frac{C_{\mathrm{EG}}\delta V_{\mathrm{PG}}}{e}$.

An explicit demonstration of the AB interference in our QHI is achieved by measuring the transmission/reflection through it as a function of variations in both the magnetic field, δB, and the plunger gate voltage, δV_{PG}. The expected phase evolution for a single revolution around the FP interferometer perimeter is given by $\frac{\delta\theta}{2\pi} \approx \frac{A\delta B}{\phi_0} + \frac{C_{\mathrm{EG}}\delta V_{PG}}{e}$. Figure 4.4 shows the measured $R_{\mathrm{T}}(B, V_{\mathrm{PG}})$ in four operating regimes of the QPCs' reflection coefficients, from relatively open (Fig. 4.4a) to pinched

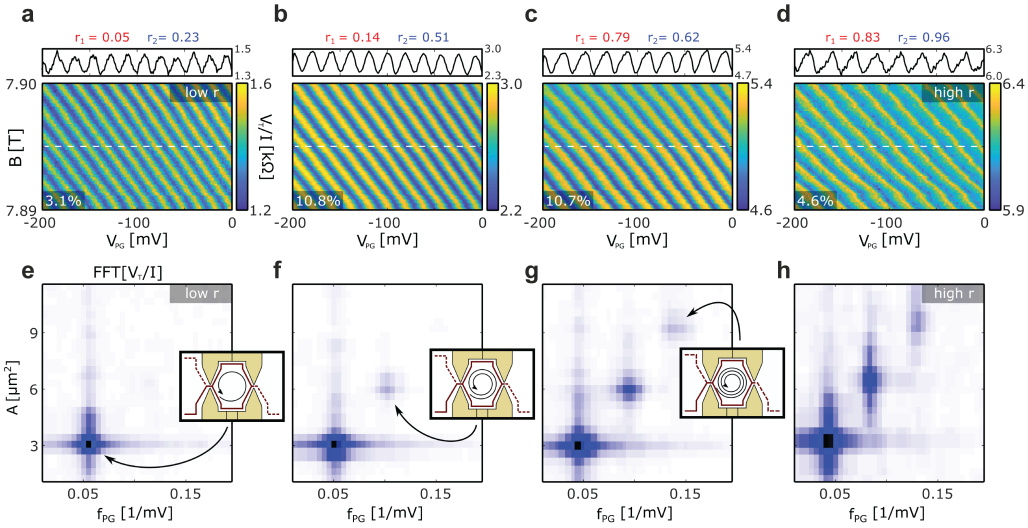


Figure 4.4: Aharonov-Bohm (AB) dominated Fabry-Pérot interference. (a-d) Transmission resistance $R_{\mathrm{T}} \equiv \frac{V_{\mathrm{T}}}{I}$ oscillations as a function of magnetic field B and plunger gate V_{PG}, showing clear AB oscillations. Filling factors are $\nu_{\mathrm{B}} = 2$ and $\nu_{\mathrm{S}} = 0$. We measure interference of the inner edge state. Reflection values r_1 and r_2 of left and right QPCs, respectively, are stated above each figure and visibility in percentage at the lower-left corner. In the upper panel of each plot we show a line cut as a function of the plunger gate along the white dashed line. $V_{\mathrm{PG}} = 0$ corresponds to the filling under the plunger gate $\nu_{\mathrm{PG}} = 0$. **(e-h)** 2D-fast Fourier transform (FFT) of the transmission resistance plots (a-d), respectively, as a function of area and plunger gate periodicity. In the insets of figs. (f), (g), and (h) we illustrate the origin of each peak in the FFT signal. Higher harmonics appear when the QPCs are pinched (large r_i), physically corresponding to contributions from single-particle trajectories that make multiple revolutions around the interferometer area.

(Fig. 4.4d). A periodically repeating stripe pattern (so-called pyjama plot), whose constant phase (i.e., $\delta\theta = 0$) inclination agrees with 'AB interference', $\frac{\delta B}{\delta V_{\mathrm{PG}}} = -\frac{C_{\mathrm{EG}}\phi_0}{eA} < 0$, is observed. We find that the slope of the stripe $\frac{\delta B}{\delta V_{\mathrm{PG}}}$ remains negative for the interference from both inner and outer QH edges (Fig. A.8), further supporting the AB interference scenario. The magnetic field periods, seen in the 2D-FFT (Fig. 4.4e-h), match an integer multiplicity of the enclosed flux in the lithographically defined area of $A = 3\ \mu\mathrm{m}^2$. The periodicity in V_{PG} yields an edge-gate capacitance C_{EG} that agrees with electrostatic considerations (Fig. A.10). Utilizing the wide tunability of our QPCs, we can correlate the visibility of the AB oscillations with the reflection coefficients of both QPCs to extract a phase coherence length for exponential suppression (see Appendix A). For the inner edge of $\nu_{\mathrm{B}} = 2$, this

process yields a characteristic phase coherence length, $L_0 = 8.0$ μm, larger than the perimeter of the cavity, $P = 6.8$ μm. We remark that the AB oscillations observed in our FP QHI are robust; for different r_i values and different ν_B, we always observe a negative $\frac{\delta B}{\delta V_{PG}}$ slope, characteristic of AB interference. The appearance of higher harmonics in the 2D FFT in the pinched QPC limit (Fig. 4.4h) suggests that the edge modes can maintain phase coherence during multiple round trips around the cavity.

Measurements in similar area FP QHIs fabricated in GaAs structures often displayed a different behavior: lines of constant phase in the B vs. V_{PG} plane had zero (field independent) or positive slopes [150,151]. This complicated behavior of the FP QHI, referred to as 'Coulomb-dominated (CD)' [169], is associated with strong Coulomb coupling between the interfering edge mode and the localized quasiparticle states in the bulk. The two regimes, AB and CD, can be understood employing a classical capacitive model. Defining $\xi \equiv \frac{C_{EB}}{C_{EB}+C_B}$, then $\xi \to 0$ ($\xi \to 1$) defines the AB (CD) regime, respectively. Here, C_{EB} is the capacitance between the interfering mode and the compressible puddle of localized charges in the bulk, and C_B is the total capacitance of the compressible bulk puddle to ground [169,161]. Experimentally, there is a trade-off between making the interferometer smaller (to increase coherence) and minimizing the interaction parameter ξ. Our device, with two hBN insulating layers ($\epsilon_r = 4$), separating the bottom (top) graphite gate 17 (50) nm away, is estimated to have $\xi \ll 0.1$ and a charging energy scale $\frac{e^2}{2C_B} \approx 8$ μeV, comparable to the screened GaAs FP QHI [163].

4.5 Coherence lengths and edge mode velocities

In our graphene FP QHI, the interfering edge mode is guided by a barrier set by the large Landau level gap underneath a biased graphite gate. This unique scheme allows us to investigate the decoherence mechanism of edge modes. Fig. 4.5a shows a wide range of AB oscillations of the inner edge of $\nu_B = 2$ as a function of plunger gate voltage V_{PG}, where the filling fraction underneath the gate ν_{PG} varies

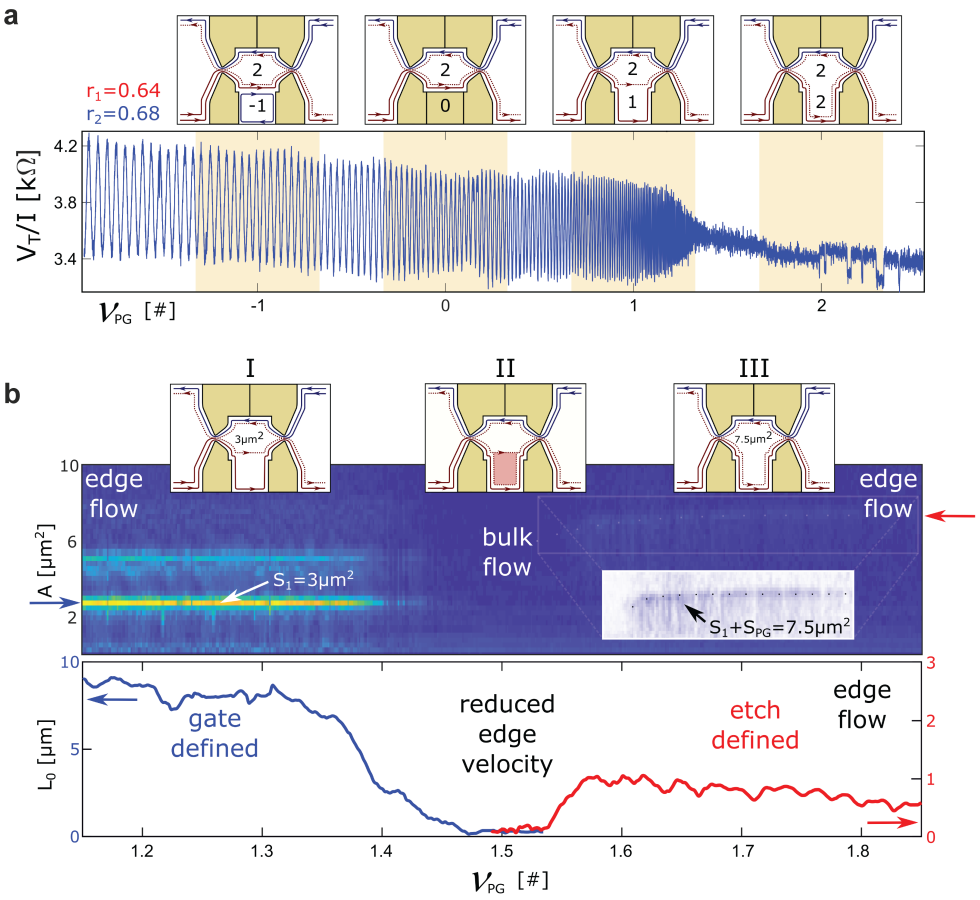


Figure 4.5: Gate vs. etch defined interferometer. (a) R_T oscillations as a function of the filling factor under the plunger gate ν_{PG} spanning -1 to 2. As ν_{PG} increases, the interfering edge's capacitance to the plunger gate increases, thereby reducing the oscillation period. As ν_{PG} transitions from 1 to 2, visibility collapses due to interaction with compressible regions followed by propagation of the edge state along the etched graphene boundary. **(b)** 1D FFT of $R_T(B)$ converted to units of area as a function of ν_{PG} showing 3 distinct regimes: I. Interference is gate-defined, showing the expected area of 3 μm^2 (blue arrow) and additional harmonics. II. Suppressed oscillation due to bulk conductance under the plunger gate. III. Suppressed interference region due to etch-defined propagation of the interfering edge matching a fabricated area of 7.5 μm^2 (red arrow). **(c)** Extracted coherence length as a function of plunger gate filling for regime I (blue) and III (red) from 3 μm^2 and 7.5 μm^2 areas, respectively. The value plotted for the etch defined edge (red) is extracted only for the portion of propagation along the etched region, where we split the perimeter in the visibility formula into two parts: a length 1.8 μm (etch defined) whose coherence length we extract (plotted here) and a length 12 μm (gate defined) with coherence length 8 μm. See Appendix A for more details. Uncertainty estimation for the gated (etched) coherence length is ± 2 μm (± 0.4 μm).

between -1 and 2. The oscillations exhibit a reduced gate periodicity as the filling ν_{PG} increases, resulting from an increased C_{EG} as the edge mode moves closer to the plunger gate. The visibility of the AB oscillations does not change appreciably in the range $\nu_{\mathrm{PG}} < 1$, suggesting that distance from the copropagating outer edge mode ($\nu_{\mathrm{PG}} = -1$) and depletion/compressible state under plunger gate ($-1 < \nu_{\mathrm{PG}} < 1$) do not play a role in decohering the interfering inner edge mode. However, the visibility drops for $\nu_{\mathrm{PG}} > 1$. Three different regimes appear in this range. First, for $1 < \nu_{\mathrm{PG}} < 1.4$ (regime I) – the outer edge mode moves away, while the interfering inner mode interferes with a slowly reducing visibility. For $1.4 < \nu_{\mathrm{PG}} < 1.6$ (regime II), inner and outer modes are separated by a compressible region, which either decoheres the interfering mode or lowers the mode's velocity (due to a softer potential). For $1.6 < \nu_{\mathrm{PG}}$ (regime III), the two edge modes approach the physical edge of the graphene layer, and the AB oscillation visibility is more than an order of magnitude suppressed. The 1D Fourier transform of $R_{\mathrm{T}}(B)$ plotted as a function of ν_{PG} (Fig. 4.5b top) shows that the enclosed area increases from 3 $\mu\mathrm{m}^2$ (regime I) to 7.5 $\mu\mathrm{m}^2$ (regime III), equal to the combined area underneath the plunger gate and the FP cavity. We estimate the characteristic dephasing length $L_0 \sim 0.9$ μm for the portion of propagation along the etched graphene edge in regime III (Fig. 4.5b bottom). We attribute this strong dephasing to the proximity of the interfering edge mode to the etched physical edge of the graphene layer. Indeed, a recent scanning probe study showed the presence of local counter propagating edge states and multiple dangling bonds at the etched graphene edge[99].

To increase visibility, one may engineer the edge states to increase L_0. In our graphene-based FP QHI, this goal can be achieved by (i) shielding the interfering edge mode from etched edges and charge puddles by guiding the edges via electrostatics and utilizing other compressible QHE edges for screening; and (ii) sharpening the electrostatic barrier potential to increase the edge mode velocity v_{edge}, which can be estimated from bias dependence[196]. Applying a finite source-drain bias V_{SD} on the interfering mode produces additional modulation, $R_{\mathrm{T}}(V_{\mathrm{SD}})$. Due to the self-interference condition, each time a full wave packet occupies the interferometer a constructive interference occurs yielding a

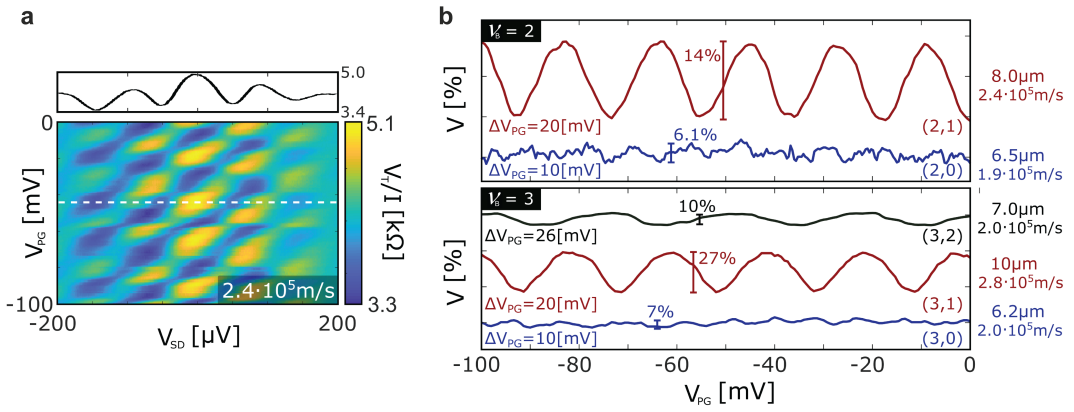


Figure 4.6: Edge mode velocity and comparison of oscillations in different filling factors. (a) R_T oscillations as a function of source-drain bias V_{SD} and V_{PG} showing a tilted checkerboard pattern. Edge mode velocity is estimated from the lobe structure. Upper panel shows a cut of the data along the white dashed line. **(b)** Comparing oscillation in the different edges at filling factor 2 (upper) and 3 (lower) as a function of plunger gate. Plunger gate periodicity, visibility, edge mode velocity, and coherence length are written next to each plot. Coherence length error is estimated to be ± 2 μm, and velocity error is $\pm 0.2 \cdot 10^5$m/s. For more information on plunger gate periods and AB interference of all edges, see Fig. A.9

phase shift of $2\pi = eV_{SD}\frac{L}{\hbar v_{edge}}$ (Refs. [163,196,152]). However, we note that the bias dependence shown in Fig. 4.6a differs from those previously reported; we see a tilted checkerboard pattern, as also seen in a concurrent graphene work [197]. The tilt is caused by an asymmetric potential drop in the cavity, possibly because energy relaxation processes are not strong enough to equilibrate the chemical potential within this length scale [197]. From the periodic modulation along the positive slope lines seen in $R_T(V_{SD}, V_{PG})$ (Fig. 4.6a), we estimate $v_{edge} = 4.5 \cdot 10^5$ m/s for the inner edge channel of $\nu_B = 2$, comparable to the velocity extracted from the temperature dependence of visibility (Fig. A.11). We further probe the interference on other edge modes; the extracted phase coherence lengths and velocities are summarized in Fig. 4.5b. The edge mode velocities are systematically more than a factor of 2 larger than those reported in the screened GaAs device [163], consistent with sharper confining potentials in our vdW heterostructure. Interestingly, we find that interfering the middle edge of filling factor 3, in the configuration $(\nu_B, \lfloor \nu_{QPC} \rfloor) = (3, 2)$, gives rise to the highest visibility ($\lfloor \nu_{QPC} \rfloor$ is the largest integer smaller than ν_{QPC}). We attribute this enhancement in visibility to screening from

both the etched physical edge and the bulk, by outer and inner edge modes, respectively, as well as to increased edge mode velocity for the middle edge, possibly due to the electrostatic profile between the surrounding compressible strips and the gates.

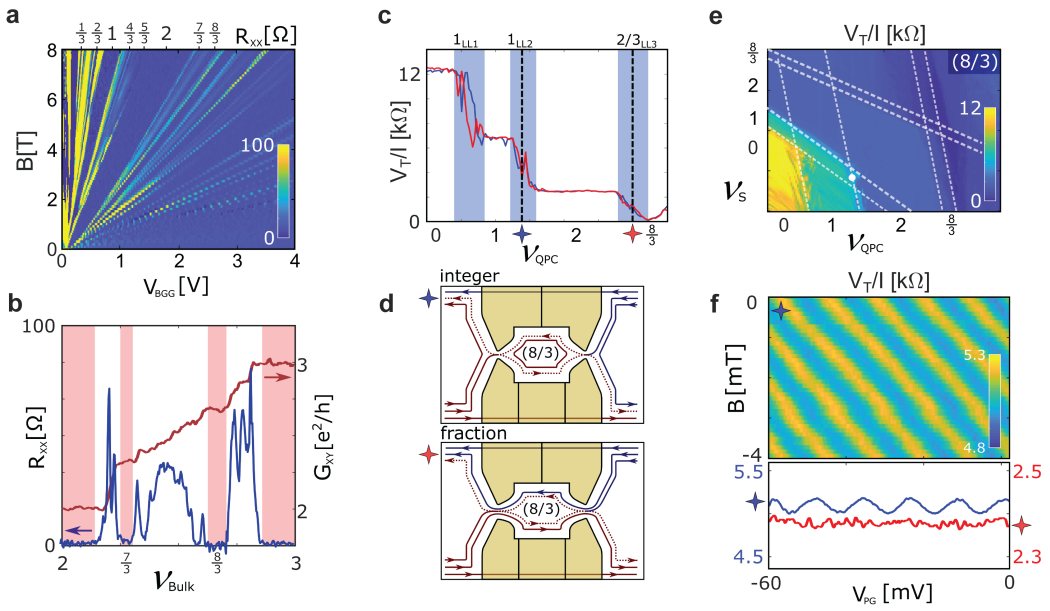


Figure 4.7: Aharonov-Bohm interference of an integer edge with a fractional bulk filling. (a) R_{XX} fan diagram, demonstrating fractional states forming at $B = 3$ T. **(b)** Measurement of R_{XX} and R_{XY} demonstrating fully developed fractional QHE states at $\nu_B = 8/3$ and $7/3$, $B = 8$ T. **(c)** $\frac{V_T}{I}$ of the left and right QPCs, red and blue respectively, showing integer and fractional edge partitioning. Blue and red star symbols represent the QPC configuration corresponding to the integer (blue) and fractional (red) edge state partition while the bulk filling factor is $8/3$. **(d)** Schematic diagrams of the edge configuration for the two QPC working points. Blue (red) marks illustrate interference configurations of an integer (fractional) edge. **(e)** 2D map of the operating points of the QPC at $\nu_B = 8/3$; $\frac{V_T}{I}$ as a function of ν_S and ν_{QPC}, tuned by the top split gates and bottom graphite gate, respectively. **(f)** Tuning to the marked point (white dot) in (e), we measure interference of the innermost integer edge. $V_{PG} = 0$ corresponds to the filling under the plunger gate $\nu_{PG} = 1$. Lower panel: $\frac{V_T}{I}$ measurement (in kΩ) tuned to interfere an integer (blue) and a fractional (red) edge for $\nu_B = 8/3$.

In Fig. 4.7a, we demonstrate the quality of our graphite encapsulated FP with FQHE realized at magnetic fields as low as 3 T. Fig. 4.7b shows a well-developed fractional state for $\nu_B = 7/3$ and $8/3$ (see SI6 for other fractions). Due to the tunability of the QPCs, we can partition integer as well as fractional edge modes, as shown in Fig. 4.7c for $\nu_B = 8/3$. The interference paths for each case are

illustrated in Fig. 4.7d. Tunability of an individual QPC in a FQHE state is demonstrated in Fig. 4.7e. By careful tuning, we observe high visibility interference for the integer edge modes (Fig. 4.7f) while keeping the bulk at an insulator fractional filling. Interfering the fractional mode did not result in visible AB interference, due to relatively high base temperature ($\sim$ 60 mK) and insufficient electronic filtering in the measurement system such that decohering and phase-averaging processes dominate the fractional mode on a length scale much smaller than the interferometer perimeter.

4.6 Conclusion

Interference of exotic excitations in the FQHE has been pursued for many years in GaAs heterostructures. A major roadblock to observing exchange statistics has been isolating the AB interference from charging effects. In this chapter, we demonstrated a graphene-based FP QHI that shows AB interference in the integer QHE, absent of charging effects, along with QPCs that operate in the FQHE. In the following chapters, we will introduce fully independent control of the two separated QPC regions, smaller perimeter devices, and lower electron temperature measurements to probe interference in the FQHE. Other promising directions include extending our QHI design utilizing graphite gates to investigate anyonic excitations in other vdW heterostructures, including bilayer graphene [117,116] and WSe_2 (ref. [198]). Furthermore, graphene can be coupled to superconductors [199,200,201] to create novel interferometry devices [202] and topological phases [203,204].

One must imagine Sisyphus happy.

Albert Camus

5

Strongly Coupled Integer Edge States

Electronic interferometers using the chiral, one-dimensional (1D) edge channels of the QHE can demonstrate a wealth of fundamental phenomena. The recent observation of phase jumps in a FP interferometer revealed anyonic quasiparticle exchange statistics in the fractional QHE. When multiple integer edge channels are involved, FP interferometers have exhibited anomalous AB interference frequency doubling, suggesting putative pairing of electrons into $2e$ quasiparticles. In this chapter, we use a highly tunable graphene-based QHE FP interferometer to observe the connection between inter-

ference phase jumps and AB frequency doubling, unveiling how strong repulsive interaction between edge channels leads to the apparent pairing phenomena. By tuning electron density in-situ from filling factor $\nu < 2$ to $\nu > 7$, we tune the interaction strength and observe periodic interference phase jumps leading to AB frequency doubling. Our observations demonstrate that the combination of repulsive interaction between the spin-split $\nu = 2$ edge channels and charge quantization is sufficient to explain the frequency doubling, through a near-perfect charge screening between the localized and extended edge channels. Our results presented in this chapter will show that interferometers are sensitive probes of microscopic interactions and enable future experiments studying correlated electrons in 1D channels using density-tunable graphene.

Electrons in 1D quantum systems exhibit striking phenomena, including the breakdown of Fermi liquid theory and quasiparticle formation in favor of collective modes[205]. Likewise, electrons confined to two dimensions and subjected to perpendicular magnetic fields exhibit the QHEs[2]. Although the microscopic details of QHE states are still an active area of research[99,100], their low-energy transport properties are known to be governed by chiral, 1D edge channels[7,11,98,101]. These edge channels (ECs) conduct charge ballistically, allowing for phase-coherent electronic experiments[145,142]. In particular, electronic FP QHE interferometry[167,168,169], was performed extensively in GaAs, culminating in the observation of interference phase jumps as evidence for anyonic statistics of fractional quasiparticles[164,165,206,104]. Recently, FPs were developed in graphene, which showed AB interference of integer ECs[207,197,208], with oscillation periodicity set by the magnetic flux quantum for electrons $\phi_0 \equiv \frac{h}{e}$. Our previous design, as discussed in Chapter 4, utilized graphite gates encapsulating the graphene channel, which screened bulk charges. Without such screening layers[180], however, interferometers exhibit 'Coulomb dominated' (CD) behavior in which strong coupling of the interfering EC to localized compressible states in the bulk determines the oscillation periodicity and obscures the expected AB oscillations[169,151,150,161].

When bulk charges were strongly screened, GaAs FPs showed unexpected doubling of the AB oscil-

lation frequency and shot noise corresponding to charge $2e$ when interfering the outermost EC with the bulk of the interferometer in filling $2.5 \leq \nu \leq 4.5$, suggesting a possibility of 'pairing' of elementary charges[209]. Furthermore, the coherence and periodicity of the interfering outer EC were related to the coherence and the enclosed flux of the adjacent inner EC[210], and the 'pairing' phenomena only occurred when the outer two modes belonged to the same spin-split Landau level[211]. Independently, single-electron capacitance measurements in GaAs quantum dots revealed that tunneling into the edge of the dot corresponded to the entrance of two electrons rather than one for $\nu \geq 2$, and that near $\nu \approx 2.5$ the charging peaks follow doubled magnetic flux frequency[212]. Mechanisms of electron pairing are important questions in emergent phenomena, e.g. high-temperature superconductivity[213] and the even-denominator fractional QHE states in GaAs[214] and bilayer graphene[116,118]. However, theoretical work concerning FP interferometers was able to explain the doubled AB oscillation frequency based on a microscopic model without explicit introduction of electron pairing, though explaining other related phenomena in GaAs remains challenging[215].

In this chapter, we experimentally address the microscopic mechanism of coupling between QHE edges by elucidating the relation between AB oscillation phase jumps and frequency doubling, employing a highly tunable QHE FP interferometer with strongly screened bulk charge in graphene. We observe periodically modulating interference phase jumps on the outer EC leading to nearly doubled AB oscillation frequency as we increase the electron density in-situ, unveiling a density-induced transition which was not explored in GaAs. We find that strong repulsive interactions between the outermost pair of spin-split ECs can explain both the observation of interference phase jumps and the approximately doubled interference frequency, without invoking pairing arguments.

5.1 Improved interferometer design and tuning

We designed a graphene-based FP interferometer tuned by a local gate array (Fig. 5.1a). The FP cavity is defined electrostatically using separated graphite top-gates, which ensures a high channel quality and allow a high degree of density tunability in-situ. Metal bridges contact each top-gate, and we additionally suspend metal bridges over the two quantum point contacts (QPCs), illustrated in Fig. 5.1b. By applying voltages V_{QPC1} and V_{QPC2} to these suspended bridge gates, we can tune the transmission of each QPC independently while keeping the filling factor of the surrounding regions fixed. See Appendix B for more details on how this is done.

In our experiments, we measure the diagonal conductance G_{D}, as defined in Fig. 5.1b and Fig. B.1. In the regime that we study, $G_{\mathrm{D}} = \frac{e^2}{h}\nu_{\mathrm{QPC}}$ where ν_{QPC} counts the number of edge channels transmitted through the device, with a partially transmitted channel counted as fraction[216,194]. To characterize the QPC transmissions, we measure G_{D} as a function of the bottom-gate voltage and split-gate voltage for each QPC with the bulk of the interferometer tuned to $\nu = 2$ at $B = 6$ T (Fig. B.3). At $\nu = 2$, there are two spin-split Landau levels, of which the lower energy spin species hosts an EC closer to the effective boundary of the sample. Hence, we refer to the EC belonging to the lower (higher) energy spin species as the 'outer' ('inner') EC. Once appropriate bottom-gate and split-gate voltages are set, we tune V_{QPC1} and V_{QPC2}, voltages applied on the suspended bridges to control the individual QPC transmissions. Fig. 5.1c and Fig. 5.1d show the measured G_{D} as a function of V_{QPC1} and V_{QPC2}, respectively, with the other QPC fully open (i.e. $\nu_{\mathrm{QPC2}} = 2$ and $\nu_{\mathrm{QPC1}} = 2$, respectively). G_{D} exhibits plateaus at $(0, 1, 2)\frac{e^2}{h}$, corresponding to (neither, outer, both) ECs transmitted. In this regime, we define $T_{\mathrm{QPC}} \equiv G_{\mathrm{D}}\frac{h}{e^2}$ as the transmission of the QPC[216], where $0 < T_{\mathrm{QPC}} < 1$ corresponds to a partially transmitted outer EC and $1 < T_{\mathrm{QPC}} < 2$ corresponds to a partially transmitted inner EC.

Tuning to partial transmission of the inner EC for both QPCs, $T_{\mathrm{QPC1}} = T_{\mathrm{QPC2}} = 1.5$, we observe

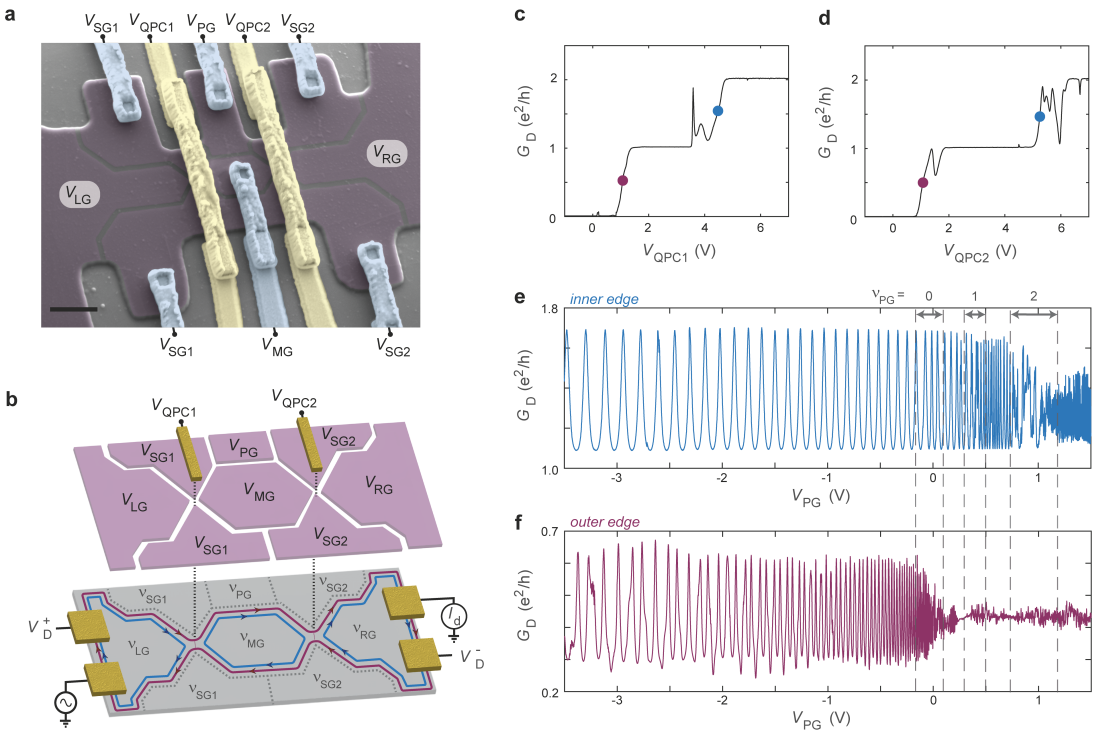


Figure 5.1: Highly tunable Fabry-Pérot interferometer in graphene. **(a)** False-colour scanning electron microscopy image of a Fabry-Pérot (FP) device identical to the device measured here. The graphite top-gate layer is selectively etched to form 8 separated top-gates (purple). Metal bridges (blue) connect to each graphite top-gate region and two additional bridges (yellow) suspend over the quantum point contacts (QPCs). The lithographic area of the interferometer cavity (area $A = 1.16\ \mu m^2$) is defined by the central hexagonal top-gate. Scale bar: 1 µm. **(b)** Simplified schematic of the FP tuned so that filling factors $\nu_{LG} = \nu_{MG} = \nu_{RG} = 2$ and $\nu_{SG1} = \nu_{PG} = \nu_{SG2} = 0$ illustrating interference of the partitioned outer edge channel (EC) (red) while the inner EC (blue) forms a closed annulus inside the FP. Voltage V_i applied to the top-gate labeled 'i' tunes the local filling factor ν_i. Voltages V_{QPC1} and V_{QPC2} applied to the suspended metal bridges selectively gate the QPC constrictions through the etched graphite gaps, tuning the QPC transmissions. We measure the diagonal conductance $G_D = \frac{I_d}{V_D^+ - V_D^-}$, where V_D and I_d are measured voltages in ($\pm$) probes and drained current, respectively. In addition to magnetic field, we tune the interference phase using voltage V_{MG} on the 'middle gate' or V_{PG} on the 'plunger gate'. **(c)** Conductance as a function of V_{QPC1} with $V_{QPC2} = 7\ V$ (i.e. $T_{QPC2} = 2$) demonstrating QPC1 tunings to interfere outer EC (red dot) and inner EC (blue dot) in $\nu = 2$. See Fig. B.3 for QPC tuning details and voltages set on the other gates to form the necessary QPC saddle-points to acquire this data. **(d)** Same type of plot as (c), but demonstrating QPC2 operation instead of QPC1. **(e-f)** Characteristic FP oscillations as a function of V_{PG} for the inner EC and outer EC, respectively, at the QPC tunings indicated in (c) and (d). Vertical dashed lines indicate edges of plateaus of filling factor ν_{PG}. All data is at fixed magnetic field $B = 6$ T.

high-visibility conductance oscillations as a function of plunger gate voltage V_{PG}, which tunes the filling factor ν_{PG} under the plunger gate, in Fig. 5.1e. Similarly, we tune to $T_{QPC1} = T_{QPC2} = 0.5$ and measure conductance oscillations on the outer EC in Fig. 5.1f. In both cases, oscillations are largest for $\nu_{PG} < 0$, which corresponds to a fully gate-defined interference path since electrons are depleted under the plunger gate. Increasing ν_{PG} brings the interfering edge closer to the etched graphene boundary, inducing dephasing[207]. Notably, the inner EC oscillations survive until $\nu_{PG} = 2$, when it flows close to the etched boundary of the graphene, while the outer EC reaches the boundary by $\nu_{PG} = 1$. Another difference is the apparent irregularity of the oscillations on the outer EC compared to the inner EC, which we will understand in this chapter.

5.2 Phase jumps and AB oscillation frequency transition

High-visibility oscillations allow us to probe the dependence of interference phase θ on magnetic field variation δB and gate voltage variations, which distinguishes the AB from the CD regimes[169,165,207,197,151]. For small variations in field and gate voltages in the AB regime, we expect

$$\frac{\delta\theta}{2\pi} \approx \frac{A\delta B}{\phi_0} + \frac{C_{PG}\delta V_{PG}}{e} + \frac{C_{MG}\delta V_{MG}}{e}$$

, where A, C_{PG}, and C_{MG}, are the (approximately constant) area enclosed by the interfering EC, interfering EC – plunger gate capacitance, and interfering EC – middle gate capacitance, respectively. Importantly, V_{MG} also directly tunes the electron density in the interferometer, so sweeping V_{MG} over a large range will change the FP cavity filling factor ν_{MG}. To calibrate the filling that we expect in the cavity, we first measure standard Hall conductance in the region gated by V_{LG} (see Fig. B.2) and observe conductance plateaus (Fig. 5.2a). Since the top gates are identically coupled to the channel directly beneath them, an identical sweep of V_{MG} will tune ν_{MG} through the same filling factors. Data in the remaining panels of Fig. 5.2 were taken with the QPCs set to $T_{QPC1} = T_{QPC2} = 0.5$ i.e. partially

transmitting the outer EC. Near the lowest density of the $\nu_{MG} = 2$ plateau (Fig. 5.2b), we observe a typical AB interference pattern. Constant phase stripes ($\delta\theta = 0$) trace out a negative slope $\frac{\delta V_{PG}}{\delta B}$ with magnetic field period ΔB yielding $\frac{\phi_0}{\Delta B} = 1.13\ \mu m^2$, matching the designed area $A = 1.16\ \mu m^2$. Plunger gate period ΔV_{PG} yields $\frac{1}{\Delta V_{PG}} = 19.2\ V^{-1}$. Increasing ν_{MG} using V_{MG} reveals more complicated interference patterns in Fig. 5.2c-d. Periodic shifts in the interference pattern persist and modulate until near the center of $\nu_{MG} = 4$, as seen in Fig. 5.2e, when a simple stripe pattern returns. However, now $\frac{\phi_0}{\Delta B} = 2.32\ \mu m^2$ and $\frac{1}{\Delta V_{PG}} = 36.3\ V^{-1}$, both approximately doubled from Fig. 5.2b. Since A is fixed, a doubling of $\frac{\phi_0}{\Delta B}$ indicates oscillations with $\frac{\phi_0}{2} = \frac{h}{2e}$ periodicity instead of ϕ_0 so that $\frac{\phi_0}{2\Delta B} = 1.16\ \mu m^2$. Similarly, assuming a fixed C_{PG}, then $\frac{1}{\Delta V_{PG}}$ doubling corresponds to adding twice as many electrons to the system per flux quanta. Both could be interpreted as an effective charge $e^* = 2e$ for the interfering particle, as argued in GaAs[209,210,211], but our observations indicate a different interpretation in our graphene-based interferometer.

Importantly, we can observe the entire density-tuned transition to the AB frequency-doubled regime at fixed B by sweeping V_{MG} and observing oscillations with V_{PG}, as shown in Fig. 5.2f. Remarkably, the frequency transition occurs continuously. From the top panel, ϕ_0 interference is apparent. As V_{MG} increases, periodic phase jumps begin to appear. Both the V_{MG} spacing and magnitude of the phase jumps increase, until eventually the most apparent periodicity corresponds to $\frac{\phi_0}{2}$ oscillations (i.e., doubled frequency $2\phi_0^{-1}$).

To better understand the phase jumps, we use a general relation between charge and phase in FP interferometers[171]. When a single EC passes through the two constrictions with weak backscattering, the interference phase seen by the device at zero temperature is $\theta = 2\pi Q + \theta_0, \mod 2\pi$, where Q is the total electron charge (in units e) in the region between the two scattering points and θ_0 is a constant for small variations in B, V_{PG}, and V_{MG}. In our experimental regime, $\nu \geq 2$, we expect this relation to hold with $Q = Q_1 + Q_2$, where Q_1 is the total charge residing in the lowest spin-split Landau level and Q_2 is the charge in the higher energy spin state (and also higher Landau levels).

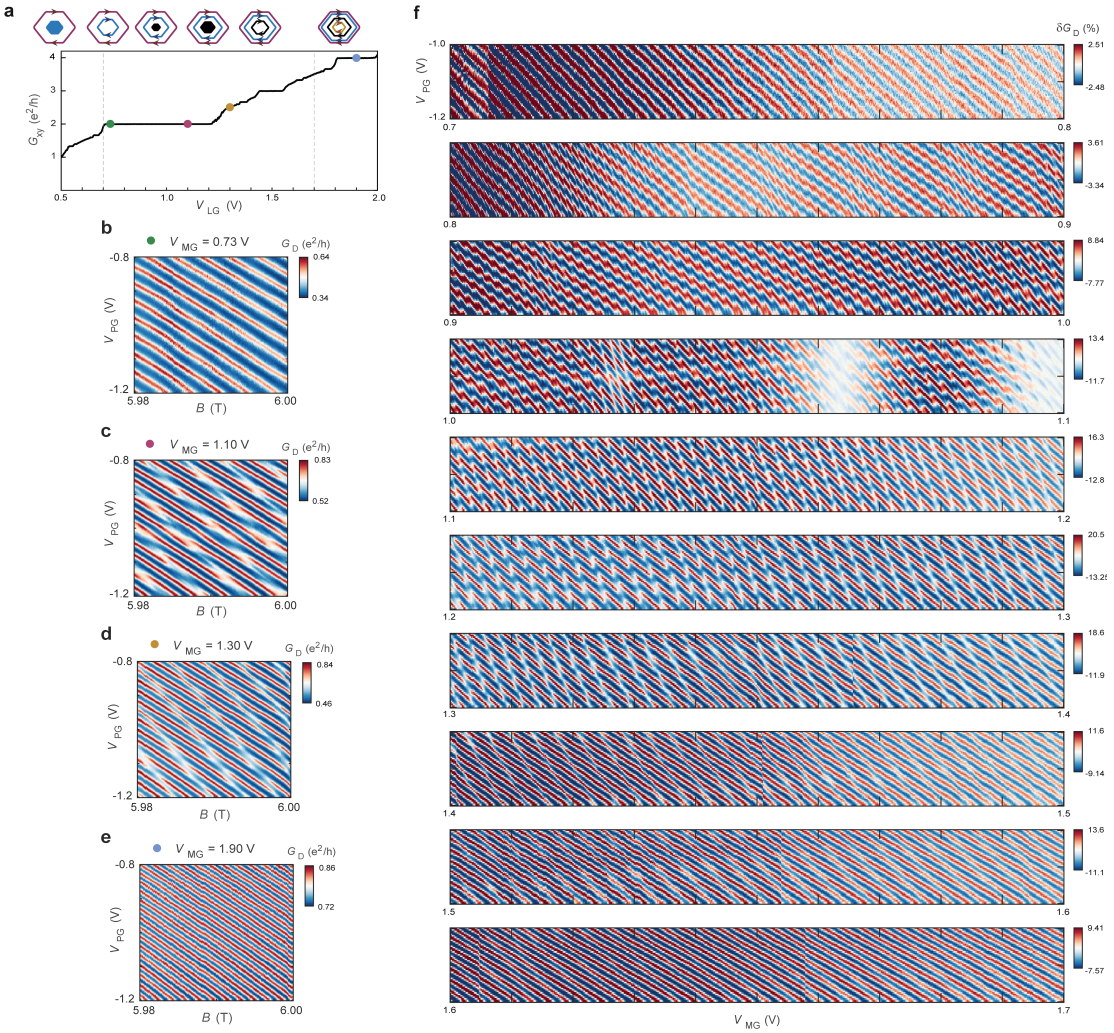


Figure 5.2: Density-tuned Aharonov-Bohm frequency doubling transition of outer EC. (a) Hall conductance G_{xy} in the region gated by V_{LG}, demonstrating that V_{LG} (equivalently, any of the top gates) tunes the filling ν underneath it at a fixed magnetic field $B = 6$ T. Coloured dots indicate the filling (set by equivalent V_{MG} voltages) at which interference data are shown in (b-e); vertical dashed lines show the range of V_{MG} swept for (f). Top inset: schematic of compressible regions expected in the FP cavity when V_{MG} is swept. **(b-e)** Conductance G_D oscillations on the outer EC with V_{PG} and B, for each of the indicated V_{MG} values. **(f)** G_D oscillations on the outer EC with V_{PG} and V_{MG}, for V_{MG} swept continuously over the transition from apparent $\frac{h}{e}$ to $\frac{h}{2e}$ oscillations periodicity, at $B = 6$ T. G_D is plotted as a percentage of $\frac{e^2}{h}$ deviation from the average value calculated for each fixed V_{MG} linecut and subtracted off. Further phase jumps or periodicity changes are not observed past $V_{MG} \approx 1.7\ V$ (checked up to $\nu = 7$). QPCs are retuned to maintain transmissions $T_{QPC1} = T_{QPC2} = 0.5$ over the dataset while $\nu_{LG} = \nu_{RG} = 2$ and $\nu_{SG1} = \nu_{SG2} = 0$ are fixed.

Q_1 can vary continuously since the outer EC is connected to the source and drain charge reservoirs. In contrast, Q_2 is required to be integer, as the corresponding energy levels are isolated through the incompressible QHE bulk. An integral change in Q_2 has no observable effect on the interference signal unless it produces a non-integral change in Q_1 due to Coulomb coupling between the two types of charge. Hence, we can redefine ϕ to include only the charge Q_1 in the lowest spin-split Landau level, and the values Q_1 in the ground state of the interferometer determine θ. Following similar models used to understand the CD regime [165,161,181] and considering small changes in Q_1 and Q_2, we expand the change in ground state energy $E = K_1\delta Q_1^2 + K_2\delta Q_2^2 + 2K_{12}\delta Q_1\delta Q_2$, where K_i is the charging energy of the charge species i and K_{12} describes the mutual capacitive coupling between them. Energetic stability requires that $|K_{12}|^2 \leq K_1K_2$. Within this capacitive coupling model, when Q_2 increases by 1, the charge Q_1 correspondingly decreases by a discrete (generically non-integral) amount ΔQ_1 to screen the added charge, leading to a phase shift $\frac{\Delta\theta}{2\pi} = \Delta Q_1 = -\frac{K_{12}}{K_1}$.

By taking 1D fast Fourier transforms (FFTs) along lines parallel to the phase jumps [164,165], we extract several values of $\frac{\Delta\theta}{2\pi}$ near the center of the periodicity transition in Fig. 5.3a. We observe that the locations where the phase jumps occur (marked by dashed lines in Fig. 5.3b) follow a steeper slope than the slope $\frac{\delta V_{\mathrm{PG}}}{\delta V_{\mathrm{MG}}}$ of constant phase lines of the main interference oscillation in the V_{MG} - V_{PG} planes. A steeper slope also occurs in the B - V_{PG} plane (Fig. 5.2c-d). Moreover, these phase jump lines have negative slopes $\frac{\delta V_{\mathrm{PG}}}{\delta B} < 0$, like the constant phase lines of AB oscillations. This observation is in sharp contrast to the phase jumps reported in the FP interferometer operated in the fractional QHE regime [164,165] or in the FP interferometer operated in the integer CD regime [181], where phase jump lines follow positive slope $\frac{\delta V_{\mathrm{PG}}}{\delta B} > 0$. The different slope suggests a different structure to the energy levels that are being populated in our sample. Considering that the outer EC is partitioned at the QPCs, while the inner ECs are well isolated, we hypothesize that the charging events seen as phase jumps represent charge added to the annular, closed inner EC, illustrated in Fig. 5.3. The dominant coupling K_{12} is directly between the outer and inner $\nu = 2$ ECs. Any charges added to higher Landau

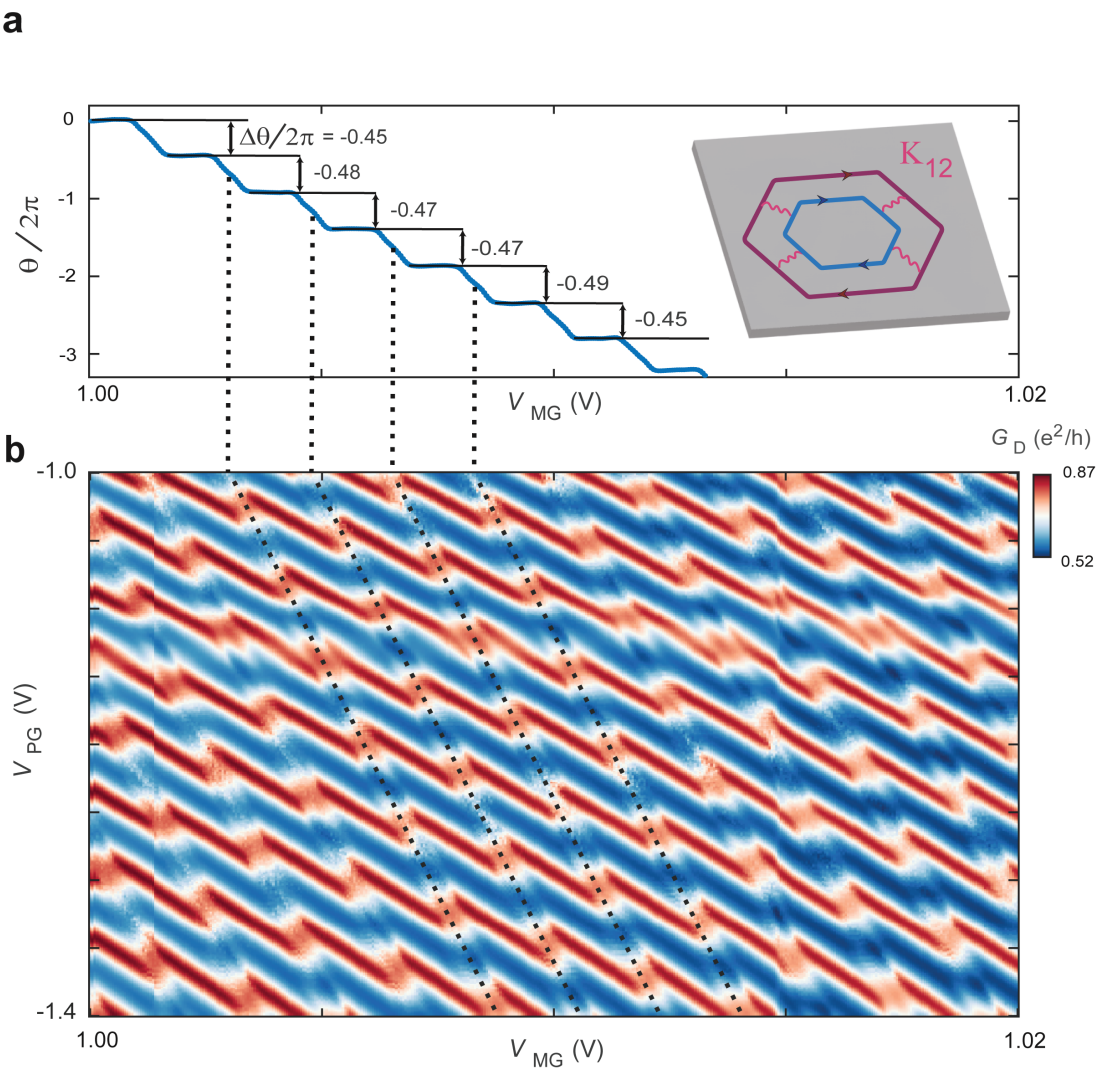


Figure 5.3: Phase jump extraction in the transition regime. (a) Phase θ of the 1D FFT extracted along linecuts parallel to the phase jumps in (b). The phase is evaluated at the dominant frequency in the FFT amplitude spectrum for the linecuts in between phase jumps. A linear increase in phase extracted from regions without phase jumps is subtracted off to make the phase jump magnitude evident as the vertical shift between plateaus in panel (a). From this data we extract an average $\Delta/2 \approx -0.47$, reflecting approximately half of an electron repelled from the outer EC for each charge added to the inner EC within this range of V_{MG}. Inset: illustration of the coupling K_{12} between the outer and inner ECs contributing to the phase jumps. **(b)** Conductance G_{D} oscillations on the outer EC with V_{PG} and V_{MG} near the center of the transition regime showing periodic phase jumps along the dashed black lines. Note that increasing V_{MG} adds electrons to the system or equivalently increases phase, so the phase jumps correspond to negative shifts in phase i.e., repulsion of electrons from the FP cavity. Similar interference patterns are observed in both the strong and weak QPC backscattering regimes (Fig. B.4) as well as at elevated temperatures (Fig. B.5).

levels or to localized states in the bulk are not measurably coupled to the outer EC, presumably because of effective screening by the gates.

5.3 AB frequency doubling from strongly coupled QHE edge states

We provide further evidence for capacitively coupled QHE edges tuning the AB frequency in Fig. 5.4. At fixed V_{MG} in the transition regime, we compare interference in the B-V_{PG} plane for the inner EC, Fig. 5.4a, to the outer EC, Fig. 5.4c. This direct comparison is only possible because we can control QPC transmissions independently of bulk filling. We observe that the slope of the oscillation maxima on the inner EC (dotted lines in Fig. 5.4a) matches the slope of the phase jump lines on the outer EC (dotted lines in Fig. 5.4c). Reducing the transmission for the inner EC, the interference maxima in Fig. 5.4a become sharper charging resonances, corresponding to charge $Q_2 \to Q_2 + 1$ through the inner EC. When the transmission of the inner EC vanishes, the inner EC is fully disconnected from the source and drain charge reservoirs, and the outer EC is now partitioned at the QPCs to form a new interference path (shown in the left inset in Fig. 5.4c). Since the bulk density and electrostatic configurations for Fig. 5.4a and Fig. 5.4c are identical, the regions in between the phase jump lines in Fig. 5.4c correspond to fixed Q_2, and we see that the interference phase on the outer EC shifts when the charge on the inner EC discretely changes.

Taking Fourier transform of the interference signal provides further understanding of interactions between the two ECs involved in the interference. Figure 5.4b(d) shows the 2D FFT of the conductance oscillations in Fig. 5.4a(c). For interference of the inner EC (Fig. 5.4b), we observe a simple FFT pattern of peaks corresponding to the fundamental frequency of the inner EC f_{i}, a vector containing the peak position in the 2D FFT, and its harmonics (nf_{i}, where n is an integer). The FFT pattern of the outer EC interference (Fig. 5.4d) exhibits a more complicated lattice of Fourier peaks. If we label one of the dominant peaks as the fundamental frequency of the outer EC, f_{o}, we can then identify

the rest of the peaks by addition or subtraction of the same vector f_{i} evident in the inner EC data. The lowest order peaks correspond to the sum $f_{\mathrm{o+i}} = f_{\mathrm{o}} + f_{\mathrm{i}}$ and the difference $f_{\mathrm{o\text{-}i}} = f_{\mathrm{o}} - f_{\mathrm{i}}$. We show a similar Fourier lattice construction in Fig. B.7 for interference in the B-V_{MG} plane.

By tuning V_{MG}, we modulate the filling factor of the interferometer cavity in a wide range and observe the evolution of the interference patterns and corresponding peaks for the outer (inner) EC in Fig. B.7 (Fig. B.8). As in Fig. 5.2, phase jumps appear only within the periodicity transition. Fig. 5.4e shows the average magnitude of individual phase jumps as a function of V_{MG}. We find that the phase jump continuously evolves from $\frac{\Delta\theta}{2\pi} \approx 0$ for $V_{\mathrm{MG}} < 0.6\,V$ through the periodicity transition to $\frac{\Delta\theta}{2\pi} \approx -1$ for $V_{\mathrm{MG}} > 1.6\,V$, corresponding to the strongly coupled limit $K_{12}/K_1 \approx 1$. The transition regime marked by non-trivial phase jumps spans from the appearance of the inner EC ($V_{\mathrm{MG}} \approx 0.6\,V$) to the strongly coupled outer two EC limit ($V_{\mathrm{MG}} \approx 1.6\,V$).

The Fourier peaks' evolution tuned by V_{MG} provides further insight into the interaction between ECs. Fig. 5.4f displays the normalized Fourier peak intensity as a function of V_{MG}. The amplitude of the Fourier peak f_{o} decays through the transition regime ($0.6\,V < V_{\mathrm{MG}} < 1.6\,V$), replaced by $f_{\mathrm{o+i}}$ as the dominant peak. We plot the magnetic field frequency multiplied by ϕ_0 (Fig. 5.4g) and the plunger gate frequency (Fig. 5.4h), respectively, for each of the lowest-order peaks f_{o}, f_{i}, $f_{\mathrm{o+i}}$, and $f_{\mathrm{o\text{-}i}}$ as a function of V_{MG}. At the beginning of the transition regime where the ECs are not interacting, both f_{o} and $f_{\mathrm{o+i}}$ approach the corresponding AB frequency $\phi_0^{-1} = \frac{e}{h}$ through the designed area. As V_{MG} increases, however, f_{o} stays nearly unchanged, while $f_{\mathrm{o+i}}$ increases to reach the doubled value $2\phi_0^{-1}$. The experimental observation that the dominant peak in the frequency-doubled regime corresponds to $f_{\mathrm{o+i}}$ precludes the possibility of $2e$ charge pairing within the outer EC alone.

Instead, our frequency-doubled regime arises from Coulomb interaction between the spin-split ECs combined with charge quantization on the inner EC (see Appendix B for more details). Electrons would naturally tend to enter the inner EC at frequency f_{i}, but, due to charge quantization, cannot enter continuously. Hence, as the magnetic flux increases continuously, the area enclosed by

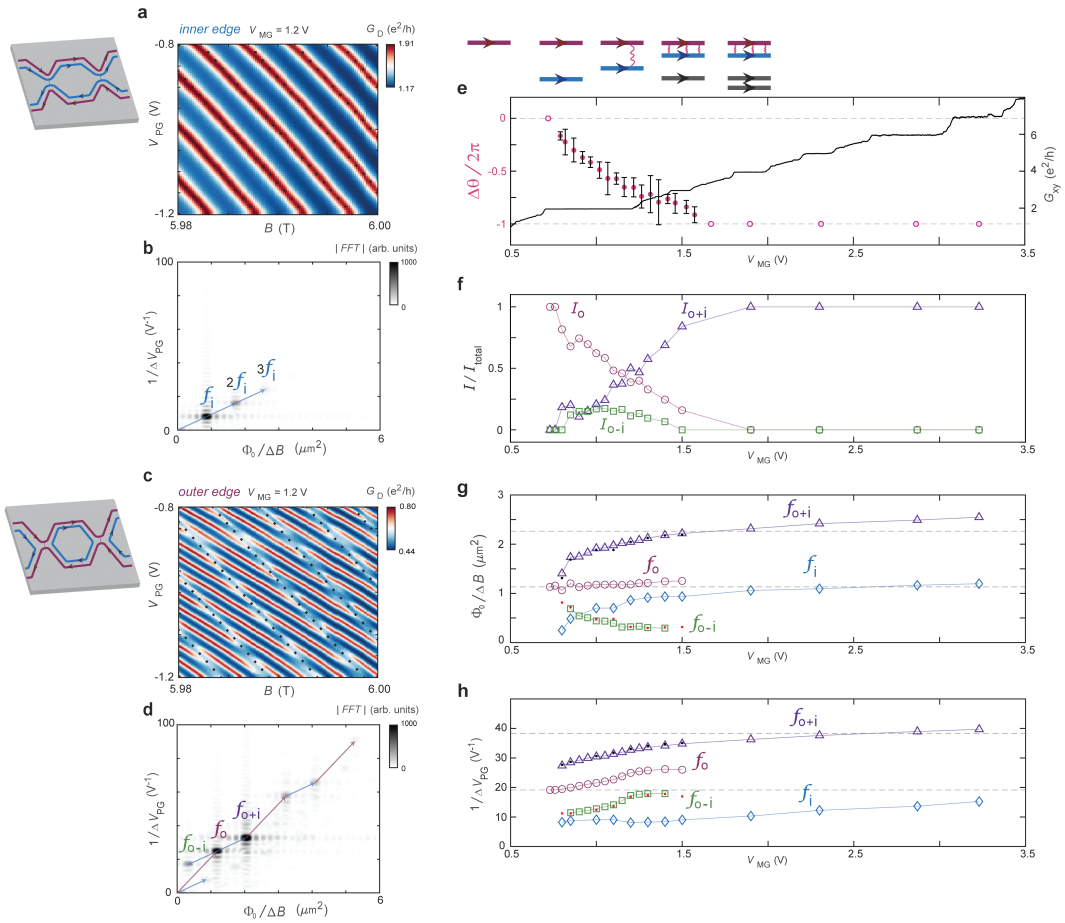


Figure 5.4: Comparison of inner and outer EC interference and couplings across transition. (a) Conductance G_D oscillations on the inner EC ($T_{QPC1} = T_{QPC2} = 1.5$) with V_{PG} and B, for $V_{MG} = 1.2$ V. Dotted black lines highlight conductance maxima. Left inset: illustration of inner EC interference configuration. **(b)** 2D FFT of the G_D oscillations in (a) showing peak f_i (vector corresponding to blue arrows) and its harmonics, where $\Phi_0 \equiv h/e$. **(c)** G_D oscillations on the outer EC ($T_{QPC1} = T_{QPC2} = 0.5$) at the same density set by V_{MG}. Dotted black lines with identical slope to (a) highlight phase jumps. Left inset: illustration of outer EC interference configuration. **(d)** 2D FFT of oscillations in (c) showing the peaks f_o (red arrows), f_{o+i}, and f_{o-i} and their harmonics. **(e)** Magnitude of the phase jump on the outer EC as a function of V_{MG}. Each data point is averaged over a ~ 0.25 V range in V_{MG}; error bars indicate ± 1 standard deviation in this range. Unfilled data points represent zero observable phase jumps over the range, hence we infer a magnitude of 0 or -1. G_{xy} of the device taken in an identical measurement to Fig. 5.2a, reflecting the expected filling $_{MG}$, is plotted for reference. Top inset: cartoon of the outer and inner EC evolution with increasing V_{MG}. **(f)** Magnitudes I_o, I_{o+i}, and I_{o-i} of the respective peaks f_o, f_{o+i}, and f_{o-i} as a function of V_{MG}. I_o, I_{o+i}, and I_{o-i} are normalized by the sum $I_o + I_{o+i} + I_{o-i}$ to show their relative contributions. Each data point is extracted from a 2D FFT (Fig. B.7). **(g)** Magnetic field frequency multiplied by Φ_0 for peaks f_o, f_i, f_{o+i}, and f_{o-i} tracked through the transition. Note that f_i is measured from a separate measurement of interference on the inner EC (Fig. B.8). **(h)** Same as (g) but for plunger gate frequency. Horizontal dashed lines in (g-h) indicate the corresponding f_o and $2f_o$ values before the transition. Black (red) dots show calculated $f_o \pm f_i$ from outer and inner EC data, which match the peaks identified as f_{o+i} and f_{o-i}, respectively.

the inner EC must shrink to maintain fixed charge. During this shrinking process, electron charge is transferred continuously into the interior, leaving missing electron charge between the outer and inner ECs. In the strongly coupled EC limit, this missing charge attracts an equal charge onto the outer EC for screening. In the absence of this screening effect, charge is continuously added to the outer EC with frequency f_{o} according to the increased AB phase. In the coupled ECs, the combination of the screening-induced charge and the natural AB effect results in the outer EC charging at a frequency $f_{\mathrm{o+i}}$. Therefore, the interference phase follows $f_{\mathrm{o+i}}$. In addition to this continuous charging effect, electrons can tunnel into the inner EC from the external reservoirs. As previously discussed, each electron addition repels some electron charge from the outer EC, causing the negative interference phase shifts that we observed. For larger values of V_{MG}, as the bulk density increases, the inner and outer EC move closer together, and the system approaches the strong coupling limit, where the phase jumps are close to -2π and unobservable, reflecting a full electron charge screening. Moreover, as the inner and outer ECs asymptotically enclose the same area, set by the confining potential of the device, the frequency $f_{\mathrm{o+i}}$ approaches $2\phi_0^{-1}$.

We note that a concurrent work also observed apparent AB frequency tripling, corresponding to the sum of the three $\nu = 3$ edge channel frequencies[217]. The framework that we developed here can be expected to naturally explain this observation, since in devices utilizing the graphene crystal edge, the sharp confining potential can lead to multiple ECs developing within a few magnetic lengths of the edge[101]. The combination of reduced spatial separation and reduced screening by nearby graphite gates may account for the observation of apparent tripling, arising from the outer EC screening both internal localized ECs.

5.4 Conclusion

We have investigated phase jumps and AB frequency modulation in a highly tunable graphene QHE FP interferometer with coupled co-propagating edge modes. We identify that interference phase jumps are related to the single electron charging events in the inner EC, and the transition of the AB frequency can be connected to the corresponding screening effect of the outer EC. As V_{MG} increases, the EC coupling becomes strong and the AB frequency doubles, indicating a near-perfect screening between the ECs. Thus, our experimental observation supports the proposal that AB frequency doubling can be explained without explicitly introducing electron pairing within the outer two ECs[215]. In other words, a half flux quantum introduced in the two strongly coupled ECs can bring a full charge from the external reservoir and a 2π evolution of the observed interferometer phase.

Our observations do not exclude the possibility of further correlation effects in the strongly coupled ECs; instead, the tunably coupled ECs discovered here provide a system to test the emergence of electron correlations in 1D systems[218]. However, AB frequency multiplication, which we explained within a single particle picture, cannot substantiate the correlation effect. Further experiments probing the transition from the weakly to strongly coupled limit, such as shot noise[209,219,220], finite-bias dependence[165,221], energy relaxation[222], and high-frequency transport[223,224,225,226] will provide further insight into the ground state and excitations. More generally, inter-edge screening could affect interferometry in fractional fillings containing multiple ECs[221,160,162,166], though fractional QHE experiments so far appear to be in the weak coupling regime[221,166]. The recent observations of interference in fractional quantum Hall states using similar bilayer and monolayer graphene devices[227,228,229] will enable further experiments to probe the interacting co-propagating fractional QHE edge modes, where it remains unclear whether the strong coupling regime can be realized between fractional edge channels.

He not busy being born is busy dying.

Bob Dylan

6

Fractional Interference: Anyon Braiding and Fluctuations

The search for anyons, quasiparticles with fractional charge and exotic exchange statistics, has inspired decades of condensed matter research. Quantum Hall interferometers enable direct observation of the anyon braiding phase via discrete interference phase jumps when the number of encircled localized quasiparticles changes. Here, we observe this braiding phase in both the $\nu = \frac{1}{3}$ and $\frac{4}{3}$ frac-

tional quantum Hall states by probing three-state random telegraph noise (RTN) in real-time. We find that the observed RTN stems from anyon quasiparticle number n fluctuations and reconstruct three Aharonov-Bohm oscillation signals phase shifted by $\frac{2\pi}{3}$, corresponding to the three possible interference branches from braiding around n mod 3 anyons. Our methods presented in this chapter can be readily extended to interference of non-abelian anyons.

The fractional quantum Hall (FQH) effects, where electrons are confined to two spatial dimensions and exposed to large magnetic fields, have long been predicted to host emergent fractionally charged excitations that obey neither fermionic nor bosonic exchange statistics [15,26,27,230,104]. These quasiparticles fall into two classes, abelian and non-abelian anyons, associated with FQH states at different filling factors ν. For abelian anyons, exchanging two quasiparticles (i.e. braiding) results in the many-body wavefunction acquiring a complex phase, as demonstrated by anyon collision and interferometry experiments [184,164]. For non-abelian anyons, the wavefunction evolves by a unitary transformation, enabling fault-tolerant topological quantum computation that has yet to be experimentally realized [30,31,32,33,34].

FQH FP interferometers enable direct measurements of the anyon braiding phase [168,169]. By partially backscattering current at two QPC constrictions, the conductance through the FP cavity modulates with the phase accumulated by edge-traveling quantum Hall (QH) quasiparticles [104,206]. When the number of localized cavity quasiparticles encircled by the interfering edge changes, the resulting phase shift in the interference signal is equivalent to twice the fundamental exchange phase (modulo 2π) [109,164]. However, because the observed discrete phase jumps represent charging events in the cavity, resultant Coulomb coupling between the bulk and edge must be accounted for when extracting the anyon braiding phase from a small number of phase jump events [165]. Consequently, mitigating Coulomb coupling while maintaining electrostatic tunability has been a major challenge in semiconductor-based interferometers [163,164].

Graphene-based interferometers offer several advantages for realizing anyon braiding, both for the

abelian and non-abelian cases. First, both QPCs [194,231] and interferometers [197,207,180,208,232,217] exhibit robust electrostatic tunability for integer QH states. Second, graphite gates reduce Coulomb coupling to reveal AB oscillations [207], which previously required complex quantum well structures in GaAs [163,164]. Simultaneously, these atomically-flat gates enhance FQH states by screening out charge disorder [173,174] while allowing precise control of QPC transmission [207,233,234] and FP cavity filling factor [232]. Encouragingly, bilayer graphene has displayed a multitude of even-denominator FQH states which may host non-abelian anyons with relatively large energy gaps [117,116,118,120,235]. Here we report direct observation of abelian anyon braiding using high-visibility Aharonov-Bohm interference and anyon fluctuations in single atomic layer graphene.

6.1 Tuning for fractional quantum Hall interference

We construct our device by performing previously described nanolithography steps [207,232] on a heterostructure consisting of monolayer graphene encapsulated with both insulating hexagonal boron nitride [172] and conducting graphite layers. By gating with separated top graphite regions, we define the interferometer cavity and construct two QPCs that introduce backscattering between the opposite chirality QH edge channels (Fig. 6.1a). The quality of the graphene is maintained in part thanks to the encapsulating graphite gates, as evident by well-developed FQH states (Fig. 6.1b and c) at $T = 20\,\mathrm{mK}$. Unlike previous FQH interferometers in GaAs, we can tune the electron density in-situ in graphene to access many FQH states while holding the magnetic field fixed. Here we set magnetic field $B = 12\,\mathrm{T}$ (unless noted otherwise) and change density to tune between filling factors $\nu = \frac{4}{3}$, $\nu = 1$, and $\nu = \frac{1}{3}$, enabling a direct comparison of interference between each state.

We begin by tuning the device such that the interferometer cavity and adjoining contact regions are set to $\nu = \frac{4}{3}$ by applying appropriate voltages V_{MG}, V_{LG}, and V_{RG}. The cavity boundary is defined by setting the plunger gate (V_{PG}) and QPC split-gate regions ($V_{\mathrm{LSG/RSG}}$) to lie within $\nu = 0$. Two

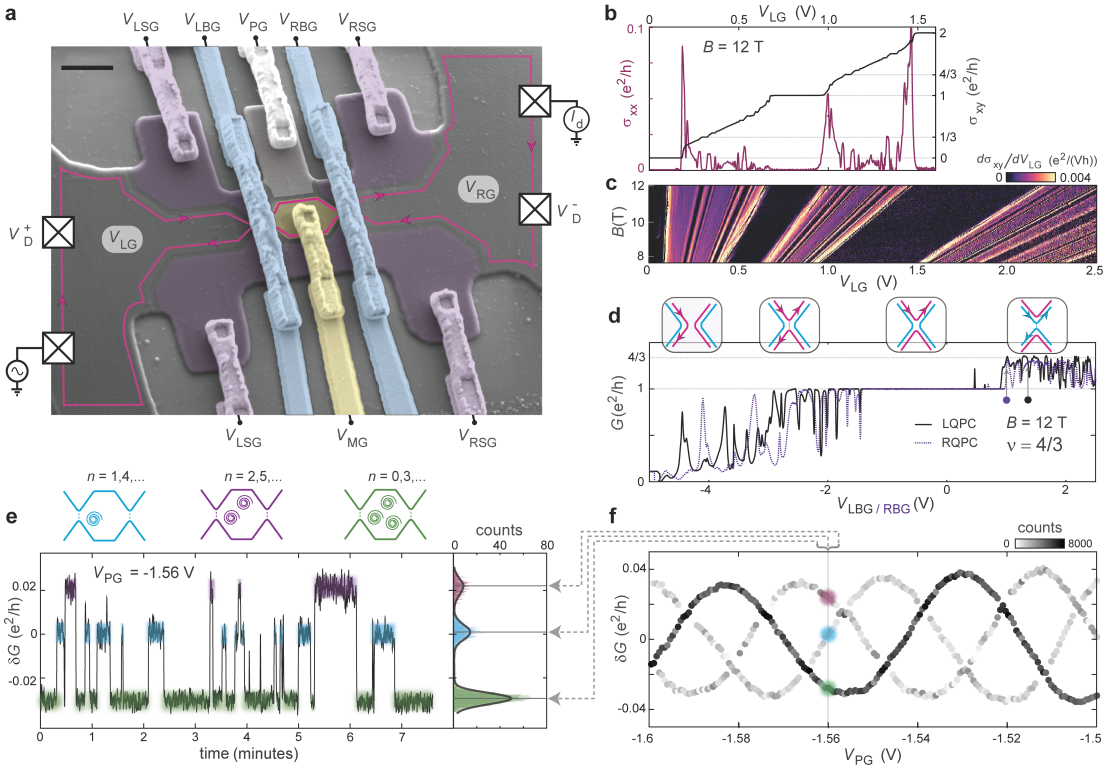


Figure 6.1: Graphene FQH interferometer telegraph noise. **(a)** False-color scanning electron microscope image of a representative device depicting an interference measurement with a single edge channel. Scale bar: $1\ \mu m$. We measure the conductance $G = I_d/(V_D^+ - V_D^-)$ where I_d is the measured drain current and $V_D^\pm$ are the measured voltages at the indicated locations. The top graphite gate is etched into 8 separately tunable regions controlled by voltages V_{LG}, V_{LSG}, V_{PG}, V_{MG}, V_{RSG}, and V_{RG}. Additionally, voltages $V_{LBG/RBG}$ applied to suspended bridges above the two QPCs independently set their transmissions. See Fig. C.1 for more details. **(b)** Hall conductivity σ_{xy} and longitudinal conductivity σ_{xx} measured with contacts in the left reservoir of the device highlighting the robust plateaus at $\nu = 0$, $\frac{1}{3}$, 1, and $\frac{4}{3}$, the quantum Hall states that we study. **(c)** Derivative of σ_{xy} showing the expected magnetic field dependence of the well-developed quantum Hall states. **(d)** Conductance G across the left/right QPC tuned by $V_{LBG/RBG}$ with the right/left QPC deactivated and the bulk in $\nu = \frac{4}{3}$. See Fig. C.2 for details. Inset: schematics of the edge channel configuration and tunneling at a QPC. As $V_{LBG/RBG}$ increases, the constriction opens and transmits the outer integer edge (pink) first and eventually transmits the inner fractional edge (blue). **(e)** Three-state RTN in the conductance G when the fractional edge of $\nu = \frac{4}{3}$ is weakly backscattering, corresponding to the tuning $V_{LBG} = 1.37\ V$ and $V_{RBG} = 1.01\ V$, marked by the black and purple dots, respectively in (d), which are chosen to set $G \approx 1.28\ \frac{e^2}{h}$ or roughly 15% backscattering at each QPC. Top inset: cartoons of the three possible interference branches from braiding around n (mod 3) anyons, corresponding to the three conductance levels. Right inset: histogram of the conductance over time with 1000 bins. **(f)** Extracted sinusoidal oscillations from histograms over approximately 8 minutes for each V_{PG} voltage. Each data point shows the central conductance value of a gaussian fit to a histogram peak, shaded by the total counts summed under the gaussian. See Fig. C.3 for similar data in $\nu = \frac{1}{3}$.

additional metallic bridge gates over the QPCs ($V_{\mathrm{LBG/RBG}}$) allow for independent control of QPC transmissions while keeping all other gates fixed. The conductance across each QPC evolves from near 0 to a plateau at $\frac{e^2}{h}$, and finally to near $\frac{4}{3}\frac{e^2}{h}$ with increasing $V_{\mathrm{LBG/RBG}}$, where e is the electron charge and h is Planck's constant (Fig. 6.1d). The resonances in the conductance in these scans indicate a relatively soft confining potential at this QPC tuning[233,195]. It is then straightforward to tune each QPC to weakly backscatter the fractional edge channel of $\nu = \frac{4}{3}$ by setting $V_{\mathrm{LBG/RBG}}$ as indicated in Fig. 6.1d.

6.2 Three-state anyon telegraph noise

By measuring the conductance through the interferometer with the fractional edge of $\nu = \frac{4}{3}$ weakly backscattering at both QPCs, we discover sporadic switches between three discrete levels as a function of time i.e. three-state RTN (Fig. 6.1e). From a histogram showing how these levels are weighted over 8 minutes, we extract the average conductance and the total weight in time associated with each level. Then, we step the plunger gate V_{PG} to modify the area[207,163,150,153], or equivalently the total charge[232,171] contained in the FP cavity, and repeat the process. Plotting the resulting average conductance values shaded by their weight in time as a function of V_{PG} reveals three interwoven, phase-shifted sinusoidal oscillations (Fig. 6.1f).

Each sinusoid represents one of the three n (mod 3) possible phase "branches" associated with braiding the interfering edge quasiparticles around a system composed of $n\,\frac{e}{3}$ abelian anyons[236,237,238]. By fitting the phase shift between the sinusoids using an improved measurement style (see next section), we are able to extract the braiding phase to high precision. Demonstrating exchange statistics with RTN is a departure from the method used in previous interferometer studies, in which discrete phase jumps in the continuously modulating AB phase $\theta_{\mathrm{AB}}(B, V_{\mathrm{PG}})$ were argued to represent the addition or subtraction of a quasiparticle in the interferometer bulk[164,165,166]. These studies rely on

modulating the AB phase using magnetic field B and plunger gate V_{PG} to probe irregularly spaced phase jumps due to anyon localization. In order to extract the anyon braiding phase, however, the experimentally observed phase jumps need to be analyzed with consideration given to the electrostatic coupling between the QH edge and localized bulk states. These analyses often become complicated as the bulk-edge capacitive coupling, the position of the chemical potential relative to the bulk Landau levels, and interferometer area A can drastically impact interference behavior, such as pivoting the interference signal into the well-studied "Coulomb-dominated" regime[169,165,150,151,170]. It has also been shown that integer quantum Hall fillings can produce similar fractional phase jumps owing to the Coulomb coupling effect described above[217,232,181,239].

The measurement scheme presented in our work, i.e. observing a time-dependent interference phase $\theta(t)$ through the RTN signal, offers a key benefit in this regard. Here the parameters (B, V_{PG}) used to modulate the AB phase

$$\theta_{\mathrm{AB}}(B, V_{\mathrm{PG}}) = 2\pi \frac{e^*}{e} \frac{A(V_{\mathrm{PG}})B}{\phi_0}$$

can be held fixed while the quasiparticle number $n(t)$ fluctuates in time. Then, the expression for the total interference phase may be simplified as

$$\theta(t) = \theta_{\mathrm{AB}}(B, V_{\mathrm{PG}}) + n(B, V_{\mathrm{PG}}, t)\, \theta_a \rightarrow \theta_{\mathrm{AB}} + n(t)\, \theta_a$$

where $\theta_a = \frac{2\pi}{3}$ is the braiding phase for an $e^* = \frac{e}{3}$ anyon around a localized counterpart (assuming that Coulomb interactions are well screened) and $\phi_0 = \frac{h}{e}$. Considering the 2π periodicity of θ, the resulting braiding phase can only be one of three values varying by $\frac{2\pi}{3}$, reflecting the total number of localized anyons $n(t)$ (mod 3) at a given time. The device accordingly remains static in configurable parameter space (B, V_{PG}) while observing conductance switching from real-time fluctuations $n(t)$.

Therefore, as this method demonstrates the existence of all three branches associated with the exchange statistics of charge $\frac{e}{3}$ anyons, we construct a complete representation of the state's braiding outcomes near a fixed device configuration set by B, V_{PG}, and density (tuned via V_{MG}).

6.3 Aharonov-Bohm magnetic field dependence

Measuring how the magnetic field B changes the total interference phase is crucial in determining if the interferometer falls into the AB or Coulomb-dominated regime [169,104]. We start for comparison with the $\nu = 1$ integer QH state. By repeatedly sweeping the plunger gate, we observe the expected single-sinusoidal oscillations devoid of phase jumps (Fig. 6.2a). As we change B, we observe magnetic-field dependent AB interference (Fig. 6.2b), where the magnetic field period ΔB_1 yields an area $\frac{\phi_0}{\Delta B_1} = 0.80\ \mu\mathrm{m}^2$, as expected for interference of electrons in $\nu = 1$. A similar measurement in $\nu = \frac{1}{3}$ with varying B and V_{PG} produces an irregular 2D map because repeated plunger gate sweeps are not consistent due to the frequent RTN fluctuations (Fig. 6.2c). However, we observe that each plunger gate scan contains stochastic switching between 3 sinusoidal branches, again shifted by $\frac{2\pi}{3}$ (Fig. 6.2d). By superimposing 100 of these sweeps and plotting the histogram of total recorded conductance values over V_{PG}, we are able to sample enough instances of the AB oscillation signal of each branch to recreate the three interwoven sinusoids seen in the previous measurement technique discussed in Fig. 6.1. Figure 6.2e exhibits the three interwoven branches at different magnetic fields. As the magnetic field decreases (from the top to bottom panels), we observe that each branch continuously drifts towards increasing V_{PG} values, creating a negative slope of constant phase (dashed line) analogous to the integer case of Fig. 6.2b. For $\nu = \frac{1}{3}$, the corresponding flux super-periodicity $\Delta B_{1/3}$ (the magnetic field period for a single branch to return to its initial V_{PG} coordinate) yields $\frac{3\phi_0}{\Delta B_{1/3}} = 0.83 \pm 0.04\ \mu\mathrm{m}^2$. See Fig. 6.3b for the linear fit that yields this value. This value is what one expects for interfering $\frac{e}{3}$ quasiparticles such that $\phi_0 \rightarrow \frac{h}{e/3} = 3\phi_0$. We similarly observe AB in-

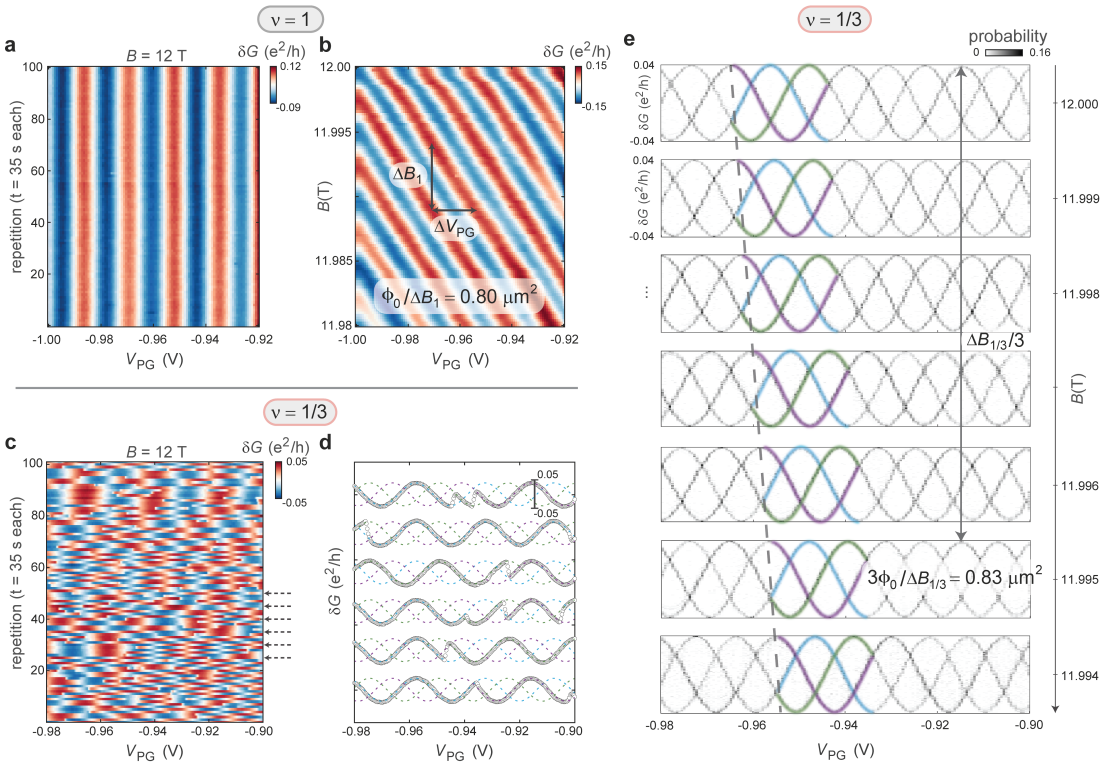


Figure 6.2: Aharonov-Bohm magnetic field trend of $\nu = \frac{1}{3}$ branches. (a) 100 repeated V_{PG} sweeps in $\nu = 1$, where each sweep takes $35\ s$, demonstrating the temporal stability of oscillations in the integer state. **(b)** Magnetic field dependence of the oscillations in $\nu = 1$ demonstrating Aharonov-Bohm periodicity; the magnetic field period yields $\frac{\phi_0}{\Delta B_1} = 0.80\ \mu m^2$, consistent with a small reduction of the area enclosed by the edge state within the designed area of $1.1\ \mu m^2$. **(c)** 100 repeated V_{PG} sweeps in $\nu = \frac{1}{3}$, using the same sweeping parameters as in (a), demonstrating the stochastic fluctuations induced by the RTN that could easily be mistaken for structure-less noise, especially if averaged over by a slow sweep. **(d)** 6 of the V_{PG} sweeps plotted to demonstrate switching between the three sinusoidal branches within a single scan. **(e)** 2D histograms showing the probability of measuring a given conductance for each V_{PG} value and its trend with the magnetic field. All three branches (partially highlighted) are made evident by this plot, and each branch trends identically with a flux super-period in the magnetic field corresponding to $\frac{e}{3}$ anyons. Note that (e) is effectively presenting the AB oscillation demonstrated in the B versus V_{PG} plane for the $\nu = \frac{1}{3}$ case, where RTN is present during each scan of V_{PG}.

terference and a flux super-periodicity on the fractional edge of $\nu = \frac{4}{3}$ (Fig. C.4), whereas the integer edge shows typical electron AB interference with no observable RTN. Note that even if the charge within the interferometer fluctuates in the integer case, the change in the interference phase caused by integer changes in electron charge will be a multiple of 2π and therefore unobservable [171].

The fact that all tested configurations show AB interference (i.e. a negative slope of constant phase with respect to V_{PG} and B) instead of Coulomb-dominated effects indicates that our graphene interferometer is sufficiently screened by the graphite gates to suppress long-range Coulomb interaction, as required for observing braiding signatures [169,164,165]. Furthermore, the observed $3\phi_0$ magnetic-flux super-period in both $\nu = \frac{1}{3}$ and $\nu = \frac{4}{3}$ agrees with the $3\phi_0$ super-period observed near the center of the $\nu = \frac{1}{3}$ plateau in GaAs-based FP interferometers [164,165], suggesting that the quasiparticle gap is large enough to prevent continuous addition of quasiparticles [240].

The repeated sweep method exhibited in Fig. 6.2, which includes hundreds of phase jumps, provides an opportune data set to extract a precise value for the anyon braiding phase and associated uncertainty (see Appendix C for detailed methodology). The fitting involves sorting each data point by least-squares proximity to sinusoidal fit functions of various phase offsets, as shown in Fig. 6.3a. By doing this procedure for each dataset at fixed B and properly accounting for the uncertainty, we can quantify the value of the anyon braiding phase. For the subplots shown in Fig. 6.2e, each containing 100 repeated sweeps and several hundred branch switches, we extract an average braiding phase of $2\pi(0.3336 \pm 0.0051)$, or $120.1^\circ \pm 1.8^\circ$. This is extracted as an average over the full range of B values shown in Fig. 6.3c. The phase shift closely agrees with the theoretical value $\frac{2\pi}{3}$ and with the value extracted from previous interferometer [164,165] and anyon collider [184] experiments. Additionally, the smallness of the fitting error to the theoretical value $\frac{2\pi}{3}$, which neglects Coulomb corrections to the interferometer area with each quasiparticle fluctuation, demonstrates that Coulomb corrections are indeed negligible in our device.

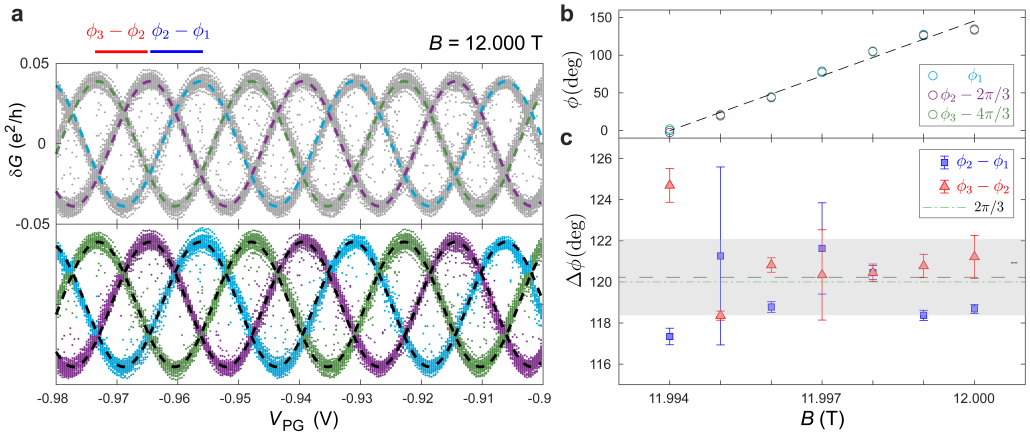


Figure 6.3: Phase fitting and uncertainty. (a) Scatter plot of 100 overlaid plunger gate sweeps in $\nu = 1/3$ at $B = 12$ T, each sweep containing multiple phase jumps between branches (same data set shown in topmost histogram of Fig. **??**e). Dashed lines in to top plot show the results of the function fitting method described in Appendix C, and the bottom plot shows the results of sorting the same data points by least-squares proximity to the fit functions. **(b)** Phases of the sinusoidal fits of each of the three branches across the seven data sets with magnetic field as shown in Fig. **??**e. ϕ_2 and ϕ_3 are shifted by $2\pi/3$ and $4\pi/3$ respectively to overlap the three phases, illustrating how close to $2\pi/3$ the relative phase difference is between each pair of the three branches for a given magnetic field. Error bars (1 standard deviation found from the bilinear regression fit) are smaller than the displayed data points. The dashed line shows a linear regression fit of ϕ_1, giving an interferometer area of 0.83 ± 0.04 μm^2 from the expected Aharonov-Bohm phase of a single branch. **(c)** Phase differences between the three branches plotted in (b). The grey dashed line/bar indicates the average/one standard deviation, $120.1° \pm 1.8°$, or $2\pi(0.3336 \pm 0.0051)$. The error bars indicate one standard deviation of the sum of the two individual phases used for finding the difference, found from a bilinear least-squares regression of each sorted data set with its associated fitted function.

6.4 Telegraph noise across the quantum Hall plateau

We gain insight into the nature of the quasiparticle fluctuations by tracking how the RTN evolves with density (filling) across the FQH plateau. Figure 6.4a exhibits subsets of 50 minute measurements of the conductance, showing the V_{MG} dependent RTN across the $\nu = \frac{1}{3}$ plateau. The trace colors indicate the select values of V_{MG} that correspond to the subrange of the $\nu = \frac{1}{3}$ QH plateau as shown in Fig. 6.4b.

Of immediate note are clear changes in both the switching rate and amplitude as V_{MG} steps across the plateau. The average switching rate from the complete 50 minute traces, τ_s^{-1}, shown in Fig. 6.4c,

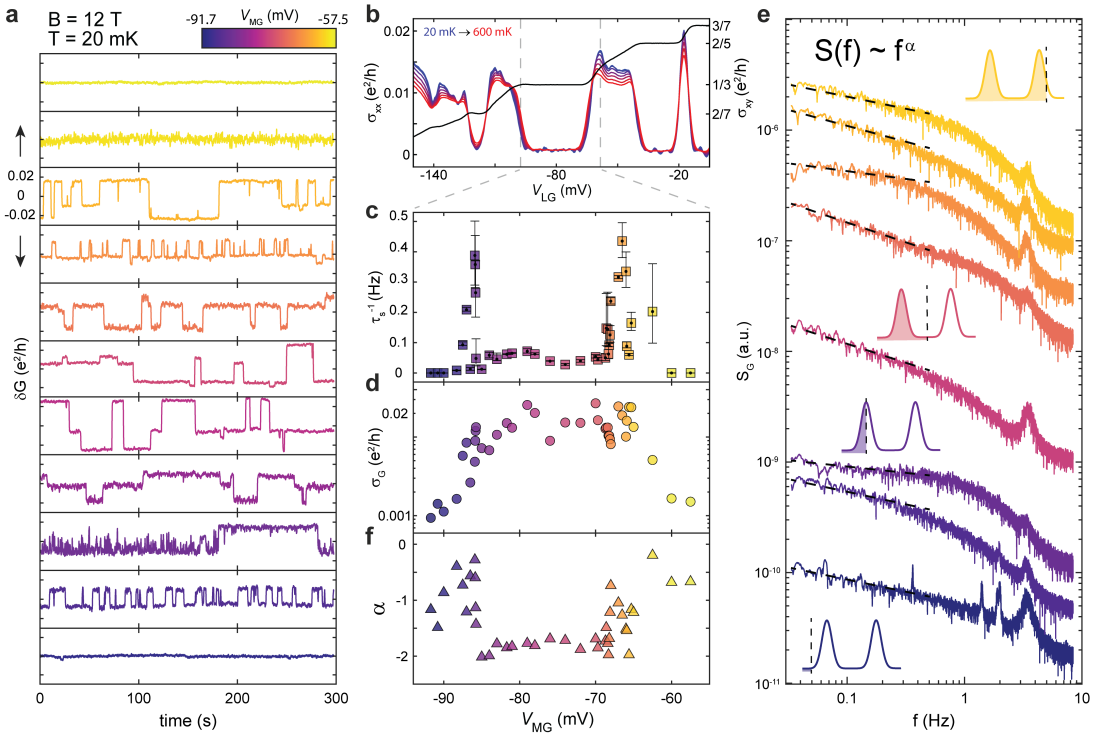


Figure 6.4: Telegraph noise dependence on filling in $\nu = \frac{1}{3}$. (a) Conductances versus time taken at different values for V_{MG}, indicated by color bar. The 300 seconds shown are from longer 50 minute datasets. **(b)** Hall data taken from the left half of the device with density tuned via V_{LG}. The dashed lines indicate the associated range shown for V_{MG} in (c-e) below. The color scale on σ_{xx} spans from 20 mK (blue) to 600 mK (red). **(c)** Average branch switching rate along the plateau. Error bars indicate uncertainty associated with the switching identification algorithm and background noise (see section 2 of). **(d)** Standard deviation of conductance computed for $G(t)$ at fixed V_{MG}. **(e)** The spectral densities of conductance plotted on a log-log scale (traces are arbitrarily vertically shifted by ordering of V_{MG}). Dotted lines are fit to the power law dependence f^{α} in the low frequency regime. Inset cartoons indicate the anyonic quasiparticle density of states versus energy, with the vertical dashed lines indicating the Fermi level for a given filling. **(f)** The exponent α extracted from the fits of the power spectrum in (e) within the frequency range associated with the RTN.

exhibits steep rises near the edges of the plateau and a relatively constant switching rate in between. Figure 6.4d shows the standard deviation, σ_G, of the diagonal conductance $G(t)$, providing a direct measure of switching amplitude.

The striking behavior of the anyon branch switching rate and amplitude along the plateau reveals that the quasiparticle fluctuations and coherence are closely correlated with the compressibility of the FQH state. A natural explanation would be that the switching rate increases as the number of localized states and anyon trapping sites increases near the edges of the FQH plateau. However, a simple increase in the individual switching rates of a constant number of traps across the plateau cannot be ruled out from this observation alone.

The noise spectral density of the diagonal conductance, S_G, can provide additional information supporting the hypothesis of an increasing trap number near the edge of the plateau. Figure 6.4e shows S_G as a function of frequency f, obtained from the Fourier transform of $G(t)$ at various V_{MG} values across the plateau region. We find that $S_G(f)$ follows a power law scaling behavior $\sim f^{\alpha}$ in the low frequency regime corresponding to the RTN signal. Figure 6.4f exhibits the scaling exponent α obtained from the line fits shown in Fig. 6.4e. In the middle of the plateau, the exponent α remains close to -2, which is expected from RTN with a single switching timescale[241]. However, near the edges α sharply increases and deviates from this stable value. It is known that when many instances of RTN with different switching timescales are convolved together, S_G is expected to approach $1/f$, or $\alpha = -1$[242]. Accordingly, the change of α near the edges of the plateau suggests that there are more unique switching timescales at the edge of the plateau than in the middle. This observation, together with the switching rate behavior discussed above, supports that the increased branch switching incidents are indeed associated with increased localized anyon states in the bulk.

6.5 Temperature scaling of telegraph noise

We also study how the RTN changes as a function of temperature T. Figure 6.5a shows $G(t)$ near the middle of the $\nu = \frac{1}{3}$ plateau at T ranging from 20 mK to 220 mK.

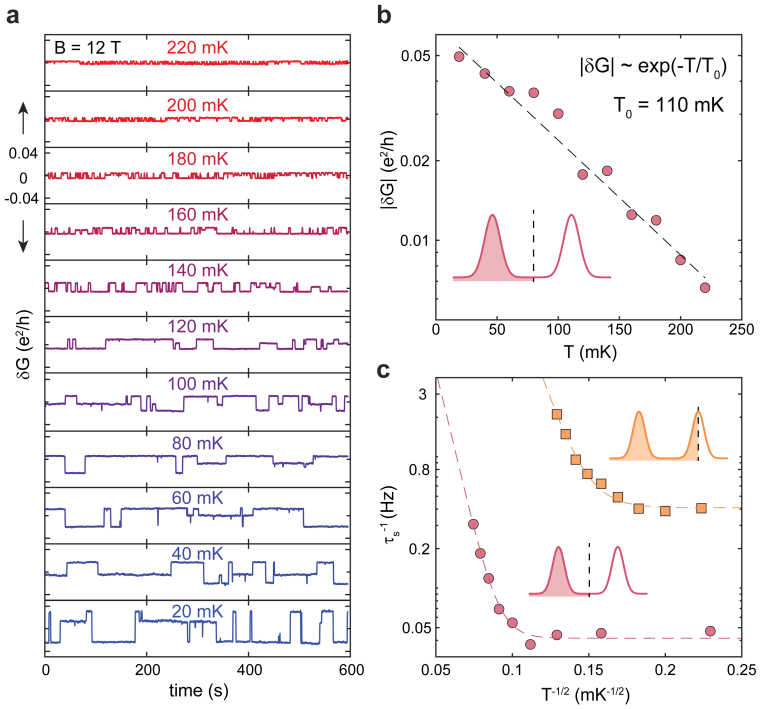


Figure 6.5: Temperature dependent telegraph noise and visibility in $\nu = \frac{1}{3}$. (a) Conductance versus time taken at different temperatures T. The 600 seconds shown are subsets of longer 50 minute datasets used for subsequent analysis. **(b)** Oscillation visibility extracted from V_{PG} sweep measurements (21 repeated scans averaged per point). The exponential decay fit to the oscillation visibility results in a characteristic temperature $T_0 = 110$ mK. **(c)** Low-temperature saturation and high-temperature activation of the average switching rate τ_s^{-1} observed for two fillings: at the center and at the edge of the $\nu = \frac{1}{3}$ plateau, as shown in the insets. Shown fit lines follow the empirical formula of Eq. 2., where $T_{ES} = 22$ K (middle of plateau) and $T_{ES} = 9.5$ K (edge of plateau), which correspond to VRH hopping lengths of 130 nm and 300 nm, respectively [243,244]

As temperature increases, the switching amplitude decreases corresponding to a decrease in AB oscillation visibility. Figure 6.5b shows separately measured AB oscillation visibility as a function of T using plunger gate sweep measurements (similar to Fig. 6.2c-e). The visibility decreases following an exponential decay as T increases, with a characteristic energy scale $T_0 = 110$ mK similar to that observed in $\nu = \frac{1}{3}$ in GaAs[164]. The fact that the exponential decay continues to the lowest base temperature indicates that our electron temperature is likely within a few mK of the mixing chamber temperature, thanks to our aggressive filtering and thermalization methods.

In addition to the decrease in visibility, the RTN also shows an increase in switching rate as temperature increases. Figure 6.5c shows temperature dependent τ_s^{-1} for two representative data sets, one at the center (red) and the other at the edge (yellow) of the plateau. While the switching rate increases quickly at the high temperature limit, there is a dramatic flat saturation of τ_s^{-1} for both data sets at low temperatures, below about 100 mK and 50 mK for the plateau center and edge, respectively. We find that an empirical formula which combines a term motivated by an Efros-Shlovskii (ES) form of variable-range hopping (VRH)[245,246] with an additional temperature-independent transition rate $\tau_{s,0}^{-1}$:

$$\tau_s^{-1} = \tau_{s,0}^{-1} + \tau_{s,1}^{-1}(T)\, e^{-(T_{ES}/T)^{1/2}}$$

can provide a reasonable fit to the data as shown by the dashed lines in Fig. 6.5c. Here $\tau_{s,1}^{-1}(T) \sim 1/T$ and T_{ES} is the characteristic ES VRH temperature scale. Although VRH has been used in the past to model longitudinal conduction caused by localized states in the quantum Hall effect[246,243,247,23], the physical mechanism behind the temperature scaling of τ_s^{-1} here remains nebulous.

Although we were able to provide evidence that the anyon fluctuations are closely associated with the number of anyon localized states, and that they have consistent temperature scaling properties, a precise mechanism for their origin remains unclear. Based on the uniformity of the AB-modulating sinusoids in Figs. 6.1f and 6.2e, we postulate that the anyons are neither hopping from nor getting

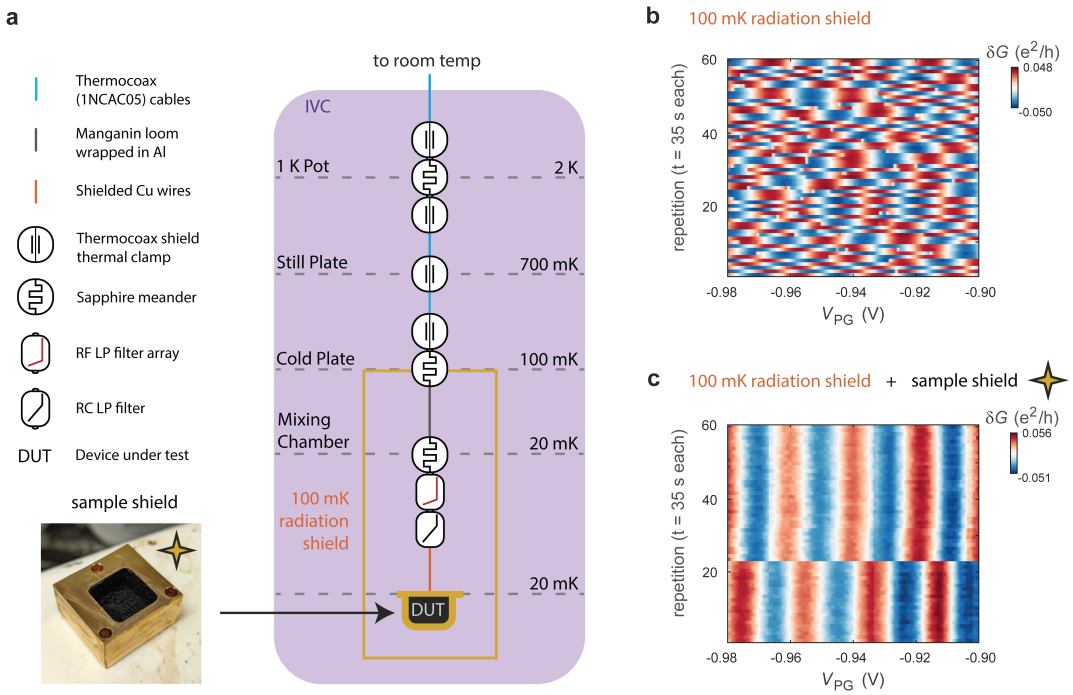


Figure 6.6: Wiring schematic and effect of shielding on telegraph noise. (a) Schematic of cryostat wiring and shielding. As detailed in Chapter 3, we measure in an Oxford MX400 wet He3/He4 dilution fridge with transport wiring that is carefully designed to achieve a low electron temperature. This is achieved by the choice of wiring materials, thermalization fixtures, and electronic filters, which are mounted at various temperatures to the probe as indicated. Moreover, we find that radiation shielding has a strong effect on the telegraph noise switching rate. In the data presented previously, we have used a single (standard) radiation shield thermalized to 100 mK. Here, we show the reduction in switching rate achieved by adding an additional sample shield (shown in the inset) directly thermalized to the coldfinger of the fridge at 20 mK. The sample shield is constructed with gold-plated Cu, and the inner surface is coated with a black epoxy-based infrared absorbing material (Berkeley black[248]). **(b)** 60 repeated V_{PG} sweeps in $\nu = 1/3$ at the same tuning as Fig. 6.2c, which contain many branch switching events, often within a single sweep. **(c)** Identical scan at an identical tuning in $\nu = 1/3$ measured during a second cooldown including the additional sample shield. Oscillations show a drastically enhanced temporal stability reflecting a stable quasiparticle number on a time scale of tens of minutes to hours. Observations of a similar stability time were made in ref.[229] .

trapped within regions close to the QPCs, as even small changes in environmental charge would drastically change their tunings and the resultant visibility of the interference signal over time. We also observe that enclosing the sample in an additional radiation shield strongly reduces the switching rate (Fig. 6.6), indicating that photons stimulate the fluctuations. Presumably the photons are radiated off of the 100 mK shield itself or penetrating through from higher temperature stages in the fridge or surrounding environment. Since subtle changes make a large difference, we hope that the anyon number can be stabilized completely with enhanced shielding, and we anticipate that it could be controlled in future works via coupling to photons at proper frequencies. Lastly, although fluctuations have not been reported in GaAs interferometry experiments [166,165,164,160,162] and more recently in bilayer graphene [249], the presence of slower or faster switching timescales could make initial observations of anyon fluctuations challenging with standard DC measurement techniques.

6.6 Conclusion

In this chapter, we have shown that anyonic quasiparticle fluctuations and the resulting RTN in a FP interferometer can be used as a powerful tool to exhibit the complete set of braiding phases present in abelian states. These techniques pave the way for future interferometer measurements of non-abelian anyon braiding in even-denominator FQH states (especially in bilayer graphene) where the small energy gap may enhance the RTN and limit the range of AB phase modulation achievable. Several theoretical studies have already discussed which signatures would be expected in such a case where RTN is present for non-abelian states [236,237,238]. Moreover, our ability to observe the slow equilibration of anyons enables future experiments to probe nontrivial anyon dynamics and to dynamically control anyon number in similar devices. This is particularly relevant to the ultimate goal of constructing a topological qubit with non-abelian anyons, which requires an understanding of how to selectively control and modulate the quasiparticle number [250,251,252].

Still round the corner there may wait
A new road or a secret gate,
And though I oft have passed them by,
A day will come at last when I
Shall take the hidden paths that run
West of the Moon, East of the Sun.

J.R.R. Tolkien

7

Discussion and Outlook

In this thesis, we have studied Fabry-Pérot interferometers constructed from the chiral quantum Hall edge states of graphene. We have seen that highly-visible resistance or conductance oscillations allowed us to probe a variety of fundamental features of the quantum Hall effects including the Aharonov-Bohm phase, edge state coherence length, edge channel velocity, inter-edge state coupling, quasiparticle charge, and especially the anyon braiding phase. In doing so, interferometry has proven to be a powerful tool in sensing the microscopic nature of quantum Hall states, unveiling the subtle phe-

nomena at the level of individual electrons and quasiparticles that can manifest with emergent (highly-nontrivial!) phenomena at larger scales. For example, we saw in chapter 5 that capacitive coupling between internal electronic degrees of freedom, two integer quantum Hall edge states, can produce phenomenology that to the outside world may look like electron pairing i.e. frequency doubling of the measured interference phase. Open questions remain about the nature of the correlated state between the the edge channels in graphene[217] and its relation to the state in GaAs[209,210,215,215] that can be clarified with further measurements in the highly-tunable graphene devices we developed, such as whether shot noise becomes doubled along with frequency. The extent to which capacitive correlations between different species of electrons could lead to pairing phenomenology in general is an open and important question, especially in systems like high temperature superconductors which host many competing phases that all seem to emerge from microscopic repulsion[213]. Furthermore, in chapter 6 we directly measured the fractional charge and anyon braiding phase of localized quasiparticles in $\nu = \frac{1}{3}$ and $\nu = \frac{4}{3}$, which we saw agreed closely with the theoretical expectation from Laughlin's state and agreed with the values previously measured in GaAs[184,164,165]. We discovered that, despite anyon fluctuations and known non-ideal characteristics of real devices, the braiding phase is extremely well-quantized, yielding an average magnitude of $2\pi(0.3336 \pm 0.0051)$, or $120.1° \pm 1.8°$. This enforces that the fractional quantum Hall states are topologically ordered, necessarily hosting the robust and universal quasiparticles that we have been able to directly probe in the first material platform other than GaAs.

Besides characterizing the braiding phase of abelian anyons, the development of interferometers in graphene extends the search for more exotic non-abelian anyons, which are theoretically hosted in even-denominator fractional quantum Hall states and predicted to be useful for topological quantum computation[31,214]. The search in GaAs at $\nu = \frac{5}{2}$ has yielded a variety of promising features, though interpreting the interference signatures remains challenging in light of the limited tunability of the devices, particularly the lack of density tunability and inaccessibility of control experiments[157,159,160,104].

I anticipate that van der Waals materials can overcome the challenges to probe these more subtle states, as we have already demonstrated robust tunability in the other fractional states, and our fractional quantum Hall interferometer device architecture has already been largely reproduced by other groups in monolayer[229] and bilayer graphene[227]. Several very robust even-denominator states have been discovered in bilayer graphene[116,117,118,119]. I expect that probing interference in these various states will yield great incites into the nature and promise of non-abelian order. Very recently, Aharonov-Bohm interference was seen in the various even-denominator states of bilayer graphene, but the signature of non-abelian quasiparticles remains elusive[249]. Perhaps more importantly, since the quantum Hall effects are simply one example of topological states of matter and graphene is just one example of a 2D van der Waals material with interesting topological states, I hope that the interferometry techniques developed in this thesis will enable many exciting future directions. One of the most exciting directions would be using similar gate-defined interferometers to probe the recently discovered fractional quantum anomalous Hall effects[253,254,255,256,257], especially the plethora of states that are accessible via conventional transport within rhombohedral graphene systems[258,259]. The prospect of topologically-robust quasiparticles analogous to fractional quantum Hall anyons existing in zero or very low magnetic fields holds great promise for technological applications.

A

Additional information for chapter 4

A.1 QPC operation

Fig. 4.3a demonstrates a single QPC device operating with bulk filling factor $\nu_B = 2$. In Fig. A.1, we show the same QPC operating in $\nu_B = 1$ (a, d); $\nu_B = 2$ (b, e); and $\nu_B = 6$ (c, f). We give the exact voltages used on the gates to create the three QPC plots in Fig. A.1h. Thus, we demonstrate control of the QPC transmission over a wide range of filling factors.

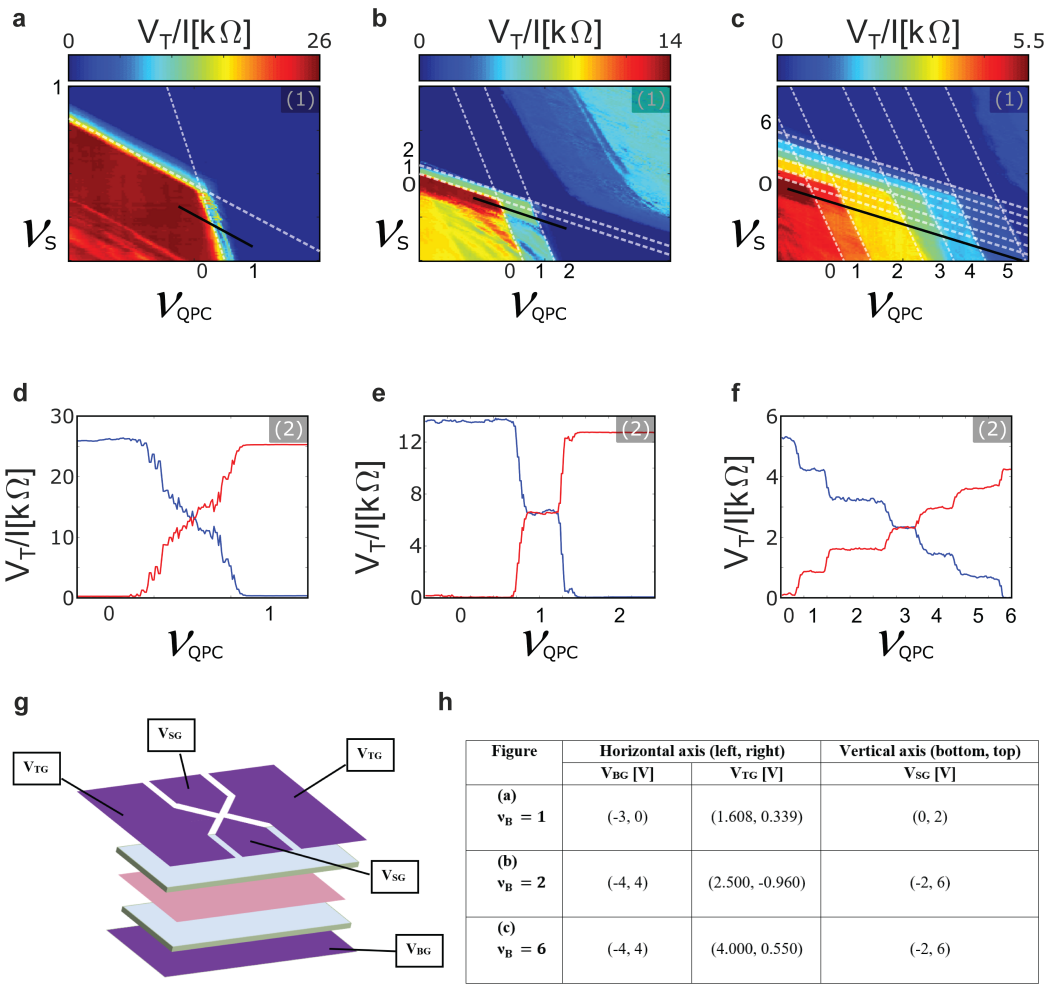
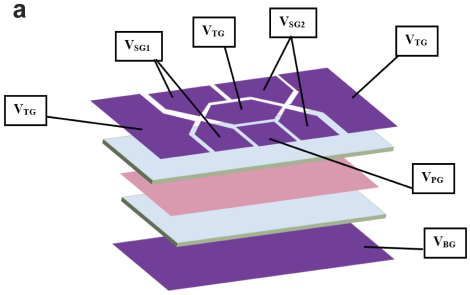


Figure	Horizontal axis (left, right)		Vertical axis (bottom, top)
	V_{BG} [V]	V_{TG} [V]	V_{SG} [V]
(a) $\nu_B = 1$	(-3, 0)	(1.608, 0.339)	(0, 2)
(b) $\nu_B = 2$	(-4, 4)	(2.500, -0.960)	(-2, 6)
(c) $\nu_B = 6$	(-4, 4)	(4.000, 0.550)	(-2, 6)

Figure A.1: QPC operating at various bulk fillings. 2D maps of the operating points of the QPC for **(a)** $\nu_B = 1$; **(b)** $\nu_B = 2$; and **(c)** $\nu_B = 6$ are shown; $\frac{V_T}{I}$ as a function of ν_S and ν_{QPC}, tuned by the top split gates and bottom graphite gate, respectively. All other topgates gates in the system compensate to keep the filling ν_B as the bottom gate sweeps on the horizontal axis. The black-solid line in the 2D map represents a constant filling under the split gate, $\nu_S = 0$, and a continuous change in ν_{QPC}. Line-cuts along the black line measuring $\frac{V_T}{I}$ and $\frac{V_R}{I}$, blue and red, respectively, are shown for **(d)** $\nu_B = 1$; **(e)** $\nu_B = 2$; and **(f)** $\nu_B = 6$. **(g)** Labels of gate voltages. **(h)** Table of gate voltages applied to collect data in panels (a), (b), and (c). Note that this QPC device has a bottom hBN (74 nm) about twice as thick as the top hBN (31 nm).

Next, we list the exact voltages that were applied to each gate to produce Fig. 4.3b in the main text, the transmission of each separate QPC in the FP device, summarized in Fig. A.2

a



b

Figure	Horizontal axis (left, right)				
	V_{BG} [V]	V_{TG} [V]	V_{PG} [V]	V_{SG1} [V]	V_{SG2} [V]
Red curve (Left QPC)	(0, 0.5)	(1.248, -0.386)	(-0.193, -1.907)	(-0.145, -2.443)	(1.248, -0.386)
Blue curve (Right QPC)	(0, 0.5)	(1.248, -0.386)	(-0.193, -1.907)	(1.248, -0.386)	(-0.165, -2.463)

Figure A.2: Gate voltages used to set QPC operating points for interferometer. **(a)** Labels of gate voltages. **(b)** Table of gate voltages applied to collect data in Fig. 4.3b. Note that this FP device has a bottom hBN (17 nm) significantly thinner than the top hBN (50 nm). V_{SG1} refers to the split gates defining the left QPC (reflection coefficient r_1) while V_{SG2} refers to the split gates defining the right QPC (reflection coefficient r_2).

A.2 Phase coherence length analysis

By including a finite phase coherence length L (precisely a length for dephasing by a factor e^{-1}) into the single-particle model, we find that the coherent oscillatory contribution (including a constant term $t_1 t_2$) to the transmission probability of the Fabry-Pérot (FP) interferometer is given by

$$t_{\mathrm{FP}} = \frac{(1-r_1)(1-r_2)}{1 + r_1 r_2 e^{-2\frac{P}{L}} - 2\sqrt{r_1 r_2}\cos(\theta) e^{-\frac{P}{L}}}.$$

where P is the perimeter of the interference loop. $P = 6.8$ μm for the FP device demonstrated in Chapter 4 and in the simulations shown. Our model is analogous to the standard treatment of coherent transmission through a double-barrier structure (e.g. pg. $252 - 261$ in ref. [13]) where here we consider a single mode with a phase θ given by the Aharonov-Bohm effect of the interference loop. As a function of r_1 and r_2, the visibility (normalized peak-to-peak amplitude of oscillations) is then

proportional to

$$V_0(r_1, r_2; L) \equiv \frac{(1-r_1)(1-r_2)}{1 + r_1 r_2 e^{-2\frac{P}{L}} - 2\sqrt{r_1 r_2}\cos(\theta) e^{-\frac{P}{L}}} - \frac{(1-r_1)(1-r_2)}{1 + r_1 r_2 e^{-2\frac{P}{L}} + 2\sqrt{r_1 r_2}\cos(\theta) e^{-\frac{P}{L}}}.$$

which we plot as a percentage of Max $[V_0(r_1, r_2; l \to \infty)] = 1$ for various values of the phase coherence length L in Fig. A.3.

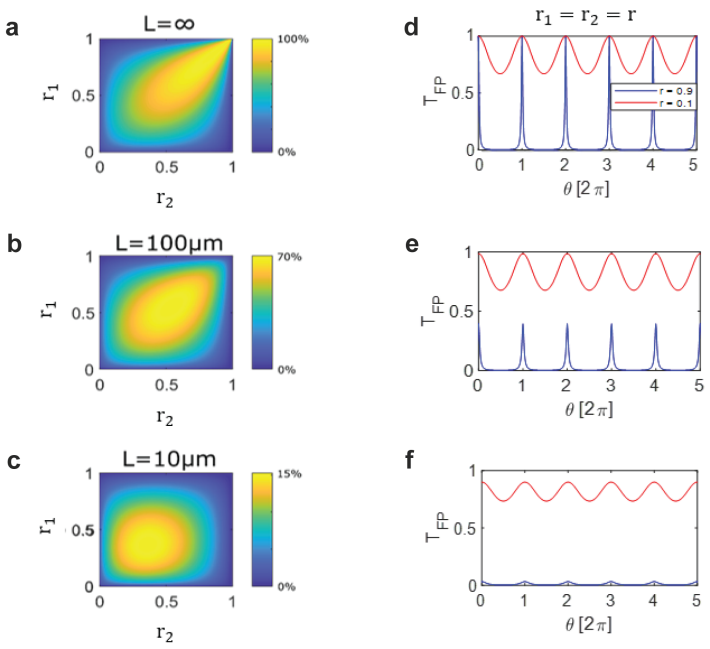


Figure A.3: Theoretical plots of oscillation amplitude and shape with finite phase coherence. The theoretical visibility V_0 is plotted as a percentage of Max $[V_0(r_1, r_2; l \to \infty)] = 1$ versus r_1 and r_2 for **(a)** $L \to \infty$, **(b)** $L = 100$ μm, and **(c)** $L = 10$ μm. In all plots we have $P = 6.8$ μm, the actual perimeter of our FP interferometer. r_{max} corresponding to the maximum amplitude $V_0(r_{\text{max}}, r_{\text{max}}; L)$ shifts to smaller values as L is reduced, and the decay of the amplitude away from the maximum point is uniquely determined by L. For two characteristic values $r = 0.9$ (blue) and $r = 0.1$ (red), we plot the shape of the oscillations with θ in for the corresponding situations **(d)** $L \to \infty$, **(e)** $L = 100$ μm, and **(f)** $L = 10$ μm. As $r \to 1$, the oscillations are sharp due to contributions from multiple revolutions, but the amplitude is suppressed with decreasing L.For $r \ll 1$, the oscillations are asymptotically sinusoidal since only the contribution from a single revolution around the cavity effectively contributes.

We see generally that the maximum visibility is achieved for $r_1 = r_2 \equiv r$ and that in the case of infinite phase coherence ($L \to \infty$) the oscillations achieve maximum visibility as $r \to 1$. Moreover,

as $r \to 1$ the shape of oscillations becomes sharp, as interference terms corresponding to multiple revolutions around the loop all contribute fully to the coherent sum. However, as L is reduced to smaller finite values, the most visible configuration shifts to $r < 1$. As L is reduced, the contributions of multiple revolution paths to the interference are suppressed exponentially, which modifies the visibility for all values of r_1 and r_2. By fitting the measured visibility of oscillations, $V \equiv (R_{\mathrm{T,max}} - R_{\mathrm{T,min}})\frac{\nu_{\mathrm{B}}^2}{R_{\mathrm{Q}}}$ for integer ν_{B}, to $V_0(r_1, r_2; L)$ as a function of r_1 and r_2, which were extracted from each QPC transmission data (Fig. 4.3b) separately, we may extract a characteristic phase coherence length L. We show a particular fit for the inner edge of $\nu_{\mathrm{B}} = 2$ in Fig. A.4a, from which we extract $L = 8.1$ μm.

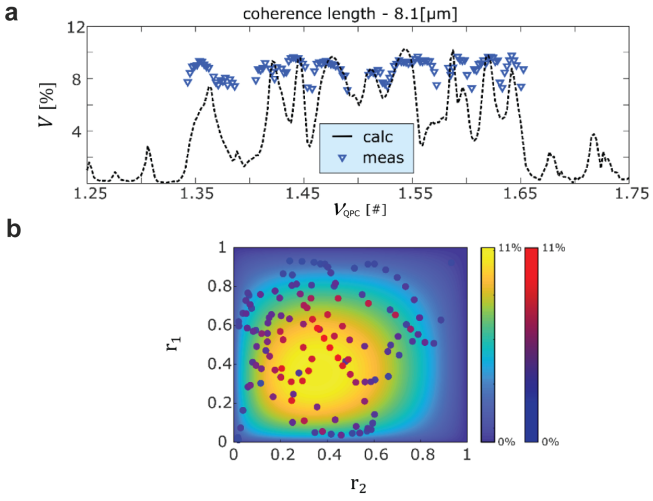


Figure A.4: Extracting phase coherence length from oscillation amplitude. (a) With $\nu_{\mathrm{B}} = 2$, the inner edge (second LL) is partitioned by setting $1 < \nu_{\mathrm{QPC}} < 2$ for each QPC. We show the measured visibility of oscillations, $V \equiv (R_{\mathrm{T,max}} - R_{\mathrm{T,min}})\frac{\nu_{\mathrm{B}}^2}{R_{\mathrm{Q}}}$ (i.e. normalized peak-to-peak amplitude as a percentage of the maximum possible oscillation $\frac{R_{\mathrm{Q}}}{\nu_{\mathrm{B}}^2} = 6.45\,\mathrm{k}\Omega$ here), plotted versus ν_{QPC} of one of the QPCs, along with the theoretical value from $V_0(r_{\mathrm{max}}, r_{\mathrm{max}}; L = 8.1\mu\mathrm{m})$. The other QPC is also varying similarly, though it experiences different transmission resonances, along this scan (as in Fig. **??**b). Hence, the x-axis is changing both r_1 and r_2, which we extract from the separate QPC scans. Using the extracted characteristic phase coherence length $L = 8.1\mu$m, we calculate the expected visibility, which fits reasonably to the measured points particularly at intermediate transmissions. **(b)** We show the theoretical plot for $L = 8.1\mu$m with a scatterplot of each data point that we measured as a function of r_1 and r_2. The scatter points fit best to this theoretical plot. Hence, we extract $L = 8.1\mu$m, and repeating this fit method for different edges allows comparison between coherence lengths.

The value reported in Chapter 4 of 8.0 μm is the average of several such fits, each sampling various

points of the 2D map over reflection coefficients (Fig. A.4b), with an estimated uncertainty of ± 2 μm. We show several fits to a different sampling of points for a few values L, along with their mean-least-squares (MLS) difference to the data, in Fig. A.5.

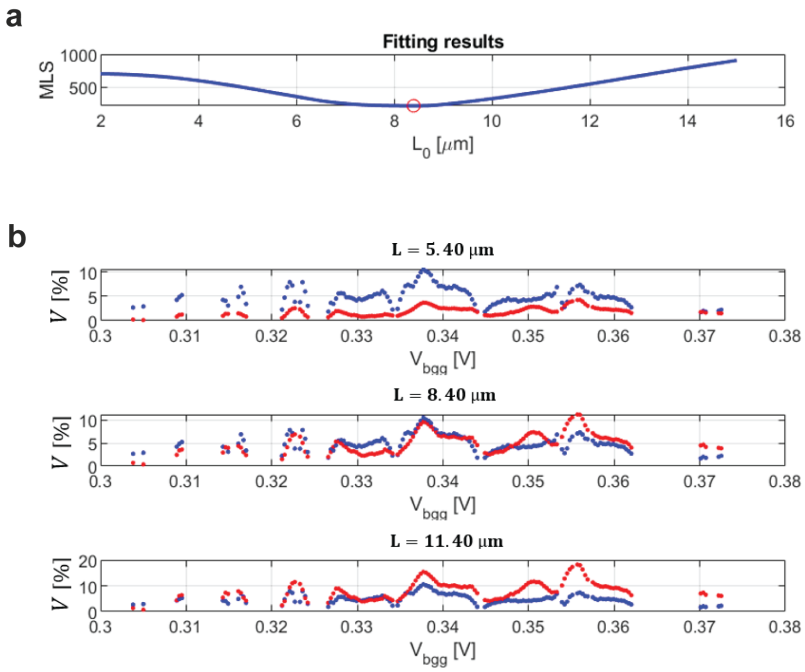


Figure A.5: Example fitting to a particular sampling of visibility over QPC transmissions. **(a)** Mean-least-squares (MLS) difference of the data to the theoretical prediction for a range of possible phase coherence length L. This fit yielded a minimum error for $L = 8.4$ μm. However, there is clearly a range of comparable fits, yielding a conservative uncertainty estimate of ± 2 μm. **(b)** Plots of the measured visibility (blue) as well as the theoretical visibility (red) for three given L. The prediction for $L = 8.4$ μm fits the data the best, while $L = 5.4$ μm $(11.4$ μm$)$ consistently under (over) estimates the data. The x-axis is changing both r_1 and r_2 along the curves shown in Fig. 4.3b. Here, only bottom graphite gate voltage V_{bgg} is displayed, though in fact all topgates are also swept to corresponding values to maintain $\nu_{\text{B}} = 2$, $\nu_{\text{S}} = 0$ along the x axis.

An additional point is the calculation of the etch-defined edge channel coherence length vs. the coherence length of the gated-defined channel region, which is shown in Fig. 4.5b. Here the analysis is identical to the analysis we performed before, however the decaying coefficient is split into two parts,

one describing the decoherence along the gated region and one along the etch region:

$$t_{\mathrm{FP}} = \frac{(1-r_1)(1-r_2)}{1 + r_1 r_2 e^{-2\left(\frac{P_\mathrm{g}}{L_\mathrm{g}} + \frac{P_\mathrm{e}}{L_\mathrm{e}}\right)} - 2\sqrt{r_1 r_2}\cos(\theta) e^{-\left(\frac{P_\mathrm{g}}{L_\mathrm{g}} + \frac{P_\mathrm{e}}{L_\mathrm{e}}\right)}}.$$

where P_g and P_e are the perimeter length of the gated and etched regions, respectively. L_g and L_e are the coherence length of the gated and etched regions, respectively. In the analysis we set $P_\mathrm{g} = 12$ μm and $P_\mathrm{e} = 1.8$ μm according to the fabrication parameters, and we also set $L_\mathrm{g} = 8.0$ μm b as extracted from the above analysis when the edge was propagating only along a gated region. Then, fitting the visibility with fixed r_1, r_2, L_g, P_g, and P_e to various L_e using MLS to choose the best fit, we calculate L_e as a function of ν_{PG} which is shown in Fig. 4.5b (red curve).

Moreover, in region III of Fig. 4.5b, the oscillation is very weak due to the short phase coherence length $L_\mathrm{e} \sim 0.9$ μm along the etched region compared to the length of the etched region $P_\mathrm{e} = 1.8$ μm and the longer gated region. While the data suffer from small signal/noise ratio in this regime, a FFT transformation reveals a small peak, above the noise level, at a corresponding area of 7.5 $\mu\mathrm{m}^2$ which is expected from fabrication parameters. To make sure that this not an artifact from FFT, we show in Fig. A.6 the bare signal as a function of B and corresponding FFT for the plunger gate corresponding to $\nu_{\mathrm{PG}} = 1.67$. Furthermore, we show a pajama plot and its 2D FFT in Fig. A.7, where the AB interference lines of constant phase can be seen with again a magnetic field period corresponding to a flux quantum threading the expected area.

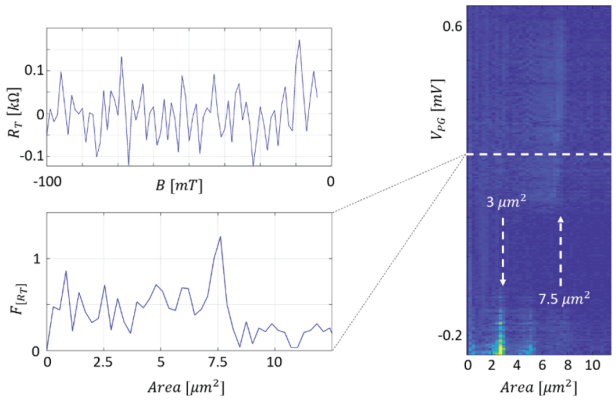


Figure A.6: $R_T(B)$ **and its Fourier transform taken at** $\nu_{PG} = 1.67$**, corresponding to region III in Fig. 4.5b.**

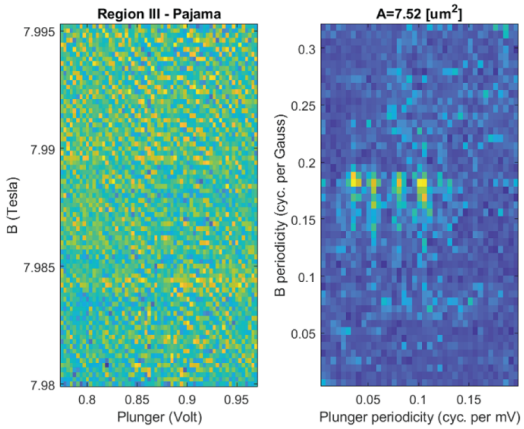


Figure A.7: $R_T(V_{PG}, B)$ **and its 2D-FFT near** $_{PG} = 1.67$**, corresponding to region III in Fig. 4.5b.**

A.3 Interference in various bulk integer fillings and plunger gate capacitance

We observe Aharonov-Bohm interference for all integer edge modes in $\nu_B = 2$ and $\nu_B = 3$, as summarized in Fig. A.8. The magnetic field values shown are relative to 8 T, and V_{PG} is relative to a filling $\nu_{PG} = 0$ under the plunger gate.

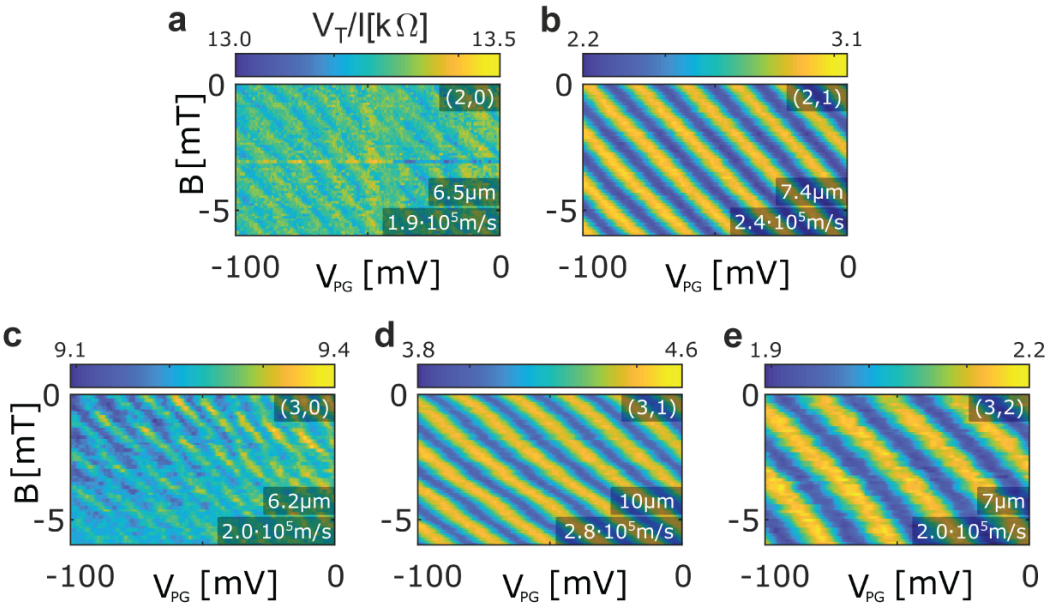


Figure A.8: AB interference in the (B, V_{PG}) plane for various integer edges. **(a)** Outer edge of $\nu_B = 2; 0 < \nu_{QPC} < 1$. **(b)** Inner edge of $\nu_B = 2; 1 < \nu_{QPC} < 2$. **(c)** Outer edge of $\nu_B = 3; 0 < \nu_{QPC} < 1$. **(d)** Middle edge of $\nu_B = 3$; $1 < \nu_{QPC} < 2$. **(e)** Innermost edge of $\nu_B = 3; 2 < \nu_{QPC} < 3$. Importantly, we see that the maximum characteristic coherence length and edge mode velocity (both inset in bottom-right) is achieved for the middle edge of $\nu_B = 3$, where the interfering edge is screened by adjacent compressible edges. The effective area of the interferometer shrinks from the middle edge to the innermost for $\nu_B = 3$, as seen from the magnetic field period increasing, which is consistent with the trend of the electrostatic profile (e.g. considering an increasing depletion length reducing the cavity area); however, the magnitude of the change cannot be judged without a detailed simulation.

The oscillation period in plunger gate voltage is inversely proportional to the mutual capacitance of the interfering edge and the plunger gate C_{EG}. In Fig. 4.4a we saw that the oscillation period de-

creases as V_{PG} increases, since C_{EG} increases as the edge channel moves closer to the plunger gate (PG). Moreover, in Fig. 4.5a the outermost edge, closest to PG, shows the smallest period, corresponding to the largest C_{EG}, while the higher LL edges show progressively larger periods, corresponding to smaller C_{EG}. The PG periods for different edges are summarized in Fig. A.9. We attribute the large difference in C_{EG} to both different spatial separations of the interfering edge to the gate as well as screening of this capacitive coupling by adjacent edges.

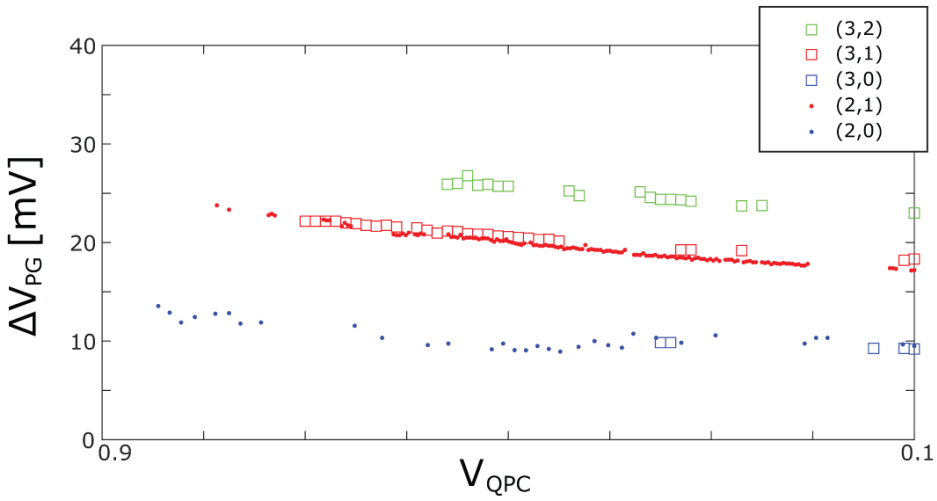


Figure A.9: Plunger gate periodicity ΔV_{PG} as a function of ν_{QPC} for various edge configurations $(\nu_B, \lfloor \nu_{QPC} \rfloor)$. The horizontal axis spans from $\lfloor \nu_{QPC} \rfloor < \nu_{QPC} < \lfloor \nu_{QPC} \rfloor + 1)$ for each configuration, e.g. for $(\nu_B, \lfloor \nu_{QPC} \rfloor) = (3, 1)$ the middle edge mode of $\nu_B = 3$ is partitioned and $1 < \nu_{QPC} < 2$, where both QPCs on average (i.e. aside from QPC resonances) move in coordination. The slow decrease as ν_{QPC} increases arises from an overall increase in C_{EG} as the PG scans to more negative voltage to maintain $\nu_{PG} = 0$, slightly sharpening the electrostatic boundary between the PG region and bulk and moving the interfering edge closer to the PG.

To make sense of the value for C_{EG}, focusing on the configuration $(\nu_B, \lfloor \nu_{QPC} \rfloor) = (2, 1)$, we compute the Fourier transform of the $R_T(V_{PG})$ to obtain the edge-gate capacitance C_{EG} as a function of V_{PG}, as V_{PG} scans towards the boundary of the plateau for $\nu_{PG} = 1$. In Fig. A.10 we show on top the same scan as in Fig. **??**a but zoomed in on the region where the visibility collapses as the PG gated area exits the $\nu_{PG} = 1$ plateau and becomes compressible. On the bottom we plot C_{EG} extracted

from the local oscillation period. As expected from the electrostatic consideration, C_{EG} increases as V_{PG} approaches to the critical voltage to push the interfering state and the electrostatic boundary to be directly beneath the edge of the gate. We found that C_{EG} we obtained is consistent with the expected electrostatic consideration given our device geometry.

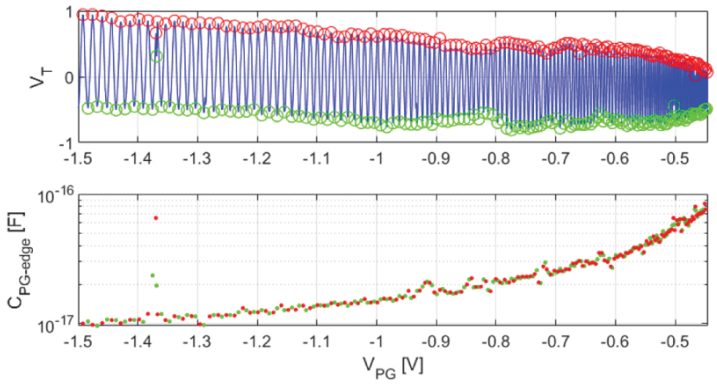


Figure A.10: Plunger gate to edge channel capacitance C_{EG} as a function of V_{PG}. Top: zoom in of Fig. 4.5a near the collapse in visibility. Bottom: the extracted edge-plunger capacitance as a function of the plunger gate voltage as ν_{PG} approaches the edge of the plateau for filling factor 1 around -0.4 V.

The value reached around $V_{\mathrm{PG}} = -0.4\,\mathrm{V}$, when the interfering mode propagates directly beneath the edge of the gate, matches the expected value $C_{\mathrm{EG}} \approx 0.8 \cdot 10^{-16}$ F. This value comes from a calculation of the capacitance between a wire (here the edge channel) of radius $r = 9$ nm, length $l = 1.7$ µm separated through hBN of thickness $h = 50$ nm, dielectric constant $\epsilon_{\mathrm{r}} = 4$, to the gate, assumed to be an infinite half-plane, using $C_{\mathrm{EG}} \approx \frac{\pi l \epsilon_0 \epsilon_{\mathrm{r}}}{\arccos(h/r)}$.

A.4 Visibility decay with temperature

Thermal blurring in the FP cavity predicts an exponential decay of the oscillation visibility:

$$V(T) \approx e^{-\frac{\pi k_B P}{\hbar v_{edge}} T}$$

where P is the total length of the cavity (perimeter) and v_{edge} is the velocity of the interfering edge mode [168]. Assuming a perimeter $P = 6.8$ μm, as defined in the lithography and similarly assumed in the bias dependence extraction, we fit the visibility to an exponential decay with temperature below and extract a velocity $v_{edge} = 3.2 \cdot 10^5$ m/s for the inner edge of the $\nu_B = 2$ QH state. This is $\sim 33\%$ larger than the value $v_{edge} = 2.4 \cdot 10^5$ m/s extracted from the DC bias dependence, but we note that there is a significant error in the temperature dependence due to unknown electron temperature.

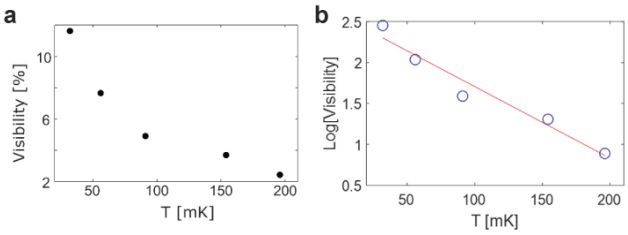


Figure A.11: Fitting the decay of visibility with temperature for the inner edge for $\nu_B = 2$. **(a)** Visibility plotted versus temperature. **(b)** Logarithm of the visibility versus temperature (blue circles) along with a line of best fit (red, $R^2 = 0.95$) which has a slope -0.0087 mK^{-1}.

A.5 Interference of additional integer edge in fractional bulk filling

In addition to the interference in bulk fractional filling $\nu_B = \frac{8}{3}$ in Chapter 4, we also observe Aharonov-Bohm interference of the nearest integer edge mode when the bulk is in $\nu_B = \frac{10}{3}$, summarized in Fig. A.12.

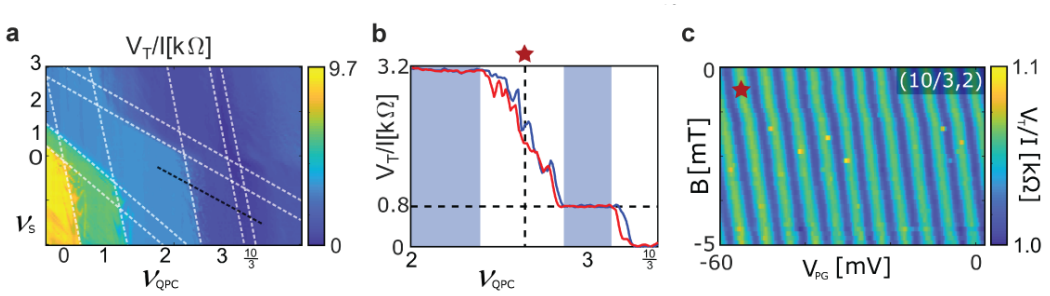


Figure A.12: Integer interference with fractional bulk filling. (a) Map of QPC operating points in bulk filling factor $\nu_B = \frac{10}{3}$ as a function of ν_S and ν_{QPC}. Black dashed line demonstrates QPC operation where the split gates are at filling factor $\nu_S = 2$. **(b)** R_T of the left and right QPC along the black dashed line in (a), showing the measured values of the integer and fractional edge portioning. **(c)** Aharonov-Bohm dominated resistance oscillations in the third integer LL in bulk filling factor $\nu_B = \frac{10}{3}$. The working point of the QPCs is depicted by the red star in (b).

B

Additional information for chapter 5

B.1 Device characterization and QPC operation

Similarly to in Chapter 4, the 8 top graphite gates in the device are separately controlled to set filling factors in each region at perpendicular magnetic field B, since Landau level filling factor $\nu \equiv \frac{n_e}{n_\phi}$, where $n_\phi = \frac{eB}{h}$ and n_e is the areal electron density. At the region in the middle of the top-gate split-gates, where the graphite is etched away for a separation of 150 nm, the electrostatics are tuned to

create a saddle-point potential at the QPC. Once an approximate saddle-point is formed at the QPCs using the graphite top-gates and bottom-gate, the suspended metal bridges over the QPCs are tuned to precisely set transmissions T_{QPC1} and T_{QPC2}. The neighboring top-gates screen out stray fields generated by the suspended bridges such that V_{QPC1} and V_{QPC2} are primarily coupled to the graphene at the saddle-point of the QPCs. We interpret non-integer values $0 < T_{\mathrm{QPC}} < 1$ as a transmission probability for electrons in the outer EC, which is partially transmitted, while for $1 < T_{\mathrm{QPC}} < 2$, the quantity $T_{\mathrm{QPC}} - 1$ gives the transmission probability for the inner EC.

Fig. B.1 shows our device after fabrication, highlighting the locations of the conducting layers and the details of the patterned top graphite gate. Fig. B.2 shows the general Hall characterization of the device, measured using the contact configuration shown in Fig. B.1c, with all top gates grounded. Fig. B.2c shows two linecuts at fixed field $B = 6$ T with V_{LG} grounded (0 V) or set to 1 V, with a dashed line connecting approximate constant filling near the center of the plateaus. This provides the required compensating top-gate voltages that must be set to keep $\nu = 2$ in the relevant interferometer regions (e.g. $\nu_{\mathrm{LG}} = \nu_{\mathrm{MG}} = \nu_{\mathrm{RG}} = 2$ and $\nu = 0$ around the boundary (i.e. $\nu_{\mathrm{SG1}} = \nu_{\mathrm{PG}} = \nu_{\mathrm{SG2}} = 0$) for any given bottom gate voltage. For example, we extract the following lines of constant filling factor (tuned near the center of the corresponding plateau) from such data, where V_{TG} is any of the graphite top gate voltages, and V_{BG} is the graphite bottom gate voltage:

$\nu = 0$:	$V_{\mathrm{TG}}(\mathrm{V}) = -1.974 \cdot V_{\mathrm{BG}}(\mathrm{V}) + 0.037$
$\nu = 1$:	$V_{\mathrm{TG}}(\mathrm{V}) = -1.978 \cdot V_{\mathrm{BG}}(\mathrm{V}) + 0.444$
$\nu = 2$:	$V_{\mathrm{TG}}(\mathrm{V}) = -1.970 \cdot V_{\mathrm{BG}}(\mathrm{V}) + 1.000$
$\nu = 3$:	$V_{\mathrm{TG}}(\mathrm{V}) = -1.949 \cdot V_{\mathrm{BG}}(\mathrm{V}) + 1.541$
$\nu = 4$:	$V_{\mathrm{TG}}(\mathrm{V}) = -1.914 \cdot V_{\mathrm{BG}}(\mathrm{V}) + 1.922$
$\nu = 5$:	$V_{\mathrm{TG}}(\mathrm{V}) = -1.949 \cdot V_{\mathrm{BG}}(\mathrm{V}) + 2.340$
$\nu = 6$:	$V_{\mathrm{TG}}(\mathrm{V}) = -1.989 \cdot V_{\mathrm{BG}}(\mathrm{V}) + 2.914$

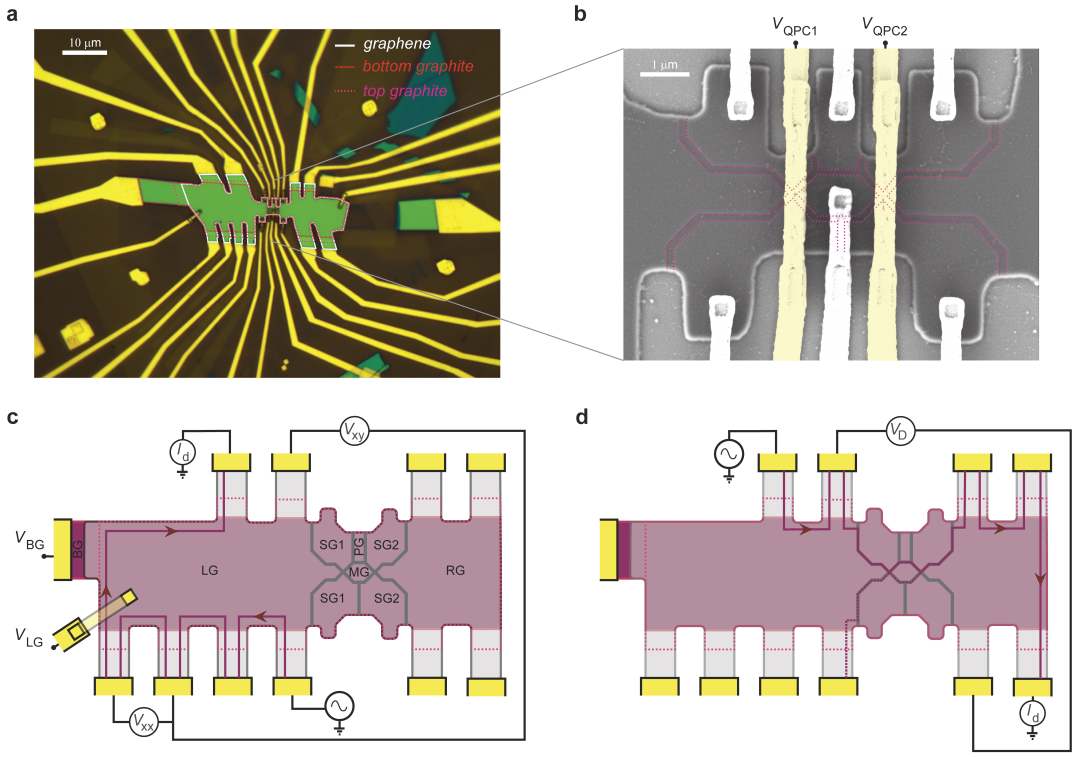


Figure B.1: Device image and gating structure. (a) Optical micrograph of the completed device, after all graphene contacts and bridge contacts/gates are connected. The graphene and bottom graphite contacts are made in the same step to the etched stack as outlined in Chapter 3. At the graphene contacts, the top graphite boundary extends beyond the bottom graphite, followed by a region with neither top nor bottom graphite gates immediately adjacent to the graphene contacts. This ungated region is doped through the oxide dielectric on the Si substrate by applying $+25$ V to the underlying conducting Si during all measurements. **(b)** Scanning electron microscope image of the central interferometer region (pointed to in (a)) on a similar device. Pink dashed lines outline the boundaries of the top graphite lines that were etched away. QPC bridge gates are shaded yellow. **(c)** Schematic of a Hall measurement under the region gated by the 'left gate' (LG). 'Split gate' (SG), 'plunger gate' (PG), 'middle gate' (MG), and 'right gate' (RG) regions are indicated. All top gate regions are contacted by metal bridges as indicated for LG, though the rest are omitted for clarity. The outer boundary of the top gates are indicated by the dashed pink lines. **(d)** Schematic of a typical QPC or interferometer measurement, where the 'diagonal' conductance is extracted as $G_D = \frac{I_d}{V_D}$.

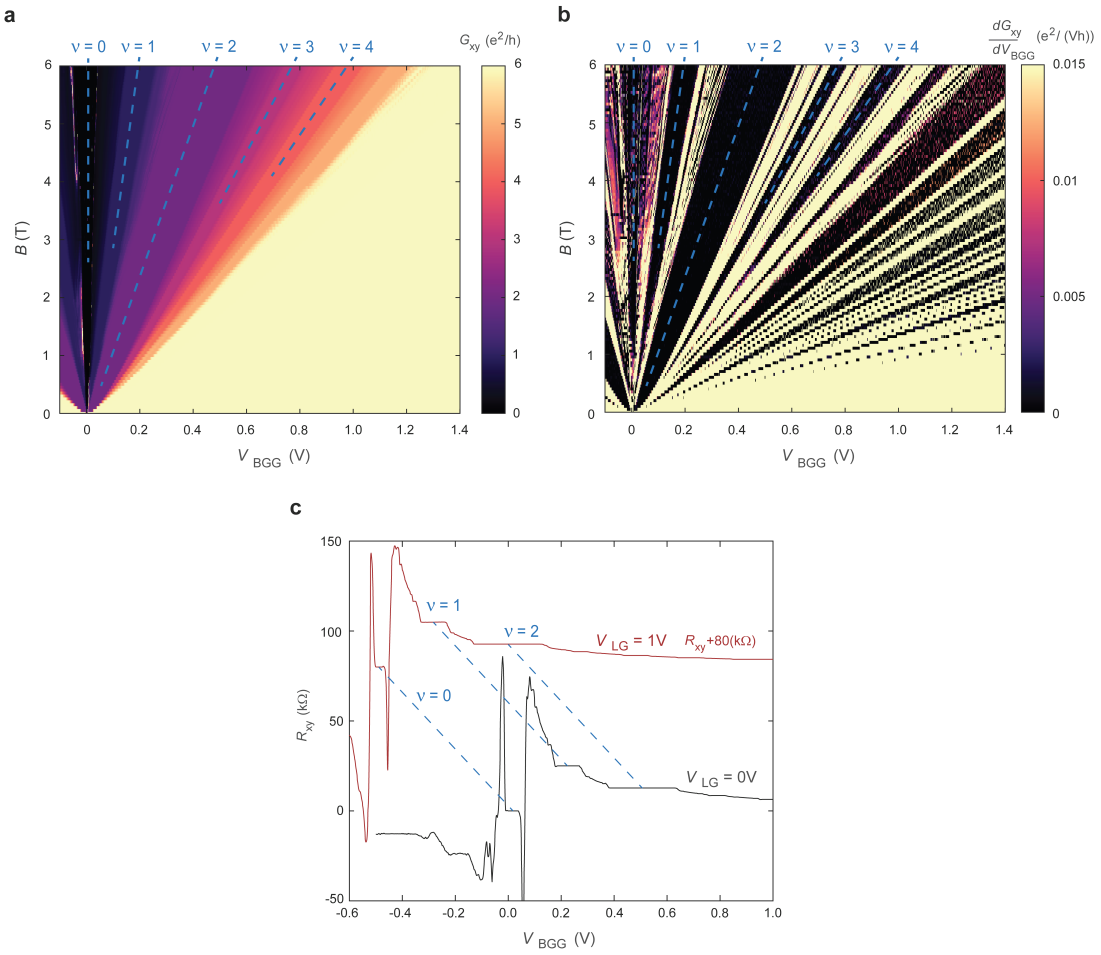


Figure B.2: Device quantum Hall characterization. (a) Hall conductance measured in the configuration shown in Fig. B.1c with density tuned via the graphite back gate. **(b)** Derivative of Hall conductance in (a) to emphasize the flat plateaus, including well-developed broken symmetry integer and fractional QHE states. **(c)** Two transverse Hall resistance measurements at different top gate voltages at $B = 6$ T. Lines corresponding to the center of plateaus superimposed, indicating the required back gate and top gate voltages extrapolated to keep constant filling.

Fig. B.3 shows how we then tune the individual QPC1 (QPC2) transmissions given that the QPC2 (QPC1) is deactivated (i.e. ν_{SG2} (ν_{SG1}) $= 2$. In panel (a), V_{LG} and V_{MG} are swept along with the back gate on the x-axis to maintain $\nu_{LG} = \nu_{MG} = 2$ to the sides of the QPC. The y-axis shows the sweep of the split gate voltages, which primarily tunes the filling ν_{SG1} but also couples to the QPC transmission (filling ν_{QPC1}). Together, these two axes effectively tune the QPC and split gate filling factors related by a linear transformation. The new axes that correspond to these more physically relevant variables are indicated by the dashed lines which separate regions of different integer filling, with the x'-axis corresponding to the QPC filling (green lines) and the y'-axis that of the split gates (grey lines).

Critical to the measurements in Chapter 5, we have added metallic QPC bridge gates to our previous device design[207] discussed in Chapter 4. This allows for the precise tuning of the exposed QPC regions without tying the back or split gates to specific values. This gives the device an increased degree of freedom for additional tunability across a broader range of gate voltages. For all data shown in the Chapter 5, the back gate and split top-gates are set to the values indicated by the blue dots in Fig. B.3, and the QPC filling (transmission) is then tuned separately by sweeping the bridge gate voltages V_{QPC1} and V_{QPC2}. Importantly this corresponds to a regime where the split gate fillings $\nu_{SG1} = \nu_{SG2} = 0$ to disallow any additional modes transmitting or tunneling through the barriers. Practically, we find that the QPCs also function for $\nu_{SG1} = \nu_{SG2} < 0$ though additional resonance features (clear in Fig. B.3a) may appear, hence we choose to operate within $\nu_{SG1} = \nu_{SG2} = 0$.

B.2 Weak and strong backscattering limits

Fig. B.4 shows diagonal interference data for weak (a) and strong (b) backscattering limits. Interferometer devices are typically measured in the weak backscattering limit where the interference signal can be interpreted as single-particle interference from a sum of particle trajectories transmitting/reflecting through the cavity. Fig. B.4a shows the AB interference signal within the intermediate inter-edge cou-

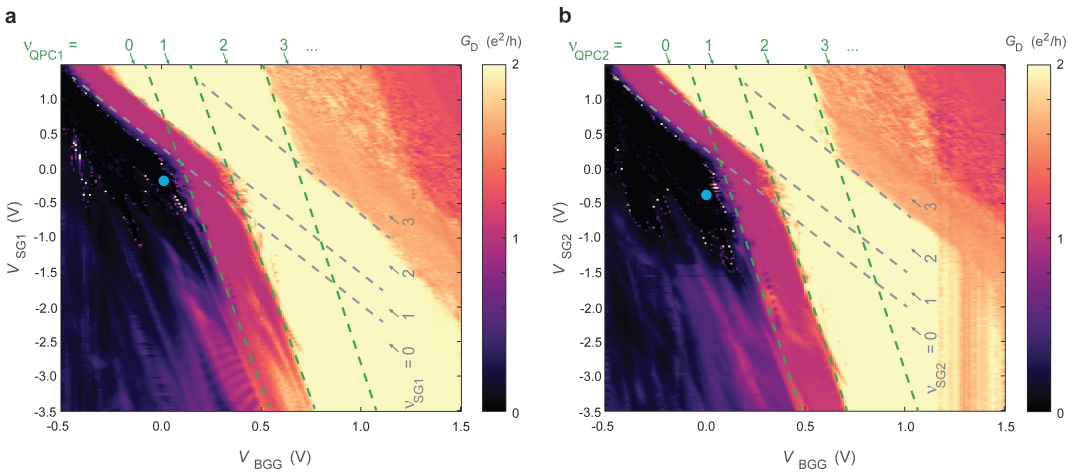


Figure B.3: QPC tuning via back and split gates. Individual transmissions of the left **(a)** and right **(b)** QPCs. For the graphite back gate sweep on the x-axis, the (left, middle)/(right, middle) graphite top gates are swept to compensate to keep the filling $\nu = 2$ underneath according to constant filling lines fit from scans like Fig. B.2c. The dashed lines indicate steps in integer filling along the transformed axes corresponding to the QPC regions (green lines) and split gate regions (grey lines). Blue dots on each plot indicate the operational point of the interferometer for all interference data shown in the Chapter 5, effectively setting the split gate filling to 0 while the QPC bridge gates are swept to choose the QPC transmissions between 0 and $2\frac{e^2}{h}$.

pling regime showing the phase jumps discussed in the main text ($T_{\mathrm{QPC1}} = T_{\mathrm{QPC2}} = 0.9$). However, when the QPCs are pinched off ($T_{\mathrm{QPC1}} = T_{\mathrm{QPC2}} = 0.01$), such as in Fig. B.4b, the center cavity becomes analogous to a quantum dot where charge tunneling dominates transmission. While the signal is heavily suppressed, the same phase-jump periodic pattern of the weak backscattering AB data is still evident. In this strong backscattering regime, a capacitively-coupled double quantum dot model may be used to explain the charge configurations localized on the inner and outer annular EC compressible regions, which due to the charge-phase relation is related to the interference pattern observed at weak-backscattering.

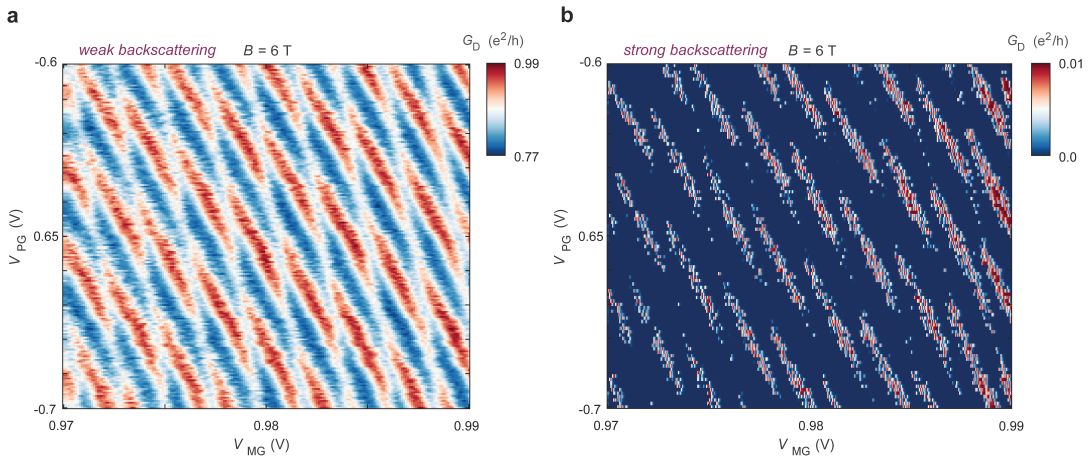


Figure B.4: Weak and strong backscattering limits of intermediate-coupling regime. Diagonal conductance of outer EC through the FP cavity with the QPCs tuned to the weak ($T_{\text{QPC1}} = T_{\text{QPC2}} = 0.9$) backscattering **(a)** and strong ($T_{\text{QPC1}} = T_{\text{QPC2}} = 0.01$) backscattering **(b)** limits. The typical AB interference signal as shown in the main text is seen in (a) along with phase jumps corresponding to inter-edge coupling, while a similar periodic pattern is seen in (b) where each QPC is functioning as a tunnel barrier..

B.3 Temperature and finite source-drain bias dependence

Fig. B.5 compares the diagonal conductance oscillations in the main text's typical operating regime ($\nu = 2$, interfering the outer EC) at two different temperatures. The phase jumps corresponding to inter-edge coupling maintain the same qualitative behavior with an identical periodicity between 60 mK and 440 mK. The visibility is drastically reduced by 440 mK, yet phase jump magnitude remains relatively unchanged, reflecting the fact that the inter-edge Coulomb coupling and ground-state charge configurations are zero temperature properties.

We also measure finite-bias dependence of the outer EC interference, which is not fully understood. We observe a typical bias dependence in the uncoupled case (Fig. B.6a), consistent with a highly asymmetrical voltage drop across the FP cavity [197]. The bias voltage spacing of visibility nodes $\Delta V_{\text{D}} = 142$ μV and designed perimeter of the FP cavity $P = 4.24$ μm suggest an edge mode velocity $v_{\text{edge}} = \frac{eV_{\text{D}}P}{h} = 1.46 \cdot 10^5$ m/s, consistent with previous observations in graphene [207,197] and

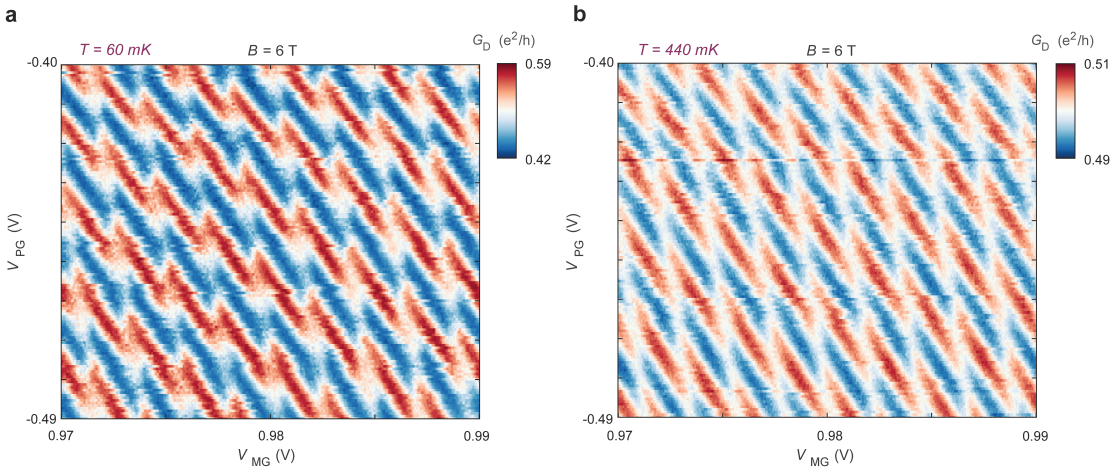


Figure B.5: Temperature dependence of intermediate-coupling regime. Conductance oscillations on the outer EC shown at identical sweeping parameters at estimated 60 mK **(a)** and 440 mK **(b)** electron temperatures.

GaAs [163,165] based FP interferometers. The intermediate coupling regimes Fig. B.6b-c show complicated behavior which we cannot understand without a detailed theoretical model. However, in the strongly coupled limit, Fig. B.6d, we again observe a relatively simple pattern corresponding to the f_{o+i} frequency. The outer node spacing is similar to the uncoupled case, but there is a reduced-width central node, a signature which may indicate chiral Luttinger liquid physics [165]. Interpreting such data requires further experimental and theoretical work.

B.4 Additional interference data across coupling transition

In Fig. B.7 we plot the interference signal and FFT analysis for a different set of parameters: fixed V_{PG} but varying both V_{MG}. We find that the relationship between the lattice of Fourier peaks on the inner EC compared to the outer EC still holds.

Furthermore, we plot a sampling of the entire range of $B - V_{\mathrm{PG}}$ interference data collected across the density-tuned coupling transition for the in Fig. B.8 and Fig. B.9. Fig. B.8 shows data from interfering the outer EC and their 2D FFTs, while Fig. B.9 shows the corresponding data and analysis at the

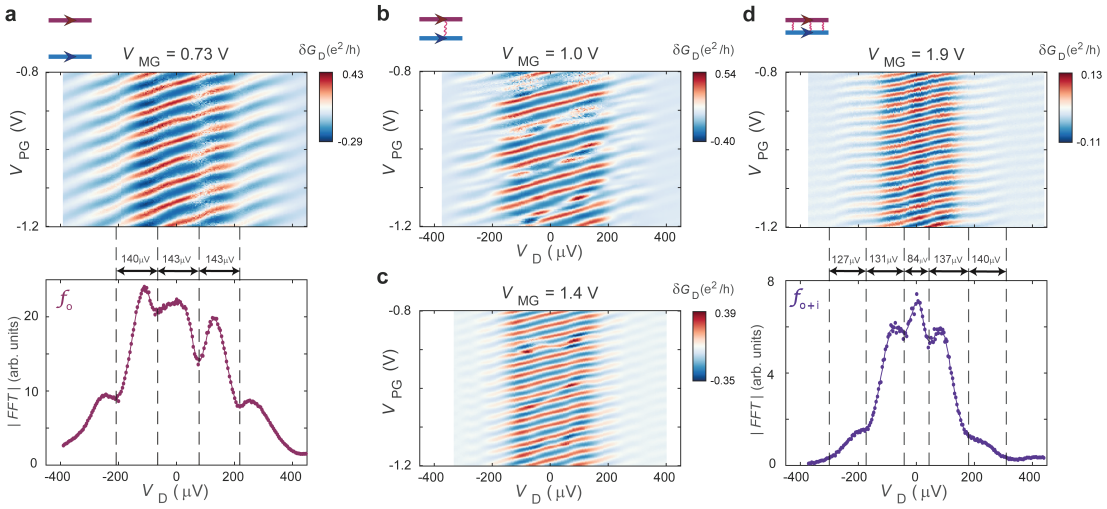


Figure B.6: Finite-bias dependence of outer EC interference. **(a)** G_D oscillations with V_{PG} and V_D in the uncoupled limit. V_D is the measured DC voltage drop on the same probes measuring the AC conductance G_D, to get the accurate voltage drop across the FP cavity on the sample for each DC bias applied to the source. Bottom: extracted 1D FFT amplitude at the frequency of the oscillations, f_o, as a function of V_D showing the visibility nodes of the interference at finite bias. **(b-c)** G_D oscillations with V_{PG} and V_D in two intermediate coupling regime tunings. **(d)** G_D oscillations with V_{PG} and V_D in the strongly coupled limit. Bottom: extracted 1D FFT amplitude at the new dominant frequency of the oscillations, f_{o+i}, as a function of V_D showing the visibility nodes of the interference at finite bias.

same densities for interfering the inner EC. These data are a subset of the data analyzed to construct Fig. 5.4.

As an additional check that interactions with the copropagating edge channel that exist outside of the interferometer cavity are contributing to the observed phase jumps and periodicity transition, we set the external filling factor to $\nu = 1$ while the cavity itself is tuned through the same range of density corresponding to $\nu > 2$ as before. Monitoring the interference signal on the outer EC in the cavity, we observe a qualitatively similar transition with phase jumps in Fig. B.10

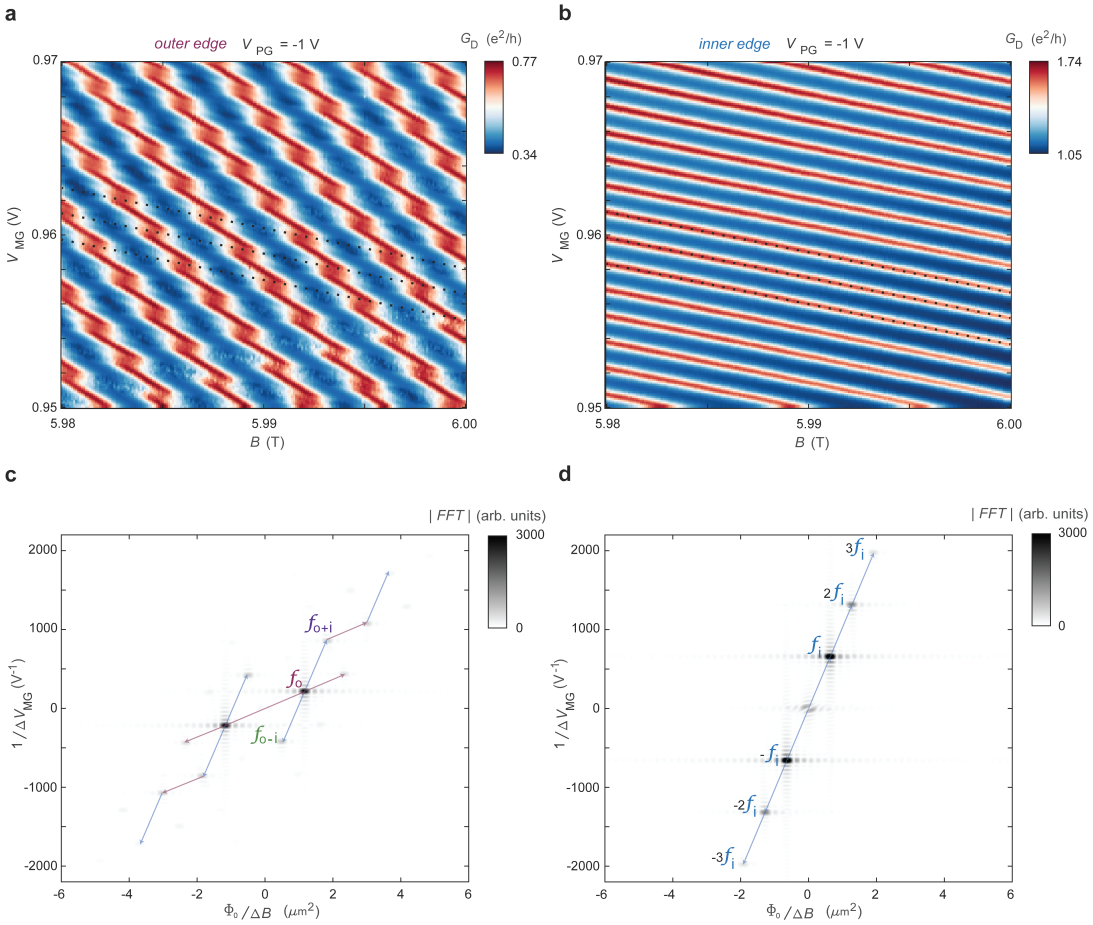


Figure B.7: Comparison of the outer and inner EC interference for different parameters. (a) Conductance G_{D} oscillations on the outer EC with $V_M G$ and B, for the indicated V_{PG} value. Dashed black lines indicate the visible phase jumps in the data. **(b)** Conductance G_{D} oscillations on the inner EC with V_{MG} and B. Dashed black lines indicate the oscillation maxima, which match the same slope as in (a). **(c)** 2D FFT of the G_{D} oscillations from panel a showing the peaks f_{o}, $f_{\mathrm{o+i}}$, $f_{\mathrm{o-i}}$, and their harmonics. **(d)** 2D FFT of the G_{D} oscillations from panel (b) showing the peak f_{i} and its harmonics. The lattice of peaks in (c) consists of sums and differences of the fundamental frequencies of the outer EC f_{o} and the inner EC f_{i}. Note that though the relative couplings to the parameters shown here are different than in Fig. 5.4, the same logic applies to understanding the peaks.

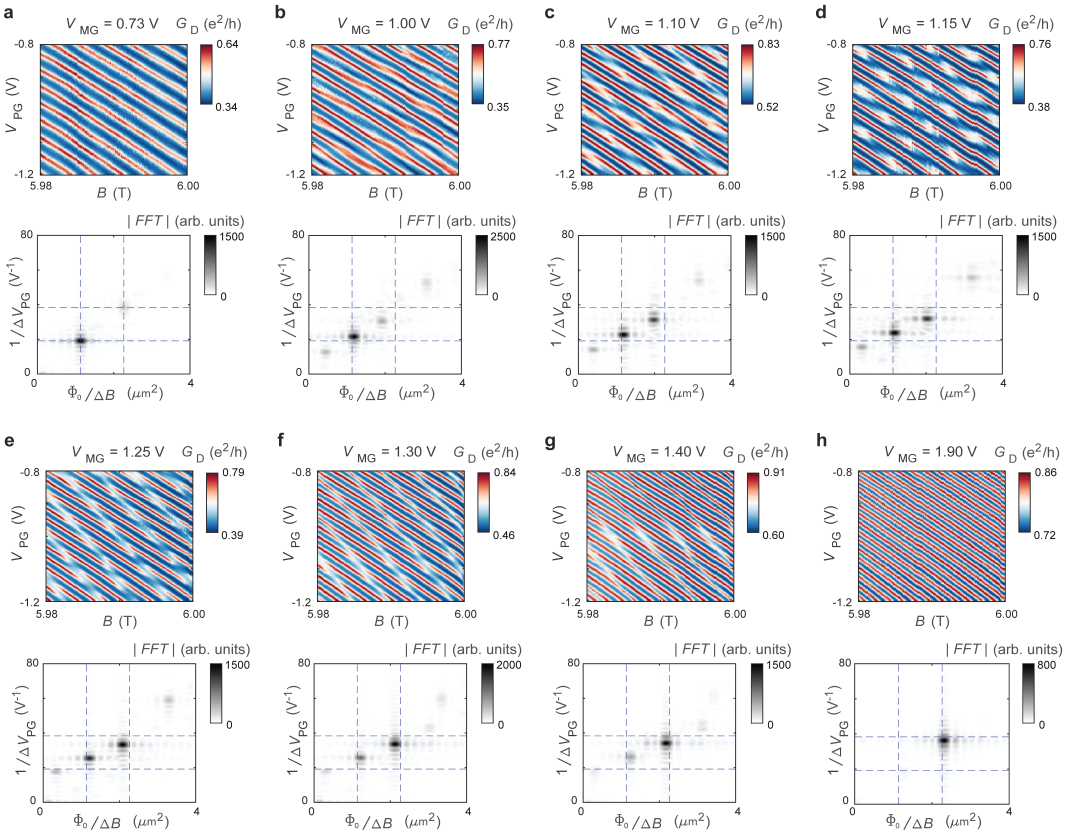


Figure B.8: Magnetic field dependence of outer EC interference through the periodicity transition. (a-h) Top: conductance G_{D} oscillations on the outer EC with V_{PG} and B, for the indicated V_{MG} values through the periodicity transition. Bottom: 2D FFT of the G_{D} oscillations from the top panels showing the peaks f_{o}, $f_{\mathrm{o+i}}$, $f_{\mathrm{o-i}}$ continuously evolving through the transition. Horizontal dashed lines indicate $\frac{1}{\Delta V_{\mathrm{PG}}} = 19.2\ \mathrm{V}^{-1}$ and $2 \times 19.2\ \mathrm{V}^{-1}$, corresponding to the frequencies f_{o} and $2f_{\mathrm{o}}$ before the transition. Similarly, vertical dashed lines indicate $\frac{\phi_0}{\Delta B} = 1.13\ \mu\mathrm{m}^2$ and $2 \times 1.13\ \mu\mathrm{m}^2$. The designed FP area $A = 1.16\ \mu\mathrm{m}^2$.

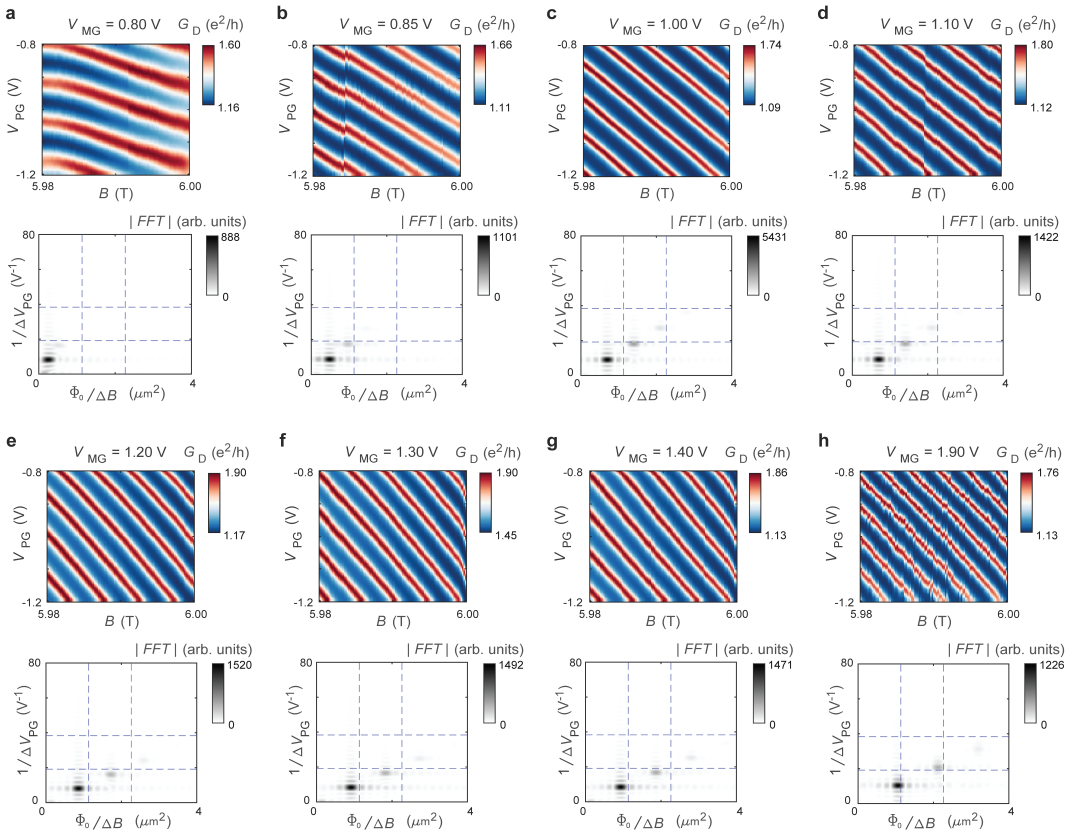


Figure B.9: Magnetic field dependence of inner EC interference through the periodicity transition. (a-h) Top: conductance G_{D} oscillations on the inner EC with V_{PG} and B, for the indicated V_{MG} values through the periodicity transition. Bottom: 2D FFT of the G_{D} oscillations from the top panels showing the peak f_{i} and its harmonics continuously evolving through same range where the interference on the outer EC undergoes the transition. . Horizontal dashed lines indicate $\frac{1}{\Delta V_{\mathrm{PG}}} = 19.2\ \mathrm{V}^{-1}$ and $2 \times 19.2\ \mathrm{V}^{-1}$, corresponding to the frequencies f_{o} and $2f_{\mathrm{o}}$ before the transition. Similarly, vertical dashed lines indicate $\frac{\phi_0}{\Delta B} = 1.13\ \mu\mathrm{m}^2$ and $2 \times 1.13\ \mu\mathrm{m}^2$. The designed FP area $A = 1.16\ \mu\mathrm{m}^2$. The area of the inner EC evidently starts from near zero and increases monotonically, approaching the same area of the outer EC, which is roughly bound by the lithographic area. Note also that phase jumps are not observed on the inner edge.

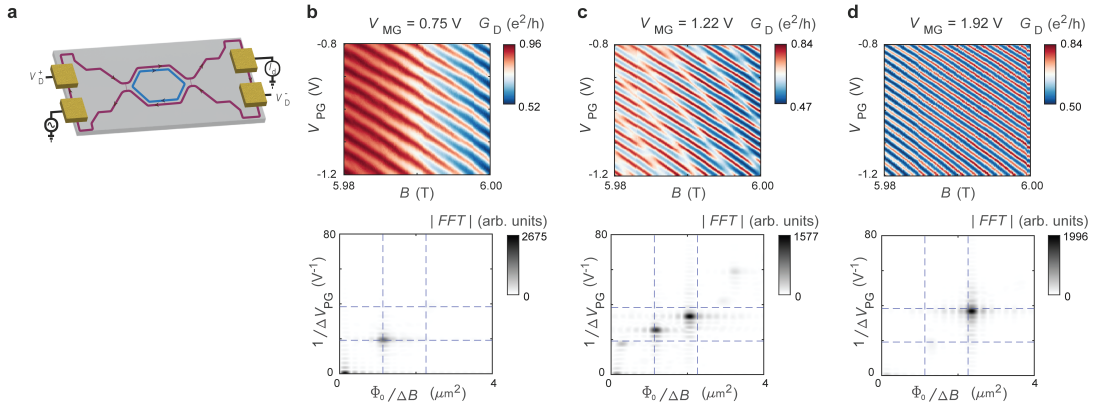


Figure B.10: Interference of a single edge into a dual-edge cavity. **(a)** Schematic of device where left/right regions are tuned to $\nu = 1$ to allow the single edge mode to partially transmit into a cavity at $\nu = 2$. **(b-d)** Diagonal conductance of the outer EC through device at increasing middle gate V_{MG} voltages with corresponding 2D FFTs below.

B.5 Estimation of the coupling strength

Although we have not attempted a detailed calculation of the coupling constants important for our analysis, we can at least advance some qualitative arguments for the trend that emerges from our analysis. The edge of the sample consists of alternating compressible and incompressible stripes whose width is set by electrostatics [11]. ECs are located in compressible stripes. It may be expected that the outermost EC is located along an electron density contour where the local Landau-level filling factor is ~ 0.5, while the second EC is located along a contour with filling ~ 1.5. Due to residual disorder and electron-electron interactions, the Hall plateau at $\nu = 2$ will set in when the bulk filling is smaller than 2, though larger than 1.5. The density profile produced by charges on confining gates should be relatively smooth, so that the spatial separation between the outer most EC and the second EC should be relatively large at this point, and the Coulomb coupling between the channels, screened by the gates, should be relatively weak. As the electron density is increased, the inner EC should move closer to the outer edge, and the coupling should become stronger, and it is plausible that by the time the device enters the $\nu = 3$ plateau, the value of $\frac{K_{12}}{K_1}$ is close to 1.

Further increases in the density should produce additional ECs, which are totally reflected at the QPCs and do not contribute directly to the transport. The number of electrons on any additional closed ECs, as on other localized states, will be restricted to integer values, and in principle, due to Coulomb interactions, there should be a jump in the interference phase of outer edge states each time this integer changes by one. However, Coulomb interactions in our system are strongly screened by the nearby gates, so if the additional channels are not close to the outer two ECs, the jumps would be too small to be observable. In monolayer graphene, the energy gap at $\nu = 2$, which is due to the cyclotron energy, is much larger than the gaps at $\nu = 1, 3, 4$,and 5, which arise from electron-electron interactions. Consequently, we expect that the spatial separation between the outermost EC and the second EC will tend to be small compared to the separation between the second EC and any additional ECs.

Another issue is the stability criterion embodied in the requirement $|K_{12}|^2 \leq K_1 K_2$. This requirement is automatically satisfied if we assume that when the two outer ECs are close together, the energy for adding an electron to either one of them is dominated by an electrostatic energy that depends primarily on the total charge on the edges, and only weakly on the difference between them, so that $E = a\delta Q_1^2 + b\delta Q_2^2 + 2K_{12}\left(\delta Q_1 + \delta Q_2\right)^2$, with a and b small compared to K_{12}. Then, K_1 and K_2 will be approximately equal to each other and slightly larger than K_{12}.

This analysis is compatible with experiments in GaAs interferometers where the ECs occur at the boundary between two QHE states of different integer filling fractions[211]. There it was found that the $\frac{h}{2e}$ periodicity occurred only if the outer EC and second EC belong to the same orbital Landau level, and not if they belong to different levels. In the first case, the energy gap for the QHE state between the two ECs will arise from electron-electron interactions, while the energy gap in the second case will be dominated by the generally larger cyclotron energy. Therefore, in the first case, when the density is increased enough to populate a third QHE state in the bulk of the sample, the two outer ECs might be pushed so close to each other that they are strongly coupled, while this might not be expected to

happen in the second case.

B.6 Physics of AB frequency doubling at strong coupling

The meaning of the charge fluctuations δQ_1 and δQ_2 can be made more precise as follows. As stated in the main text, we define Q_1 as the number of electrons in the lowest spin-split Landau level enclosed by the outer edge mode and Q_2 as the number of electrons in the higher spin state enclosed by the inner mode. These charges are related to the enclosed areas A_1 and A_2 by $Q_i = \frac{A_i B}{\phi_0}$, where $i = 1$ or 2. These areas are allowed to deviate slightly from the ideal areas $\bar{A}_i$, which are assumed to be smooth functions of V_{PG} and, at most weakly varying functions of B and V_{MG}. Then $\delta Q_i = Q_i - \frac{B\bar{A}_i}{\phi_0}$, and the energy E may be expanded to quadratic order in δQ_i as stated above.

When the inner mode is completely reflected at the QPC, the charge Q_2 is constrained to be an integer, while the charge Q_1 can change continuously, assuming that the outer edge is mostly transmitted through the QPCs. At low temperatures the charges will be determined so as to minimize E, subject to the integer constraint.

If Q_2 is held fixed while the magnetic field is increased by a small amount dB, the inner edge charge δQ_2 will change by an amount $-\frac{\bar{A}_2}{\phi_0} dB$. This happens because, as the area shrinks, charge is transferred from the edge region to the interior, where it is effectively screened by the gates, leaving a charge deficit at the edge. In the strong coupling limit, this will cause δQ_1 to increase by an equal amount. Thus, the total charge Q_1 in the lowest spin-split Landau level will increase by $dQ_1 = -\frac{\bar{A}_1+\bar{A}_2}{\phi_0} dB$, and the interferometer phase θ will increase by $2\pi dQ_1$.

If B is increased by a large amount, the value of Q_2 will not be fixed but will undergo periodic integer jumps. In the strong coupling limit, the jump in Q_1 caused by a jump in Q_2 will also be an integer. This will cause θ to jump by a multiple of 2π, which will be invisible in an interferometer experiment. Thus, the observed rate of change of the phase will be $\frac{d\theta}{dB} = 2\pi \frac{\bar{A}_1+\bar{A}_2}{\phi_0}$, which is equal

to $4\pi\frac{\bar{A}_1}{\phi_0}$, if we neglect the difference between $\bar{A}_1$ and $\bar{A}_2$. This rate of change is twice as fast as would have been observed in the absence of coupling between the inner and outer edge modes.

We remark that in the course of adding one flux quantum to the area $\bar{A}_1$ one would expect on average to have a jump by one electron in each spin state. So, in general, one will have one positive jump in Q_2 and one negative jump in Q_1. Thus, while the observed interference phase will change by an amount equivalent to a change of two electrons, the actual change in Q_1 will only be one electron.

B.7 Influence of bulk-edge coupling and screening by nearby gates

Screening of long-range Coulomb interactions by nearby gates in our device is essential to consider when determining the influence of edge-edge and bulk-edge coupling on the interference signal. In the data analysis and preceding discussion, we have neglected bulk-edge coupling since the radius of the interference loop extracted from the outer EC interference (600 nm) is always much larger than the average distance to the graphite screening gates (38 nm), as shown in Fig. B.11. Therefore, bulk-edge interaction should be well screened by the gates. In contrast, the distance between the inner and outer EC approaches 85 nm in the strong-coupling limit, which enables strong Coulomb interaction that will not be screened out by the gates. We also observe that the contribution of edge-edge coupling, as evidenced by the presence of the f_{o+i} component in the signal, becomes significant only when the edge-edge separation becomes about 200 nm or less, within about a factor of 5 of the gate distance. The behavior of the inner EC interference over the range of density we explored is also consistent with these rough estimates, as the interference signal continues to show Aharonov-Bohm interference (Fig. B.9) through a shrinking area down to an enclosed radius of 200 nm. Hence, we find that bulk-edge coupling is negligible in all experimental regimes that we explored.

According to the model by Frigeri et al. (ref. [215]), for negligible bulk-edge coupling, the transition to frequency doubling occurs when the inter-channel interaction drops to roughly half of the charging

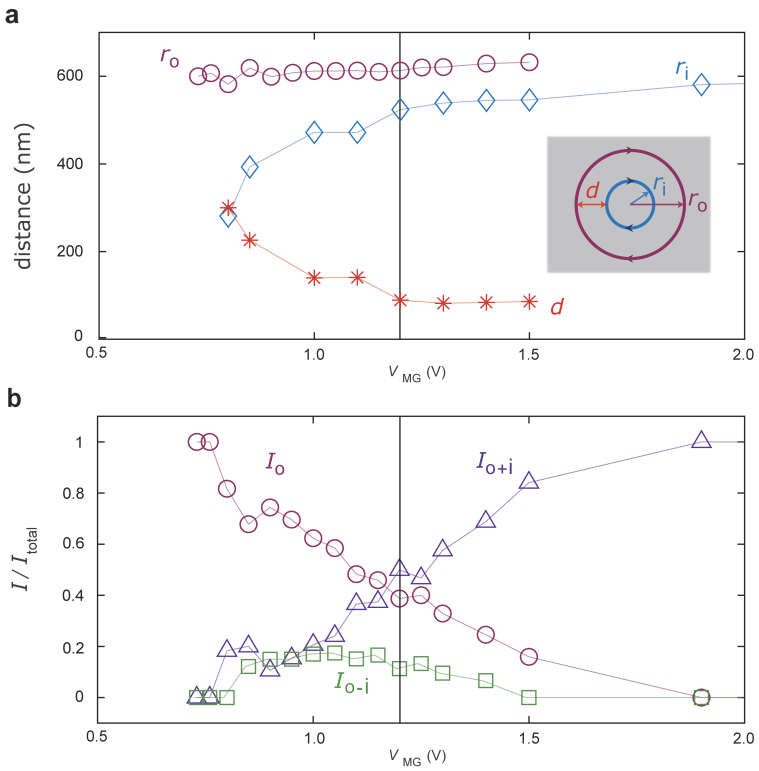


Figure B.11: Extracted radii and EC separation through the periodicity transition. (a) Approximate radii r_o and r_i of the outer and inner EC, respectively, as well as the edge channel separation $d = r_o - r_i$ assuming the ECs enclose a circular area, as illustrated in the inset. **(b)**, Evolution with V_{MG} of the FFT peaks f_o, f_{o+i}, and f_{o-i} normalized amplitudes I_o, I_{o+i}, and I_{o-i}, respectively, from the outer EC interference. This is the same data that is shown in Fig. 5.4d, replotted to match the range of (a). Vertical line indicates the approximate transition where the component f_{o+i} becomes dominant over f_o in the interference pattern. In this regime, the average edge channel separation d saturates at around 85 nm. Note that coupling between the ECs does not contribute significantly to the interference signal until the separation d becomes approximately 200 nm or less.

energy for a bare outer EC. This would correspond to the point where the inter-channel distance is comparable to the distance to the screening gates. We find that indeed this agrees with our data, since the system enters the strongly coupled limit when the average inter-channel separation approaches 85 nm, approximately twice the average distance to the top and bottom gates (Fig. B.11).

B.8 Robustness of the theoretical predictions

As discussed in ref. [171], when a single EC passes through the two constrictions, with weak backscattering at the constrictions, the interference phase seen at low temperatures and low source-drain voltage is given by $\theta = 2\pi Q + \theta_0, \mod 2\pi$, where Q is the total electron charge (in units e) in the region between the two scattering points (the expectation value of the charge on the interferometer in its ground state) and θ_0 is a constant for small variations in B, V_{PG}, and V_{MG}. The argument is essentially the same if the backscattering is not weak. The principal effect of stronger backscattering at the QPCs is to add a term to the energy E that favors integer values of the charge Q_1 and hence integer values of the total charge on the interferometer. This means that as the control parameters are varied continuously, the phase difference $\theta - \theta_0$ will undergo an additional modulation pulling it towards the nearest integer multiple of 2π. If we define θ_{b} as the value of the interferometer phase that would occur in the limit of weak backscattering, for the given value of the control parameters, then the actual value of θ should have the form $\theta = \theta_{\mathrm{b}} + \delta\theta$, where $\delta\theta$ is a periodic function of $\theta_{\mathrm{b}} - \theta_0$. In addition, in the presence of finite back scattering, interference contribution to the measured resistivity may no longer be a simple sinusoidal function of θ but can contain higher harmonics. The combination of these effects means that the interference current will remain a periodic function of θ_{b}, with period 2π, but the relative amplitudes of various harmonics may be modified. In the main text, it was argued that $\cos(\theta_{\mathrm{b}})$ should be a two-dimensional periodic function of B and the gate voltages, with frequencies expressed in terms of two non-collinear fundamental vectors in reciprocal parameter space. The

effect of finite backscattering at the QPCs will be to modify the amplitudes of the various Fourier components, but not to change their positions.

Using similar arguments, we may argue that measurement at finite temperature should not change the locations of the fundamental frequency vectors, but thermal fluctuations will reduce the Fourier amplitudes. In general, at high temperatures T, the amplitude of a given Fourier component will fall off, proportional to $e^{-T\varepsilon}$, where ε will be different for each Fourier component. At sufficiently high temperatures, therefore, only the one or two components with the largest values of ε will remain visible. The values of ε will depend on details of the system, but typically the Fourier components that are most prominent at $T = 0$ will be the ones that persist to highest temperatures.

For our system, in the case where there is only a single EC, as we find for bulk filling less than 2, the value of ε for the lowest Fourier mode is predicted to be $\varepsilon = \frac{hv}{2\pi^2 P}$, where v is the EC velocity and P is the perimeter of the interferometer path. For the case of two strongly coupled edge channels, the prediction is $\varepsilon = \frac{hv}{4\pi^2 P}$, where v is now the velocity of the fast charge mode. In both cases, the dominant effects come from thermal fluctuations $e\delta Q$ of the charge on the edge, whose energy cost is given by $\frac{(e\delta Q)^2}{2\gamma P}$, where γ is the capacitance per unit length of the edge. The velocity v is given by $v = \frac{\delta\sigma_{xy}}{\gamma}$, where $\delta\sigma_{xy}$ is the change in Hall conductance across the edge. Using our lithographically defined perimeter $P = 4.24$ μm and the velocity $v_{edge} = \frac{e\Delta V_D P}{h} = 1.46 \cdot 10^5$ m/s extracted from finite-bias dependence in the uncoupled case (Fig. B.4), we find $\varepsilon = 83.7$ mK, well above our estimated electron temperature.

C

Additional information for chapter 6

C.1 Device tuning details

We show an optical image of our device and schematics of the gating and measurement schemes in Fig. C.1. The 8 separated top graphite regions (Fig. C.1b) are separately tuned to electrostatically define each QPC as described later. We additionally employ a global bottom graphite gate, which can set an overall density offset at the QPC saddle points, where the top graphite has been etched away at a width

of $\sim$ 150 nm. The density offset is necessary to allow full transmission of edge channels at the QPCs while the side split-gates deplete electrons to maintain $\nu = 0$. Finally, we typically apply $+40$ V to the doped Si substrate to dope the graphene channel contacts through the $\sim$ 300 nm surface oxide and bottom hBN layers. This contact doping is necessary since we contact the channel at regions that extend outward from both the top and bottom graphite gates. In Fig. C.1c we show the arrangement of the gates from a top-down view and which contacts are used for a typical Hall measurement. We perform these calibration measurements within a single region of the device (tuned by V_{LG}) to get the most accurate measurements. Lastly, we show the typical configuration for all measurements of QPC and interferometer conductance reported in this work in Fig. C.1d.

Our process to tune the QPC transmissions for both $\nu = \frac{4}{3}$ and $\nu = \frac{1}{3}$ is shown in Fig. C.2. We begin (Fig. C.2a) by taking a large range parameter sweep of the left QPC split gate V_{LSG} vs. the global bottom-gate V_{BG} with the filling factor in the other regions of the device fixed to $\nu = \frac{4}{3}$ (this required sweeping V_{RSG}, V_{LG}, V_{MG}, V_{PG}, and V_{RG} simultaneously to maintain constant density as V_{BG} sweeps). We show a parameter sweep for the right QPC in Fig. C.2b. These scans enable us to distinguish the regions in which the split-gates are in $\nu = 0$ or below, hence reducing conductance to zero along a line controlled predominantly by $V_{\mathrm{LSG}}/V_{\mathrm{RSG}}$, from regions in which QPC saddle point transitions from zero to full conductance, controlled predominantly by V_{BG}. Informed by these scans, we then set V_{BG} close to the saddle point transition from $\nu = 1$ to $\nu = \frac{4}{3}$ (and set V_{RSG}, V_{LG}, V_{MG}, V_{PG}, and V_{RG} accordingly to $\nu = \frac{4}{3}$) and perform another parameter sweep now of V_{LSG} and V_{LBG} in Fig. C.2c. We show similar data for the right QPC in Fig. C.2d. QPC tunings shown in Fig. 1D were chosen from this data set such that the fractional edge mode could be directly tuned from full reflection to full transmission using only $V_{\mathrm{LBG/RBG}}$ while holding all other gates fixed. We similarly show QPC parameter scans for $\nu = \frac{1}{3}$ in Fig. C.2e/f and the resulting tunings chosen for the interference measurements performed in $\nu = \frac{1}{3}$ in Fig. C.2g.

The particular voltages (V_{BG}, V_{LSG}, V_{RSG}) are chosen so that a simple scan of $V_{\mathrm{LBG/RBG}}$ can tune the

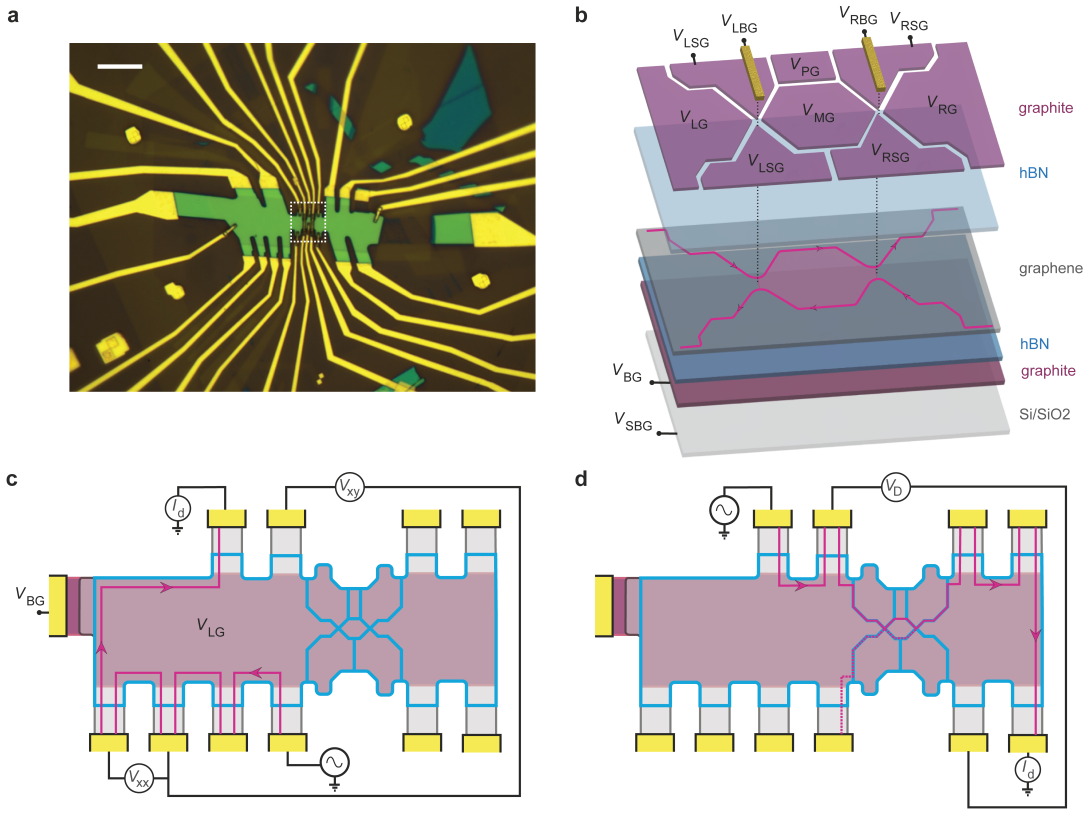


Figure C.1: Device contacts, gates, and measurement schemes. **(a)** Optical micrograph of the device measured in this paper. Scale bar: 10 µm. **(b)** Schematic of the gating structure at the center of the interferometer i.e. zoomed in section outline by the dashed white line in (a). The bridge gates tune QPC transmissions by gating through the etched QPC gaps in the graphite top-gate. **(c)** Measurement schematic for quantum Hall transport measurements as reported in Fig. 6.1b-c and Fig. 6.4b. Here the signal source, drain, and chirality are such that the transport is confined to the left top-gate region. Hence, we tune density using only V_{LG} and perform a standard Hall measurement to calibrate the expected filling factors for a given top-gate voltage. Blue lines indicate edges of the top-graphite gate and highlight the boundaries of the 8 separated regions. The purple region indicated the location of the graphite bottom-gate, while gray indicates the extent of the graphene layer. An ohmic contact to an extended graphite bottom-gate region allows an additional degree of freedom in tuning the QPCs by applying V_{BG}. Leads contact to the graphene channel in regions without a graphite top or bottom gate, necessitating the use of the silicon substrate to highly dope the region between the metal contact and channel. **(d)** Measurement schematic for QPC or interferometer conductance. Here the signal source and drain are on opposite sides of the QPCs, such that measurement of the 'diagonal' voltage drop V_{D} yields the conductance of the QPC or interferometer as $G = \frac{I_{\mathrm{d}}}{V_{\mathrm{D}}}$ where I_{d} is the measured drain current.

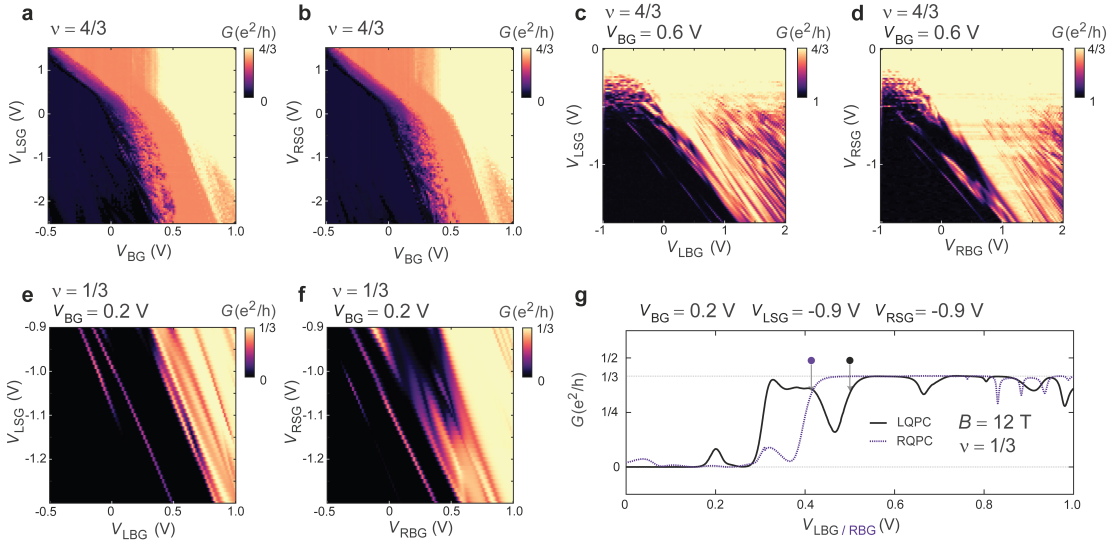


Figure C.2: QPC tuning details in $\nu = \frac{4}{3}$ and $\nu = \frac{1}{3}$. (a) Conductance of the left QPC as a function of left split-gate voltage V_{LSG} and back-gate voltage V_{BG} with the bulk of the device fixed at the center of the $\nu = \frac{4}{3}$ plateau. **(b)** Conductance of the right QPC as a function of right split-gate voltage V_{RSG} and back-gate voltage V_{BG} at the same filling in $\nu = \frac{4}{3}$. **(c)** Conductance of the left QPC with an appropriate back-gate voltage chosen as indicated to bias the QPC near an optimal operating point, which requires a larger density at the saddle-point to allow full transmission of both $\nu = \frac{4}{3}$ edge channels in this case. With this back-gate voltage, we can now tune the transmission of the inner fractional edge channel using only the left split-gate and the left bridge-gate V_{LBG}, as shown, which simplifies further tuning. The outer integer channel is fully transmitted over this parameter space while $V_{\text{RSG}} = V_{\text{RG}} = V_{\text{MG}} = V_{\text{PG}} = V_{\text{LG}} = -61.2$ mV and $V_{\text{RBG}} = 0$ V are held fixed. **(d)** Same type of plot as (c) but for the right QPC, where now $V_{\text{LSG}} = V_{\text{LG}} = V_{\text{MG}} = V_{\text{PG}} = V_{\text{RG}} = -61.2$ mV and $V_{\text{LBG}} = 0$ V are held fixed. **(e)** Conductance of the left QPC with the bulk of the device fixed within the $\nu = \frac{1}{3}$ plateau with $V_{\text{RSG}} = V_{\text{RG}} = V_{\text{MG}} = V_{\text{PG}} = V_{\text{LG}} = -81.6$ mV and $V_{\text{RBG}} = 0$ V at the indicated back-gate voltage. **(f)** Same type of plot as (e) for the right QPC, where $V_{\text{LSG}} = V_{\text{LG}} = V_{\text{MG}} = V_{\text{PG}} = V_{\text{RG}} = -81.6$ mV and $V_{\text{RBG}} = 0$ V. **(g)** Conductance through each QPC (left/right QPC tuned by $V_{\text{LBG}}/V_{\text{RBG}}$ respectively) with $\nu = 1/3$ set in the bulk and (V_{BG}, V_{LSG}, V_{RSG}) fixed as indicated. Black and purple dots indicate the left and right QPC tunings, $V_{\text{LBG}} = 0.50$ V and $V_{\text{RBG}} = 0.42$V, respectively, used to measure the data reported in the Chapter 6, corresponding to roughly 85% transmission (roughly 15% backscattering) of the $\nu = \frac{1}{3}$ edge channel at each QPC.

left/right QPC from full reflection to full transmission with a minimum of transmission resonances (i.e. sharp, reproducible conductance oscillations) in between. Resonances are believed to be caused by random quantum dot sites near the QPC saddle point, which can be pinned by disorder and which strongly affect the conductance as they tune through a resonant condition [195]. By tuning to a sharper confining potential, the effect of these resonances and edge state reconstruction can be reduced [233]. Hence, we generally attempt to increase the sharpness of the local confining potential at the QPCs by choosing gate voltages that increase the local electric field, practically meaning we tune to more negative split-gate voltages if possible.

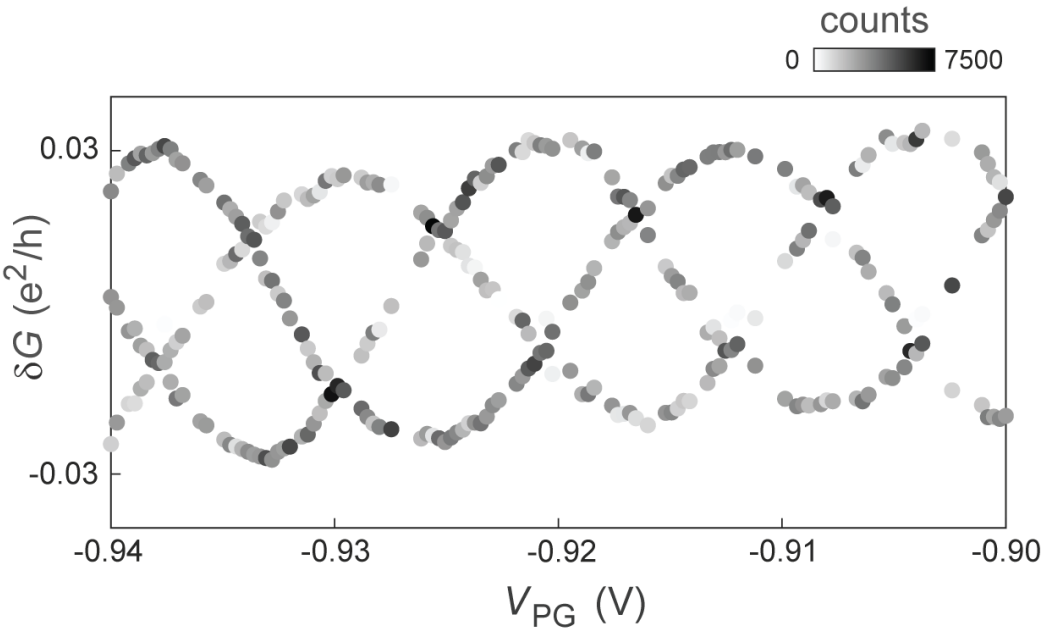


Figure C.3: Interwoven conductance branches extracted from static measurements in $\nu = \frac{1}{3}$. Equivalent measurement in $\nu = \frac{1}{3}$ to that shown in Chapter 6 for the fractional edge of $\nu = \frac{4}{3}$ (Fig. 6.1e). Again, three phase-shifted branches are revealed weighted according to their total counts recorded at a sampling rate of 20 samples/s over an ~ 8 minute time window for each V_{PG} voltage.

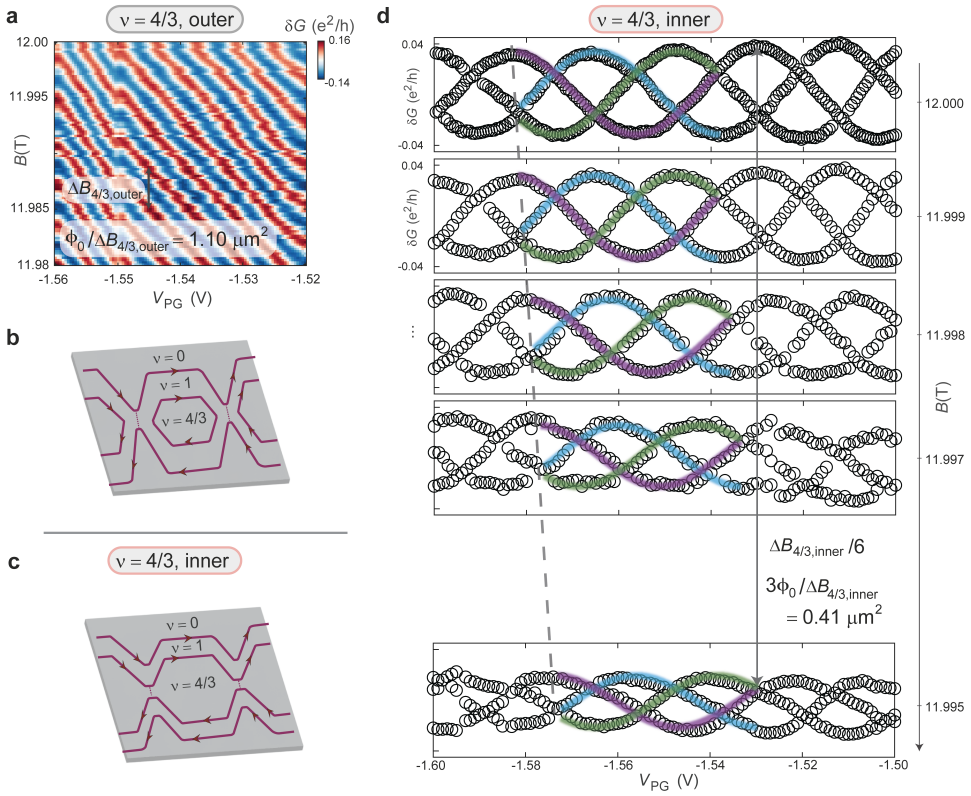


Figure C.4: Magnetic field dependence in $\nu = \frac{4}{3}$. Equivalent measurement in $\nu = \frac{4}{3}$ to that shown in Chapter 6 for $\nu = \frac{1}{3}$ (Fig. 6.2). Here, however, there is also an outer integer edge channel (i.e. $\nu = 1$) in addition to the inner fractional channel. Hence, we can tune to interfere either the outer integer or the inner fractional channel while holding the bulk filling $\nu = \frac{4}{3}$ fixed. **(a)** Magnetic field dependence of conductance oscillations with V_{PG} while the outer integer edge channel is partitioned at both QPCs. We observe a typical AB interference pattern with a magnetic field period yielding an enclosed area 1.1 μm^2 which matches the lithographic design. Notably, we do not observe telegraph noise, which enforces that interference of fractional quasiparticles is required to observe the phase shift due to anyon braiding. **(b)** Schematic showing interference of the outer integer edge channel, which flows at the boundary of the $\nu = 0$ and $\nu = 1$ incompressible regions. **(c)** Schematic showing interference of the inner fractional edge channel, which flows at the boundary of the $\nu = 1$ and $\nu = \frac{4}{3}$ incompressible regions. **(d)** Magnetic field dependent panels extracted using the method in Fig. 6.1e/f, where we plot the three mean conductance values for each V_{PG} without a weighting, for clarity. The interwoven sinusoidal oscillations trend in the same AB direction with decreasing magnetic field (downward in this plot) and exhibit a periodicity consistent with a $3\phi_0$ flux super-period. The flux period is consistent with the fractional edge enclosing an area of 0.41 μm^2, which is plausible since the area enclosed by the inner channel should be smaller than the area enclosed by the outer channel due to the width of the incompressible/compressible regions.

Since the interferometer cavity is defined using gates, the precise area depends on details of the confinement potential around the cavity and channel density. We attempted to keep the confining potential fixed between the tunings for $\nu = 1$ and $\nu = \frac{1}{3}$, which is possible since the main difference between the two is a small offset in density. At both tunings though, with $V_{\mathrm{BG}} = 0.2$ V and $V_{\mathrm{PG}} = V_{\mathrm{LSG}} = V_{\mathrm{LSG}} = -0.9$ V, we expect the confining potential (determined by the electric field between the top and bottom graphite gates) to be relatively less steep than at the $\nu = \frac{4}{3}$ tuning ($V_{\mathrm{BG}} = 0.6$ V and $V_{\mathrm{PG}} = V_{\mathrm{LSG}} = V_{\mathrm{RSG}} = -1.4$ V). Indeed, the area ≈ 0.8 $\mu\mathrm{m}^2$ extracted for both $\nu = 1$ and $\nu = \frac{1}{3}$ is consistent with a uniform shrinkage by 100 nm inside of the 1.1 $\mu\mathrm{m}^2$ area middle gate.

C.2 Algorithm used for determining RTN switching events

To determine when a RTN switching event between conductance plateaus occurs, we use the following algorithm: The derivative of the raw diagonal conductance data is taken and then smoothed with a Gaussian-weighted average over a window of 30 data points. The smoothing is performed in order to reduce the background noise to allow for fitting of faster switching events to ensure accurate and consistent sampling across scans. Then, all peaks above a threshold magnitude are found and recorded. The threshold value is set to be $\sqrt{2}$ times the peak-to-peak noise floor of the raw conductance signal's derivative, which is an arbitrary yet consistent decision across all data. The background noise appears to be sensitive to temperature and not the value of V_{MG} (i.e. location within the filling factor plateau). Consequently, the threshold value is identical for the data presented in Fig. 6.4c and is scaled for that shown in Fig. 6.5c. The final output of the algorithm is cross-checked with the raw conductance data as shown in Fig. C.5 ensuring accuracy and consistency in picking out switching events and disregarding noise spikes.

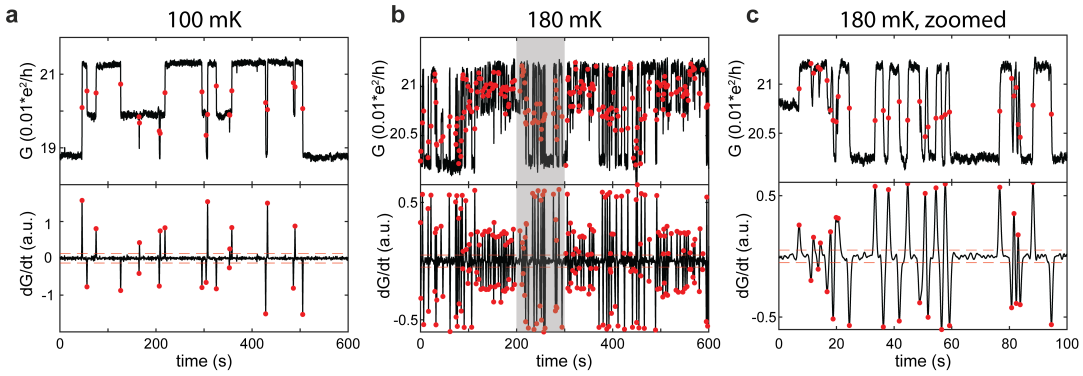


Figure C.5: Branch switching detection algorithm. (a) Raw conductance data and derivative of the RTN signal taken within the middle of the $\nu = \frac{1}{3}$ plateau at $T = 100$ mK, $B = 12$ T. The output of the switch detection algorithm is indicated by the red dots. The red dashed line on the derivative signal shows the peak finding threshold value ($\sqrt{2}$ times the derivative's peak-to-peak noise floor). **(b)** RTN signal taken at the same device configuration but at 180 mK. Grey box indicates zoom window shown in **(c)**.

C.3 Phase fitting and uncertainty

To find the magnitude of the phase jumps between branches, we employ the following procedure. Starting with the repeated plunger gate sweep measurements shown in Fig. 6.2e, for a given magnetic field we combine the data points of all 100 sweeps into a single data set as shown in the scatter plot of Fig. 6.3a. To find the three closest sinusoids that describe each branch, we minimize a function that is the sum of the shortest distance squared of every data point to three candidate sinusoidal functions, $\min(y_i - \sin(f_{\{1,2,3\}}x_i + \phi_{\{1,2,3\}}))^2$. The optimization of the parameters of each of the sinusoids is performed via MatLab's Optimization toolbox, which we provide with a large array of initial conditions that are iterated through the optimization procedure. An example of the final output is shown as the dashed colored lines in Fig. 6.3a, and the phases of the branches of each of the seven data sets are shown in Fig. 6.3b. From the slope of how any one of these three branch phases evolve with field, we can extract the area associated with the Aharonov-Bohm phase. All three give the same value of $0.83 \pm 0.04\ \mu\text{m}^2$.

The differences between any two of the three branch phases for a given data set fully defines the possible braiding phases from one branch to another, as the third phase difference is constrained to be $2\pi - \Delta\phi_{1,2} - \Delta\phi_{2,3}$. These phase differences are plotted for the seven data sets shown in Fig. 6.2e in Fig. 6.3c. The average and standard deviation is $2\pi(0.3336 \pm 0.0051)$, or $120.1^\circ \pm 1.8^\circ$.

To determine the quality of this fitting procedure, we sort each data point by the closest fitted sinusoid (the same as determined by the previous least-squares fit) by calculating the new least-squares distance $(y_i - \sin(f_{\{1,2,3\}}x_i + \phi_{\{1,2,3\}}))^2$. The results of this sorting for the 12 T data set are shown in the bottom plot of Fig. 6.3a. By writing $y_i = A\sin(fx_i + \phi) = A\cos(\phi)\sin(fx_i) + A\sin(\phi)\cos(fx_i)$, we then perform a bilinear least-squares regression on each of these three pairs of data and sinusoidal fits to find the standard deviation of each function's phase, which are smaller than the data points shown in Fig. 6.3b. The error bars shown in Fig. 6.3c are then the sum of the standard deviations of the two compared individual phases, and are close to the value of the standard deviation of the phase differences (shown as the grey bar), supporting the accuracy of the fitting method.

We attribute the accuracy of the extracted anyon braiding phase to the fact that this set of 100 plunger gate sweeps is comprised of many hundreds of individual phase jump events, giving a large statistical ensemble. While the dwell-type of measurement exhibited in Figs. 6.1f, C.3, and C.4 offer an advantage in analyzing characteristics of the RTN itself, they contain significantly fewer phase jump events compared to the sweep-type of measurement in Figs. 6.2 and 6.3. Also, since each "slice" of the sinusoids in the plunger gate x-axis is extracted sequentially for the dwell-type measurement over nearly 10 minutes each, detunings and drifts of the interference signal (caused by a temperature drift, field drift, or QPC detuning from gate drifts for example) will distort the shape of the sinusoids. This explains why the traces in Figs. 6.1f, C.3, and C.4 look significantly less uniform than Figs. 6.2 and 6.3, since for these sweep-type measurements each sweep takes just half a minute, and the entire set of 100 sweeps takes less time than it takes to acquire a few points of the dwell-type measurement.

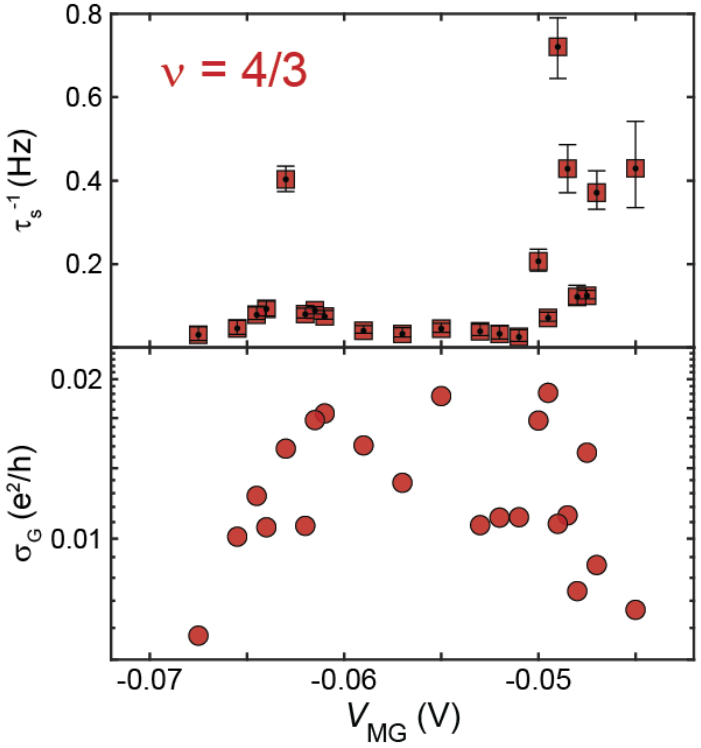


Figure C.6: Plateau analysis of RTN for $\nu = \frac{4}{3}$. Top: Average branch switching rate along the $\nu = \frac{4}{3}$ plateau, analogous to Fig. 6.4c which shows $\nu = \frac{1}{3}$. **Bottom:** Standard deviation σ_G of conductance, analogous to Fig. 6.4d.

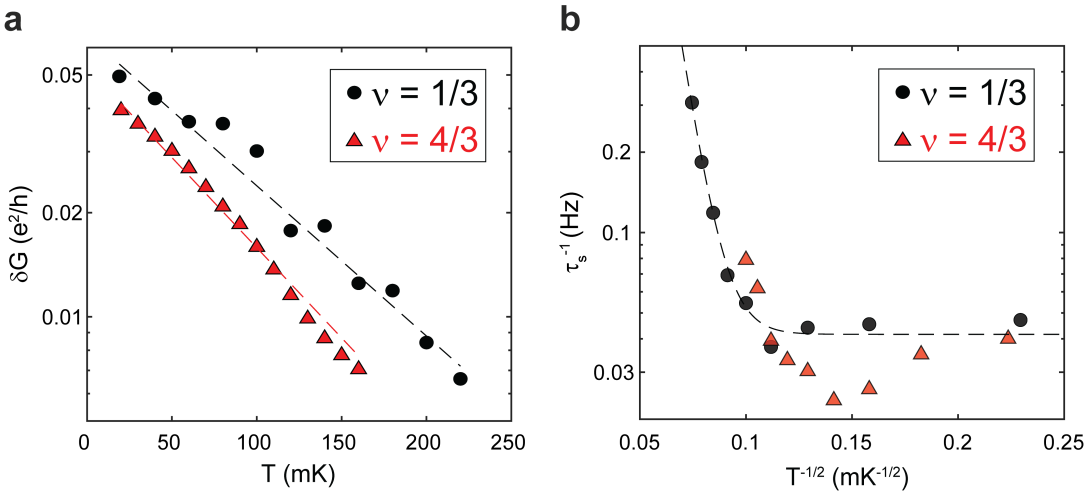


Figure C.7: $\nu = \frac{4}{3}$ **RTN temperature scaling. (a)** Oscillation visibility extracted from V_{PG} sweep measurements for $\nu = \frac{1}{3}$ (same data shown in Fig. 6.5b) and $\nu = \frac{4}{3}$, both taken with V_{MG} set to be in the middle of each filling factor's respective plateau. **(b)** Average switching rate for each filling factor ($\nu = \frac{1}{3}$ data copied from Fig. 6.5). The $\nu = \frac{4}{3}$ data is only taken up to 100 mK due to the noise floor overwhelming the separation between two of the three conductance plateaus.

References

[1] P. W. Anderson, "More Is Different," *Science*, vol. 177, pp. 393–396, Aug. 1972.

[2] X.-G. Wen, *Quantum Field Theory of Many-body Systems: From the Origin of Sound to an Origin of Light and Electrons*. Oxford Graduate Texts, Oxford, New York: Oxford University Press, Oct. 2007.

[3] K. v. Klitzing, G. Dorda, and M. Pepper, "New Method for High-Accuracy Determination of the Fine-Structure Constant Based on Quantized Hall Resistance," *Physical Review Letters*, vol. 45, pp. 494–497, Aug. 1980.

[4] K. von Klitzing, T. Chakraborty, P. Kim, V. Madhavan, X. Dai, J. McIver, Y. Tokura, L. Savary, D. Smirnova, A. M. Rey, C. Felser, J. Gooth, and X. Qi, "40 years of the quantum Hall effect," *Nature Reviews Physics*, vol. 2, pp. 397–401, Aug. 2020.

[5] R. B. Laughlin, "Quantized Hall conductivity in two dimensions," *Physical Review B*, vol. 23, pp. 5632–5633, May 1981.

[6] H. Aoki and T. Ando, "Effect of localization on the hall conductivity in the two-dimensional system in strong magnetic fields," *Solid State Communications*, vol. 38, pp. 1079–1082, June 1981.

[7] B. I. Halperin, "Quantized Hall conductance, current-carrying edge states, and the existence of extended states in a two-dimensional disordered potential," *Physical Review B*, vol. 25, pp. 2185–2190, Feb. 1982.

[8] P. Streda, "Theory of quantised Hall conductivity in two dimensions," *Journal of Physics C: Solid State Physics*, vol. 15, p. L717, Aug. 1982.

[9] D. J. Thouless, M. Kohmoto, M. P. Nightingale, and M. den Nijs, "Quantized Hall Conductance in a Two-Dimensional Periodic Potential," *Physical Review Letters*, vol. 49, pp. 405–408, Aug. 1982.

[10] M. Büttiker, "Absence of backscattering in the quantum Hall effect in multiprobe conductors," *Physical Review B*, vol. 38, pp. 9375–9389, Nov. 1988.

[11] D. B. Chklovskii, B. I. Shklovskii, and L. I. Glazman, "Electrostatics of edge channels," *Physical Review B*, vol. 46, pp. 4026–4034, Aug. 1992.

[12] R. J. Haug, "Edge-state transport and its experimental consequences in high magnetic fields," *Semiconductor Science and Technology*, vol. 8, pp. 131–153, Feb. 1993.

[13] S. Datta, *Electronic Transport in Mesoscopic Systems*. Cambridge Studies in Semiconductor Physics and Microelectronic Engineering, Cambridge: Cambridge University Press, 1995.

[14] D. C. Tsui, H. L. Stormer, and A. C. Gossard, "Two-Dimensional Magnetotransport in the Extreme Quantum Limit," *Physical Review Letters*, vol. 48, pp. 1559–1562, May 1982.

[15] R. B. Laughlin, "Anomalous Quantum Hall Effect: An Incompressible Quantum Fluid with Fractionally Charged Excitations," *Physical Review Letters*, vol. 50, pp. 1395–1398, May 1983.

[16] R. B. Laughlin, "Nobel Lecture: Fractional quantization," *Reviews of Modern Physics*, vol. 71, pp. 863–874, July 1999.

[17] H. L. Stormer, D. C. Tsui, and A. C. Gossard, "The fractional quantum Hall effect," *Reviews of Modern Physics*, vol. 71, pp. S298–S305, Mar. 1999.

[18] V. J. Goldman and B. Su, "Resonant Tunneling in the Quantum Hall Regime: Measurement of Fractional Charge," *Science*, vol. 267, pp. 1010–1012, Feb. 1995.

[19] C. L. Kane and M. P. A. Fisher, "Nonequilibrium noise and fractional charge in the quantum Hall effect," *Physical Review Letters*, vol. 72, pp. 724–727, Jan. 1994.

[20] R. de-Picciotto, M. Reznikov, M. Heiblum, V. Umansky, G. Bunin, and D. Mahalu, "Direct observation of a fractional charge," *Nature*, vol. 389, pp. 162–164, Sept. 1997.

[21] L. Saminadayar, D. C. Glattli, Y. Jin, and B. Etienne, "Observation of the $e/3$ fractionally charged laughlin quasiparticle," *Physical Review Letters*, vol. 79, pp. 2526–2529, Sept. 1997.

[22] M. Reznikov, R. de Picciotto, T. G. Griffiths, M. Heiblum, and V. Umansky, "Observation of quasiparticles with one-fifth of an electron's charge," *Nature*, vol. 399, pp. 238–241, May 1999.

[23] J. Martin, S. Ilani, B. Verdene, J. Smet, V. Umansky, D. Mahalu, D. Schuh, G. Abstreiter, and A. Yacoby, "Localization of Fractionally Charged Quasi-Particles," *Science*, vol. 305, pp. 980–983, Aug. 2004.

[24] M. Kapfer, P. Roulleau, M. Santin, I. Farrer, D. A. Ritchie, and D. C. Glattli, "A Josephson relation for fractionally charged anyons," *Science*, vol. 363, pp. 846–849, Feb. 2019.

[25] R. Bisognin, H. Bartolomei, M. Kumar, I. Safi, J.-M. Berroir, E. Bocquillon, B. Plaçais, A. Cavanna, U. Gennser, Y. Jin, and G. Fève, "Microwave photons emitted by fractionally charged quasiparticles," *Nature Communications*, vol. 10, p. 1708, Apr. 2019.

[26] B. I. Halperin, "Statistics of Quasiparticles and the Hierarchy of Fractional Quantized Hall States," *Physical Review Letters*, vol. 52, pp. 1583–1586, Apr. 1984.

[27] D. Arovas, J. R. Schrieffer, and F. Wilczek, "Fractional Statistics and the Quantum Hall Effect," *Physical Review Letters*, vol. 53, pp. 722–723, Aug. 1984.

[28] J. M. Leinaas and J. Myrheim, "On the theory of identical particles," *Nuovo Cimento B Serie*, vol. 37, pp. 1–23, Jan. 1977.

[29] F. Wilczek, "Quantum Mechanics of Fractional-Spin Particles," *Physical Review Letters*, vol. 49, pp. 957–959, Oct. 1982.

[30] A. Kitaev, "Anyons in an exactly solved model and beyond," *Annals of Physics*, vol. 321, pp. 2–111, Jan. 2006.

[31] C. Nayak, S. H. Simon, A. Stern, M. Freedman, and S. Das Sarma, "Non-Abelian anyons and topological quantum computation," *Reviews of Modern Physics*, vol. 80, pp. 1083–1159, Sept. 2008.

[32] A. Stern and N. H. Lindner, "Topological Quantum Computation—From Basic Concepts to First Experiments," *Science*, vol. 339, pp. 1179–1184, Mar. 2013.

[33] S. D. Sarma, M. Freedman, and C. Nayak, "Majorana zero modes and topological quantum computation," *npj Quantum Information*, vol. 1, pp. 1–13, Oct. 2015.

[34] A. Yazdani, F. von Oppen, B. I. Halperin, and A. Yacoby, "Hunting for Majoranas," *Science*, vol. 380, p. eade0850, June 2023.

[35] M. M. Vopson, "Estimation of the information contained in the visible matter of the universe," *AIP Advances*, vol. 11, p. 105317, Oct. 2021.

[36] J. S. Townsend, *A Modern Approach to Quantum Mechanics*. Mill Valley, California: University Science Books, second edition. ed., 2012.

[37] J. Napolitano and J. J. Sakurai, "Modern Quantum Mechanics," in *Modern Quantum Mechanics*, United Kingdom: Cambridge University Press, 2017.

[38] A. Comtet, T. Jolicœur, S. Ouvry, and F. David, eds., *Aspects Topologiques de La Physique En Basse Dimension. Topological Aspects of Low Dimensional Systems*, vol. 69 of *Les Houches - Ecole d'Ete de Physique Theorique*. Berlin, Heidelberg: Springer, 1999.

[39] T. Ando, A. B. Fowler, and F. Stern, "Electronic properties of two-dimensional systems," *Reviews of Modern Physics*, vol. 54, pp. 437–672, Apr. 1982.

[40] Y. J. Chung, K. A. Villegas Rosales, K. W. Baldwin, P. T. Madathil, K. W. West, M. Shayegan, and L. N. Pfeiffer, "Ultra-high-quality two-dimensional electron systems," *Nature Materials*, vol. 20, pp. 632–637, May 2021.

[41] D. Kamburov, K. W. Baldwin, K. W. West, M. Shayegan, and L. N. Pfeiffer, "Interplay between quantum well width and interface roughness for electron transport mobility in GaAs quantum wells," *Applied Physics Letters*, vol. 109, p. 232105, Dec. 2016.

[42] K. A. Villegas Rosales, P. T. Madathil, Y. J. Chung, L. N. Pfeiffer, K. W. West, K. W. Baldwin, and M. Shayegan, "Fractional Quantum Hall Effect Energy Gaps: Role of Electron Layer Thickness," *Physical Review Letters*, vol. 127, p. 056801, July 2021.

[43] P. Rickhaus, M.-H. Liu, M. Kurpas, A. Kurzmann, Y. Lee, H. Overweg, M. Eich, R. Pisoni, T. Taniguchi, K. Watanabe, K. Richter, K. Ensslin, and T. Ihn, "The electronic thickness of graphene," *Science Advances*, vol. 6, p. eaay8409, Mar. 2020.

[44] P. C. Hohenberg, "Existence of Long-Range Order in One and Two Dimensions," *Physical Review*, vol. 158, pp. 383–386, June 1967.

[45] N. D. Mermin and H. Wagner, "Absence of Ferromagnetism or Antiferromagnetism in One- or Two-Dimensional Isotropic Heisenberg Models," *Physical Review Letters*, vol. 17, pp. 1133–1136, Nov. 1966.

[46] B. I. Halperin, "On the Hohenberg–Mermin–Wagner Theorem and Its Limitations," *Journal of Statistical Physics*, vol. 175, pp. 521–529, May 2019.

[47] N. D. Mermin, "Crystalline Order in Two Dimensions," *Physical Review*, vol. 176, pp. 250–254, Dec. 1968.

[48] K. S. Novoselov, A. K. Geim, S. V. Morozov, D. Jiang, Y. Zhang, S. V. Dubonos, I. V. Grigorieva, and A. A. Firsov, "Electric Field Effect in Atomically Thin Carbon Films," *Science*, vol. 306, pp. 666–669, Oct. 2004.

[49] K. S. Novoselov, A. K. Geim, S. V. Morozov, D. Jiang, M. I. Katsnelson, I. V. Grigorieva, S. V. Dubonos, and A. A. Firsov, "Two-dimensional gas of massless Dirac fermions in graphene," *Nature*, vol. 438, pp. 197–200, Nov. 2005.

[50] Y. Zhang, Y.-W. Tan, H. L. Stormer, and P. Kim, "Experimental observation of the quantum Hall effect and Berry's phase in graphene," *Nature*, vol. 438, pp. 201–204, Nov. 2005.

[51] P. R. Wallace, "The Band Theory of Graphite," *Physical Review*, vol. 71, pp. 622–634, May 1947.

[52] A. H. Castro Neto, F. Guinea, N. M. R. Peres, K. S. Novoselov, and A. K. Geim, "The electronic properties of graphene," *Reviews of Modern Physics*, vol. 81, pp. 109–162, Jan. 2009.

[53] E. McCann, "Electronic Properties of Monolayer and Bilayer Graphene," in *Graphene Nanoelectronics*, pp. 237–275, Springer, Berlin, Heidelberg, 2011.

[54] M. O. Goerbig, "Electronic properties of graphene in a strong magnetic field," *Reviews of Modern Physics*, vol. 83, pp. 1193–1243, Nov. 2011.

[55] N. W. Ashcroft, *Solid State Physics*. New York: Holt, Rinehart and Winston, 1976.

[56] T. Ihn, *Semiconductor Nanostructures: Quantum States and Electronic Transport*. Oxford, New York: Oxford University Press, Feb. 2010.

[57] S. Konschuh, M. Gmitra, and J. Fabian, "Tight-binding theory of the spin-orbit coupling in graphene," *Physical Review B*, vol. 82, p. 245412, Dec. 2010.

[58] P. A. M. Dirac, "The quantum theory of the electron," *Proceedings of the Royal Society of London. Series A, Containing papers of a mathematical and physical character*, vol. 117, no. 778, pp. 610–624, 1928.

[59] A. F. Young and P. Kim, "Quantum interference and Klein tunnelling in graphene heterojunctions," *Nature Physics*, vol. 5, pp. 222–226, Mar. 2009.

[60] A. Schmitt, P. Vallet, D. Mele, M. Rosticher, T. Taniguchi, K. Watanabe, E. Bocquillon, G. Fève, J. M. Berroir, C. Voisin, J. Cayssol, M. O. Goerbig, J. Troost, E. Baudin, and B. Plaçais, "Mesoscopic Klein-Schwinger effect in graphene," *Nature Physics*, vol. 19, pp. 830–835, June 2023.

[61] F. D. M. Haldane, "Nobel Lecture: Topological quantum matter," *Reviews of Modern Physics*, vol. 89, p. 040502, Oct. 2017.

[62] D. Tong, "Lectures on the Quantum Hall Effect," Sept. 2016.

[63] J. K. Jain, *Composite Fermions*. Cambridge: Cambridge University Press, 2007.

[64] B. I. Halperin and J. K. Jain, *Fractional Quantum Hall Effects: New Developments*. Singapore ; Hackensack, NJ: World Scientific Publishing Co. Pte. Ltd., 2020.

[65] M. H. Johnson and B. A. Lippmann, "Motion in a Constant Magnetic Field," *Physical Review*, vol. 76, pp. 828–832, Sept. 1949.

[66] W. Kohn, "Theory of Bloch Electrons in a Magnetic Field: The Effective Hamiltonian," *Physical Review*, vol. 115, pp. 1460–1478, Sept. 1959.

[67] Y. Kim, A. C. Balram, T. Taniguchi, K. Watanabe, J. K. Jain, and J. H. Smet, "Even denominator fractional quantum Hall states in higher Landau levels of graphene," *Nature Physics*, vol. 15, pp. 154–158, Feb. 2019.

[68] C. R. Dean, A. F. Young, P. Cadden-Zimansky, L. Wang, H. Ren, K. Watanabe, T. Taniguchi, P. Kim, J. Hone, and K. L. Shepard, "Multicomponent fractional quantum Hall effect in graphene," *Nature Physics*, vol. 7, pp. 693–696, Sept. 2011.

[69] B. E. Feldman, B. Krauss, J. H. Smet, and A. Yacoby, "Unconventional Sequence of Fractional Quantum Hall States in Suspended Graphene," *Science*, vol. 337, pp. 1196–1199, Sept. 2012.

[70] B. E. Feldman, A. J. Levin, B. Krauss, D. A. Abanin, B. I. Halperin, J. H. Smet, and A. Yacoby, "Fractional Quantum Hall Phase Transitions and Four-Flux States in Graphene," *Physical Review Letters*, vol. 111, p. 076802, Aug. 2013.

[71] F. Amet, A. J. Bestwick, J. R. Williams, L. Balicas, K. Watanabe, T. Taniguchi, and D. Goldhaber-Gordon, "Composite fermions and broken symmetries in graphene," *Nature Communications*, vol. 6, p. 5838, Jan. 2015.

[72] C. Tőke, P. E. Lammert, V. H. Crespi, and J. K. Jain, "Fractional quantum Hall effect in graphene," *Physical Review B*, vol. 74, p. 235417, Dec. 2006.

[73] D. A. Abanin, B. E. Feldman, A. Yacoby, and B. I. Halperin, "Fractional and integer quantum Hall effects in the zeroth Landau level in graphene," *Physical Review B*, vol. 88, p. 115407, Sept. 2013.

[74] G. Li and E. Y. Andrei, "Observation of Landau levels of Dirac fermions in graphite," *Nature Physics*, vol. 3, pp. 623–627, Sept. 2007.

[75] L.-J. Yin, K.-K. Bai, W.-X. Wang, S.-Y. Li, Y. Zhang, and L. He, "Landau quantization of Dirac fermions in graphene and its multilayers," *Frontiers of Physics*, vol. 12, p. 127208, Apr. 2017.

[76] K. S. Novoselov, Z. Jiang, Y. Zhang, S. V. Morozov, H. L. Stormer, U. Zeitler, J. C. Maan, G. S. Boebinger, P. Kim, and A. K. Geim, "Room-Temperature Quantum Hall Effect in Graphene," *Science*, vol. 315, pp. 1379–1379, Mar. 2007.

[77] S. A. Trugman, "Localization, percolation, and the quantum Hall effect," *Physical Review B*, vol. 27, pp. 7539–7546, June 1983.

[78] K.-S. Kim and S. A. Kivelson, "The quantum Hall effect in the absence of disorder," *npj Quantum Materials*, vol. 6, pp. 1–3, Mar. 2021.

[79] S. Ilani, J. Martin, E. Teitelbaum, J. H. Smet, D. Mahalu, V. Umansky, and A. Yacoby, "The microscopic nature of localization in the quantum Hall effect," *Nature*, vol. 427, pp. 328–332, Jan. 2004.

[80] R. E. Prange, "Quantized Hall resistance and the measurement of the fine-structure constant," *Physical Review B*, vol. 23, pp. 4802–4805, May 1981.

[81] K. Nomura and A. H. MacDonald, "Quantum Hall Ferromagnetism in Graphene," *Physical Review Letters*, vol. 96, p. 256602, June 2006.

[82] A. F. Young, C. R. Dean, L. Wang, H. Ren, P. Cadden-Zimansky, K. Watanabe, T. Taniguchi, J. Hone, K. L. Shepard, and P. Kim, "Spin and valley quantum Hall ferromagnetism in graphene," *Nature Physics*, vol. 8, pp. 550–556, July 2012.

[83] J. G. Checkelsky, L. Li, and N. P. Ong, "Zero-Energy State in Graphene in a High Magnetic Field," *Physical Review Letters*, vol. 100, p. 206801, May 2008.

[84] A. F. Young, J. D. Sanchez-Yamagishi, B. Hunt, S. H. Choi, K. Watanabe, T. Taniguchi, R. C. Ashoori, and P. Jarillo-Herrero, "Tunable symmetry breaking and helical edge transport in a graphene quantum spin Hall state," *Nature*, vol. 505, pp. 528–532, Jan. 2014.

[85] D. A. Abanin, P. A. Lee, and L. S. Levitov, "Spin-Filtered Edge States and Quantum Hall Effect in Graphene," *Physical Review Letters*, vol. 96, p. 176803, May 2006.

[86] H. A. Fertig and L. Brey, "Luttinger Liquid at the Edge of Undoped Graphene in a Strong Magnetic Field," *Physical Review Letters*, vol. 97, p. 116805, Sept. 2006.

[87] M. Kharitonov, S. Juergens, and B. Trauzettel, "Interplay of topology and interactions in quantum Hall topological insulators: U(1) symmetry, tunable Luttinger liquid, and interaction-induced phase transitions," *Physical Review B*, vol. 94, p. 035146, July 2016.

[88] L. Veyrat, C. Déprez, A. Coissard, X. Li, F. Gay, K. Watanabe, T. Taniguchi, Z. Han, B. A. Piot, H. Sellier, and B. Sacépé, "Helical quantum Hall phase in graphene on $SrTiO_3$," *Science*, vol. 367, pp. 781–786, Feb. 2020.

[89] X. Liu, G. Farahi, C.-L. Chiu, Z. Papic, K. Watanabe, T. Taniguchi, M. P. Zaletel, and A. Yazdani, "Visualizing broken symmetry and topological defects in a quantum Hall ferromagnet," *Science*, vol. 375, pp. 321–326, Jan. 2022.

[90] A. Coissard, D. Wander, H. Vignaud, A. G. Grushin, C. Repellin, K. Watanabe, T. Taniguchi, F. Gay, C. B. Winkelmann, H. Courtois, H. Sellier, and B. Sacépé, "Imaging tunable quantum Hall broken-symmetry orders in graphene," *Nature*, vol. 605, pp. 51–56, May 2022.

[91] R. Delagrange, M. Garg, G. Le Breton, A. Zhang, Q. Dong, Y. Jin, K. Watanabe, T. Taniguchi, P. Roulleau, O. Maillet, P. Roche, and F. D. Parmentier, "Vanishing bulk heat flow in the $\nu = 0$ quantum Hall ferromagnet in monolayer graphene," *Nature Physics*, vol. 20, pp. 1927–1932, Dec. 2024.

[92] A. H. MacDonald and P. Středa, "Quantized Hall effect and edge currents," *Physical Review B*, vol. 29, pp. 1616–1619, Feb. 1984.

[93] D. S. Wei, T. van der Sar, S. H. Lee, K. Watanabe, T. Taniguchi, B. I. Halperin, and A. Yacoby, "Electrical generation and detection of spin waves in a quantum Hall ferromagnet," *Science*, vol. 362, pp. 229–233, Oct. 2018.

[94] A. Assouline, M. Jo, P. Brasseur, K. Watanabe, T. Taniguchi, T. Jolicoeur, D. C. Glattli, N. Kumada, P. Roche, F. D. Parmentier, and P. Roulleau, "Excitonic nature of magnons in a quantum Hall ferromagnet," *Nature Physics*, vol. 17, pp. 1369–1374, Dec. 2021.

[95] A. T. Pierce, Y. Xie, S. H. Lee, P. R. Forrester, D. S. Wei, K. Watanabe, T. Taniguchi, B. I. Halperin, and A. Yacoby, "Thermodynamics of free and bound magnons in graphene," *Nature Physics*, vol. 18, pp. 37–41, Jan. 2022.

[96] R. Kumar, S. K. Srivastav, U. Roy, J. Park, C. Spånslätt, K. Watanabe, T. Taniguchi, Y. Gefen, A. D. Mirlin, and A. Das, "Electrical noise spectroscopy of magnons in a quantum Hall ferromagnet," *Nature Communications*, vol. 15, p. 4998, June 2024.

[97] D. B. Chklovskii, K. A. Matveev, and B. I. Shklovskii, "Ballistic conductance of interacting electrons in the quantum Hall regime," *Physical Review B*, vol. 47, pp. 12605–12617, May 1993.

[98] S. Kim, J. Schwenk, D. Walkup, Y. Zeng, F. Ghahari, S. T. Le, M. R. Slot, J. Berwanger, S. R. Blankenship, K. Watanabe, T. Taniguchi, F. J. Giessibl, N. B. Zhitenev, C. R. Dean, and J. A. Stroscio, "Edge channels of broken-symmetry quantum Hall states in graphene visualized by atomic force microscopy," *Nature Communications*, vol. 12, p. 2852, May 2021.

[99] A. Marguerite, J. Birkbeck, A. Aharon-Steinberg, D. Halbertal, K. Bagani, I. Marcus, Y. Myasoedov, A. K. Geim, D. J. Perello, and E. Zeldov, "Imaging work and dissipation in the quantum Hall state in graphene," *Nature*, vol. 575, pp. 628–633, Nov. 2019.

[100] A. Uri, Y. Kim, K. Bagani, C. K. Lewandowski, S. Grover, N. Auerbach, E. O. Lachman, Y. Myasoedov, T. Taniguchi, K. Watanabe, J. Smet, and E. Zeldov, "Nanoscale imaging of equilibrium quantum Hall edge currents and of the magnetic monopole response in graphene," *Nature Physics*, vol. 16, pp. 164–170, Feb. 2020.

[101] A. Coissard, A. G. Grushin, C. Repellin, L. Veyrat, K. Watanabe, T. Taniguchi, F. Gay, H. Courtois, H. Sellier, and B. Sacépé, "Absence of edge reconstruction for quantum Hall edge channels in graphene devices," *Science Advances*, vol. 9, p. eadf7220, May 2023.

[102] U. Klaß, W. Dietsche, K. von Klitzing, and K. Ploog, "Imaging of the dissipation in quantum-Hall-effect experiments," *Zeitschrift für Physik B Condensed Matter*, vol. 82, pp. 351–354, Oct. 1991.

[103] T. H. Hansson, M. Hermanns, S. H. Simon, and S. F. Viefers, "Quantum Hall physics: Hierarchies and conformal field theory techniques," *Reviews of Modern Physics*, vol. 89, p. 025005, May 2017.

[104] D. E. Feldman and B. I. Halperin, "Fractional charge and fractional statistics in the quantum Hall effects," *Reports on Progress in Physics*, vol. 84, p. 076501, June 2021.

[105] M. Greiter and F. Wilczek, "Fractional Statistics," *Annual Review of Condensed Matter Physics*, vol. 15, pp. 131–157, Mar. 2024.

[106] F. D. M. Haldane, "Fractional Quantization of the Hall Effect: A Hierarchy of Incompressible Quantum Fluid States," *Physical Review Letters*, vol. 51, pp. 605–608, Aug. 1983.

[107] M. V. Berry, "Quantal Phase Factors Accompanying Adiabatic Changes," *Proceedings of the Royal Society of London. Series A, Mathematical and physical sciences*, vol. 392, no. 1802, pp. 45–57, 1984.

[108] F. Wilczek and A. Shapere, *Geometric Phases in Physics*. Advanced Series in Mathematical Physics ; v. 5, Singapore ; [Teaneck], N.J.: World Scientific, 1989.

[109] N. Read and S. Das Sarma, "Clarification of braiding statistics in Fabry–Perot interferometry," *Nature Physics*, vol. 20, pp. 381–382, Mar. 2024.

[110] Y. Aharonov and D. Bohm, "Significance of Electromagnetic Potentials in the Quantum Theory," *Physical Review*, vol. 115, pp. 485–491, Aug. 1959.

[111] Y. Aharonov and D. Bohm, "Further Considerations on Electromagnetic Potentials in the Quantum Theory," *Physical Review*, vol. 123, pp. 1511–1524, Aug. 1961.

[112] J. K. Jain, "Composite-fermion approach for the fractional quantum Hall effect," *Physical Review Letters*, vol. 63, pp. 199–202, July 1989.

[113] F. Ghahari, Y. Zhao, P. Cadden-Zimansky, K. Bolotin, and P. Kim, "Measurement of the $\ensuremath{\nu}=1/3$ Fractional Quantum Hall Energy Gap in Suspended Graphene," *Physical Review Letters*, vol. 106, p. 046801, Jan. 2011.

[114] H. Polshyn, H. Zhou, E. M. Spanton, T. Taniguchi, K. Watanabe, and A. F. Young, "Quantitative Transport Measurements of Fractional Quantum Hall Energy Gaps in Edgeless Graphene Devices," *Physical Review Letters*, vol. 121, p. 226801, Nov. 2018.

[115] R. Willett, J. P. Eisenstein, H. L. Störmer, D. C. Tsui, A. C. Gossard, and J. H. English, "Observation of an even-denominator quantum number in the fractional quantum Hall effect," *Physical Review Letters*, vol. 59, pp. 1776–1779, Oct. 1987.

[116] J. I. A. Li, C. Tan, S. Chen, Y. Zeng, T. Taniguchi, K. Watanabe, J. Hone, and C. R. Dean, "Even-denominator fractional quantum Hall states in bilayer graphene," *Science*, vol. 358, pp. 648–652, Nov. 2017.

[117] A. A. Zibrov, C. Kometter, H. Zhou, E. M. Spanton, T. Taniguchi, K. Watanabe, M. P. Zaletel, and A. F. Young, "Tunable interacting composite fermion phases in a half-filled bilayer-graphene Landau level," *Nature*, vol. 549, pp. 360–364, Sept. 2017.

[118] K. Huang, H. Fu, D. R. Hickey, N. Alem, X. Lin, K. Watanabe, T. Taniguchi, and J. Zhu, "Valley Isospin Controlled Fractional Quantum Hall States in Bilayer Graphene," *Physical Review X*, vol. 12, p. 031019, July 2022.

[119] R. Kumar, A. Haug, J. Kim, M. Yutushui, K. Khudiakov, V. Bhardwaj, A. Ilin, K. Watanabe, T. Taniguchi, D. F. Mross, and Y. Ronen, "Quarter- and half-filled quantum Hall states and their competing interactions in bilayer graphene," Oct. 2024.

[120] A. Assouline, T. Wang, H. Zhou, L. A. Cohen, F. Yang, R. Zhang, T. Taniguchi, K. Watanabe, R. S. K. Mong, M. P. Zaletel, and A. F. Young, "Energy Gap of the Even-Denominator Fractional Quantum Hall State in Bilayer Graphene," *Physical Review Letters*, vol. 132, p. 046603, Jan. 2024.

[121] B. I. Halperin, "Theory of the quantized Hall conductance," *helv. phys. acta*, vol. 56, no. 1-3, p. 75, 1983.

[122] F. D. M. Haldane and E. H. Rezayi, "Spin-singlet wave function for the half-integral quantum Hall effect," *Physical Review Letters*, vol. 60, pp. 956–959, Mar. 1988.

[123] X. G. Wen, "Non-Abelian statistics in the fractional quantum Hall states," *Physical Review Letters*, vol. 66, pp. 802–805, Feb. 1991.

[124] G. Moore and N. Read, "Nonabelions in the fractional quantum hall effect," *Nuclear Physics B*, vol. 360, pp. 362–396, Aug. 1991.

[125] M. Greiter, X. G. Wen, and F. Wilczek, "Paired Hall states," *Nuclear Physics B*, vol. 374, pp. 567–614, May 1992.

[126] K. K. W. Ma and D. E. Feldman, "The sixteenfold way and the quantum Hall effect at half-integer filling factors," *Physical Review B*, vol. 100, p. 035302, July 2019.

[127] N. Read and D. Green, "Paired states of fermions in two dimensions with breaking of parity and time-reversal symmetries and the fractional quantum Hall effect," *Physical Review B*, vol. 61, pp. 10267–10297, Apr. 2000.

[128] M. Ascher, *Mathematics of the Incas: Code of the Quipu*. Mineola: Dover Publications, 1997.

[129] P. Beynon-Davies, "Significant threads: The nature of data," *International Journal of Information Management*, vol. 29, pp. 170–188, June 2009.

[130] S. M. Frolov, M. J. Manfra, and J. D. Sau, "Topological superconductivity in hybrid devices," *Nature Physics*, vol. 16, pp. 718–724, July 2020.

[131] M. Aghaee, A. Alcaraz Ramirez, Z. Alam, R. Ali, M. Andrzejczuk, A. Antipov, M. Astafev, A. Barzegar, B. Bauer, J. Becker, U. K. Bhaskar, A. Bocharov, S. Boddapati, D. Bohn, J. Bommer, L. Bourdet, A. Bousquet, S. Boutin, L. Casparis, B. J. Chapman, S. Chatoor, A. W. Christensen, C. Chua, P. Codd, W. Cole, P. Cooper, F. Corsetti, A. Cui, P. Dalpasso, J. P. Dehollain, G. de Lange, M. de Moor, A. Ekefjärd, T. El Dandachi, J. C. Estrada Saldaña, S. Fallahi, L. Galletti, G. Gardner, D. Govender, F. Griggio, R. Grigoryan, S. Grijalva, S. Gronin, J. Gukelberger, M. Hamdast, F. Hamze, E. B. Hansen, S. Heedt, Z. Heidarnia, J. Herranz Zamorano, S. Ho, L. Holgaard, J. Hornibrook, J. Indrapiromkul, H. Ingerslev, L. Ivancevic, T. Jensen, J. Jhoja, J. Jones, K. V. Kalashnikov, R. Kallaher, R. Kalra, F. Karimi, T. Karzig, E. King, M. E. Kloster, C. Knapp, D. Kocon, J. V. Koski, P. Kostamo, M. Kumar, T. Laeven, T. Larsen, J. Lee, K. Lee, G. Leum, K. Li, T. Lindemann, M. Looij, J. Love, M. Lucas, R. Lutchyn, M. H. Madsen, N. Madulid, A. Malmros, M. Manfra, D. Mantri, S. B. Markussen, E. Martinez, M. Mattila, R. McNeil, A. B. Mei, R. V. Mishmash, G. Mohandas, C. Mollgaard, T. Morgan, G. Moussa, C. Nayak, J. H. Nielsen, J. M. Nielsen, W. H. P. Nielsen, B. Nijholt, M. Nystrom, E. O'Farrell, T. Ohki, K. Otani, B. Paquelet Wütz, S. Pauka, K. Petersson, L. Petit, D. Pikulin, G. Prawiroatmodjo, F. Preiss, E. Puchol Morejon, M. Rajpalke, C. Ranta, K. Rasmussen, D. Razmadze, O. Reentila, D. J. Reilly, Y. Ren, K. Reneris, R. Rouse, I. Sadovskyy, L. Sainiemi, I. Sanlorenzo, E. Schmidgall, C. Sfiligoj, M. B. Shah, K. Simoes, S. Singh, S. Sinha, T. Soerensen, P. Sohr, T. Stankevic, L. Stek, E. Stuppard, H. Suominen, J. Suter, S. Teicher, N. Thiyagarajah, R. Tholapi, M. Thomas, E. Toomey, J. Tracy, M. Turley, S. Upadhyay, I. Urban, K. Van Hoogdalem, D. J. Van Woerkom, D. V. Viazmitinov, D. Vogel, J. Watson, A. Webster, J. Weston, G. W. Winkler, D. Xu, C. K. Yang, E. Yucelen, R. Zeisel, G. Zheng, and J. Zilke, "Interferometric single-shot parity measurement in InAs–Al hybrid devices," *Nature*, vol. 638, pp. 651–655, Feb. 2025.

[132] T. I. Andersen, Y. D. Lensky, K. Kechedzhi, I. K. Drozdov, A. Bengtsson, S. Hong, A. Morvan, X. Mi, A. Opremcak, R. Acharya, R. Allen, M. Ansmann, F. Arute, K. Arya, A. Asfaw, J. Atalaya, R. Babbush, D. Bacon, J. C. Bardin, G. Bortoli, A. Bourassa, J. Bovaird, L. Brill, M. Broughton, B. B. Buckley, D. A. Buell, T. Burger, B. Burkett, N. Bushnell, Z. Chen, B. Chiaro, D. Chik, C. Chou, J. Cogan, R. Collins, P. Conner, W. Courtney, A. L. Crook, B. Curtin, D. M. Debroy, A. Del Toro Barba, S. Demura, A. Dunsworth, D. Eppens, C. Erickson, L. Faoro, E. Farhi, R. Fatemi, V. S. Ferreira, L. F. Burgos, E. Forati, A. G. Fowler, B. Foxen, W. Giang, C. Gidney, D. Gilboa, M. Giustina, R. Gosula, A. G. Dau, J. A. Gross, S. Habegger, M. C. Hamilton, M. Hansen, M. P. Harrigan, S. D. Harrington, P. Heu, J. Hilton, M. R. Hoffmann, T. Huang, A. Huff, W. J. Huggins, L. B. Ioffe, S. V. Isakov, J. Iveland, E. Jeffrey, Z. Jiang, C. Jones, P. Juhas, D. Kafri, T. Khattar, M. Khezri, M. Kieferová, S. Kim, A. Kitaev, P. V. Klimov, A. R. Klots, A. N. Korotkov, F. Kostritsa, J. M. Kreikebaum, D. Landhuis, P. Laptev, K.-M. Lau, L. Laws, J. Lee, K. W. Lee, B. J. Lester, A. T. Lill, W. Liu, A. Locharla, E. Lucero, F. D. Malone, O. Martin, J. R. McClean, T. McCourt, M. McEwen, K. C. Miao, A. Mieszala, M. Mohseni, S. Montazeri, E. Mount, R. Movassagh, W. Mruczkiewicz, O. Naaman, M. Neeley, C. Neill, A. Nersisyan, M. Newman, J. H. Ng, A. Nguyen, M. Nguyen, M. Y. Niu, T. E.

O'Brien, S. Omonije, A. Petukhov, R. Potter, L. P. Pryadko, C. Quintana, C. Rocque, N. C. Rubin, N. Saei, D. Sank, K. Sankaragomathi, K. J. Satzinger, H. F. Schurkus, C. Schuster, M. J. Shearn, A. Shorter, N. Shutty, V. Shvarts, J. Skruzny, W. C. Smith, R. Somma, G. Sterling, D. Strain, M. Szalay, A. Torres, G. Vidal, B. Villalonga, C. V. Heidweiller, T. White, B. W. K. Woo, C. Xing, Z. J. Yao, P. Yeh, J. Yoo, G. Young, A. Zalcman, Y. Zhang, N. Zhu, N. Zobrist, H. Neven, S. Boixo, A. Megrant, J. Kelly, Y. Chen, V. Smelyanskiy, E.-A. Kim, I. Aleiner, P. Roushan, and Google Quantum AI and Collaborators, "Non-Abelian braiding of graph vertices in a superconducting processor," *Nature*, vol. 618, pp. 264–269, June 2023.

[133] M. Iqbal, N. Tantivasadakarn, R. Verresen, S. L. Campbell, J. M. Dreiling, C. Figgatt, J. P. Gaebler, J. Johansen, M. Mills, S. A. Moses, J. M. Pino, A. Ransford, M. Rowe, P. Siegfried, R. P. Stutz, M. Foss-Feig, A. Vishwanath, and H. Dreyer, "Non-Abelian topological order and anyons on a trapped-ion processor," *Nature*, vol. 626, pp. 505–511, Feb. 2024.

[134] X.-G. Wen, "*Colloquium* : Zoo of quantum-topological phases of matter," *Reviews of Modern Physics*, vol. 89, p. 041004, Dec. 2017.

[135] L. Savary and L. Balents, "Quantum spin liquids: A review," *Reports on Progress in Physics*, vol. 80, p. 016502, Nov. 2016.

[136] Y. Zhou, K. Kanoda, and T.-K. Ng, "Quantum spin liquid states," *Reviews of Modern Physics*, vol. 89, p. 025003, Apr. 2017.

[137] C. Broholm, R. J. Cava, S. A. Kivelson, D. G. Nocera, M. R. Norman, and T. Senthil, "Quantum spin liquids," *Science*, vol. 367, p. eaay0668, Jan. 2020.

[138] C. Kallin and J. Berlinsky, "Chiral superconductors," *Reports on Progress in Physics*, vol. 79, p. 054502, Apr. 2016.

[139] J. E. Moore, "The birth of topological insulators," *Nature*, vol. 464, pp. 194–198, Mar. 2010.

[140] M. Z. Hasan and C. L. Kane, "Colloquium: Topological insulators," *Reviews of Modern Physics*, vol. 82, pp. 3045–3067, Nov. 2010.

[141] X.-G. Wen, "Topological orders and edge excitations in fractional quantum Hall states," *Advances in Physics*, vol. 44, pp. 405–473, Oct. 1995.

[142] E. Bocquillon, V. Freulon, F. D. Parmentier, J.-M. Berroir, B. Plaçais, C. Wahl, J. Rech, T. Jonckheere, T. Martin, C. Grenier, D. Ferraro, P. Degiovanni, and G. Fève, "Electron quantum optics in ballistic chiral conductors," *Annalen der Physik*, vol. 526, no. 1-2, pp. 1–30, 2014.

[143] H. Chakraborti, C. Gorini, A. Knothe, M.-H. Liu, P. Makk, F. D. Parmentier, D. Perconte, K. Richter, P. Roulleau, B. Sacépé, C. Schönenberger, and W. Yang, "Electron wave and quantum optics in graphene," *Journal of Physics: Condensed Matter*, vol. 36, p. 393001, July 2024.

[144] B. J. van Wees, H. van Houten, C. W. J. Beenakker, J. G. Williamson, L. P. Kouwenhoven, D. van der Marel, and C. T. Foxon, "Quantized conductance of point contacts in a two-dimensional electron gas," *Physical Review Letters*, vol. 60, pp. 848–850, Feb. 1988.

[145] Y. Ji, Y. Chung, D. Sprinzak, M. Heiblum, D. Mahalu, and H. Shtrikman, "An electronic Mach–Zehnder interferometer," *Nature*, vol. 422, pp. 415–418, Mar. 2003.

[146] F. E. Camino, W. Zhou, and V. J. Goldman, "Realization of a Laughlin quasiparticle interferometer: Observation of fractional statistics," *Physical Review B*, vol. 72, p. 075342, Aug. 2005.

[147] F. E. Camino, W. Zhou, and V. J. Goldman, "Aharonov-Bohm Superperiod in a Laughlin Quasiparticle Interferometer," *Physical Review Letters*, vol. 95, p. 246802, Dec. 2005.

[148] F. E. Camino, W. Zhou, and V. J. Goldman, "$e/3$ Laughlin Quasiparticle Primary-Filling $\ensuremath{\nu}=1/3$ Interferometer," *Physical Review Letters*, vol. 98, p. 076805, Feb. 2007.

[149] I. Neder, N. Ofek, Y. Chung, M. Heiblum, D. Mahalu, and V. Umansky, "Interference between two indistinguishable electrons from independent sources," *Nature*, vol. 448, pp. 333–337, July 2007.

[150] N. Ofek, A. Bid, M. Heiblum, A. Stern, V. Umansky, and D. Mahalu, "Role of interactions in an electronic Fabry–Perot interferometer operating in the quantum Hall effect regime," *Proceedings of the National Academy of Sciences*, vol. 107, pp. 5276–5281, Mar. 2010.

[151] Y. Zhang, D. T. McClure, E. M. Levenson-Falk, C. M. Marcus, L. N. Pfeiffer, and K. W. West, "Distinct signatures for Coulomb blockade and Aharonov-Bohm interference in electronic Fabry-Perot interferometers," *Physical Review B*, vol. 79, p. 241304, June 2009.

[152] D. T. McClure, Y. Zhang, B. Rosenow, E. M. Levenson-Falk, C. M. Marcus, L. N. Pfeiffer, and K. W. West, "Edge-State Velocity and Coherence in a Quantum Hall Fabry-P\'erot Interferometer," *Physical Review Letters*, vol. 103, p. 206806, Nov. 2009.

[153] D. T. McClure, W. Chang, C. M. Marcus, L. N. Pfeiffer, and K. W. West, "Fabry-Perot Interferometry with Fractional Charges," *Physical Review Letters*, vol. 108, p. 256804, June 2012.

[154] A. Kou, C. M. Marcus, L. N. Pfeiffer, and K. W. West, "Coulomb Oscillations in Antidots in the Integer and Fractional Quantum Hall Regimes," *Physical Review Letters*, vol. 108, p. 256803, June 2012.

[155] H. Choi, P. Jiang, M. D. Godfrey, W. Kang, S. H. Simon, L. N. Pfeiffer, K. W. West, and K. W. Baldwin, "Aharonov–Bohm-like oscillations in Fabry–Perot interferometers," *New Journal of Physics*, vol. 13, p. 055007, May 2011.

[156] S. An, P. Jiang, H. Choi, W. Kang, S. H. Simon, L. N. Pfeiffer, K. W. West, and K. W. Baldwin, "Braiding of Abelian and Non-Abelian Anyons in the Fractional Quantum Hall Effect," Dec. 2011.

[157] R. L. Willett, L. N. Pfeiffer, and K. W. West, "Measurement of filling factor 5/2 quasiparticle interference with observation of charge e/4 and e/2 period oscillations," *Proceedings of the National Academy of Sciences*, vol. 106, pp. 8853–8858, June 2009.

[158] R. L. Willett, L. N. Pfeiffer, and K. W. West, "Alternation and interchange of e/4 and e/2 period interference oscillations consistent with filling factor 5/2 non-Abelian quasiparticles," *Physical Review B*, vol. 82, p. 205301, Nov. 2010.

[159] R. L. Willett, C. Nayak, K. Shtengel, L. N. Pfeiffer, and K. W. West, "Magnetic-Field-Tuned Aharonov-Bohm Oscillations and Evidence for Non-Abelian Anyons at $\ensuremath{\nu}=5/2$," *Physical Review Letters*, vol. 111, p. 186401, Oct. 2013.

[160] R. L. Willett, K. Shtengel, C. Nayak, L. N. Pfeiffer, Y. J. Chung, M. L. Peabody, K. W. Baldwin, and K. W. West, "Interference Measurements of Non-Abelian $e/4$ & Abelian $e/2$ Quasiparticle Braiding," *Physical Review X*, vol. 13, p. 011028, Mar. 2023.

[161] I. Sivan, H. K. Choi, J. Park, A. Rosenblatt, Y. Gefen, D. Mahalu, and V. Umansky, "Observation of interaction-induced modulations of a quantum Hall liquid's area," *Nature Communications*, vol. 7, p. 12184, July 2016.

[162] H. K. Kundu, S. Biswas, N. Ofek, V. Umansky, and M. Heiblum, "Anyonic interference and braiding phase in a Mach-Zehnder interferometer," *Nature Physics*, vol. 19, pp. 515–521, Apr. 2023.

[163] J. Nakamura, S. Fallahi, H. Sahasrabudhe, R. Rahman, S. Liang, G. C. Gardner, and M. J. Manfra, "Aharonov–Bohm interference of fractional quantum Hall edge modes," *Nature Physics*, vol. 15, pp. 563–569, June 2019.

[164] J. Nakamura, S. Liang, G. C. Gardner, and M. J. Manfra, "Direct observation of anyonic braiding statistics," *Nature Physics*, vol. 16, pp. 931–936, Sept. 2020.

[165] J. Nakamura, S. Liang, G. C. Gardner, and M. J. Manfra, "Impact of bulk-edge coupling on observation of anyonic braiding statistics in quantum Hall interferometers," *Nature Communications*, vol. 13, p. 344, Jan. 2022.

[166] J. Nakamura, S. Liang, G. C. Gardner, and M. J. Manfra, "Fabry-Pérot Interferometry at the $\nu = 2 / 5$ Fractional Quantum Hall State," *Physical Review X*, vol. 13, p. 041012, Oct. 2023.

[167] B. J. van Wees, L. P. Kouwenhoven, C. J. P. M. Harmans, J. G. Williamson, C. E. Timmering, M. E. I. Broekaart, C. T. Foxon, and J. J. Harris, "Observation of zero-dimensional states in a one-dimensional electron interferometer," *Physical Review Letters*, vol. 62, pp. 2523–2526, May 1989.

[168] C. de C. Chamon, D. E. Freed, S. A. Kivelson, S. L. Sondhi, and X. G. Wen, "Two point-contact interferometer for quantum Hall systems," *Physical Review B*, vol. 55, pp. 2331–2343, Jan. 1997.

[169] B. I. Halperin, A. Stern, I. Neder, and B. Rosenow, "Theory of the fabry-perot quantum hall interferometer," *Physical Review B*, vol. 83, p. 155440, Apr. 2011.

[170] C. W. von Keyserlingk, S. H. Simon, and B. Rosenow, "Enhanced Bulk-Edge Coulomb Coupling in Fractional Fabry-Perot Interferometers," *Physical Review Letters*, vol. 115, p. 126807, Sept. 2015.

[171] D. E. Feldman and B. I. Halperin, "Robustness of quantum Hall interferometry," *Physical Review B*, vol. 105, p. 165310, Apr. 2022.

[172] C. R. Dean, A. F. Young, I. Meric, C. Lee, L. Wang, S. Sorgenfrei, K. Watanabe, T. Taniguchi, P. Kim, K. L. Shepard, and J. Hone, "Boron nitride substrates for high-quality graphene electronics," *Nature Nanotechnology*, vol. 5, pp. 722–726, Oct. 2010.

[173] Y. Zeng, J. I. A. Li, S. A. Dietrich, O. M. Ghosh, K. Watanabe, T. Taniguchi, J. Hone, and C. R. Dean, "High-Quality Magnetotransport in Graphene Using the Edge-Free Corbino Geometry," *Physical Review Letters*, vol. 122, p. 137701, Apr. 2019.

[174] R. Ribeiro-Palau, S. Chen, Y. Zeng, K. Watanabe, T. Taniguchi, J. Hone, and C. R. Dean, "High-Quality Electrostatically Defined Hall Bars in Monolayer Graphene," *Nano Letters*, vol. 19, pp. 2583–2587, Apr. 2019.

[175] A. Fasolino, J. H. Los, and M. I. Katsnelson, "Intrinsic ripples in graphene," *Nature Materials*, vol. 6, pp. 858–861, Nov. 2007.

[176] R. J. T. Nicholl, H. J. Conley, N. V. Lavrik, I. Vlassiouk, Y. S. Puzyrev, V. P. Sreenivas, S. T. Pantelides, and K. I. Bolotin, "The effect of intrinsic crumpling on the mechanics of free-standing graphene," *Nature Communications*, vol. 6, p. 8789, Nov. 2015.

[177] S. Deng and V. Berry, "Wrinkled, rippled and crumpled graphene: An overview of formation mechanism, electronic properties, and applications," *Materials Today*, vol. 19, pp. 197–212, May 2016.

[178] D. G. Purdie, N. M. Pugno, T. Taniguchi, K. Watanabe, A. C. Ferrari, and A. Lombardo, "Cleaning interfaces in layered materials heterostructures," *Nature Communications*, vol. 9, p. 5387, Dec. 2018.

[179] K. S. Novoselov, D. Jiang, F. Schedin, T. J. Booth, V. V. Khotkevich, S. V. Morozov, and A. K. Geim, "Two-dimensional atomic crystals," *Proceedings of the National Academy of Sciences*, vol. 102, pp. 10451–10453, July 2005.

[180] L. Zhao, E. G. Arnault, T. F. Q. Larson, Z. Iftikhar, A. Seredinski, T. Fleming, K. Watanabe, T. Taniguchi, F. Amet, and G. Finkelstein, "Graphene-Based Quantum Hall Interferometer with Self-Aligned Side Gates," *Nano Letters*, vol. 22, pp. 9645–9651, Dec. 2022.

[181] M. P. Röösli, L. Brem, B. Kratochwil, G. Nicolí, B. A. Braem, S. Hennel, P. Märki, M. Berl, C. Reichl, W. Wegscheider, K. Ensslin, T. Ihn, and B. Rosenow, "Observation of quantum Hall interferometer phase jumps due to a change in the number of bulk quasiparticles," *Physical Review B*, vol. 101, p. 125302, Mar. 2020.

[182] L. Wang, I. Meric, P. Y. Huang, Q. Gao, Y. Gao, H. Tran, T. Taniguchi, K. Watanabe, L. M. Campos, D. A. Muller, J. Guo, P. Kim, J. Hone, K. L. Shepard, and C. R. Dean, "One-Dimensional Electrical Contact to a Two-Dimensional Material," *Science*, vol. 342, pp. 614–617, Nov. 2013.

[183] A. Perot and C. Fabry, "On the Application of Interference Phenomena to the Solution of Various Problems of Spectroscopy and Metrology," *The Astrophysical Journal*, vol. 9, p. 87, Feb. 1899.

[184] H. Bartolomei, M. Kumar, R. Bisognin, A. Marguerite, J.-M. Berroir, E. Bocquillon, B. Plaçais, A. Cavanna, Q. Dong, U. Gennser, Y. Jin, and G. Fève, "Fractional statistics in anyon collisions," *Science*, vol. 368, pp. 173–177, Apr. 2020.

[185] A. A. Zibrov, E. M. Spanton, H. Zhou, C. Kometter, T. Taniguchi, K. Watanabe, and A. F. Young, "Even-denominator fractional quantum Hall states at an isospin transition in monolayer graphene," *Nature Physics*, vol. 14, pp. 930–935, Sept. 2018.

[186] J. Li, R.-X. Zhang, Z. Yin, J. Zhang, K. Watanabe, T. Taniguchi, C. Liu, and J. Zhu, "A valley valve and electron beam splitter," *Science*, vol. 362, pp. 1149–1152, Dec. 2018.

[187] P. Rickhaus, R. Maurand, M.-H. Liu, M. Weiss, K. Richter, and C. Schönenberger, "Ballistic interferences in suspended graphene," *Nature Communications*, vol. 4, p. 2342, Aug. 2013.

[188] N. F. Ahmad, K. Komatsu, T. Iwasaki, K. Watanabe, T. Taniguchi, H. Mizuta, Y. Wakayama, A. M. Hashim, Y. Morita, S. Moriyama, and S. Nakaharai, "Fabry–Pérot resonances and a crossover to the quantum Hall regime in ballistic graphene quantum point contacts," *Scientific Reports*, vol. 9, p. 3031, Feb. 2019.

[189] L. Veyrat, A. Jordan, K. Zimmermann, F. Gay, K. Watanabe, T. Taniguchi, H. Sellier, and B. Sacépé, "Low-Magnetic-Field Regime of a Gate-Defined Constriction in High-Mobility Graphene," *Nano Letters*, vol. 19, pp. 635–642, Feb. 2019.

[190] G.-Q. Zhang, L. Lin, H. Peng, Z. Liu, N. Kang, and H.-Q. Xu, "Coulomb-dominated oscillations in a graphene quantum Hall Fabry–Pérot interferometer*," *Chinese Physics B*, vol. 28, p. 127203, Dec. 2019.

[191] S. Morikawa, S. Masubuchi, R. Moriya, K. Watanabe, T. Taniguchi, and T. Machida, "Edge-channel interferometer at the graphene quantum Hall pn junction," *Applied Physics Letters*, vol. 106, p. 183101, May 2015.

[192] D. S. Wei, T. van der Sar, J. D. Sanchez-Yamagishi, K. Watanabe, T. Taniguchi, P. Jarillo-Herrero, B. I. Halperin, and A. Yacoby, "Mach-Zehnder interferometry using spin- and valley-polarized quantum Hall edge states in graphene," *Science Advances*, vol. 3, p. e1700600, Aug. 2017.

[193] S. Nakaharai, J. R. Williams, and C. M. Marcus, "Gate-Defined Graphene Quantum Point Contact in the Quantum Hall Regime," *Physical Review Letters*, vol. 107, p. 036602, July 2011.

[194] K. Zimmermann, A. Jordan, F. Gay, K. Watanabe, T. Taniguchi, Z. Han, V. Bouchiat, H. Sellier, and B. Sacépé, "Tunable transmission of quantum Hall edge channels with full degeneracy lifting in split-gated graphene devices," *Nature Communications*, vol. 8, p. 14983, Apr. 2017.

[195] S. Baer, C. Rössler, E. C. de Wiljes, P.-L. Ardelt, T. Ihn, K. Ensslin, C. Reichl, and W. Wegscheider, "Interplay of fractional quantum Hall states and localization in quantum point contacts," *Physical Review B*, vol. 89, p. 085424, Feb. 2014.

[196] I. Neder, M. Heiblum, Y. Levinson, D. Mahalu, and V. Umansky, "Unexpected Behavior in a Two-Path Electron Interferometer," *Physical Review Letters*, vol. 96, p. 016804, Jan. 2006.

[197] C. Déprez, L. Veyrat, H. Vignaud, G. Nayak, K. Watanabe, T. Taniguchi, F. Gay, H. Sellier, and B. Sacépé, "A tunable Fabry–Pérot quantum Hall interferometer in graphene," *Nature Nanotechnology*, vol. 16, pp. 555–562, May 2021.

[198] Q. Shi, E.-M. Shih, M. V. Gustafsson, D. A. Rhodes, B. Kim, K. Watanabe, T. Taniguchi, Z. Papić, J. Hone, and C. R. Dean, "Odd- and even-denominator fractional quantum Hall states in monolayer WSe2," *Nature Nanotechnology*, vol. 15, pp. 569–573, July 2020.

[199] F. Amet, C. T. Ke, I. V. Borzenets, J. Wang, K. Watanabe, T. Taniguchi, R. S. Deacon, M. Yamamoto, Y. Bomze, S. Tarucha, and G. Finkelstein, "Supercurrent in the quantum Hall regime," *Science*, vol. 352, pp. 966–969, May 2016.

[200] G.-H. Lee, K.-F. Huang, D. K. Efetov, D. S. Wei, S. Hart, T. Taniguchi, K. Watanabe, A. Yacoby, and P. Kim, "Inducing superconducting correlation in quantum Hall edge states," *Nature Physics*, vol. 13, pp. 693–698, July 2017.

[201] L. Zhao, E. G. Arnault, A. Bondarev, A. Seredinski, T. F. Q. Larson, A. W. Draelos, H. Li, K. Watanabe, T. Taniguchi, F. Amet, H. U. Baranger, and G. Finkelstein, "Interference of chiral Andreev edge states," *Nature Physics*, vol. 16, pp. 862–867, Aug. 2020.

[202] X.-L. Huang and Y. V. Nazarov, "Interaction-induced supercurrent in quantum Hall setups," *Physical Review B*, vol. 100, p. 155411, Oct. 2019.

[203] D. J. Clarke, J. Alicea, and K. Shtengel, "Exotic non-Abelian anyons from conventional fractional quantum Hall states," *Nature Communications*, vol. 4, p. 1348, Jan. 2013.

[204] R. S. K. Mong, D. J. Clarke, J. Alicea, N. H. Lindner, P. Fendley, C. Nayak, Y. Oreg, A. Stern, E. Berg, K. Shtengel, and M. P. A. Fisher, "Universal Topological Quantum Computation from a Superconductor-Abelian Quantum Hall Heterostructure," *Physical Review X*, vol. 4, p. 011036, Mar. 2014.

[205] T. Giamarchi, *Quantum Physics in One Dimension*. Clarendon Press, Dec. 2003.

[206] M. Carrega, L. Chirolli, S. Heun, and L. Sorba, "Anyons in quantum Hall interferometry," *Nature Reviews Physics*, vol. 3, pp. 698–711, Oct. 2021.

[207] Y. Ronen, T. Werkmeister, D. Haie Najafabadi, A. T. Pierce, L. E. Anderson, Y. J. Shin, S. Y. Lee, Y. H. Lee, B. Johnson, K. Watanabe, T. Taniguchi, A. Yacoby, and P. Kim, "Aharonov–Bohm effect in graphene-based Fabry–Pérot quantum Hall interferometers," *Nature Nanotechnology*, vol. 16, pp. 563–569, May 2021.

[208] H. Fu, K. Huang, K. Watanabe, T. Taniguchi, M. Kayyalha, and J. Zhu, "Aharonov–Bohm Oscillations in Bilayer Graphene Quantum Hall Edge State Fabry–Pérot Interferometers," *Nano Letters*, vol. 23, pp. 718–725, Jan. 2023.

[209] H. K. Choi, I. Sivan, A. Rosenblatt, M. Heiblum, V. Umansky, and D. Mahalu, "Robust electron pairing in the integer quantum hall effect regime," *Nature Communications*, vol. 6, p. 7435, June 2015.

[210] I. Sivan, R. Bhattacharyya, H. K. Choi, M. Heiblum, D. E. Feldman, D. Mahalu, and V. Umansky, "Interaction-induced interference in the integer quantum Hall effect," *Physical Review B*, vol. 97, p. 125405, Mar. 2018.

[211] S. Biswas, H. K. Kundu, V. Umansky, and M. Heiblum, "Electron Pairing of Interfering Interface-Based Edge Modes," *Physical Review Letters*, vol. 131, p. 096302, Sept. 2023.

[212] A. Demir, N. Staley, S. Aronson, S. Tomarken, K. West, K. Baldwin, L. Pfeiffer, and R. Ashoori, "Correlated Double-Electron Additions at the Edge of a Two-Dimensional Electronic System," *Physical Review Letters*, vol. 126, p. 256802, June 2021.

[213] B. Keimer, S. A. Kivelson, M. R. Norman, S. Uchida, and J. Zaanen, "From quantum matter to high-temperature superconductivity in copper oxides," *Nature*, vol. 518, pp. 179–186, Feb. 2015.

[214] R. L. Willett, "The quantum Hall effect at 5/2 filling factor," *Reports on Progress in Physics*, vol. 76, p. 076501, June 2013.

[215] G. A. Frigeri, D. D. Scherer, and B. Rosenow, "Sub-periods and apparent pairing in integer quantum Hall interferometers," *Europhysics Letters*, vol. 126, p. 67007, July 2019.

[216] M. Büttiker, "Quantized transmission of a saddle-point constriction," *Physical Review B*, vol. 41, pp. 7906–7909, Apr. 1990.

[217] W. Yang, D. Perconte, C. Déprez, K. Watanabe, T. Taniguchi, S. Dumont, E. Wagner, F. Gay, I. Safi, H. Sellier, and B. Sacépé, "Evidence for correlated electron pairs and triplets in quantum Hall interferometers," *Nature Communications*, vol. 15, p. 10064, Nov. 2024.

[218] G. Shavit and Y. Oreg, "Electron pairing induced by repulsive interactions in tunable one-dimensional platforms," *Physical Review Research*, vol. 2, p. 043283, Nov. 2020.

[219] G. A. Frigeri and B. Rosenow, "Electron pairing in the quantum Hall regime due to neutralon exchange," *Physical Review Research*, vol. 2, p. 043396, Dec. 2020.

[220] H. Inoue, A. Grivnin, N. Ofek, I. Neder, M. Heiblum, V. Umansky, and D. Mahalu, "Charge Fractionalization in the Integer Quantum Hall Effect," *Physical Review Letters*, vol. 112, p. 166801, Apr. 2014.

[221] Z. Wei, D. E. Feldman, and B. I. Halperin, "Quantum Hall interferometry at finite bias with multiple edge channels," *Physical Review B*, vol. 110, p. 075306, Aug. 2024.

[222] C. Altimiras, H. le Sueur, U. Gennser, A. Cavanna, D. Mailly, and F. Pierre, "Non-equilibrium edge-channel spectroscopy in the integer quantum Hall regime," *Nature Physics*, vol. 6, pp. 34–39, Jan. 2010.

[223] E. Bocquillon, V. Freulon, J.-M. Berroir, P. Degiovanni, B. Plaçais, A. Cavanna, Y. Jin, and G. Fève, "Separation of neutral and charge modes in one-dimensional chiral edge channels," *Nature Communications*, vol. 4, p. 1839, May 2013.

[224] V. Freulon, A. Marguerite, J.-M. Berroir, B. Plaçais, A. Cavanna, Y. Jin, and G. Fève, "Hong-Ou-Mandel experiment for temporal investigation of single-electron fractionalization," *Nature Communications*, vol. 6, p. 6854, Apr. 2015.

[225] M. Hashisaka, N. Hiyama, T. Akiho, K. Muraki, and T. Fujisawa, "Waveform measurement of charge- and spin-density wavepackets in a chiral Tomonaga–Luttinger liquid," *Nature Physics*, vol. 13, pp. 559–562, June 2017.

[226] M. Hashisaka and T. Fujisawa, "Tomonaga–Luttinger-liquid nature of edge excitations in integer quantum Hall edge channels," *Reviews in Physics*, vol. 3, pp. 32–43, Nov. 2018.

[227] J. Kim, H. Dev, R. Kumar, A. Ilin, A. Haug, V. Bhardwaj, C. Hong, K. Watanabe, T. Taniguchi, A. Stern, and Y. Ronen, "Aharonov–Bohm interference and statistical phase-jump evolution in fractional quantum Hall states in bilayer graphene," *Nature Nanotechnology*, vol. 19, pp. 1619–1626, Nov. 2024.

[228] T. Werkmeister, J. R. Ehrets, M. E. Wesson, D. H. Najafabadi, K. Watanabe, T. Taniguchi, B. I. Halperin, A. Yacoby, and P. Kim, "Anyon braiding and telegraph noise in a graphene interferometer," *Science*, vol. 388, pp. 730–735, May 2025.

[229] N. L. Samuelson, L. A. Cohen, W. Wang, S. Blanch, T. Taniguchi, K. Watanabe, M. P. Zaletel, and A. F. Young, "Anyonic statistics and slow quasiparticle dynamics in a graphene fractional quantum Hall interferometer," Mar. 2024.

[230] A. Stern, "Anyons and the quantum Hall effect—A pedagogical review," *Annals of Physics*, vol. 323, pp. 204–249, Jan. 2008.

[231] H. Overweg, H. Eggimann, X. Chen, S. Slizovskiy, M. Eich, R. Pisoni, Y. Lee, P. Rickhaus, K. Watanabe, T. Taniguchi, V. Fal'ko, T. Ihn, and K. Ensslin, "Electrostatically Induced Quantum Point Contacts in Bilayer Graphene," *Nano Letters*, vol. 18, pp. 553–559, Jan. 2018.

[232] T. Werkmeister, J. R. Ehrets, Y. Ronen, M. E. Wesson, D. Najafabadi, Z. Wei, K. Watanabe, T. Taniguchi, D. E. Feldman, B. I. Halperin, A. Yacoby, and P. Kim, "Strongly coupled edge states in a graphene quantum Hall interferometer," *Nature Communications*, vol. 15, p. 6533, Aug. 2024.

[233] L. A. Cohen, N. L. Samuelson, T. Wang, K. Klocke, C. C. Reeves, T. Taniguchi, K. Watanabe, S. Vijay, M. P. Zaletel, and A. F. Young, "Nanoscale electrostatic control in ultraclean van der Waals heterostructures by local anodic oxidation of graphite gates," *Nature Physics*, pp. 1–7, June 2023.

[234] L. A. Cohen, N. L. Samuelson, T. Wang, T. Taniguchi, K. Watanabe, M. P. Zaletel, and A. F. Young, "Universal chiral Luttinger liquid behavior in a graphene fractional quantum Hall point contact," *Science*, vol. 382, pp. 542–547, Nov. 2023.

[235] Y. Hu, Y.-C. Tsui, M. He, U. Kamber, T. Wang, A. S. Mohammadi, K. Watanabe, T. Taniguchi, Z. Papic, M. P. Zaletel, and A. Yazdani, "High-Resolution Tunneling Spectroscopy of Fractional Quantum Hall States," Aug. 2023.

[236] C. L. Kane, "Telegraph Noise and Fractional Statistics in the Quantum Hall Effect," *Physical Review Letters*, vol. 90, p. 226802, June 2003.

[237] E. Grosfeld, S. H. Simon, and A. Stern, "Switching Noise as a Probe of Statistics in the Fractional Quantum Hall Effect," *Physical Review Letters*, vol. 96, p. 226803, June 2006.

[238] B. Rosenow and S. H. Simon, "Telegraph noise and the Fabry-Perot quantum Hall interferometer," *Physical Review B*, vol. 85, p. 201302, May 2012.

[239] M. P. Röösli, M. Hug, G. Nicolí, P. Märki, C. Reichl, B. Rosenow, W. Wegscheider, K. Ensslin, and T. Ihn, "Fractional Coulomb blockade for quasi-particle tunneling between edge channels," *Science Advances*, vol. 7, p. eabf5547, May 2021.

[240] B. Rosenow and A. Stern, "Flux Superperiods and Periodicity Transitions in Quantum Hall Interferometers," *Physical Review Letters*, vol. 124, p. 106805, Mar. 2020.

[241] M. B. Weissman, "1/f noise and other slow, nonexponential kinetics in condensed matter," *Reviews of Modern Physics*, vol. 60, pp. 537–571, Apr. 1988.

[242] "1/f noise and random telegraph noise," in *Electronic Noise and Fluctuations in Solids* (Sh. Kogan, ed.), pp. 203–286, Cambridge: Cambridge University Press, 1996.

[243] K. Bennaceur, P. Jacques, F. Portier, P. Roche, and D. C. Glattli, "Unveiling quantum Hall transport by Efros-Shklovskii to Mott variable-range hopping transition in graphene," *Physical Review B*, vol. 86, p. 085433, Aug. 2012.

[244] A. L. Efros, N. Van Lien, and B. I. Shklovskii, "Variable range hopping in doped crystalline semiconductors," *Solid State Communications*, vol. 32, pp. 851–854, Dec. 1979.

[245] A. L. Efros and B. I. Shklovskii, "Coulomb gap and low temperature conductivity of disordered systems," *Journal of Physics C: Solid State Physics*, vol. 8, p. L49, Feb. 1975.

[246] G. Ebert, K. von Klitzing, C. Probst, E. Schuberth, K. Ploog, and G. Weimann, "Hopping conduction in the Landau level tails in GaAs-AlxGa1-xAs heterostructures at low temperatures," *Solid State Communications*, vol. 45, pp. 625–628, Feb. 1983.

[247] A. J. M. Giesbers, U. Zeitler, L. A. Ponomarenko, R. Yang, K. S. Novoselov, A. K. Geim, and J. C. Maan, "Scaling of the quantum Hall plateau-plateau transition in graphene," *Physical Review B*, vol. 80, p. 241411, Dec. 2009.

[248] M. J. Persky, "Review of black surfaces for space-borne infrared systems," *Review of Scientific Instruments*, vol. 70, pp. 2193–2217, May 1999.

[249] J. Kim, H. Dev, A. Shaer, R. Kumar, A. Ilin, A. Haug, S. Iskoz, K. Watanabe, T. Taniguchi, D. F. Mross, A. Stern, and Y. Ronen, "Aharonov-Bohm Interference in Even-Denominator Fractional Quantum Hall States," Dec. 2024.

[250] S. Das Sarma, M. Freedman, and C. Nayak, "Topologically Protected Qubits from a Possible Non-Abelian Fractional Quantum Hall State," *Physical Review Letters*, vol. 94, p. 166802, Apr. 2005.

[251] A. Stern and B. I. Halperin, "Proposed experiments to probe the non-abelian $\nu = 5/2$ quantum hall state," *Physical Review Letters*, vol. 96, p. 016802, Jan. 2006.

[252] P. Bonderson, A. Kitaev, and K. Shtengel, "Detecting Non-Abelian Statistics in the $\nu = 5 / 2$ Fractional Quantum Hall State," *Physical Review Letters*, vol. 96, p. 016803, Jan. 2006.

[253] L. Ju, A. H. MacDonald, K. F. Mak, J. Shan, and X. Xu, "The fractional quantum anomalous Hall effect," *Nature Reviews Materials*, pp. 1–5, June 2024.

[254] J. Cai, E. Anderson, C. Wang, X. Zhang, X. Liu, W. Holtzmann, Y. Zhang, F. Fan, T. Taniguchi, K. Watanabe, Y. Ran, T. Cao, L. Fu, D. Xiao, W. Yao, and X. Xu, "Signatures of fractional quantum anomalous Hall states in twisted MoTe2," *Nature*, vol. 622, pp. 63–68, Oct. 2023.

[255] H. Park, J. Cai, E. Anderson, Y. Zhang, J. Zhu, X. Liu, C. Wang, W. Holtzmann, C. Hu, Z. Liu, T. Taniguchi, K. Watanabe, J.-H. Chu, T. Cao, L. Fu, W. Yao, C.-Z. Chang, D. Cobden, D. Xiao, and X. Xu, "Observation of fractionally quantized anomalous Hall effect," *Nature*, vol. 622, pp. 74–79, Oct. 2023.

[256] Y. Zeng, Z. Xia, K. Kang, J. Zhu, P. Knüppel, C. Vaswani, K. Watanabe, T. Taniguchi, K. F. Mak, and J. Shan, "Thermodynamic evidence of fractional Chern insulator in moiré MoTe2," *Nature*, vol. 622, pp. 69–73, Oct. 2023.

[257] K. Kang, B. Shen, Y. Qiu, Y. Zeng, Z. Xia, K. Watanabe, T. Taniguchi, J. Shan, and K. F. Mak, "Evidence of the fractional quantum spin Hall effect in moiré MoTe2," *Nature*, vol. 628, pp. 522–526, Apr. 2024.

[258] Z. Lu, T. Han, Y. Yao, A. P. Reddy, J. Yang, J. Seo, K. Watanabe, T. Taniguchi, L. Fu, and L. Ju, "Fractional quantum anomalous Hall effect in multilayer graphene," *Nature*, vol. 626, pp. 759–764, Feb. 2024.

[259] Z. Lu, T. Han, Y. Yao, Z. Hadjri, J. Yang, J. Seo, L. Shi, S. Ye, K. Watanabe, T. Taniguchi, and L. Ju, "Extended quantum anomalous Hall states in graphene/hBN moiré superlattices," *Nature*, vol. 637, pp. 1090–1095, Jan. 2025.



This thesis was typeset using LaTeX, originally developed by Leslie Lamport and based on Donald Knuth's TeX. The body text is set in 11 point Egenolff-Berner Garamond, a revival of Claude Garamont's humanist typeface. A template that can be used to format a PhD thesis with this look and feel has been released under the permissive MIT (X11) license, and can be found online at github.com/suchow/Dissertate or from its author, Jordan Suchow, at suchow@post.harvard.edu. The sunset above was seen on the Adriatic Sea by Trieste.